

Enabling Stroke Theranostics with Hyperpolarized Magnetic Resonance

Présentée le 22 septembre 2023

Faculté des sciences de base
Laboratoire Leenaards-Jeantet d'imagerie fonctionnelle et métabolique
Programme doctoral en physique

pour l'obtention du grade de Docteur ès Sciences

par

Thanh Phong Kevin LÊ

Acceptée sur proposition du jury

Prof. H. Brune, président du jury
Prof. R. Gruetter, Prof. J.-N. Hyacinthe, directeurs de thèse
Prof. S. Jannin, rapporteur
Prof. F. Schilling, rapporteur
Prof. J.-Ph. Ansermet, rapporteur

Acknowledgements

This thesis has been a rewarding adventure over the past years and I am deeply grateful to all those who have supported me and made it possible.

I would like to start with my thesis advisors. Rolf, thank you for hosting me in your lab, sharing your advice, and for giving me the freedom to explore the paths I have chosen. Jean-Noël, I am beyond grateful for your constant support. Your unfailing enthusiasm, patience, perseverance and resilience, no matter the mountainous obstacles, have been invaluable. Thank you so much for guiding and encouraging me throughout this journey, for sharing your vision with me, and most of all for your trust in every circumstance.

I am very obliged to Prof. Sami Jannin, Prof. Franz Schilling, Prof. Jean-Philippe Ansermet and Prof. Harald Brune, for being part of my thesis committee, for their stimulating questions, as well as for their precious feedback on my manuscript and research.

There can only be two thesis advisors, but several other people also played a key role. I am really thankful to Mor for introducing me to the practicalities of HP MR, for sharing your passion for biochemistry, and for the many long rewriting sessions. Lorenz, thank you for the stimulating exchanges over all these years. In particular, your clinical perspective has made my work more concrete by relating it to current important challenges. Andrea, it has been a blessing to have the opportunity to work with you on many amazing hardware projects.

Lara, I cannot thank you enough for being such an important pillar: your surgical skills, but also your cheering talents were a guarantee for a successful experiment outcome. Analina, Mario, Roxane, Stefan and Valentine, the veterinary team, your animal-related work with full dedication, even when things went off plans, was so valuable.

Hikari, with whom I share a similar taste for tidiness, you have been a great help teaching me the ins and outs of these hand-crafted polarizers and keeping them up and running. Jacques, thank you for sharing your extensive experience in experimental physics and embarking me on even more hardware projects.

Acknowledgements

Bernard, Cristina, Hongxia, Ileana, the animal magnet managers, I really appreciated your availability and support with the MRIs, as well as the many fruitful discussions. Bernard, it was very kind of you to take the time to correct punctiliously my imaging chapter.

I am very grateful to João and Özlem, with whom my journey in biomedical imaging started. You patiently taught me about MRI and RF electromagnetism, and more importantly, linked my physics studies to real and concrete applications.

I had the great pleasure of sharing the office with Alice for six years, and will keep plenty of good memories. I will not forget the countless coffee and ice-cream breaks, our wonderful basil, nor your tiramisù ☺. I also thank my former office neighbors: Emmanuelle and Claudia with their contagious cheerfulness, Radek and his constant presence, and Jérémie my RF lab buddy. We had a blast on post-conference trips! We also hosted many cheerful short-term office mates: Irene, Catarina, Alexandre and Punitkumar.

Dunja and Jessie, *la grande et la petite*, your positivity and humor are incredible! Thank you for being so helpful and supportive whenever I was stuck, as well as for our daily (late) morning coffees. Jessie, I send you all my encouragement for your last stretch, you are next! Brayan, Jessie, Dunja and Davor, the Parmentier/Alpine's loyal customers, I greatly enjoyed all the lunches spent together!

I am very thankful to Yves, always here to fiddle with broken equipment, Lillian and Anh who solved all my administrative problems, indeed "*There are only solutions!*", and Nasreen, who always brings her good mood and makes sure everything stays spotless.

I also extend my appreciation to the remaining users, students, colleagues and staff of the EPFL MRI labs: Andreea, Antoine, Antonia, Carole, Christina, Christopher, Daniel, Dario, Dimitri, Elise, Emine, Emma, Estelle, Eulalia, Fatemeh, Florian, Francesca, Frédéric, Gilles, Guillaume, Jan, Jessica, Katarzyna, Lijing, Lionel, Lucie, Marc, Mark, Masoumeh, Nathalie, Nicolas, Nikolaos, Olivier, Pina, Rajesh, Sandra, Sarah, Song-I, Steffen, Tanja, Ting, Valerio, Veronika, Wiktor, Xinyu, Ying, Yohan (×2), Yujian, Zhiwei. Thank you for creating a great atmosphere and the many fun activities. My apologies to anyone I may have forgotten!

I want to express my gratitude to my friends, in particular my high school classmates, *la 3M03*, with whom we continue to share wonderful moments together, especially during our traditional summer *grillades*, and winter *crêpes*.

Finally, and most importantly, my deepest thanks and eternal gratitude go to my family, my sister Phuong Lan, my parents Xuan and Lang, who have always encouraged me to achieve my dreams, and have been supporting me unconditionally all these years.

Lausanne, August 2023

Thanh Phong Lê

Abstract

The severe social and economic burden of stroke is a strong motivation for the exploration of innovative medical approaches. In this context, magnetic resonance (MR) of hyperpolarized (HP) molecular agents via dissolution dynamic nuclear polarization (dDNP) allows tracking their metabolic fate *in vivo*. This may not only provide novel insights into the underlying metabolic mechanisms, but also pave the way to a theranostic approach for stroke when applied to neuroprotective agents.

This thesis focuses on the development of novel theranostic approaches to acute ischemic stroke based on HP neuroprotective agents, specifically [1-¹³C] lactate and [1-¹³C] pyruvate, in the preclinical setting. To achieve this goal, it entails two parallel aspects: exploring their aptitude as molecular biomarkers for stroke, and reinforcing the exploitation of this potential by optimizing technical and methodological aspects of HP MR experiments.

The dynamics of HP lactate and pyruvate metabolism were quantified via global MR spectroscopic measurements and kinetic modeling. Both substrates underscored their potential as biomarkers for acute ischemic stroke, showing distinct biochemical transport and metabolism in a mouse model of stroke compared to healthy animals. Although lactate is more challenging to acquire as a result of lower polarization and metabolism than pyruvate, it is of greater interest in theranostics with better demonstrated neuroprotective effects.

The effects of the nitroxyl radical TEMPOL, a dDNP polarizing agent and known neuroprotective agent, on cerebral lactate metabolism were studied to understand the dissimilar metabolic trends observed compared to previous studies. The simultaneous injection of this radical with a bolus of lactate, prepolarized with the trityl radical OX063, resulted in a higher pyruvate labeling. This emphasizes that free radicals used as polarizing agents in dDNP, despite their low dose, are not biologically inert and must be carefully considered to avoid experimental bias.

A successful HP MR experiment requires repeatable production of HP substrates. To this end, the custom fluid path (CFP) and the corresponding cryogenic probe were implemented on a dDNP polarizer to reduce user variability. This not only improved the consistency

Abstract

of both the polarization and concentration, but also enhanced the overall cryogenic and DNP performance, and facilitated the optimization of sample formulations via longitudinally detected electron spin resonance (LOD-ESR) measurements.

A multi-sample dDNP probe was built to extend the application range of HP MR. Up to three samples can be polarized simultaneously while being individually monitored, even with distinct nuclei and radicals, and then sequentially dissolved. This increases the throughput of dDNP several folds and could enable the investigation of HP multi-agent theranostic approaches to gain a more comprehensive view and target multiple facets of stroke.

To characterize the dynamic regional metabolic patterns in stroke, a ^{13}C cross-coil setup was constructed to provide sensitive coverage of the entire mouse brain, and a model-based dynamic multi-slice MR spectroscopic imaging sequence was implemented to achieve efficient sampling. This allowed mapping the cerebral biodistribution and metabolism of HP [1- ^{13}C] pyruvate with high spatiotemporal resolution, showing a distinct higher and faster lactate labeling in infarcted tissue compared to healthy regions.

Keywords: Ischemic stroke, brain, reperfusion injury, cerebral metabolism, theranostic agent, neuroprotection, hyperpolarization, dissolution dynamic nuclear polarization (dDNP), magnetic resonance spectroscopic imaging (MRSI), electron spin resonance (ESR)

Résumé

L'accident vasculaire cérébral (AVC), un lourd fardeau avec de fortes conséquences socioéconomiques, représente une importante source de motivation pour l'exploration d'approches médicales innovatrices. Dans ce contexte, les mesures de résonance magnétique (RM) d'agents hyperpolarisés (HP) par la méthode de polarisation dynamique nucléaire avec dissolution (PDN-d) offrent l'unique opportunité de suivre leur assimilation et métabolisme *in vivo* et en temps réel. Ceci permet non seulement de placer une fenêtre sur les processus biochimiques sous-jacents à l'échelle moléculaire, mais également d'ouvrir la voie vers une approche thérapeutique pour la prise en charge de l'AVC lorsqu'elle est appliquée à des agents neuroprotecteurs.

Cette thèse porte sur le développement dans un contexte préclinique d'approches thérapeutiques novatrices pour l'AVC ischémique basées sur des agents HP neuroprotecteurs, spécifiquement le [1-¹³C] lactate et le [1-¹³C] pyruvate. Afin de parvenir à cet objectif, elle se concentre sur deux aspects parallèles : l'exploration de leur aptitude en tant que biomarqueurs moléculaires de l'AVC, ainsi que le renforcement de l'exploitation de ce potentiel par l'optimisation des aspects techniques et méthodologiques de l'expérience de RM HP.

Les dynamiques métaboliques respectives du lactate et pyruvate hyperpolarisés ont été quantifiées à l'aide de mesures globales de spectroscopie par résonance magnétique (SRM) et la modélisation mathématique de leurs transformations biochimiques. Les deux substrats ont révélé leur potentiel en tant que biomarqueurs pour l'AVC ischémique, mettant en évidence une assimilation et un métabolisme cérébral distinct dans des souris ayant subi un AVC. Bien que le lactate HP soit plus difficile à mesurer de par sa polarisation inférieure et de la plus faible conversion métabolique par rapport au pyruvate, il revêt d'un meilleur intérêt dans le cadre d'une approche neuroprotectrice en raison de ses effets neuroprotecteurs plus marqués et mieux étudiés.

L'effet du radical nitroxyle TEMPOL, un agent polarisant pour la PDN-d et également une molécule neuroprotectrice, sur le métabolisme cérébral du lactate a été étudié afin d'élucider les différences observées par rapport à de précédentes études dans le même modèle animal.

L'injection conjointe de ce radical avec le lactate, préalablement hyperpolarisé avec le radical trityle OX063, a considérablement augmenté la production de pyruvate. Ceci souligne que les radicaux utilisés en tant qu'agents polarisants en PDN, malgré leur faible dose, ne sont pas biologiquement inertes et doivent être soigneusement pris en considération afin d'éviter de biaiser les mesures.

Une expérience de RM HP nécessite des substrats polarisés de manière répétable. À cet effet, un système de dissolution par circuit fluide customisé ainsi que la sonde cryogénique adaptée ont été implémentés sur un polariseur PDN-d afin de réduire la variabilité relative à l'utilisateur. Ceci a non seulement amélioré l'uniformité de la polarisation et de la concentration des substrats, mais également les performances PDN et cryogéniques du système. De plus, l'optimisation de la formulation des échantillons de PDN a été facilitée grâce à l'implémentation des mesures de résonance de spin électronique détectée longitudinalement.

Une sonde à échantillons multiples pour la PDN-d a été conçue afin d'étendre la portée des applications de la RM HP. Jusqu'à trois échantillons peuvent être polarisés simultanément tout en surveillant leur accroissement respectif, même avec des noyaux et radicaux différents, puis dissous successivement. Ceci a permis de démultiplier la capacité de production, et d'envisager des études exploitant de multiples agents théranostiques HP afin de diagnostiquer et traiter des facettes complémentaires de l'AVC.

Dans le but de localiser les changements dynamiques régionaux induits par l'AVC, un système de double antenne radiofréquence pour le carbone 13 a été mis au point afin de sonder l'entier du cerveau de la souris de manière homogène et avec une grande sensibilité. En parallèle, une séquence dynamique d'imagerie SRM multicoupe basée sur modèle a été implémentée pour permettre un échantillonnage efficace. Ainsi, la distribution et le métabolisme cérébral du pyruvate HP ont pu être cartographiés avec une grande résolution spatiotemporelle, indiquant une production de lactate plus rapide et élevée au sein des tissus nécrosés.

Mots-clés : *Accident vasculaire cérébral ischémique, cerveau, lésion de reperfusion, métabolisme cérébral, agent théranostique, neuroprotection, hyperpolarisation, polarisation dynamique nucléaire avec dissolution (PDN-d), imagerie spectroscopique par résonance magnétique, résonance de spin électronique (RSE)*

Contents

Acknowledgements	i
Abstract	iii
Résumé	v
List of figures	xiii
List of tables	xvii
List of acronyms and abbreviations	xix
List of symbols	xxv
Scope of this thesis	1
1 Introduction	5
1.1 Stroke	5
1.1.1 Ischemic stroke management	7
1.1.2 Reperfusion injuries and neuroprotection	10
1.2 MRI/S in the context of stroke	13
1.3 Spin polarization and sensitivity in MR	16
1.4 Nuclear spin hyperpolarization	19
1.4.1 Brute-force method	19
1.4.2 Spin-exchange optical pumping (SEOP)	20
1.4.3 Parahydrogen-induced polarization (PHIP)	21
1.4.4 Dissolution dynamic nuclear polarization (dDNP)	22
1.4.4.1 DNP Mechanisms	24
1.4.4.2 Indirect nuclear polarization mechanisms	28
1.4.4.3 Practical considerations for dDNP	29
1.5 Stroke theranostics with hyperpolarized probes	35

2	<i>In vivo</i> assessment of the metabolic impact of cerebral ischemia using MRS and hyperpolarized [1-¹³C] lactate and [1-¹³C] pyruvate	37
2.1	Abstract	38
2.2	Introduction	39
2.3	Experimental methods	40
2.3.1	Animal experimentation	40
2.3.2	Study design	40
2.3.3	Transient middle cerebral artery occlusion (MCAO) model of stroke . . .	41
2.3.4	Hyperpolarization	42
2.3.5	Magnetic resonance measurements	43
2.3.6	¹ H imaging	44
2.3.7	¹ H MRS	44
2.3.8	Hyperpolarized ¹³ C MRS	45
2.4	Data processing	45
2.4.1	¹³ C metabolite ratios	45
2.4.2	Kinetic modeling	45
2.4.3	Statistical analysis	48
2.5	Results	49
2.6	Discussion	63
2.7	Conclusion	65
3	Influence of DNP polarizing agents on biochemical processes: TEMPOL in transient ischemic stroke	67
3.1	Abstract	68
3.2	Introduction	69
3.3	Methods	70
3.3.1	Animal experimentation	71
3.3.2	Transient middle cerebral artery occlusion (MCAO) model of stroke . . .	71
3.3.3	Hyperpolarization	71
3.3.4	Magnetic resonance measurements	71
3.3.5	Animal groups	72
3.3.6	Determination of the injected dose	72
3.3.7	¹³ C MRS data processing	73
3.3.8	Statistical analysis	73
3.4	Results and discussion	73
3.5	Conclusion	78
4	Design and performance of a fluid path compatible dDNP/LOD-ESR probe	79
4.1	Abstract	80

4.2	Introduction	81
4.3	Methods	82
4.3.1	Original setup	82
4.3.2	Custom Fluid Path (CFP)	85
4.3.3	CFP compatible DNP probe	86
4.3.3.1	LOD-ESR setup	88
4.3.3.2	Estimation of cryogenic performance	90
4.3.3.3	A simple thermal model for heat conduction	91
4.3.4	DNP of [1- ¹³ C] pyruvate	92
4.3.4.1	Sample preparation	92
4.3.4.2	Solid-state DNP measurements	92
4.3.4.3	Liquid-state polarization measurements	93
4.3.4.4	Characterization of [1- ¹³ C] pyruvate T_1	94
4.3.5	Optimization of [1- ¹³ C] lactate DNP sample formulation	94
4.3.5.1	Sample preparation	94
4.3.5.2	Solid-state characterization	95
4.3.5.3	Liquid-state polarization measurements	95
4.3.6	Statistical analysis	96
4.4	Results and discussion	96
4.4.1	Cryogenic performance	96
4.4.2	DNP spectrum and LOD-ESR results	98
4.4.3	Solid-state polarization and microwave power density	99
4.4.4	Dissolution and liquid-state polarization	101
4.4.5	Characterization and optimization of [1- ¹³ C] lactate DNP samples	103
4.5	Conclusion	106
5	Highly versatile dDNP: implementation of a multi-sample/multi-nucleus cryogenic probe with parallel NMR detection	107
5.1	Abstract	108
5.2	Introduction	109
5.3	Methods	110
5.3.1	Multi-sample DNP probe design and NMR setup	110
5.3.2	dDNP of [1- ¹³ C] pyruvic acid	114
5.3.3	Evaluation of cryogenic performance	115
5.3.4	Simultaneous DNP monitoring and optimization of samples prepared with different nuclei and radicals	116
5.3.5	Sequential <i>in vivo</i> cerebral HP-MRS	117
5.3.6	Statistical analysis	119
5.4	Results and discussion	119

Contents

5.4.1	Cryogenic, DNP and NMR performance of the multi-sample probe . . .	119
5.4.2	Solid-state and liquid-state polarization of pyruvic acid	122
5.4.3	Solid-state polarization and monitoring of different nuclei	125
5.4.4	Sequential <i>in vivo</i> cerebral HP MRS	125
5.5	Conclusion and perspectives	129
6	Improving the spatiotemporal efficiency of spectrally resolved ^{13}C MRI to probe the dynamic metabolic interplay in a mouse model of stroke	131
6.1	Abstract	132
6.2	Introduction	133
6.2.1	MRSI acquisition schemes	134
6.2.2	IDEAL spiral CSI	137
6.2.2.1	Spectroscopic image reconstruction	138
6.2.2.2	Chemical-shift reconstruction	138
6.2.2.3	Spatial reconstruction	141
6.3	Methods	142
6.3.1	MRI system	142
6.3.2	RF coils and animal setup	143
6.3.2.1	Design considerations	143
6.3.2.2	^{13}C receive-only surface coil	144
6.3.2.3	$^1\text{H}/^{13}\text{C}$ volume coil	145
6.3.2.4	Animal setup	147
6.3.3	RF coil characterization	149
6.3.4	Implementation of the IDEAL spiral CSI method	149
6.3.5	<i>In vitro</i> MRSI	150
6.3.6	<i>In vivo</i> MRSI	151
6.3.7	MRSI data analysis	152
6.4	Results	153
6.4.1	RF coil characterization	153
6.4.2	<i>In vitro</i> MRSI	155
6.4.3	<i>In vivo</i> MRSI	158
6.5	Discussion	165
6.6	Conclusion	170
7	General conclusions and outlook	171
A	Ancillary dDNP polarizer equipment	175
A.1	CFP pressure-test station	176
A.2	Dissolution head	177
A.3	LOD-ESR differential amplifier	179

B NMR preamplifiers	183
B.1 Design	184
B.2 Characterization	186
C Metabolite-specific stack-of-spirals MRSI sequence	189
C.1 Introduction	190
C.2 MRSI sequence	190
C.3 Methods	192
C.4 Results	193
C.5 Discussion	193
Bibliography	199
Publications and conference proceedings	225
Curriculum vitæ	231

List of figures

1.1	Regional pattern of an acute ischemic stroke lesion	8
1.2	MRI assessment of diffusion-perfusion mismatch with DWI and PWI contrasts . .	10
1.3	Final infarct size reduction by lactate neuroprotection in a mouse model of permanent focal ischemia	12
1.4	Example of ^1H MRSI performed in the acute phase of stroke in a human patient .	16
1.5	Thermal polarization of electrons, ^1H and ^{13}C at 7 T as a function of the temperature	23
1.6	Energy-level diagram for the solid effect DNP mechanism	25
1.7	Energy-level diagram for the cross-effect DNP mechanism	26
1.8	Schematic illustration of the electron spin distribution involved in thermal mixing	28
2.1	Outline of the experimental design for characterizing the potential of $[1-^{13}\text{C}]$ lactate and $[1-^{13}\text{C}]$ pyruvate as biomarkers for stroke	41
2.2	Transient MCAO surgery procedure	42
2.3	Sketch of the 7T/1K dDNP / 9.4T MRI setup	43
2.4	Mouse head ^1H quadrature/ ^{13}C linear surface coil for acquisitions at 9.4T	44
2.5	Sketch of HP $[1-^{13}\text{C}]$ lactate and HP $[1-^{13}\text{C}]$ pyruvate cerebral transport/metabolism	47
2.6	Mathematical kinetic model for the cerebral metabolism of HP $[1-^{13}\text{C}]$ lactate. . .	47
2.7	Mathematical kinetic model for the cerebral metabolism of HP $[1-^{13}\text{C}]$ pyruvate. .	47
2.8	Representative axial T_2W in sham and MCAO animals	49
2.9	Representative dynamic ^{13}C MRS acquired in healthy and stroke mice following injections of HP $[1-^{13}\text{C}]$ lactate or $[1-^{13}\text{C}]$ pyruvate	50
2.10	Averaged ^{13}C metabolic time courses of HP $[1-^{13}\text{C}]$ lactate or $[1-^{13}\text{C}]$ pyruvate . . .	51
2.11	Metabolite ratios quantified in HP $[1-^{13}\text{C}]$ lactate experiments	52
2.12	Metabolite ratios quantified in HP $[1-^{13}\text{C}]$ pyruvate experiments	53
2.13	Kinetic rates quantified in HP $[1-^{13}\text{C}]$ lactate experiments	54
2.14	Kinetic rates quantified in HP $[1-^{13}\text{C}]$ pyruvate experiments	55
2.15	Correlation between kinetic rate constants and metabolite ratios in HP $[1-^{13}\text{C}]$ pyruvate and $[1-^{13}\text{C}]$ lactate MRS experiments.	56
2.16	Representative single-voxel ^1H MRS in the striatum of ischemic and healthy mice	57

List of figures

2.17	Endogenous metabolite concentrations in the striatum at 75 min post-reperfusion or surgery.	58
2.18	Endogenous metabolite concentrations in the striatum at 110 min post-reperfusion or surgery.	59
2.19	Time course of endogenous metabolites quantified from ^1H MRS (1/3)	60
2.20	Time course of endogenous metabolites quantified from ^1H MRS (2/3)	61
2.21	Time course of endogenous metabolites quantified from ^1H MRS (3/3)	62
2.22	Comparison of the pyruvate labeling measured in HP [$1\text{-}^{13}\text{C}$] lactate experiments to previous studies	64
3.1	Representative dynamic cerebral ^{13}C MRS acquired after a bolus infusion of [$1\text{-}^{13}\text{C}$] lactate, and T_2W axial images illustrating the surgically-induced ischemic stroke lesion in the mouse brain	74
3.2	Simplified schematics of cerebral [$1\text{-}^{13}\text{C}$] lactate metabolism	75
3.3	Metabolite ratios measured following injection of HP [$1\text{-}^{13}\text{C}$] lactate	76
3.4	Chemical reactions potentially involved in the metabolic effect of TEMPOL	77
4.1	Overview of the dDNP setup being upgraded	83
4.2	Old components of the dDNP polarizer replaced in this study	84
4.3	Details of the custom fluid path (CFP)	85
4.4	Photos of the dDNP/LOD-ESR probe	87
4.5	LOD-ESR probe, based on the CFP design	89
4.6	Schematic representation of the LOD-ESR signal.	90
4.7	Comparison of the lHe hold time between the old and new cryogenic probes	96
4.8	Calculation of the conductive heat transfer of the old and new probes	97
4.9	Representative DNP enhancement profile, LOD-ESR spectrum and T_{1e} of [$1\text{-}^{13}\text{C}$] pyruvic acid doped with trityl radical at 5 T and 1.15 K	99
4.10	Microwave power sweep, buildup and polarization level of [$1\text{-}^{13}\text{C}$] pyruvic acid	100
4.11	Liquid-state polarization measurements of [$1\text{-}^{13}\text{C}$] pyruvate at 14.1 T	102
4.12	T_1 of sodium [$1\text{-}^{13}\text{C}$] pyruvate at physiological pH as a function of temperature, measured at 14.1 T.	102
4.13	T_{1e} measurements, ESR spectra and DNP enhancement profiles of [$1\text{-}^{13}\text{C}$] lactate samples at various Gd-DO3A-butrol dopings	104
4.14	Solid-state DNP of [$1\text{-}^{13}\text{C}$] lactate samples doped with OX063 trityl	105
4.15	Liquid-state polarization measurements of HP [$1\text{-}^{13}\text{C}$] lactate	105
5.1	Multi-sample dDNP cryogenic probe for up to three custom fluid paths (CFPs)	111
5.2	Detailed section views of the multi-sample microwave cavity	113
5.3	Sketch of the 5T dDNP / 14.1T MRI setup for multi-sample experiments	118
5.4	Mouse head ^1H quadrature/ ^{13}C linear surface coil for acquisitions at 14.1 T	118

5.5	Temperature and pressure trends of the polarizer sample space with the multi-sample dDNP probe, and simultaneous microwave frequency and power sweeps . . .	120
5.6	Sample space temperature and pressure and NMR signal during simultaneous polarization and sequential dissolutions with the multi-sample dDNP probe . . .	121
5.7	Cross talk between the three slots during a homonuclear experiment	123
5.8	Summary of the dDNP performance of the multi-sample probe with PA-samples . .	124
5.9	Simultaneous microwave frequency sweeps and buildup of Lac-sample, H ₂ O-sample and Xe-sample	126
5.10	Simultaneous microwave frequency sweep of the Lac-sample and PA-sample . . .	127
5.11	Simultaneous HP of lactate and pyruvate, and multi-substrate <i>in vivo</i> experiment	128
6.1	Schematic scheme of the multi-slice IDEAL spiral CSI sequence	139
6.2	Flowchart of the spectroscopic image reconstruction	140
6.3	¹³ C surface receive-only array for the mouse brain	144
6.4	Electrical diagram of one receive element	145
6.5	¹ H/ ¹³ C volume coil with integrated mouse holder and fixation device	146
6.6	Simplified electrical diagram of the double saddle coil	147
6.7	Setup for HP MRS(I) measurements in mice with up to two injections of HP substrates	148
6.8	Effective number of spatial averages (NSA) for series with 7 images as a function of the echo time increment	150
6.9	<i>k</i> -space trajectory and density of the spiral readout	152
6.10	Characterization of the ¹³ C transmit and receive homogeneity of the cross-coil setup	154
6.11	Characterization of the ∅11 mm ¹³ C linear surface coil	155
6.12	Multislice MRSI acquired in a phantom using the IDEAL spiral CSI sequence . . .	156
6.13	Spatial point spread function of the spiral acquisition	157
6.14	Axial ¹ H images representing the slices where dynamic MRSI was performed . . .	158
6.15	Dynamic slice-selective cerebral ¹³ C MRS acquired after a bolus infusion of [1- ¹³ C] pyruvate in a stroke mouse	159
6.16	Dynamic MRSI in an MCAO transient stroke mouse after a bolus injection of HP [1- ¹³ C] pyruvate (anterior slice)	160
6.17	Dynamic MRSI in an MCAO transient stroke mouse after a bolus injection of HP [1- ¹³ C] pyruvate (central slice)	161
6.18	Dynamic MRSI in an MCAO transient stroke mouse after a bolus injection of HP [1- ¹³ C] pyruvate (posterior slice)	162
6.19	Regions of interest for the signal comparison between either brain sides	163
6.20	Time course of [1- ¹³ C] pyruvate and [1- ¹³ C] lactate signals and ratio quantified within each slice and hemisphere	163
6.21	Averaged [1- ¹³ C] pyruvate, [1- ¹³ C] pyruvate hydrate, [1- ¹³ C] lactate and lactate-to-pyruvate ratio (LPR) maps	164

List of figures

6.22 Averaged signals and ratios within each slice and hemisphere	165
A.1 CFP pressure-test station	176
A.2 Dissolution head	178
A.3 Schematics of the LOD-ESR differential amplifier	180
A.4 LOD-ESR differential amplifier circuit and enclosure	181
B.1 Schematics of the broadband LNA (NMR version)	184
B.2 Schematics of the broadband LNA (MRI version)	185
B.3 Picture of the broadband LNA (NMR version)	185
B.4 Picture of the broadband LNA (MRI version)	186
B.5 Gain and noise figure of the low-noise preamplifiers	187
C.1 Diagram of the metabolite specific 3D stack-of-spirals acquisition scheme	191
C.2 Dynamic <i>in vivo</i> MRSI of HP [1- ¹³ C] lactate	194
C.3 Averaged maps of <i>in vivo</i> MRSI of HP [1- ¹³ C] lactate	195
C.4 Dynamic <i>in vivo</i> MRSI of HP [1- ¹³ C] pyruvate (1/2)	196
C.5 Dynamic <i>in vivo</i> MRSI of HP [1- ¹³ C] pyruvate (2/2)	197
C.6 Averaged maps of <i>in vivo</i> MRSI of HP [1- ¹³ C] pyruvate	198

List of tables

4.1	Components and materials for the dDNP probe heat conduction simulations . . .	92
4.2	Solid-state parameters of [1- ¹³ C] lactate/OX063 samples at 5 T and 1.15 K with varying Gd-DO3A-butrol dopings	103
6.1	Non-exhaustive list of dynamic ¹³ C HP MRSI studies in mice or rat brain	169
6.2	Non-exhaustive list of single-time point ¹³ C HP MRSI studies in mice or rat brain .	169

List of acronyms and abbreviations

ACAR	Acetyl CARnitine
ADC	Apparent Diffusion Coefficient
AG	Alderman-Grant
AH111501	Tris(8-carboxyl-2,2,6,6-tetrakis(2-methoxyethyl)benzo(1,2-d:4,5-d')bis(1,3)dithiol-4-yl)methyl trisodium salt
Ala	Alanine
ALR	Alanine-to-Lactate Ratio
ALT	ALanine aminoTransferase
ALTADENA	Adiabatic Longitudinal Transport After Dissociation Engenders Net Alignment
ANOVA	ANalysis Of VAriance
APR	Alanine-to-Pyruvate Ratio
APT	Amide Proton Transfer
ATP	Adenosine TriPhosphate
AUC	Area Under the Curve
BBB	Blood-Brain Barrier
Bic	Bicarbonate
BIR	B ₁ -Insensitive Rotation
BLR	Bicarbonate-to-Lactate Ratio
BNC	Bayonet Neill-Concelman
BPR	Bicarbonate-to-Pyruvate Ratio
bSSFP	Balanced Steady-State Free Precession
CA	Carbonic Anhydrase
cALR	Corrected Alanine-to-Lactate Ratio
cAPR	Corrected Alanine-to-Pyruvate Ratio
cBLR	Corrected Bicarbonate-to-Lactate Ratio
cBPR	Corrected Bicarbonate-to-Pyruvate Ratio

List of acronyms and abbreviations

CCA	Common Carotid Artery
CE	Cross Effect
CEST	Chemical Exchange Saturation Transfer
CFP	Custom Fluid Path
cLPR	Corrected Lactate-to-Pyruvate Ratio
CP	Cross-Polarization
cPLR	Corrected Pyruvate-to-Lactate Ratio
Cr	Creatine
CRLB	Cramer-Rao Lower Bounds
CSI	Chemical Shift Imaging
CT	Computed Tomography
dDNP	Dissolution Dynamic Nuclear Polarization
DMSO	DiMethyl SulfOxide
DNP	Dynamic Nuclear Polarization
DQ	Double-Quantum
DWI	Diffusion Weighted Imaging
ECA	External Carotid Artery
EDTA	EthyleneDiamineTetraAcetic acid
ELDOR	ELectron-electron DOuble Resonance
EPSI	Echo Planar Spectroscopic Imaging
ESR	Electron Spin Resonance
FASTESTMAP	Fast, Automatic Shim Technique using Echo-planar Signal readout for Mapping Along Projections
FID	Free Induction Decay
FLAIR	FLuid Attenuated Inversion Recovery
FOV	Field Of View
FP	Fluid Path
FWHM	Full Width at Half Maximum
GABA	Gamma-AminoButyric Acid
Gln	Glutamine
Glu	Glutamate
Gly	Glycine
GPC	GlyceroPhoshoCholine
HCAR1	HydroxyCarboxylic Acid Receptor 1

HP	HyperPolarized
HYPOP	HYperPOLarizing Polymers
HYPSO	HYbrid Polarizing SOLids
ICA	Internal Carotid Artery
ID	Inner Diameter
IDEAL	Iterative Decomposition of water and fat with Echo Asymmetry and Least-squares estimation
IVC	Inner Vacuum Chamber
KIC	KetoIsocaproic acid
Lac	Lactate
LDH	Lactate DeHydrogenase
Leu	Leucine
LO	Local Oscillator
LOD-ESR	LOngitudinally-Detected Electron Spin Resonance
LPR	Lactate-to-Pyruvate Ratio
LVO	Large Vessel Occlusion
Mac	MacroMolecules
MCA	Middle Cerebral Artery
MCAO	Middle Cerebral Artery Occlusion
MCT	MonoCarboxylate Transporter
MPC	Mitochondrial Pyruvate Carrier
MR	Magnetic Resonance
MRA	Magnetic Resonance Angiography
MRI	Magnetic Resonance Imaging
MRS	Magnetic Resonance Spectroscopy
MRSI	Magnetic Resonance Spectroscopic Imaging
MW	MicroWave
NAA	N-Acetyl-Aspartate
NAAG	N-Acetyl-Aspartyl-Glutamate
NBR	Nitrile Butadiene Rubber
NMDA	N-Methyl-D-Aspartate
NMR	Nuclear Magnetic Resonance
NSA	Number of Signal Averages
OD	Outer Diameter

List of acronyms and abbreviations

OX063	Tris(8-carboxyl-2,2,6,6-tetrakis(2-hydroxyethyl)benzo(1,2-d:4,5-d')bis(1,3)dithiol-4-yl)methyl trisodium salt
p.r.	Post-Reperfusion
PAI	Polyamide Imide
PASADENA	Parahydrogen And Synthesis Allow Dramatically Enhanced Nuclear Alignment
PCho	PhosphoCholine
PCr	PhosphoCreatine
PDH	Pyruvate DeHydrogenase
PEEK	PolyEther Ether Ketone
PHIP	ParaHydrogen-Induced Polarization
PLR	Pyruvate-to-Lactate Ratio
ppm	Parts-Per-Million
PSF	Point Spread Function
PTFE	PolyTetraFluoroEthylene
PWI	Perfusion Weighted Imaging
Pyr	Pyruvate
rCBF	Regional Cerebral Blood Flow
RF	Radio Frequency
ROS	Reactive Oxygen Species
rtPA	Recombinant Tissue Plasminogen Activator
Rx	Receive
SABRE	Signal Amplification By Reversible Exchange
SD	Standard Deviation
SE	Solid Effect
SEOP	Spin-Exchange Optical Pumping
SMA	SubMiniature version A
SNR	Signal-to-Noise Ratio
SOD	SuperOxide Dismutase
SPECIAL	SPin ECho, full Intensity Acquired Localized
SPEN	SPatiotemporal ENcoding
SPSP	SPectral-SPatial
STP	Standard Temperature and Pressure
SVO	Small Vessel Occlusion

Tx/Rx	Transmit/Receive
Tau	Taurine
TBI	Traumatic Brain Injury
TCA	TriCarboxylic Acid
TE	Echo Time
TEMPO	2,2,6,6-tetramethylpiperidine-1-oxyl
TEMPOL	4-hydroxy-2,2,6,6-tetramethylpiperidin-1-oxyl
TM	Thermal Mixing
TORO	Transmit-Only/Receive-Only
TR	Repetition Time
TRIS	Tris(hydroxymethyl)aminomethane
Tx	Transmit
UHF	Ultra High Field
UV	UltraViolet
v:v	Volume per Volume
VTI	Variable Temperature Insert
ZQ	Zero-Quantum

List of symbols

α	Flip angle
γ	Gyromagnetic ratio
$\Delta\omega_S$	Radical ESR linewidth
ΔTE	Echo time increment
λ	Wavelength
$\boldsymbol{\mu}_I$	Nuclear magnetic moment
$\boldsymbol{\xi}(\mathbf{k})$	k -space metabolite images
τ	LOD-ESR probe characteristic time constant
ω_I	Nuclear spin Larmor frequency
ω_{MW}	Microwave frequency
ω_S	Electron spin Larmor frequency
B_0	Static magnetic field
B_1	Radio frequency field
B_1^+	Transmit field
ck_{LP}	Corrected lactate-to-pyruvate kinetic rate constant
ck_{PA}	Corrected pyruvate-to-alanine kinetic rate constant
ck_{PB}	Corrected pyruvate-to-bicarbonate kinetic rate constant
ck_{PL}	Corrected pyruvate-to-lactate kinetic rate constant
\mathbf{E}	Chemical shift encoding matrix
E_{m_I}	Nuclear Zeeman energy level
E_{NZ}	Electron non-Zeeman reservoir
E_S	Total energy of the spin system
E_Z	Electron Zeeman reservoir
F	RF-related depolarization term
\hbar	Reduced Planck constant
\mathcal{H}_{ZI}	Nuclear Zeeman Hamiltonian

List of symbols

I	Nuclear spin quantum number
\mathbf{I}	Nuclear spin
\mathbf{k}	Position in reciprocal space
$k_{A, \text{out}}$	Alanine elimination kinetic rate constant
k_B	Boltzmann constant
$k_{B, \text{out}}$	Bicarbonate elimination kinetic rate constant
$k_{L, \text{out}}$	Lactate elimination kinetic rate constant
k_{LP}	Lactate-to-pyruvate kinetic rate constant
k_{PA}	Pyruvate-to-alanine kinetic rate constant
k_{PB}	Pyruvate-to-bicarbonate kinetic rate constant
k_{PL}	Pyruvate-to-lactate kinetic rate constant
\mathbf{M}	Macroscopic magnetization
m_I	Nuclear spin magnetic quantum number
m_S	Electron spin magnetic quantum number
N	Number of spins
N_E	Number of echo images
N_M	Number of metabolites
N_R	Number of repetitions
N_S	Number of slices
N_{Sp}	Number of sampling points
N_Z	Nuclear Zeeman reservoir
P	Polarization
Q	Quality factor
\mathbf{r}	Position in real space
S	Electron spin quantum number
\mathbf{S}	Electron spin
T	Temperature
T_1	Nuclear spin-lattice relaxation time
T_{1e}	Electron spin-lattice relaxation time
T_2	Nuclear spin-spin relaxation time
T_2^*	Effective nuclear spin-spin relaxation time
T_b	Buildup time constant
T_{ENZ}	Spin temperature of the electron non-Zeeman reservoir
T_{EZ}	Spin temperature of the electron Zeeman reservoir

T_L	Lattice temperature
T_{Nz}	Spin temperature of the nuclear Zeeman reservoir
TE_0	Initial echo time
$\mathbf{x}(\mathbf{r})$	Real space metabolite images
\mathbf{y}	Series of spiral-encoded images in k -space

Scope of this thesis

Context and aims

Stroke is among the leading causes of death and disability, causing a growing public health challenge given the current demographic evolution. Eight out of ten strokes are of the ischemic subtype, for which the most efficient treatment in the acute phase is to restore blood perfusion by mechanical or chemical removal of the obstruction. Paradoxically, although contributing to salvage non-irreversibly damaged tissues, sudden reoxygenation can exacerbate the destructive processes triggered by stroke. Neuroprotective strategies aim to reduce these reperfusion injuries. Although they have shown promising results at the preclinical level, none of them has been successfully translated into clinics so far.

Magnetic resonance imaging and spectroscopy (MRI/S), being non-invasive, non-ionizing, and offering a wide range of contrasts for soft tissues, are particularly useful approaches in neuroimaging. The advent of hyperpolarization, for example via the dissolution dynamic nuclear polarization (dDNP) method, enables one to enhance the signal of small molecules, including theranostic agents, to follow their fate *in vivo* in real time. This can shed light on the underlying metabolic processes involved in neuroprotection and provide invaluable knowledge towards the development of new treatments for ischemic stroke. Furthermore, the combination of diagnostic components in the therapeutic agent could offer a theranostic approach for stroke, allowing early response monitoring to proactively tailor subsequent treatment procedures to the specific medical condition of each patient.

This thesis focuses on the development of novel theranostic approaches for stroke based on hyperpolarized magnetic resonance. The ultimate goal is to add a diagnostic component to known neuroprotectants and demonstrate their efficacy as HP contrast agents in a mouse model of transient cerebral ischemia. Towards this objective, it prospectively explores the potential of ^{13}C labeled lactate and pyruvate as neuroprotective molecular biosensors for stroke. In parallel, it improves technical and methodological aspects of dDNP and MRI/S to advance their capabilities for the characterization of impaired metabolic patterns after stroke.

Outline

In **Chapter 1**, we describe the framework of this thesis, beginning with a brief introduction to ischemic stroke, currently available treatments, and imaging modalities. We then discuss the growing interest in better characterizing the stroke condition at the molecular level, as well as the potential benefits of neuroprotective treatments. The main hyperpolarization techniques are briefly reviewed, before focusing on the mechanisms and practical aspects of dissolution DNP. Finally, we discuss how the dramatic signal enhancement provided by hyperpolarization can be combined into a theranostic approach to provide key information for a personalized treatment to improve recovery after stroke.

As a first step, in **Chapters 2 and 3**, we focus on characterizing the global metabolic contrasts of HP ^{13}C neuroprotective molecules in the ischemic mouse brain using a 7T/1K dDNP polarizer and a 9.4T MRI scanner.

Chapter 2 compares the ability of the HP neuroprotective agents [1- ^{13}C] lactate and [1- ^{13}C] pyruvate to provide global metabolic contrasts after transient ischemic stroke. The high sensitivity of the measurement allowed quantifying the timecourse of all downstream metabolites, including [^{13}C] bicarbonate. We investigated whether the cerebral metabolic kinetics determined using a mathematical modeling approach could provide additional information compared to the model-free ratio analysis. Finally, we characterized the effect of the bolus of the HP neuroprotective agent on the neurochemical profile of the ischemic core using ^1H MRS.

Chapter 3 examines how the dDNP methodology might interfere with the biological processes under investigation, in order to relate the measurements realized in this thesis to previous studies. The hyperpolarization process requires mixing the substrate with a polarizing agent, usually in the form of a stable free radical. In preclinical studies, the latter is usually not filtered prior to the administration to the animal. This chapter assesses whether the presence of the nitroxyl radical TEMPO, at the small dose used in dDNP, affects the cerebral metabolic response to a bolus of HP [1- ^{13}C] lactate in a stroke mouse.

Chapters 4 through 6 are focused on improving the efficiency and versatility of investigation tools to allow a deeper understanding of the metabolic processes. Since the aforementioned dDNP/MRI setup was used extensively for routine experiments, we pursued our technical developments on another setup with a 5T/1.15K polarizer and 14.1T MRI scanner.

Chapter 4 presents the design and characterization of a cryogenic probe for the implementation of the custom fluid path (CFP) dissolution system into a wet 5T/1.15K DNP polarizer. The new hardware enabled better repeatability of the polarization and substrate concentration, as well as better cryogenic and hyperpolarization performance and lower helium consump-

tion. Finally, longitudinally detected electron spin resonance (LOD-ESR) was implemented to measure the properties of the polarizing agents under DNP conditions. It was then used to guide the optimization of the [1-¹³C] lactate DNP sample via gadolinium doping to optimize the ESR properties and boost the polarization.

Chapter 5 presents the design of a multi-sample probe, which not only enables simultaneous hyperpolarization of up to three samples, but also allows their individual parallel NMR detection. This can even be achieved with distinct nuclei and polarizing agents. The substantially higher throughput enables more complex solid-state and liquid-state experiments. To prove the concept, back-to-back dissolution, injection and dynamic MRS of HP [1-¹³C] lactate then [1-¹³C] pyruvate are performed in a healthy mouse with a 15-minute time interval.

Chapter 6 begins with a brief summary of the constraints and technical considerations required to implement HP MRSI. It then presents the implementation of model-based dynamic HP MRSI on a 14.1T MRI scanner, and the development of a ¹H/¹³C RF coil setup for the mouse brain. The new setup, geared towards enhanced sensitivity and efficiency, was tested *in vitro* and *in vivo*. In a proof-of-concept experiment, dynamic HP MRSI is performed in a stroke mouse following the injection of HP [1-¹³C] pyruvate at a neuroprotective dose to map regional metabolic differences induced by ischemia.

Finally, **Chapter 7** summarizes the main findings of this thesis and offers perspectives for future extensions and applications.

1 Introduction

1.1 Stroke

The human brain is the most complicated organ and the command center of the human body. Responsible for the coordination of all bodily functions, it consists of various specialized cells. Neurons, about 85 billion in the human brain¹, are the building block of the nervous system and play a crucial role in processing and transmitting information throughout the brain and body in the form of electrical and chemical signals. To ensure their protection, structural and metabolic support, neurons are organized into multicellular complexes known as the neurovascular unit^{2,3} (NVU), which is additionally made up of glial (oligodendrocytes, astrocytes and microglia) and vascular (endothelial cells and pericytes) cells. It plays a crucial role in cerebral homeostasis, detecting and responding to the needs of neuronal supply by adjusting the cerebral blood flow and modulating the blood-brain barrier, and therefore regulating the exchange of oxygen, nutrients and waste products between the brain and circulatory system.

The brain is a highly metabolically active organ, using glucose as the primary energy source as well as oxygen through the cellular respiration process for the generation of adenosine triphosphate (ATP). Although it represents only 2% of body mass, the brain accounts for approximately 20% of body oxygen and glucose consumption⁴. Since the brain lacks substantial energy stores, it is entirely dependent on a constant supply of glucose and energy to function properly. Powerful but fragile, the brain is a very delicate organ, sensitive to physical trauma, and relies on its energy supply. The brain is unable to replenish dead neurons as neurogenesis in the adult is very limited. Instead, it adapts to these losses by building and reassigning connections between neurons through a process called plasticity. However, since this repair mechanism is entirely dependent on the pool of surviving cells, it shows its limits after severe brain injuries killing a substantial number of brain cells.

Chapter 1. Introduction

Stroke, also known as brain attack, is one of the most severe conditions that could endanger the brain. It is the second⁵ cause of death and leading⁶ cause of disability in the adult world-wide. In Switzerland, it affects about 20000 people annually, of which 2700 succumb⁷. This severe medical condition results from an abrupt disruption of the blood supply to the brain that quickly causes loss of neurological function. All of a sudden, the patient experiencing a stroke may show many severe symptoms, including, for example, signs of confusion, dizziness, numbness, muscular weakness, trouble understanding, seeing, speaking, or walking. Broadly speaking, strokes can be categorized into two types: hemorrhagic and ischemic, accounting for about 15% and 85% of cases, respectively.

Hemorrhagic stroke is caused by the rupture of a weakened blood vessel. As a result, the uncontrolled blood accumulation quickly provokes damage by irritating brain tissues, inducing swelling, and building pressure. Hemorrhagic strokes can be subdivided into two categories: intracerebral hemorrhage whether bleeding occurs within the brain, and subarachnoid hemorrhage if bleeding is in the space surrounding the brain.

Ischemic stroke, on which this thesis focuses, occurs when the blood supply to the brain, or part of it, is obstructed, in most cases by a blood clot. The latter may develop in the arteries directly supplying blood to the brain (thrombotic stroke). Alternatively, the clot can develop elsewhere in the body, often the heart, then be carried by the blood stream to block a brain artery (embolic stroke).

Based on the specific occluded vessel, ischemic stroke can be broadly classified⁸ into large vessel occlusion (LVO) strokes, defined as the occlusion of the proximal arteries of the brain and representing 24-46% of acute ischemic strokes⁹ depending on which segments are included in the definition, as well as small vessel occlusion (SVO) strokes.

In some cases, the blockage of blood flow may dislodge itself, with symptoms lasting only a few minutes. This is known as a transient ischemic attack. Although tissues are quickly reperfused and suffer only minimal damage, such events should not be neglected, as they could be a warning sign for more severe accidents.

The size of the SVO stroke lesion is typically less than 1.5 cm in diameter. LVO strokes result from the occlusion of large primary vessels, therefore cause larger infarct volumes, typically in the range¹⁰ of 70-300 mL, as well as more severe neurological deficits and a worse outcome compared to SVO strokes^{11,12}. As a result of the more important collateral irrigation, the time frame allowed for an effective treatment is typically longer in LVO compared to SVO strokes.

Regardless of the mechanism of ischemic stroke, reduced cerebral blood flow results in neurological function impairment¹³. At the cellular level, the insufficient oxygen and glucose supply prevent neurons from producing ATP through normal aerobic metabolism.

As a compensatory action, ATP is synthesized instead via anaerobic metabolism, a far more inefficient process that produces lactic acid, which will accumulate especially in the presence of hypoperfusion and induce further damage via tissue acidosis. The lack of ATP causes the dysfunction of ion pumps, which are specialized proteins responsible for maintaining the proper ionic gradient across cellular membranes. In particular, dysfunction of the $\text{Na}^+ - \text{K}^+$ -ATPase pump leads to the accumulation of sodium ions within the cells. As a result, this osmotic gradient causes an influx of water, creating cellular swelling and cytotoxic edema¹⁴. Similarly, the Ca^{2+} -ATPase pump fails, leading to increased calcium levels. This is exacerbated by the still functioning $\text{Na}^+ / \text{Ca}^{2+}$ exchanger, producing a large influx of calcium into cells. Overall, the high calcium levels cause excitatory neurotransmitters, such as glutamate to be released. This excites other neurons and leads to a vicious cycle of neuron excitement called excitotoxicity. High calcium concentration also activates degradative enzymes, which will break down the neuron cell membrane, and provoke the generation of free radicals and reactive oxygen species, resulting in oxidative stress. Finally, disruption of the normal cellular environment leads to mitochondrial failure, releasing apoptotic factors that lead to cell death.

The ischemic stroke injury presents a pattern with two main regions: the ischemic core, the area that has suffered irreversible damage, and the ischemic penumbra, which is characterized by reduced blood flow with loss of function but preserved tissue viability (Figure 1.1). Initially, the ischemic core is composed of the tissues closest to the occluded artery. With a blood flow below 20% of baseline normal, the cascade of cellular events ultimately results in irreversible damage and neuronal death within minutes of stroke onset¹⁵. On the other hand, the ischemic penumbra^{16,17} benefits from collateral perfusion from neighboring unobstructed arteries and is capable of maintaining a certain degree of metabolic activity to slow the cascade of cellular damaging events. The ischemic penumbra represents the portion of brain tissues at risk of death but it could be potentially salvaged by blood flow restoration and therefore represents the therapeutic target in ischemic stroke management.

1.1.1 Ischemic stroke management

During ischemic stroke, it is estimated that about 120 million neurons die every hour, the equivalent of 3.6 years of normal aging¹⁹. To preserve brain function, the key to ischemic stroke management is early intervention. Among the most important steps of stroke management upon arrival of the patient in a medical facility, a brain scan with computed tomography (CT) or magnetic resonance imaging (MRI) is performed to rule out other brain abnormalities, such as a tumor, confirm the presence of a stroke, and determine whether it is hemorrhagic or ischemic.

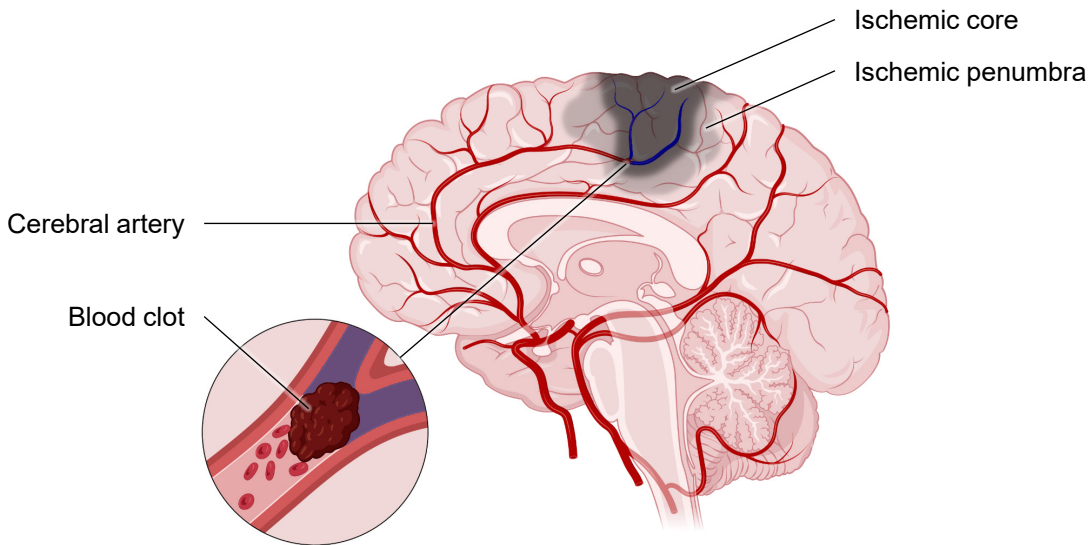


Figure 1.1: Schematic illustration of the regional pattern of an acute ischemic stroke lesion: the infarct core (dark gray), close to the obstructed artery, is surrounded by penumbral tissues (light gray). Neurons in the ischemic core are considered beyond repair. However, neurons in the penumbra may still be rescued and are the potential target of a therapeutic intervention.¹⁸

In non-contrast CT images, occluding clots appear as hyperdense areas^{20,21} soon after stroke onset due to the high density of red blood cells causing a large attenuation. Non-contrast CT is very sensitive for acute intracranial hemorrhage, but not for ischemic stroke²². Intravenous contrast dyes can be injected into the blood stream to enable CT angiography to map the vasculature, in particular the occluded or narrowed arteries. MRI enables as well to diagnose acute ischemic stroke infarction. Within minutes of stroke onset, cytotoxic edema, caused by the accumulation of intracellular water, restricts water diffusion at a microscopic level compared to normal tissues. This phenomenon translates into reduced apparent diffusion coefficients (ADC) and a higher signal in diffusion weighted imaging (DWI)²³. Nowadays, DWI is the gold standard for infarct core identification²⁴. While MRI delivers better sensitivity and specificity to ischemic stroke, CT offers several advantages in the emergency setting, such as shorter scan times, as well as fewer counter-indications compared to MRI.

In the acute phase of ischemic stroke, once the diagnostic is confirmed, therapy entails restoring blood flow to brain tissues using either or both of the currently approved recanalization strategies:

- **Thrombolysis** is a minimally invasive procedure to break up blood clots using a recombinant tissue plasminogen activator (rtPA). It can be injected intravenously to travel

to and dissolve the clot. Thrombolysis is typically efficient up to 4.5 h following stroke onset²⁵.

- **Thrombectomy**, which is typically efficient up to 7.3 h after ischemic onset²⁶, is an image-guided surgical procedure to physically remove the blood clot. A catheter is passed through an artery to reach the brain, and the clot is then sucked or trapped via a specific meshed device and removed from the body.

While SVOs are efficiently treated with thrombolysis, the larger clots in LVOs cannot be fully dissolved with thrombolysis and requires to be removed with thrombectomy.

Acute stroke treatment is very time sensitive, as the efficiency of both recanalization therapies rapidly decreases with infarction progression²⁷. Upon suspicion of stroke, the challenge starts with the need for an accurate triage by paramedics such that the patient can be brought to the right place to receive the right treatment. Indeed, not all treatments are available everywhere. For example, in Switzerland, stroke emergency care is provided primarily in 10 *stroke centers* and 14 smaller *stroke units*²⁸. Both can provide the necessary imaging capabilities, as well as thrombolysis, but thrombectomy intervention can only be performed in stroke centers.

Nonetheless, the time from stroke onset is not a strict criterion: recent clinical trials have shown that the administration of recanalization therapy based on tissue viability can improve patient outcome in an extended time window²⁹. Patients having a stroke lesion with a substantial mismatch between the volume of the ischemic core and the penumbral region, that is, with a large salvageable penumbral region compared to the small ischemic core, may still benefit from thrombolysis up to 9 h after stroke onset³⁰ and thrombectomy up to 24 h post stroke onset³¹. In the first case, the penumbral volume was identified using perfusion MRI or CT perfusion imaging, while the ischemic core was identified with diffusion-weighted³² MRI or defined as areas with cerebral blood flow below 30% of the baseline on CT perfusion imaging. In the second case, the mismatch was established on the basis of a disproportionately severe clinical deficit as a surrogate to estimate the penumbral region compared to the volume of stroke. An example of diffusion-perfusion stroke lesion mismatch is illustrated in Figure 1.2. The administration of recanalization therapy based on a favorable perfusion imaging profile also enables the treatment of selected patients with an unknown time of ischemia.

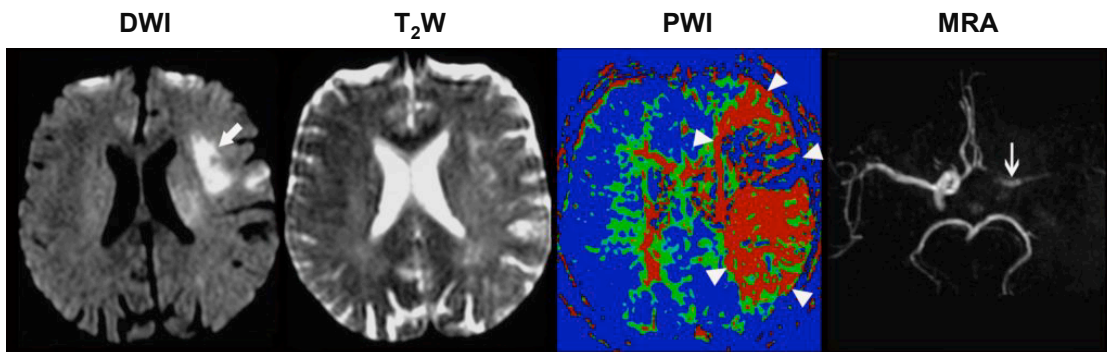


Figure 1.2: Example of diffusion-perfusion mismatch assessed using MRI in the acute phase of ischemic stroke. A small infarct core is observed in DWI (hypersignal region), while T_2W contrast may detect early signs of edema. A large perfusion deficit is depicted with perfusion weighted imaging (PWI). The regions with an abnormally long mean transit time are colored in red. MR angiography (MRA) reports the occlusion of a large vessel (white arrow). The difference between the abnormalities observed via PWI and DWI represents the penumbral ischemic tissues which may be saved by stroke therapy. Figure adapted from Raper³³.

1.1.2 Reperfusion injuries and neuroprotection

As described in Section 1.1, ischemic brain tissues undergo a series of damaging physiological and biochemical mechanisms as a result of the lack of oxygen and nutrients. While tissues in the ischemic core die within minutes of necrosis, penumbral tissues still benefit from collateral perfusion to maintain sufficient metabolism and survive for a short period of time.

Although ischemic stroke therapy aims to restore blood flow to mitigate hypoxia and salvage penumbral tissues, paradoxically, the sudden blood influx leads to additional injuries that exacerbate tissue damage³⁴. The biochemical mechanisms of reperfusion injuries are complex and interconnected. A large proportion of reperfusion injuries start with excessive oxidative stress and ionic imbalance, which progresses into cellular damages and inflammation. Following reperfusion, the resupply of oxygen and energy can cause overreaction of enzymes and pumps previously inhibited by the ischemic condition. The reintroduction of oxygen induces the resumption of aerobic mitochondrial respiration, therefore increasing the production of reactive oxygen species (ROS), which momentarily overwhelms the antioxidant abilities of the tissue and causing oxidative stress. As described above, during ischemia, the lack of ATP production impairs pumps function, leading to disruption of cellular ion homeostasis, specifically increased sodium and calcium concentrations. Upon reperfusion, the reactivation of sodium/calcium ion pumps exacerbate the calcium overload and causes further cellular damage. Reperfusion injuries, particularly oxidative stress and inflammation, directly damage endothelial cells, which are lining the blood vessels. This increases³⁵ the permeability of the

blood-brain barrier (BBB), allowing the infiltration of molecules and fluids into the brain, and increasing the risk of a hemorrhagic transformation of the stroke injury³⁶.

Neuroprotection, in the context of ischemic stroke, refers to strategies used to promote the recovery of reversibly damaged cerebral tissues and minimize the extent of cerebral damage after stroke^{37,38}, potentially prolonging the indication period of recanalization therapies³⁹, and improving the long-term neurological outcome. Applied on top of recanalization therapies, they mainly aim at mitigating secondary injuries after the initial ischemic event, by treating or inhibiting one or more toxic cellular mechanisms of the ischemic cascade.

A large fraction of neuroprotective approaches aim to reduce excitotoxicity, one of the main¹⁵ mechanisms of neuronal injury following stroke, by using N-methyl-D-aspartate (NMDA) receptor antagonists^{40,41}. Two examples in the context of MR-detectable agents are the noble gases xenon^{42,43} and helium^{44,45}.

Another approach is the use of antioxidative agents to neutralize reactive oxygen species released in large quantities after ischemia-reperfusion and reduce oxidative stress-induced injuries. Two examples of free radical scavengers are NXY-059^{46,47} and Edaravone^{48,49}.

One of the main and immediate consequences of ischemic stroke is metabolic failure due to the sudden interruption of glucose and oxygen supply. In this work, we focus on metabolic approaches that could mitigate mitochondrial dysfunction by supplying additional energy substrates to restore ATP synthesis for rebuilding the depleted energy stores following the stroke.

Although glucose is the primary brain energy substrate and is critical for maintaining healthy cerebral function, elevated levels of glucose in ischemia are associated with a worse outcome^{50,51}. Therefore, the administration of glucose as a supplemental energy substrate does not provide neuroprotection. Indeed, glycolysis produces ROS as byproducts, further increasing oxidative stress, and elevated glucose levels raise glutamate release causing excitotoxicity⁵². Finally, a higher glucose availability in the context of limited oxygen provides material for anaerobic metabolism, leading to lactic acidosis and increasing the inflammatory response after stroke. On the other hand, reducing the body's blood sugar levels, usually by administering insulin, has been found to improve stroke outcome^{53,54}.

Apart from glucose, alternative energy substrates, such as lactate, pyruvate, glutamate, or acetate, can be metabolized to produce energy in the brain⁵⁵. Pyruvate is a key metabolic intermediate: at the end of glycolysis, it is located at an important metabolic crossroad with different possible fates. It can be reduced to lactate via lactate dehydrogenase (LDH), transaminated to alanine by alanine transferase (ALT), or more importantly, transported into mitochondria to be oxidized into acetyl-CoA via pyruvate dehydrogenase (PDH), then enter

into the Krebs cycle (tricarboxylic acid (TCA) cycle). Several studies have established the neuroprotective effect of pyruvate at a preclinical level, reducing the final infarct volume and functional deficit^{56–59}. In addition to supporting mitochondrial metabolism and contributing to reducing energy deficiency⁵⁷, pyruvate reduces glutamate excitotoxicity, oxidative stress, and neuroinflammation, additionally contributing to neuroprotection⁶⁰.

Another metabolic probe investigated for its neuroprotective effects after stroke is lactate. Interestingly, although it is usually viewed as a waste product of glycolysis and is produced in large quantities during ischemia as a result of anaerobic metabolism, the administration of lactate has been found to provide neuroprotection in preclinical models of stroke^{61–66}, improving functional outcome and reducing infarct size (Figure 1.3). Lactate is suggested to contribute to neuroprotection through several aspects: In addition to being metabolized via pyruvate to enter the TCA cycle^{67,68}, lactate can act as a signaling molecule via the hydroxycarboxylic acid receptor 1 (HCAR1)^{61,69}. However, recent *in vivo* studies reported that lactate neuroprotection in hypoxia-ischemia is independent of HCAR1 activation and is rather related to different signaling pathways or metabolic effects^{65,70}.

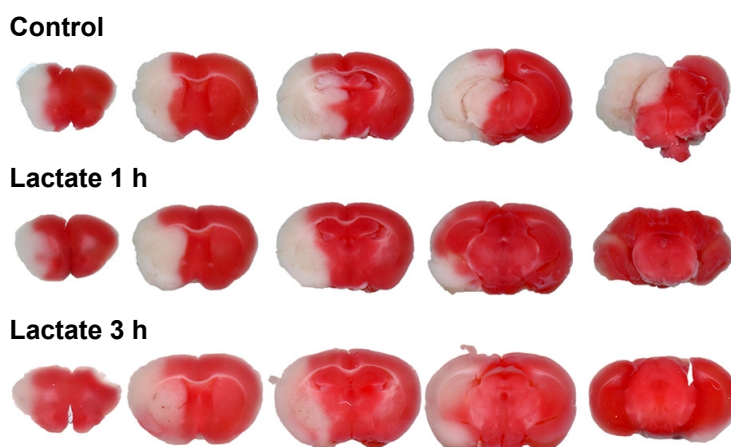


Figure 1.3: Illustration of lactate neuroprotection in a mouse model of permanent focal ischemia. Mice were treated with a therapeutic dose of lactate at either 1 h or 3 h post stroke onset. Brain slices were obtained 24 h post-stroke onset, and stained with triphenyl tetrazolium chloride (TTC), a redox indicator to differentiate between metabolically inactive and active tissues. Colored and discolored areas indicate healthy and damaged tissue, respectively. The administration of a therapeutic dose of lactate at 1 h post stroke onset decreased both the direct and indirect lesion volume compared to control animals. In addition, this study found that mice treated with lactate at 1 h had fewer neurological deficits. Figure adapted from Buscemi et al.⁶⁴.

Although the mechanisms and the proportion at which they contribute to the overall lactate neuroprotection are not yet clearly identified, the results of preclinical studies together with research performed in the context of traumatic brain injury (TBI)^{71–73} were sufficiently

promising to proceed with a clinical trial of lactate neuroprotection in acute stroke, which is currently in phase 2 at the time of writing⁷⁴.

Unfortunately, despite the large interest in finding neuroprotective treatments for stroke and the identification of several promising treatments in preclinical research, none of them has yet been successfully translated into the clinical setup^{37,75,76}. In particular, some of the challenging aspects that preclinical studies fail to take into account are the preexisting comorbidities known to worsen the stroke outcome⁷⁷ present in a large majority⁷⁸ of human patients, as well as the discrepancy of therapeutic window⁷⁹ and drug dose⁸⁰ between preclinical studies and clinical studies.

A better understanding, in both preclinical and clinical settings, of the mechanisms intervening after stroke at the molecular level, particularly the fate of neuroprotective treatments and their interplay to the ischemic injury, could identify key information for the development of efficient neuroprotective strategies³⁷. In the next section, we describe how magnetic resonance measurements could provide better insights into the molecular processes in ischemic stroke.

1.2 MRI/S in the context of stroke

Magnetic resonance imaging (MRI) is an imaging modality based on the principles of nuclear magnetic resonance (NMR), using a strong magnetic field, radiofrequency pulses, and spatial magnetic field gradients to manipulate and detect MR-active nuclei. Two key advantages of MRI are its ability to produce a wide range of contrasts without the need for exogenous contrast agents nor using ionizing radiation. Therefore, it makes it safer for patients compared to CT, which is particularly important for the examination of more vulnerable segments of the population, such as elderly patients or pregnant women, minimizing the risk of potential long-term effects from radiation exposure. This also makes it easier to follow up the disease longitudinal progression. Thanks to these advantages, MRI is nowadays a key modality in biomedical imaging, covering a wide range of applications, with a continuous increasing usage: in Switzerland, the number of clinical MRI examinations almost doubled between 2014 and 2019, increasing from 0.54 to 1.06 million^{81,82}. In comparison, in the same period of time, the number of CT screenings evolved from 0.80 to 1.18 million^{81,82}.

In the context of biomedical imaging, MRI is mostly used to detect protons from hydrogen nuclei, which are found in large abundance in biological soft tissues, primary in the form of water and fat. The relaxation properties of the observed nuclei, namely the longitudinal relaxation time T_1 and spin-lattice relaxation time T_2 , are greatly influenced by the local molecular environment, which is specific to each tissue and enables their differentiation. MRI is known

Chapter 1. Introduction

to offer high-resolution and superior soft-tissue contrast than other techniques, enabling clear differentiation of their structure. This is particularly useful for brain examinations to provide a comprehensive view and to better evaluate cerebral diseases. Furthermore, by adjusting the acquisition parameters, various types of contrast can be achieved to highlight different aspects of tissue properties.

MRI's capabilities extend beyond morphological assessments. For instance, valuable insights into tissue microstructure can be obtained using diffusion-weighted imaging (DWI) to measure the random displacement of water molecules in tissues. This technique proves particularly beneficial in stroke, as it allows for the evaluation of microstructural integrity in affected tissues. Specifically, in acute ischemic stroke, it provides a clinical imaging marker of the infarction core by highlighting tissues with restricted water diffusion resulting from cytotoxic edema⁸³.

Perfusion weighted imaging (PWI) denotes a variety of MR techniques to measure hemodynamic parameters. In ischemic stroke, PWI enables the assessment of regions with impaired blood perfusion, typically both the ischemic core and the penumbra, therefore complementing DWI. Magnetic resonance angiography (MRA), a subclass of PWI, enables visualization of blood vessels, as well as identification of vascular narrowing or occlusions to assist with reperfusion therapy preparation.

In standard MRI stroke protocols, DWI and PWI are typically combined to assess the extent of the lesion, in particular to delimit the extent of the ischemic penumbra, which is the tissue volume that could potentially be salvaged by a timely reperfusion. While the blood perfusion deficit, the initial step of ischemic stroke, can be assessed via PWI maps, DWI visualizes the effects of cytotoxic edema, which is among the last steps of the ischemic cascade. As a result, these standard MR imaging protocols are only able to probe either the early or late stage of ischemia. Nonetheless, they do not depict the intermediate biochemical and physiological processes. Being able to establish this progression towards infarction could shed light on the viability of penumbral tissues and provide key information to help balance the risk benefit to provide the most adequate treatment to the patient.

Chemical exchange saturation transfer (CEST)⁸⁴ is an MR molecular imaging contrast providing information on tissue biochemistry. This method relies on the proton exchange between water and its solutes (such as metabolites, proteins, ...), both of which resonate at a different Larmor frequencies. The selective RF saturation at the resonant frequency of protons bound to the solute of interest leads to the saturation of the local water proton pool via chemical exchange. With a sufficiently long saturation time compared to the exchange rate, this leads to a measurable and frequency-dependent change of the water signal, thus enabling indirect imaging of the low-concentration solute. In the context of stroke, CEST can

for instance detect tissue acidosis via the pH-dependent rate of amide proton transfer (APT)⁸⁵ to provide additional information to PWI and DWI in assessing cerebral tissue viability⁸⁶.

MRI is not limited to the measurement of water molecules and their interaction with the surrounding tissues. After removing the overwhelming signal from water protons, MR spectroscopy (MRS) enables the investigation of tissue biochemistry by instead measuring the signal of protons attached to the various biomolecules present in the body. The chemical structure of each molecule yields a specific set of resonant frequencies, enabling their differentiation and quantification using MRS. Dysregulation of metabolic pathways is a common occurrence in most diseases. Therefore, MRS could offer key information on diseases and the response of the body to therapies prior to morphological changes.

In stroke, variations of the neurochemical profile, the collection of cerebral biomarkers detected by ¹H MRS, were first measured in 1988 by Berkelbach van der Sprenkel et al.⁸⁷. The main biochemical alterations detected by ¹H MRS are elevated lactate, resulting from anaerobic analysis, as well as decreased N-Acetylaspartic acid (NAA)⁸⁸, which is a marker of neuronal integrity. The evolution of these biomarkers could provide an indication about tissue damage^{89,90}. Nowadays, following substantial improvements in the sensitivity and acquisition schemes, ¹H MRSI achieves a sufficiently high spatial resolution mapping of lactate and NAA to resolve the lesions within a clinically acceptable time frame for sick patients^{91,92} (Figure 1.4). However, due to limited sensitivity and small ¹H chemical shift dispersion, causing overlap of the metabolite peaks, only the most prominent metabolites can be reliably detected and quantified. In contrast, preclinical studies, benefiting from better spectral separation and sensitivity due to higher magnetic field strengths, are able to perform a better quantification of the neurochemical profile and identification of additional biomarkers^{93,94}.

As a result of the presence of endogenous background signal, it is difficult to directly assess the fate of a therapeutic agent apart from the overall metabolic changes produced on the imaging subject. Furthermore, the timescale of ¹H MRS measurements, limited by their inherent low sensitivity (Section 1.3), only provides steady-state metabolite concentrations. Access to information about metabolic fluxes can be achieved by measuring thermally-polarized (i.e. non-hyperpolarized) isotopically labeled molecules, in particular with ²H or ¹³C. Due to the low natural abundance of some MR-active isotopes (0.016% for ²H and 1.1% for ¹³C), there is no endogenous background signal. Therefore, the metabolism of the injected MR-active agent can be directly assessed to deduce its metabolic kinetics. However, the main limitation of such measurements is the low sensitivity achievable using low-gamma nuclei, requiring long infusion and acquisition times. This is particularly difficult to perform in the context of stroke and does not allow resolving the rapidly changing metabolic conditions in the acute phase of ischemia.

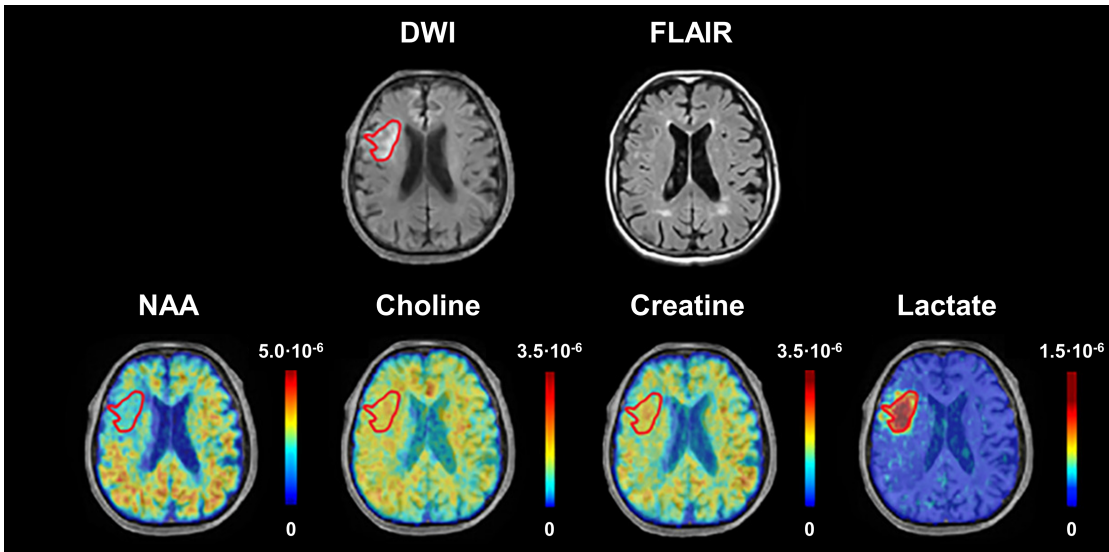


Figure 1.4: Example of ^1H MRI (top row) and ^1H MRSI (bottom row) performed in the acute phase of stroke, at around 2.5 h post stroke onset. The red contours delimit the extent of the ischemic core, as observed in diffusion-weighted imaging. No signs of the lesion is visible on the fluid attenuated inversion recovery (FLAIR) contrast image at this stage. The MRSI images are registered to the structural images and normalized to the unsuppressed water signal intensity. The spectroscopic images report a decrease of NAA and increase of lactate at the lesion site. Figure adapted from Lin et al.⁹²

1.3 Spin polarization and sensitivity in MR

Matter is made of atoms, which are the smallest particles carrying the properties of elements. Each atom consists of a cloud of one or more electrons, as well as a nucleus made of nucleons, at least one proton and typically a similar number of neutrons. One of the fundamental properties of an atomic nucleus, resulting from the coupling between nucleons, is its nuclear spin I to which a nuclear spin quantum number I is attributed. Depending on the constituents of the nucleus, I can be null, take an integer (bosons) or a half-integer (fermions) value. Nuclei with an odd mass number have a half-integer spin, while those with an even mass and an odd atomic number have an integer spin. For MR purposes, only nuclei having a net non-zero nuclear spin are detectable.

The magnitude of the nuclear spin angular momentum relates to the spin quantum number as follows:

$$|I| = \hbar\sqrt{I(I+1)} \quad (1.1)$$

where \hbar is the reduced Planck constant. Due to the quantization of the angular momentum, the projection of I along a given axis (typically z by NMR conventions) are restricted to a set of $2I + 1$ spin states to which an integer or half-integer nuclear spin magnetic quantum number

m_I is associated:

$$m_I = -I, -I + 1, \dots, I - 1, I \quad (1.2)$$

The nuclear spin angular momentum gives rise to a nuclear magnetic moment:

$$\boldsymbol{\mu}_I = \gamma_I \mathbf{I} \quad (1.3)$$

where γ_I is the nuclear gyromagnetic ratio, which is a constant for each nuclear isotope possessing a spin that can be measured experimentally. The nuclear magnetic moment and the nuclear spin angular momentum, being proportionally related, obey the same quantization rules:

$$|\boldsymbol{\mu}_I| = \gamma_I \hbar \sqrt{I(I+1)} \quad (1.4)$$

$$\mu_{I,z} = \gamma_I \hbar m_I \quad (1.5)$$

When placed in an external magnetic field $\mathbf{B}_0 = B_0 \hat{z}$, by convention chosen to be oriented along the z axis, the spin magnetic moment interacts with the magnetic field, with an interaction energy given by the Zeeman Hamiltonian:

$$\mathcal{H}_{ZI} = -\boldsymbol{\mu}_I \cdot \mathbf{B}_0 = -\gamma_I \hbar I_z B_0 \quad (1.6)$$

Since the projection of the angular momentum along the static field direction can only have discrete values m_I , the energy states that the spins can occupy are discrete:

$$E_{m_I} = -\gamma_I \hbar m_I B_0 \quad (1.7)$$

Nuclei with a $\frac{1}{2}$ spin such as ^1H or ^{13}C on which we will focus in this thesis, can therefore take two discrete states $m_I = +\frac{1}{2}$ (parallel to B_0 , $|\uparrow\rangle$) and $m_I = -\frac{1}{2}$ (antiparallel to B_0 , $|\downarrow\rangle$) corresponding to the following energy levels:

$$E_{+\frac{1}{2}} = -\frac{1}{2} \gamma_I \hbar B_0 \quad (1.8)$$

$$E_{-\frac{1}{2}} = \frac{1}{2} \gamma_I \hbar B_0 \quad (1.9)$$

The energy gap between both nuclear spin states is $\Delta E = \gamma_I \hbar B_0 = \hbar \omega_I$, where ω_I is the resonance frequency of the nucleus and is known as the Larmor frequency.

Let us consider an ensemble of N spins in equilibrium within the external field B_0 and at a temperature T . Let N_\uparrow and N_\downarrow denote the number of nuclei in the $|\uparrow\rangle$ and $|\downarrow\rangle$ states, respectively, and $N = N_\uparrow + N_\downarrow$.

The population of spins across the energy levels follows a Boltzmann distribution:

$$N_{\uparrow} = N \frac{\exp\left(-\frac{E_{+\frac{1}{2}}}{k_B T}\right)}{\exp\left(-\frac{E_{+\frac{1}{2}}}{k_B T}\right) + \exp\left(-\frac{E_{-\frac{1}{2}}}{k_B T}\right)} \quad (1.10)$$

$$N_{\downarrow} = N \frac{\exp\left(-\frac{E_{-\frac{1}{2}}}{k_B T}\right)}{\exp\left(-\frac{E_{+\frac{1}{2}}}{k_B T}\right) + \exp\left(-\frac{E_{-\frac{1}{2}}}{k_B T}\right)} \quad (1.11)$$

where k_B is the Boltzmann constant. The spin-up state $|\uparrow\rangle$ being at a lower energy, its probability of occupation is higher. The nuclear polarization P is defined as the proportion of the spin population with a spin aligned along B_0 :

$$P = \frac{N_{\uparrow} - N_{\downarrow}}{N_{\uparrow} + N_{\downarrow}} = \tanh\left(\frac{\gamma_I \hbar B_0}{2k_B T}\right) = \tanh\left(\frac{\hbar \omega_I}{2k_B T}\right) \quad (1.12)$$

In a classical approach, the sum of the magnetic moment of the N nuclear spins yields a macroscopic magnetization \mathbf{M} . In NMR/MRI experiments, it is manipulated using RF electromagnetic fields that generate an oscillating magnetization component in the transverse plane (xy), which will induce an electromotive force in the detection RF coil.

By combining equations 1.5 and 1.12, at thermal equilibrium, the magnetization is aligned along the z axis and reads:

$$\mathbf{M}_0 = N \mu_{I,z} P \hat{\mathbf{z}} = N \frac{\gamma_I \hbar}{2} \tanh\left(\frac{\gamma_I \hbar B_0}{2k_B T}\right) \hat{\mathbf{z}} \quad (1.13)$$

The MR signal, excluding the contribution of the acquisition sequence and hardware, depends on the number of spins and the polarization. In typical conditions for NMR and MRI we have $k_B T \ll \gamma_I \hbar B_0$. Therefore, the population difference between $|\uparrow\rangle$ and $|\downarrow\rangle$ is very small. To provide an example, at 310 K and 7 T, the static field strength of the highest MRI scanner currently approved for clinical use, the polarization of ^1H is only 23 ppm, and 5.8 ppm for ^{13}C due to the 4-fold smaller gyromagnetic ratio. As a consequence, MRI and NMR are inherently insensitive techniques.

In MRI, which mainly measures water protons, the low polarization is compensated by the body's high water content (approx. 55 M), resulting in a large number of spins. On the other hand, MRS is more difficult, as it focuses on measuring low-concentration metabolites at millimolar levels. Additionally, the measurement of nuclei other than ^1H (X-nuclei) is more difficult due to the lower gyromagnetic ratio, which results in a weaker magnetic moment and smaller thermal polarization. Moreover, a lower natural abundance of MR-active isotopes

characterizes certain X-nuclei. For example, ^{13}C only has a natural abundance of 1.1%, and may require isotopic labeling to yield measurable MR signals.

A higher MR signal can be achieved through a larger thermal polarization by increasing the magnetic field strength. Currently, the highest field strength is 11.7 T for research-only human MRI⁹⁵, 21.1 T for preclinical small-rodent MRI^{96,97}, 28.2 T for persistent NMR magnets⁹⁸. Although this leads to a higher sensitivity, as well as better spectral separation for spectroscopy, MR at higher field strengths is not only exponentially expensive, but also comes with several disadvantages such as exacerbated static field inhomogeneity, inhomogeneous RF excitation and reception, increased RF power deposition, as well as undesirable physiological effects on living subjects⁹⁹.

Electron spins can be described in a similar way as nuclear spins, using the superscript S instead of I by convention. Electrons are spin $\frac{1}{2}$ particles with a negative gyromagnetic ratio, therefore their magnetic moment and angular momentum are oriented in opposite directions. As a result, the states $m_S = -\frac{1}{2}$ and $+\frac{1}{2}$ correspond to the low and high energy states, respectively. One of the particularities of electron spins is their large gyromagnetic ratio compared to nuclear spins, for example $|\gamma_e/\gamma_{\text{H}}| = 658$ and $|\gamma_e/\gamma_{^{13}\text{C}}| = 2620$, which confers them a substantially larger polarization at a given temperature and magnetic field strength.

1.4 Nuclear spin hyperpolarization

Hyperpolarization refers to processes that significantly increase the alignment of nuclear spins by creating a non-equilibrium polarization state beyond the Boltzmann thermal distribution. This enables a substantial improvement of the NMR/MRI sensitivity allowing the detection of smaller material amounts, faster image acquisition, or the observation of phenomena that would otherwise be invisible. While the large spin order requires a highly specialized apparatus for its production, it can, under specific conditions, be transported to enable off-site MR signal enhancement. In this section, we provide a brief overview of the different methods that can be used to hyperpolarize substrates relevant for biological MR applications.

1.4.1 Brute-force method

The brute-force method¹⁰⁰ consists in subjecting the sample to a very low temperature and intense magnetic field. By reducing the thermal agitation and increasing the Zeeman energy gap, a larger population difference between spin states is achieved, as determined via the Boltzmann distribution (Equation 1.12). Hirsch et al.¹⁰¹ demonstrated that after being polarized, the sample can be ejected from the polarizer, passing through a low-field region (down to ≈ 20 mT), and dissolved at a high magnetic field (2 T) to yield a liquid-state hyperpolarized

solution, with an estimated polarization loss of 20% compared to the theoretical maximum. The brute-force approach benefits from a high versatility, as it can be applied to any type of substrate and does not require any specific sample formulation. By avoiding the need for polarizing agents or chemical reactions, the brute-force approach reduces the potential sources of contamination. Furthermore, this method allows extracting the solid sample for transportation of hyperpolarization in cryogenic conditions: at 30 K and 2 T, the ^{13}C T_1 is about 5 h, and exceeds 20 h at liquid helium temperature¹⁰². The main limitation of this method is the slow polarization buildup resulting from a long longitudinal relaxation time, which may be in the range of tens of hours or days in such low-T and high-B conditions. As an example, Hirsch et al.¹⁰¹ achieved ^{13}C liquid-state of up to 0.13% for [1- ^{13}C] pyruvic acid following several tens of hours of polarization at 14 T and 2.3 K, and attempts at lower temperatures did not result in higher polarizations in the liquid state. Nonetheless, higher and faster polarization levels could be attained by polarizing at lower temperatures (10-100 mK) with the help of aluminum or copper nanoparticles to increase the nuclear relaxation rate¹⁰³.

1.4.2 Spin-exchange optical pumping (SEOP)

Spin-exchange optical pumping¹⁰⁴ is the gold standard for the hyperpolarization of noble gases such as ^3He , ^{83}Kr and ^{129}Xe . The process is performed within an optical cell placed in a static magnetic field (mT range) filled with the noble gas, an alkali metal vapor (usually rubidium or cesium), as well as a buffer inert gas (nitrogen or helium) to improve the process efficiency.

The first step consists in the optical pumping of alkali metal valence electrons. A high-power circularly polarized laser light, whose wavelength matches the lowest energy transition of the alkali metal (for rubidium, the D_1 resonance at 794.7 nm), is shined at the optical cell in the same direction as the magnetic field. Due to the angular momentum conservation, the circularly polarized light selectively moves the population from one m_S spin state to the other, leading to an electronic spin hyperpolarization. The buffer gas suppresses the fluorescence of alkali metal atoms to avoid photon emission with opposite polarization. In the second step, the alkali metal valence electrons and noble gas nuclei exchange their spins, specifically their angular momentum through Fermi-contact hyperfine interactions. This exchange occurs during binary gas-phase collisions between the two species, or three-body collisions through the intermediary of the buffer gas that leads to the momentary formation of a Van der Waals alkali metal-noble gas molecule. Binary collisions dominate at low gas pressure, while high pressure favor the occurrence of tertiary collisions¹⁰⁵.

The SEOP process is typically operated in either of two primary modes: *continuous flow* in which the gas mixture flows through the optical cell while being hyperpolarized and *stopped*

flow in which the gas mixture is sealed within the optical cell and only extracted once a sufficient polarization level is achieved. The choice of the mode depends on the specific requirements of the application: while the former enables the delivery of a continuous supply of hyperpolarized noble gas, the latter allows longer exposure of the gas to enable higher polarization levels, but at the cost of a lower throughput. As examples, Nikolaou et al.¹⁰⁶ achieved the production of 0.5 L at standard temperature and pressure (STP) ^{129}Xe polarized at $(74 \pm 7)\%$ within 80 min in stopped flow mode, while Norquay et al.¹⁰⁷ reported the continuous production of ^{129}Xe polarized at 30% at a flow rate of 1.8 L h^{-1} at STP.

In the context of biomedical imaging, the high-throughput production of polarized noble gases allows probing lung ventilation, microstructure, and gas exchange, with each clinical scan protocol typically requiring a dose of 1 to 3.5 L per human patient^{108,109}. The use of HP xenon as a tool for visualizing pulmonary ventilation has recently received approval for clinical use from the Food and Drug Administration (FDA) in 2022¹¹⁰. In addition, xenon can also dissolve into the blood stream and be used as a molecular imaging biosensor^{111,112}.

1.4.3 Parahydrogen-induced polarization (PHIP)

Parahydrogen-induced polarization uses the parahydrogen nuclear singlet state as a source of hyperpolarization. Hydrogen molecules (H_2) exist in two nuclear spin isomer forms: orthohydrogen ($o\text{-H}_2$) and parahydrogen ($p\text{-H}_2$), corresponding to a parallel and antiparallel alignment of the proton nuclear spins, respectively. $p\text{-H}_2$ is the lowest energy spin isomer, which accounts for a 25% fraction of the total H_2 population at room temperature. Cooling the gas increases this proportion to 50% at 77 K, and near-unity¹¹³ around 22 K, right above the hydrogen boiling point at atmospheric pressure. To speed up the interconversion from $o\text{-H}_2$ to $p\text{-H}_2$, a catalyst, for example activated charcoal or iron oxide, is typically used. After reaching an equilibrium parahydrogen fraction at low temperature, the hydrogen gas can be separated from the catalyst and warmed up. In the absence of paramagnetic impurities¹¹⁴, and in an appropriate storage container¹¹⁵, the interconversion rate is extremely slow between hydrogen spin isomers, such that the non-equilibrium parahydrogen enrichment can be conserved for months at ambient temperature¹¹⁶.

Once a supply of parahydrogen is available, it remains to transfer this high spin order to the molecule of interest.

One way to prepare a hyperpolarized substrate via PHIP is by adding parahydrogen to an unsaturated molecular precursor, under either high ($>1 \text{ T}$) or low (1-10 mT) magnetic field conditions via the PASADENA¹¹⁷ (parahydrogen and synthesis allow dramatically enhanced nuclear alignment) or ALTADENA¹¹⁸ (adiabatic longitudinal transport after dissociation engenders net alignment) protocols, respectively. The pairwise addition of parahydrogen at

non-equivalent chemical sites of the target molecule breaks their symmetry and yields a large measurable proton hyperpolarization. The large polarization is not limited to protons and can be transferred to adjacent X-nuclei, typically^{119,120} ^{13}C or ^{15}N , which is especially beneficial to biomedical applications, as it provides a slower spin-lattice relaxation, a broader chemical shift dispersion, and avoids the large ^1H background signal. This transfer occurs spontaneously at low magnetic field via J-couplings, or using a spin transfer RF pulse sequence at high magnetic field.

Alternatively, PHIP can be performed in a non-hydrogenative process via the SABRE¹²¹ (signal amplification by reversible exchange) method. Using a polarization transfer catalyst, typically a hexacoordinate iridium complex¹²², the p- H_2 and target molecules are momentarily and reversibly bonded together, creating a transient J-coupling network enabling the polarization transfer from p- H_2 to the target substrate. Compared to hydrogenative PHIP, the hyperpolarized substrate is chemically identical throughout the process, and can repeatedly undergo multiple hyperpolarization steps to build up the polarization.

The polarization level achieved with PHIP-based methods greatly depends on the optimization of the polarization transfer protocol to the specific structure of the target molecule. For ^{13}C substrates, polarization levels in the range of 10-50% can be achieved¹²³⁻¹²⁷, allowing biomedical applications. Unlike other nuclear spin hyperpolarization methods, which slowly build up the polarization, PHIP presents the advantage of achieving the preparation of hyperpolarized substrates within seconds. Nevertheless, the main challenges are the range of substrates that can be hyperpolarized, as well as the filtration of the residual reaction catalyst, solvents, and products before administering the polarized substrate.

1.4.4 Dissolution dynamic nuclear polarization (dDNP)

Dissolution dynamic nuclear polarization is the method on which we will focus throughout this thesis. It is a class of methods which consists in transferring the polarization of unpaired electron spins to nuclear spin via microwave irradiation. The large gyromagnetic ratio of electron spins provides them with a substantially higher polarization at thermal equilibrium than any nuclear spin, as discussed earlier in Section 1.3. At a high magnetic field strength and sub-liquid helium temperatures, the electron spin polarization approaches unity (Figure 1.5).

In 1953, Overhauser¹²⁸ provided the first theoretical description of DNP, predicting that the polarization transfer from electrons to nuclear spins could be induced via microwave radiation at the resonant frequency of the conduction band electrons. The same year, Carver and Slichter¹²⁹ performed the first experimental demonstration of DNP by enhancing the NMR signal of a ^7Li metal sample by two orders of magnitude at 3 mT. Shortly after, this technique was extended to non-conducting solids theoretically by Jeffries¹³⁰ in 1957, and

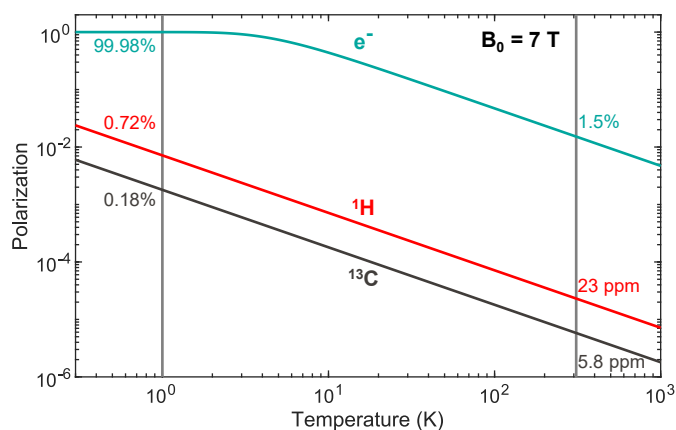


Figure 1.5: Thermal polarization of electrons, ^1H and ^{13}C at 7 T as a function of the temperature. The vertical gray lines at 1 K and 310 K represent the operating conditions of the 7T/1K polarizer (Used in Chapters 2 and 3) and the human or mouse body temperature, respectively. The numbers refer to the thermal polarization of unpaired electrons, ^1H and ^{13}C at 7 T and either 1 K or 310 K.

experimentally demonstrated by Abragam and Proctor¹³¹ in a LiF crystal the following year. Initially, DNP was mainly restricted to solid-state applications in cryogenic environments and applied in high energy physics to produce polarized targets for scattering experiments, as well as for signal enhancement in magic angle spinning NMR (MAS-NMR)¹³².

In 2003, the invention of the dissolution DNP protocol by Ardenkjær-Larsen et al.¹³³, enabled the production of physiologically compatible hyperpolarized solutions. The basic principle of dDNP consists in reaching a high polarization level in the solid-state, then melting the prepolarized sample using a hot pressurized solvent. Provided that the phase transition is achieved in a quick manner and within a strong magnetic field, the transient hyperpolarized state is conserved throughout the process, yielding signal enhancements of about four orders of magnitude in the liquid state¹³³.

Nowadays, dDNP is among the most versatile hyperpolarization techniques for biomedical applications, not only enabling the production of a wide range of polarized solutions for the study of physiology, function, and metabolism¹³⁴, but also of gases^{135,136}. Despite this wide range of possible hyperpolarized tracers, an overwhelming majority of clinical and preclinical research studies the metabolism of HP [1- ^{13}C] pyruvate, which is considered the gold standard of hyperpolarized metabolic imaging. On the technical side, [1- ^{13}C] pyruvate is an ideal agent for dDNP, having a long liquid-state spin-lattice relaxation time (71 s at 1 T¹³⁷, 67 s at 3 T, and 44 s at 14.1 T¹³⁴), being self-glassing to produce highly concentrated samples, and allowing high polarization levels^{138,139}. On the biological aspects, pyruvate, the end product of glycolysis, is located at a key crossroad of cellular metabolism. Following an injection

of HP [1-¹³C] pyruvate, its uptake and metabolic conversion provide an assessment of the underlying transport and reaction mechanisms. In particular, one can observe the uptake via monocarboxylate transporters, and conversion of the ¹³C label of pyruvate into alanine via alanine aminotransferase (ALT), into lactate through anaerobic metabolism via lactate dehydrogenase (LDH) or into bicarbonate through oxidative mitochondrial respiration.

The fate of pyruvate being substantially modulated by the tissue conditions, it represents a useful metabolic contrast agent for the detection of pathologies. One of the prominent applications is the detection and grading of tumors by observing elevated pyruvate-to-lactate exchange compared to healthy tissues resulting from the Warburg effect¹⁴⁰, and led to the first clinical trial involving dDNP in 2013 by Nelson et al.¹⁴¹.

1.4.4.1 DNP Mechanisms

Under typical conditions for dDNP, i.e. sub-liquid helium temperature and strong magnetic field strength of several Teslas, the transfer of polarization from electron to nuclear spins can be mainly driven by three mechanisms: the solid effect (SE), cross effect (CE) and thermal mixing (TM).

The solid effect is a process involving one electron spin and one nuclear spin at a short spatial distance such that they interact via dipolar coupling^{142,143}. The hyperfine splitting of this two-spins system leads to a four-level energy diagram, as illustrated in Figure 1.6. The application of a microwave field at the frequency $\omega_{MW} = \omega_S + \omega_I$, where ω_S and ω_I are the Larmor frequencies of the electron and nuclear spins, respectively, simultaneously flips the electron and nuclear spins orientations. This results in a zero-quantum (ZQ) transition from $|m_S, m_I\rangle = |\downarrow, \uparrow\rangle$ to $|\uparrow, \downarrow\rangle$ (pink diagonal arrow in Figure 1.6). Similarly, applying the microwaves at $\omega_{MW} = \omega_S - \omega_I$ induces the double-quantum (DQ) transition $|\downarrow, \downarrow\rangle \rightarrow |\uparrow, \uparrow\rangle$ (green diagonal arrow in Figure 1.6). Since the solid effect arises from forbidden quantum transitions, their probability is low and requires a large microwave power to yield an observable effect.

In typical dDNP conditions, the microwave frequency is applied at a single or a narrow range of frequencies. The so-called well-resolved solid effect occurs when the ESR linewidth of the electron spins is smaller than ω_I , such that the ZQ and DQ transitions are not pumped simultaneously. As a result, the DNP enhancement profile, also called DNP microwave frequency sweep, will be characterized by a positive and a negative lobe separated by $2\omega_I$ around ω_S . On the other case, the differential solid effect happens when the ESR line of the radical is similar to the nuclear Larmor frequencies. As a result, for a given microwave frequency, certain electron spin packets may satisfy the conditions of both the ZQ and DQ transitions. The resulting nuclear polarization will then be the difference between both competing processes.

In dDNP, the solid effect is rarely distinctively observed, since the ESR line of most polarizing agents is usually larger than the Larmor frequency of the nucleus of interest. When polarizing a sample with trityl radicals, the solid effect can be observed on the DNP profile of proton spins¹⁴⁴, although this process is relatively inefficient and the focus of DNP with a trityl radical would rather be the polarization of lower γ nuclei.

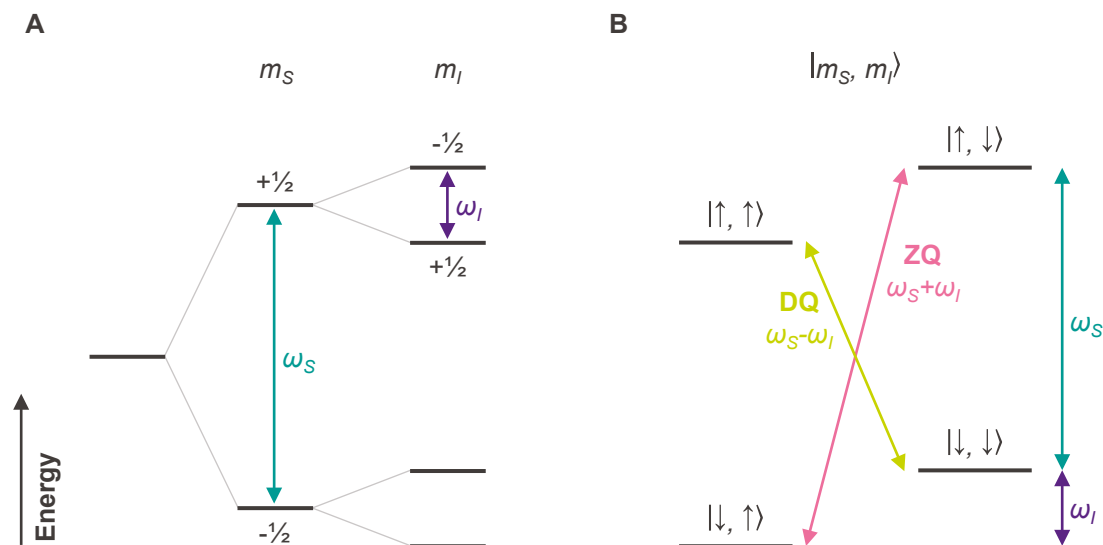


Figure 1.6: (A) Energy-level diagram for the solid effect DNP mechanism, representing the hyperfine splitting for a two spin system (one electron and one nucleus). ω_S and ω_I are the Larmor frequencies of the electron and nuclear spins, respectively. (B) Representation of the $|m_S, m_I\rangle = |\downarrow, \downarrow\rangle \rightarrow |\uparrow, \uparrow\rangle$ double-quantum (green, positive DNP enhancement) and $|\downarrow, \uparrow\rangle \rightarrow |\uparrow, \downarrow\rangle$ zero-quantum (pink, negative DNP enhancement) transitions, occurring at the microwave frequencies $(\omega_S - \omega_I)$ and $(\omega_S + \omega_I)$ respectively.

The cross effect and thermal mixing are two mechanisms that involve a three-spin system composed of two electron and one nuclear spins. Following the spin flip of one electron via the application of microwaves, this electronic depolarization propagates through the ESR spectrum via spectral diffusion, which consists in energy-conserving flip-flop transitions via electronic dipolar interactions. Finally, the polarization is transferred in the so-called triple spin flip process, in which two electrons and one nucleus simultaneously change their relative orientation in an energy-conserving transition. To achieve CE or TM, the ESR linewidth of the radical ($\Delta\omega_S$) is required to be comparable or broader than the nuclear Larmor frequency (ω_I) to find a pair of electrons capable of exchanging the required amount of energy with the nuclear spin, which is typically the case in dDNP conditions for the polarization of ^1H with a broad-line radical such as TEMPOL, and any X-nuclei even with narrow-line radicals. In typical dDNP conditions, TM and CE are the dominant mechanisms as they involve only the saturation of allowed electron spin transitions, which has a higher probability and therefore

Chapter 1. Introduction

requires a lower microwave power compared to the forbidden transitions in SE. The difference between CE and TM resides in the source or sink reservoir providing or absorbing the energy to enable the triple spin flip^{145–147}.

In **cross effect**, the difference in Zeeman energy between both electron spins is exchanged with the nuclear spin during the triple spin process, requiring the following condition to be satisfied:

$$|\omega_{S_1} - \omega_{S_2}| = \omega_I \quad (1.14)$$

where ω_{S_1} , ω_{S_2} are the Larmor frequencies of the electrons S_1 and S_2 , ω_I is the Larmor frequency of the nuclear spin I . In Figure 1.7, the energy level diagram resulting from the hyperfine interaction for the three-spin system is depicted at the CE matching conditions, choosing $\omega_{S_1} > \omega_{S_2}$. The states $|m_{S_1}, m_{S_2}, m_I\rangle = |\uparrow, \downarrow, \uparrow\rangle$ and $|\downarrow, \uparrow, \downarrow\rangle$ are degenerate, which facilitates the CE. By saturating the electron spins with microwaves around the frequencies ω_{S_1} or ω_{S_2} , a negative or positive DNP enhancement, respectively, is achieved.

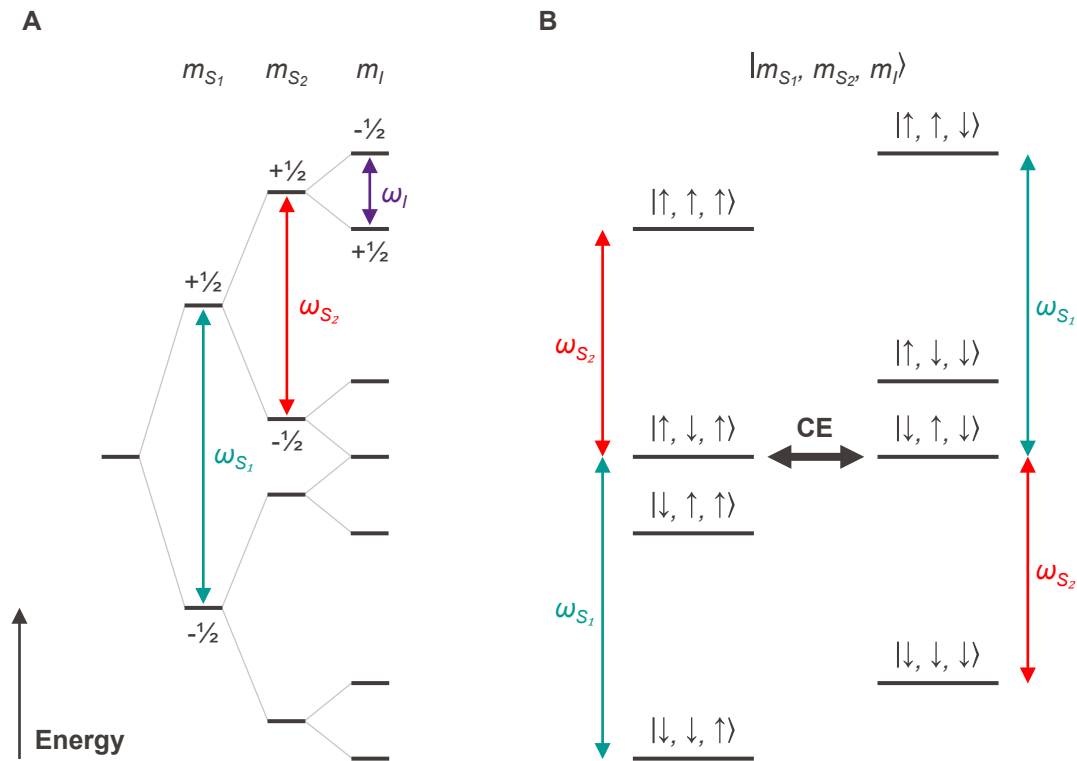


Figure 1.7: (A) Energy-level diagram representing the hyperfine splitting for a three spins (two dipolar-coupled electrons and one nucleus) system, at the cross effect matching conditions: $|\omega_{S_1} - \omega_{S_2}| = \omega_I$, $\omega_{S_1} > \omega_{S_2}$, where ω_{S_1} , ω_{S_2} and ω_I are the Larmor frequencies of the electrons and nuclear spins, respectively. (B) At the matching cross effect conditions, both states $|m_{S_1}, m_{S_2}, m_I\rangle = |\uparrow, \downarrow, \uparrow\rangle$ and $|\downarrow, \uparrow, \downarrow\rangle$ are degenerate and allow efficient CE. Positive and negative DNP enhancement via the cross effect are achieved with microwave irradiation around the frequencies ω_{S_2} and ω_{S_1} respectively.

Thermal mixing, occurs in the presence of a radical ESR line ($\Delta\omega_S$) comparable or larger than the nuclear Larmor frequency (ω_I) such that the reservoir of dipolar energy of the whole electron system is able to sink or source the energy for the triple spin flip process, and mainly broadened by dipolar interaction rather than **g**-anisotropy.

A qualitative description of the working principles of TM can be achieved using a thermodynamic approach by considering the interaction between three energy reservoirs, the electron Zeeman (E_Z), the electron non-Zeeman (E_{NZ} , also known as electron spin-spin), and the nuclear Zeeman reservoirs (N_Z). The concept of spin temperature¹⁴⁸ considers the population of the energy levels of a large isolated spin system to follow a Boltzmann distribution, to which a characteristic spin temperature is attributed. Here, the reservoirs are not totally isolated, however the rate of internal equilibrium within a reservoir is typically faster than the exchange rate between different reservoirs such that the concept of spin temperature is still applicable.

At equilibrium, and without the presence of microwave radiation, both electron spin reservoirs are at the same temperature, i.e. $T_{E_Z} = T_{E_{NZ}} = T_L$, where T_{E_Z} , $T_{E_{NZ}}$ are the characteristic temperatures of the Boltzmann distribution of the electron Zeeman and non-Zeeman reservoirs, respectively, and T_L is characteristic temperature of the lattice, which corresponds to the helium bath temperature in practice. For this condition, the distribution of the population of the electronic spin system is illustrated in Figure 1.8A. The electron spin population follows a Boltzmann distribution with characteristic temperature T_L , and is distributed among two Zeeman energy levels broadened by the spin-spin dipolar couplings.

DNP via thermal coupling occurs in two successive steps. First, using off-resonance microwave radiation, the electron spin population is shifted from the lower to the higher Zeeman energy level. As a result, the E_Z reservoir starts to heat up and the E_{NZ} reservoir is cooled down. Depending on the microwave frequency, the spin temperature of the E_{NZ} reservoir is either positive if $\omega_{MW} < \omega_S$, or negative if $\omega_{MW} > \omega_S$, corresponding to the population distributions illustrated in Figure 1.8B and C, respectively. The second step involves thermal mixing, which is the exchange of electron spin-spin dipolar energy with the nuclear spins Zeeman energy via cross-relaxing events. The simultaneous triple spin flips of two electron and one nuclear spins, with the energy conserving condition $|\omega_{S_1} - \omega_{S_2}| = \omega_I$, lower the spin temperature of the nuclear spin reservoir T_{N_Z} . The electron and nuclear spins tend to equalize their spin temperature: $T_{N_Z} \rightarrow |T_{E_{NZ}}|$, leading to the hyperpolarization of the nuclear spin pool.

To establish spin temperature and enable thermal mixing, electronic spectral diffusion is required to be relatively faster than electronic spin-lattice relaxation such that the ESR saturation propagates across the ESR spectrum to involve more electron spins into the polar-

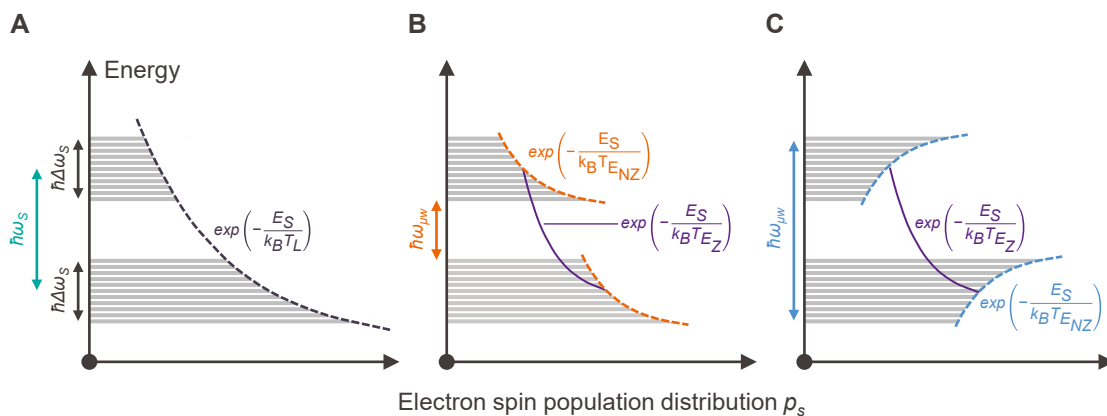


Figure 1.8: Schematic illustration of the electron spin population distribution p_s across different energy levels during thermal mixing. **(A)** At thermal equilibrium, without microwave irradiation, the spin population distribution follows a Boltzmann distribution, where E_S is the total energy of the spin system, and T_L is the lattice temperature. **(B)** Distribution of the spin population while applying microwaves at a frequency $\omega_{MW} < \omega_s$, leading to a positive spin temperature T_{ENZ} in the non-Zeeman reservoir. The electron spins are preferably shifted from the top of the lower Zeeman level to the bottom of the higher Zeeman level. T_{EZ} is the temperature of the electron Zeeman reservoir. **(C)** Distribution of the spin population while applying microwaves at a frequency $\omega_{MW} > \omega_s$, leading to a negative spin temperature T_{ENZ} . The electron spins are preferably shifted from the bottom of the lower Zeeman level to the top of the higher Zeeman level.

ization transfer process. Slow spectral diffusion can be compensated by applying microwave frequency modulation¹⁴⁹.

1.4.4.2 Indirect nuclear polarization mechanisms

Nuclear spin diffusion is an important process in DNP, enabling the spontaneous transport of polarization through space by exchanging spin polarization between neighboring nuclei via dipolar couplings. In fact, the DNP mechanisms presented above require spatial proximity to exchange electron and nuclear spin polarization via mutual dipolar coupling. As a consequence, most nuclear spins are polarized via spin diffusion, since they would be too far away from an electron to be directly polarized.

Cross-polarization (CP) is an approach that enables the transfer of polarization between two nuclear reservoirs, typically from a high-gamma nucleus such as ^1H to a low-gamma nucleus. The basic principle of CP is to force both nuclei to precess at an identical frequency in the rotating frame using locking RF pulses to fulfill the Hartmann-Hahn conditions¹⁵⁰. This aligns their energy levels in the rotating frame and enables a spontaneous magnetization transfer.

The polarization of ^1H being typically faster and higher than that of X-nuclei, especially with the application of microwave frequency modulation¹⁴⁹, the indirect DNP of X-nuclei via CP is beneficial both in terms of buildup time and polarization levels^{151,152}, provided that adequate hardware and experimental conditions are met to achieve the necessary RF pulses.

1.4.4.3 Practical considerations for dDNP

DNP sample: Hyperpolarization via dissolution DNP requires the formulation of a sample containing an MR-active substrate and a polarizing agent as the source of unpaired electrons, at least. A wide range of substrates is available to prepare hyperpolarized solutions^{134,153} or gases^{135,154,155}. The most important requirement is the spin-lattice relaxation time (T_1) of the hyperpolarized nucleus at room temperature, and in fluid state, which must be at least comparable to the processes under investigation so that the measurement can be completed before the complete loss of the HP signal. When the MR-active nucleus has a low natural abundance, for example ^{13}C , isotopically enriched substrates are employed to increase the amount of MR-active spins. This also promotes more efficient nuclear spin diffusion and faster polarization¹⁵⁶.

Typically, the DNP sample is produced by flash-freezing droplets of a solution of the substrate and the polarizing agent to form an amorphous glassy solid. The vitreous structure is important to ensure a homogeneous distribution of the polarizing agent with, at the same time, a random orientation of the molecules. The latter ensures more efficient spectral diffusion and DNP, because molecules far in frequency can be close in space. If the substrate is not found in a liquid form at room temperature or does not form a glassy matrix upon freezing, it is incorporated into a solvent and/or a glassing agent, typically water, a water:glycerol mixture, dimethyl sulfoxide (DMSO), or an alcohol.

The post-dissolution concentration, typically in the range of 20-250 mM^{141,153}, necessitates the formulation of highly concentrated samples¹⁵⁷. In some cases, this requires increasing the substrate solubility by modifying the counter ion¹⁵³, the solvent (for example, fumaric acid is weakly soluble in water but highly soluble in DMSO¹⁵³; specific alcohol chains could incorporate a larger amount of gases¹⁵⁴), the pH (in particular for amino acids¹⁵⁸), or using the acidic form of a salt (such as lactic acid instead of sodium lactate¹⁵⁹).

Together with the substrate, the polarizing agent is an indispensable component of the DNP sample. In most cases, a stable radical is mixed with the substrate solution. They can be broadly classed into two categories depending on their ESR linewidth. Broad line radicals ($\Delta\omega_S \approx \gamma_{^1\text{H}}$), typically the nitroxides TEMPO (2,2,6,6-tetramethylpiperidine 1-oxyl) or TEMPOL (4-hydroxy-TEMPO), are affordable and allow a high and rapid ^1H polarization¹⁴⁹. On the other hand, narrow line radicals ($\gamma_{^1\text{H}} > \Delta\omega_S \approx \gamma_{^{13}\text{C}}$), typically the trityls OX063 (tris(8-carboxyl-

2,2,6,6-tetrakis(2-hydroxyethyl)benzo(1,2-d:4,5-d')bis(1,3)dithiol-4-yl)methyl trisodium salt) or AH111501 (tris(8-carboxyl-2,2,6,6-tetrakis(2-methoxyethyl)benzo(1,2-d:4,5-d')bis(1,3)dithiol-4-yl)methyl trisodium salt), are more efficient for direct polarization of low-gamma nuclei, as their narrow ESR line prevents them from polarizing protons attached to substrate molecule itself or in the solvent.

In certain cases, the polarizing agent properties can be optimized by the addition of a small amount of paramagnetic metal ion complex¹⁶⁰. This causes a moderate shortening of the electron spin–lattice relaxation time (T_{1e}), lowering the achievable spin temperature by increasing the thermal coupling between the electron Zeeman system and the lattice^{160,161}. In addition, another observation is the slight narrowing of the ESR line, which decreases the electron non-Zeeman reservoir spin temperature by reducing its heat capacity. Altogether, both effects lessen the nuclear Zeeman spin temperature and boost the DNP enhancement¹⁶². Typically, a 50-100% polarization improvement is observed by adding Gd^{3+} for DNP with trityl radicals of neat pyruvic acid at 3.35 T¹⁶³, or ^{13}C substrates in H_2O :glycerol at higher fields^{162,164,165}. In Chapter 4, we present the measurement and optimization of ESR properties for trityl-doped [1- ^{13}C] lactate samples in H_2O :glycerol.

Solvent and glassing agent deuteration typically improves the direct polarization of low-gamma nuclei with broad line radicals, by lowering the heat capacity of the hydrogen Zeeman system^{164,166,167}. On the other hand, the opposite effect is observed with narrow-line radicals: while DNP of 1H via TM is prevented by the larger 1H Larmor frequency compared to the ESR linewidth, 2H spins would instead be in thermal contact with the E_{NZ} reservoir, increasing the heat load of the nuclear Zeeman system, therefore raising the spin temperature and reducing the polarization of the target nucleus.

Although the polarizing agent is necessary to perform DNP, it becomes highly undesirable when we want to exploit the HP signal. Indeed, the radical may exacerbate the polarization relaxation, be toxic or interfere with the metabolism being studied, which will be discussed in Chapter 3. To facilitate their removal, the radical can be bonded onto larger non-soluble structures, for example using thermoresponsive polymers¹⁶⁸ or hydrogels^{169,170}, as well as non-structured porous silica matrices known as HYPISO (hybrid polarizing solids)¹⁷¹⁻¹⁷⁴. Most importantly, since paramagnetic relaxation is prohibitively fast in the solid state at low magnetic field¹⁷⁵, the dissolution step is key to shelter the high spin order, achieved at low temperature and high magnetic field, along the path to extract the sample from the polarizer. Indeed, dissolving and diluting the sample have two consequences: liquid-state relaxation is more forgiving while traveling through low-field regions, and dilution increases the distance between the HP nuclei and the radicals. The price to pay is that this severely limits the possibilities for long-term storage and off-site transport of the polarized sample.

Lifting this restriction could contribute to a broader democratization of dDNP. A possible approach is the use of non-persistent polarizing agents. It consists in photo-inducing the radical, via ultraviolet or visible irradiation of a particular family of molecules known as alpha-keto acids¹⁷⁶. The radical precursor can be the MR-active substrate itself, for example, while using pyruvic acid¹⁷⁷, another substance specifically chosen for achieving ideal ESR properties¹⁷⁸, or selecting an endogenous agent to reduce potential toxic effects¹⁷⁹. Once the sample is polarized, the radical is annihilated by thermalizing the sample slightly above 190 K¹⁸⁰. The radical-free sample then behaves similarly to samples polarized via the brute-force method^{101,102}, and exhibits a slow nuclear relaxation with a ^{13}C T_1 in the order of tens of hours at DNP conditions. Provided that a magnetic field of at least ≈ 40 mT is kept at all times to avoid low-field nuclear thermal mixing between ^1H and ^{13}C ^{181,182}, it has been demonstrated that the sample can be taken out from the polarizer as a solid while retaining the high spin order and moved to a transportation device¹⁸³ working at 1 T and 4.2 K, and benefit from a T_1 of about 18 h under transport conditions for ^{13}C labeled glucose samples.

Another approach consists in deliberately creating an inhomogeneous sample. By keeping the polarizing agent and the target ^{13}C substrate in distinct phases¹⁸², a sufficient physical distance is achieved to reduce paramagnetic relaxation. Both phases contain a high abundance of ^1H spins, such that efficient ^{13}C DNP can be achieved in three steps: first, the abundant ^1H in the radical phase are directly polarized. Then, ^1H spin diffusion relays this polarization to the substrate phase. Finally, cross-polarization^{151,152} transfers the ^1H polarization to ^{13}C . Once hyperpolarized, the ^{13}C spins in the substrate are immune from radical-induced depolarization by the physical isolation of the paramagnetic centers as well as inefficient ^{13}C spin diffusion in the non-enriched radical phase. With such substrates, a long lifetime of the ^{13}C polarization is achieved: for example, micro-particulate samples of ^{13}C -labeled molecules dispersed into a hydrophobic radical glass-forming solution exhibited a T_1 between 5 and 37 h at 4.2 K and 6.7 T¹⁸². This enabled the transfer of the solid DNP sample to an external storage container, using the same precautions as in brute-force hyperpolarization or DNP with photo-induced polarizing agents, to allow the storage and transport of hyperpolarization¹⁸². Recently, porous hyperpolarizing polymers (HYPOP)¹⁸⁴, which are epoxy resins having embedded free radicals within their bulk, were conceived to provide a simple matrix for the preparation, hyperpolarization, storage and transport of impregnated ^{13}C solutions. A ^{13}C T_1 above 5.7 h for a multi-substrate sample was observed at liquid helium temperature and 6.7 T. Following dissolution and filtration, a pure hyperpolarized solution is obtained, specifically without the presence of radicals or glassing agents.

dDNP polarizer: A so-called “dDNP polarizer” provides the necessary conditions to achieve high electronic polarization, i.e. high magnetic field (typically 3.35 T to 10.1 T) and sub-liquid

helium temperature (typically 0.8-1.4 K), microwaves around the ESR to initiate polarization transfer from electrons to nuclei, as well as a system to load and dissolve or extract the sample.

In most dDNP polarizers, such conditions are achieved using a superconducting magnet and through evaporative cooling of liquid helium, with the sample being immersed in a bath of superfluid liquid helium to ensure a good thermal conduction. In the early days of dDNP, the cooling was achieved using an open-cycle cryostat relying on a fresh supply of liquid helium. The original device designed by Ardenkjær-Larsen et al.¹³³ is based on a narrow-bore 7T NMR magnet, which was modified to incorporate a variable temperature insert (VTI). The liquid helium pool is replenished from the magnet helium reservoir through a capillary and needle valve. A 1.2 K helium bath is achieved by lowering the vapor pressure to about 0.8 mbar through a 200 m³ h⁻¹ roots pump backed by a 40 m³ h⁻¹ vane pump. A probe inserted into the VTI is terminated with a cylindrical cavity to which microwaves are delivered through a rectangular waveguide. A saddle coil inside the cavity allows measuring the NMR signal of the sample.

dDNP was initially performed at 3.35 T, corresponding to an ESR frequency of 94 GHz for which microwave equipment, typically used for radar applications, was widely available. Over the years, the quest towards higher polarization levels gradually pushed researchers to increase the magnetic field strength, principally to 5 T¹⁸⁵ (140 GHz ESR) and 6.7-7.0 T^{186,187} (188-196 GHz ESR). Magnetic field strengths higher than 7 T were not found to provide substantial advantages in terms of polarization for direct ¹³C polarization, while requiring longer buildup times, and higher radical concentrations¹³⁹. Based on similar principles, several research polarizers have been developed. Most of them are based on an unmodified wide-bore NMR magnet, into which an independent VTI is inserted. In this case, the liquid helium is supplied from an external tank via a liquid helium transfer line¹⁸⁸⁻¹⁹¹. Such a system is used throughout this thesis, and a more detailed description of it is provided in Section 4.3.1.

These wet systems from the early days were quite impractical, particularly due to the large consumption of cryogenic fluids, which are costly and difficult to handle. This motivated the development of zero-boil off, or cryogen-free, polarizers which rely on a cold head to keep the magnet at superconducting temperature and reliquefy a small amount of helium in a closed loop. Cryogen-free polarizers are characterized by a separate static helium bath in which the sample is immersed, which helps to reduce the risk of contamination of the cryogenic system due to leaks during handling of the sample. Several designs have been developed over the years. The first cryogen-free dDNP polarizer¹⁹², later developed into the only one approved for clinical use (GE SPINlab™), employs a helium bath pumped by a sorption pump to achieve a sample temperature of 0.8 K. Once saturated, the charcoal trap is warmed up to a few tens of Kelvin to release the helium, which is then recondensed to the bath by the cold head. Although this process is cryogenically very efficient, since the helium is kept cold at

all times, it cannot sustain continuous operation as it needs to be regenerated periodically, typically overnight. Another family of cryogen-free polarizers^{139,193} continuously liquefies the helium into a small helium pot, which then flows to the VTI through a capillary and a needle valve. The VTI is pumped on to achieve sub-liquid helium temperatures, and then the helium gas undergoes purification and liquefaction to close the cycle. Finally, the polarizer proposed by Cheng et al.¹⁹⁴ is different and cryogenically more refined because it has a static sample space thermally anchored to both stages of the cold head and to a separate closed-cycle 1K-pot.

To drive the DNP processes, a small microwave source is required, in most cases based on either a voltage-controlled oscillator (VCO) or an arbitrary frequency synthesizer, followed by a frequency multiplication and power amplification chain to deliver microwaves at 94-282 GHz. Depending on the sample being investigated, magnetic field strength, temperature, as well as the efficiency of the waveguide and microwave cavity, a typical power of 10 to 200 mW at the source output is sufficient to achieve maximum DNP enhancement^{133,139,195,196}.

Dissolution and transport: The DNP sample is brought to physiological conditions before being administered to the imaging subject. In most cases, this process is performed within the polarizer. The sample is lifted above the liquid helium bath to avoid excessive boil-off during the process, but still kept within a region of high magnetic field strength to avoid extreme low-field paramagnetic relaxation. The dissolution melts and dilutes the sample, moving the hyperpolarized nuclei away from the paramagnetic centers, and pushed the resulting solution out of the cryostat. Usually, the dissolution is achieved using 3-10 mL (for preclinical applications) of superheated D₂O, which reduces dipolar relaxation¹⁹⁷ compared to water. It may contain a buffering agent to bring the basic/acidic substrates to a physiological pH. Furthermore, a small amount of ethylenediaminetetraacetic acid (EDTA) is often added to chelate the traces of paramagnetic impurities introduced by the dissolution apparatus.

Originally, the dissolution was performed by inserting a dissolution wand (stick) into the polarizer, which requires the cryostat to be pressurized to ambient pressure^{133,188}, unless it features a hermetic seal to remain in vacuum^{198,199}. Towards the requirements of clinical dDNP polarizers, the so-called fluid path (FP) technology¹⁹² has been developed to offer a sample handling/dissolution system, which is sterile, simple to use, and with a reduced heat load. Later, this technology has been adapted to preclinical polarizers, both of cryogen-free^{139,194} and wet types²⁰⁰⁻²⁰². In Chapters 4 and 5, we demonstrate how the fluid path technology can improve the handling, performance, and versatility of wet DNP polarizers.

Lower dilution factors, which are particularly beneficial for the low-volume requirements of NMR applications, can be achieved using the Bullet DNP method^{203,204}, which performs the

dissolution outside the polarizer in a smaller solvent volume (0.5-1 mL) following fast transfer (70 ms) through a magnetic tunnel (60 mT) to limit radical-induced low-field relaxation.

Post-dissolution, the lifetime of the hyperpolarized agent is limited by its nuclear spin-lattice relaxation. This is additionally exacerbated by residual paramagnetic polarizing agents. Several approaches can be undertaken to minimize the polarization losses before dispensing the substrate to the imaging subject. First, for non-clinical applications, the transfer time can be drastically shortened by quickly flowing the hyperpolarized solution using an automated transfer system between the DNP polarizer and the NMR/MRI measurement magnet²⁰⁵⁻²⁰⁸. This also reduces human input and drastically improves experimental reproducibility. Along the transfer path, the fast relaxation in low-field regions²⁰⁹ can be avoided by using a magnetic tunnel²¹⁰. Similarly, for transfers over moderate distances (100-1000 m), the polarization can be sheltered using a portable permanent magnet²¹¹. Several parameters such as pH²¹² or temperature²¹¹ (See also Figure 4.12) can be adjusted to yield a more favorable spin-lattice relaxation. Finally, the polarizing agents can be removed to eliminate their contribution. For example, trityls can be precipitated then filtered¹³⁹, nitroxyl radicals can be reduced using ascorbic acid²¹³, photoinduced agents are quenched by the temperature jump during dissolution²⁰², and radicals bound to an insoluble phase can be mechanically filtered^{168,171,184}. Clinical applications require removal of the polarizing agent, followed by a safety and quality control of the pH, temperature, polarization, radical and pyruvate concentration prior to injection.

Acquisition: Hyperpolarized substrates offer a large, but finite and quickly decaying nuclear polarization within minutes. The specific nature of this signal brings unique challenges and opportunities to MR acquisitions. The substantial signal enhancement, by about four or five orders of magnitude¹³³, drastically lowers the detection limit of MR techniques, enabling the measurement of functional or metabolic processes in real time²¹⁴. By probing the non-steady-state flux and metabolism of hyperpolarized tracers, and in the absence of background signal, the kinetics of specific metabolic pathways can be studied to offer a complementary assessment to other imaging modalities.

Fast measurements are required, not only to resolve the rapid time evolution of the functional or metabolic processes under investigation, but also because of the limited lifetime of the hyperpolarized signal reservoir. In addition, efficient sampling is critical, since the nonrenewable longitudinal magnetization is reduced by each subsequent RF excitation. The acquisition scheme is a tradeoff²¹⁵⁻²¹⁷ between the encoding of five dimensions (3 spatial, 1 temporal, and 1 spectral), and is selected depending on the specific requirements of the probe and application. In Chapter 6, we present an overview of the benefits and trade-offs of the main pulse sequences used for HP MRSI.

In conventional MR, the sensitivity roughly scales²¹⁸ with $B_0^{\frac{3}{2}}$: both the thermal polarization and voltage induced in the coil for a given amount of transverse magnetization are proportional to B_0 , while the noise scales with $B_0^{\frac{1}{2}}$. In contrast, HP MR decouples the non-Boltzman nuclear polarization from the magnetic field strength, such that the sensitivity only scales with $B_0^{\frac{1}{2}}$. Although a majority of hyperpolarized MR studies are performed at high field strength (clinical studies at 3 T²¹⁹ and up to 14.1 T in preclinical studies²²⁰), lower field strengths could, in fact, be more favorable due to slower nuclear relaxation²²¹, reduced B_0 artefacts, lower requirements of the gradient system, and more importantly while keeping a similar sensitivity^{222–224}.

1.5 Stroke theranostics with hyperpolarized probes

Theranostics is an emerging and rapidly evolving field in which **therapeutics** and **diagnostics** are combined into a single multifunctional agent²²⁵, with the aim of providing personalized patient-centered care. In most cases, a therapeutic molecule or nanoparticle, which binds, accumulates, or reacts with pathological tissues, is labeled with a diagnostic component such that it can be detected with an imaging modality, such as MRI, positron emission tomography, computed tomography, fluorescence imaging, or ultrasound imaging.

The incorporation of a diagnostic tool into the therapeutic agent could, for example, monitor the drug delivery at the lesion site, enhance specific cell/tissue targeting, or perform real time monitoring of the treatment efficiency. For instance, this allows personalized treatments by tailoring the therapeutic dose to the specific needs and characteristics of each patient.

As described earlier, with the use of dDNP, a wide range of molecules, provided that they can be isotopically labeled with MR-active nuclei, can be hyperpolarized to boost their MR sensitivity, enabling their metabolism and/or biodistribution *in vivo* to be measured. In the context of neurological disorders, a variety of substrates can be used as tracers to highlight different aspects of metabolic disruption²²⁰. For ischemic stroke, [1-¹³C] pyruvate^{226,227} or [1-¹³C] lactate²²⁸ could be used as biomarkers for aberrant metabolism after stroke, while abnormal cerebral perfusion can be probed using HP ¹²⁹Xe²²⁹. However, these probes are not solely limited as a tracer role: at a sufficient dose, as discussed earlier in Section 1.1.2, they could also provide a therapeutic neuroprotective effect, therefore becoming potential theranostic molecules for stroke. Being able to monitor the biochemical conversion or biodistribution of these therapeutic agents in the ischemic brain could contribute to a better understanding of how they interact with the pathology, their efficiency, and tailor the subsequent treatment steps to the specificity and needs of the patient.

Chapter 1. Introduction

In this work, the objective is to further investigate and develop the potential of known neuroprotectants as HP diagnostic agents for cerebral ischemia in the preclinical setting, ultimately paving the way to a theranostic approach for stroke. We compare the potential of the neuroprotective agents [1-¹³C] lactate and [1-¹³C] pyruvate as metabolic contrast agents for stroke. To provide a better characterization of the altered dynamic and regional metabolic patterns after stroke, we improve the HP MR setup and acquisition methods to enhance the sensitivity and spatiotemporal resolution of our acquisitions. Stroke being a multifaceted medical condition, causing substantial physiological, morphological, microstructural, and metabolic changes, we develop the methodology to enable simultaneous hyperpolarization and combined administration of multiple neuroprotective agents to provide a more comprehensive view of this disease condition.

2 *In vivo* assessment of the metabolic impact of cerebral ischemia using MRS and hyperpolarized [1-¹³C] lactate and [1-¹³C] pyruvate

2.1 Abstract

Following ischemic stroke, the administration of alternative energy substrates to support the recovery of reversibly damaged brain tissues could contribute to limit the extent of permanent damages and lead to a better neurological outcome. Both pyruvate and lactate have been found in preclinical studies to provide neuroprotection in ischemia-reperfusion models of stroke. Hyperpolarization via dDNP, enables one to assess their metabolic fate within the brain, which could not only provide better insights about their neuroprotective mechanisms, but also turn them into theranostic agents for stroke, to monitor the therapy efficiency in real time.

Here, we demonstrate the feasibility of quantifying the global cerebral metabolic kinetics of HP [1-¹³C] lactate and HP [1-¹³C] pyruvate while being used at therapeutic doses in a mouse model of ischemia-reperfusion. Both substrates depicted distinct cerebral transport and metabolism between the ischemic and healthy brains, highlighting their potential as metabolic contrasts for stroke theranostics. Compared to the metabolite ratios analysis, kinetic modeling enabled a better distinction between healthy and stroke animals in HP lactate experiments, while both methods provided equivalent results in HP pyruvate measurements. Compared to HP pyruvate, HP lactate offered equivalent biomarkers despite a substantially lower initial polarization and turnover. Being injected at a more physiological dose compared to pyruvate, lactate, which also benefits from better established neuroprotective effects, represents an interesting hyperpolarized substrate for theranostic applications.

This chapter is adapted from the following manuscript: **Lê Thanh Phong**, Buscemi Lara, Lepore Mario, Hirt Lorenz, Hyacinthe Jean-Noël, Mishkovsky Mor. *In vivo assessment of the metabolic impact of cerebral ischemia using MRS and hyperpolarized [1-¹³C] lactate and [1-¹³C] pyruvate*. In preparation

This study was conceived by MM, HL and HJN. BL and LM performed the stroke surgery. I acquired all experimental data. BL, MM and myself analyzed and interpreted the data. All authors contributed to drafting and revising the manuscript.

2.2 Introduction

Theranostic approaches combine both therapeutic and diagnostic capabilities, thus having the potential to lead to a targeted, more personalized medicine²²⁵. Magnetic resonance spectroscopy (MRS) is a non-invasive tool for studying *in vivo* metabolism, with a large variety of applications in oncology and neuroimaging²³⁰. The sensitivity of MRS can be increased by several orders of magnitude taking advantage of the recently developed hyperpolarization techniques, which enhance the signal of magnetic resonance active nuclei. Using this strategy, compounds with biomedical relevance, like metabolic precursors, can be labeled with nuclear magnetic resonance active isotopes, their signal enhanced by hyperpolarization, and their metabolic transformations assessed *in vivo* and in real time^{214,231}. Consequently, one can envision a new avenue for MRS theranostic applications by using hyperpolarization of therapeutic agents labeled with MR-active nuclei, whose *in vivo* transformations will be followed in real time while providing therapy.

Ischemic stroke is the second⁵ leading cause of mortality in the world and the main cause of disability in adults⁶. In the acute phase, recanalization within a narrow time window by intravenous thrombolysis and mechanical clot removal, alone or in combination are the only available treatment options^{26,232,233}. These time-windows can be extended by careful selection of patients based on imaging properties of the ischemic brain^{29,31}. Despite these important improvements in patient care, only a fraction of stroke patients can receive treatment due to the limited eligibility, as well as the demanding technical requirements only available in major hospitals²⁸ and even for those treated, many retain a handicap. Aiming at improving patient outcome, several preclinical studies have tested neuroprotective strategies targeted at recovering reversibly damaged cerebral tissues in the acute phase of ischemic stroke^{37,38}. However, due to a variety of constraints, none of the several promising treatments found in preclinical studies has yet been successfully translated into clinics^{37,75,76}.

Administration of lactate⁶¹⁻⁶⁵ or pyruvate⁵⁶⁻⁵⁹ after stroke are among the neuroprotective strategies found efficient at the preclinical level, resulting in a reduction of the infarct size and improvement of the neurological outcome. It is hypothesized that lactate, metabolized to pyruvate by lactate dehydrogenase (LDH), enters the TCA cycle^{67,68}, and that both of these metabolites may be used as energy substrates providing neuroprotection after stroke^{57,61}. Lactate can also act as a signaling molecule via its receptor HCAR1 but receptor agonists did not induce protection after MCAO and mice lacking the receptor were not more sensitive to ischemia, arguing in favor of a metabolic mode of action⁷⁰. Both pyruvate and lactate can be readily hyperpolarized and the pyruvate-lactate interconversion can be detected with high sensitivity for molecular imaging. The vast majority of HP MR preclinical research has employed [1-¹³C] pyruvate for real-time molecular imaging²³¹, and it is the first HP ¹³C-labeled

Chapter 2. *In vivo* assessment of the metabolic impact of cerebral ischemia using MRS and hyperpolarized [1-¹³C] lactate and [1-¹³C] pyruvate

metabolic contrast agent translated into clinical studies¹⁴¹. A complementary view of the same metabolic pathway can be attained by starting from HP [1-¹³C] lactate^{234–237}.

In this chapter, we investigate the potential of HP [1-¹³C] pyruvate and HP [1-¹³C] lactate as theranostic agents for ischemic stroke with reperfusion. Both substrates have demonstrated to provide metabolic biomarkers in preclinical models of ischemic stroke^{226–228}. Considering that HP [1-¹³C] pyruvate and HP [1-¹³C] lactate provide routes for measuring the exchange between the two metabolites with a different directionality, we wanted to compare the cerebral metabolism of a bolus of these HP compounds at their therapeutic doses in the transient middle cerebral artery occlusion (MCAO) mouse stroke model. Firstly, we evaluated the HP contrast based on the analysis of metabolite ratios calculated from the summed ¹³C MRS spectra. Secondly, we developed metabolic models to quantify the apparent kinetic rates and compared the dynamics of HP [1-¹³C] pyruvate and HP [1-¹³C] lactate metabolism in sham-operated mice and stroke mice. Finally, as the therapeutic dose (1 mmol kg⁻¹) is about 10-20 times higher than the typical dose employed when using HP tracers (≈ 0.10 mmol kg⁻¹ with pyruvate¹⁴¹ and ≈ 0.06 mmol kg⁻¹ with lactate²³⁸), we assessed using ¹H MRS whether the bolus of these substrates induced changes in the neurochemical profiles.

2.3 Experimental methods

2.3.1 Animal experimentation

All experimental procedures with mice were approved by the regulatory body of the Canton de Vaud, Switzerland (Service de la Consommation et des Affaires Vétérinaires), license numbers VD2017.5 and VD2017.6, were conducted according to federal and local ethical guidelines, and complied with the ARRIVE guidelines. Male C57BL/6J mice (6-10 weeks, Charles River, France) were maintained in an animal facility with controlled humidity and temperature, a 12 h light/dark cycle and free access to food and water.

2.3.2 Study design

The cerebral metabolism of the HP neuroprotective agents [1-¹³C] lactate and [1-¹³C] pyruvate was measured in C57BL6/J mice subjected to either sham or transient MCAO surgery. An outline of the experimental design is summarized in Figure 2.1. Each animal received a single bolus of either HP pyruvate or HP lactate for HP ¹³C MRS. Mice that underwent transient MCAO surgery received an injection of either HP lactate or pyruvate at either 1 h or 2 h post-reperfusion (4 groups: MCAO 1 h lactate, MCAO 2 h lactate, MCAO 1 h pyruvate, and MCAO 2 h pyruvate). Control animals that underwent sham surgery received an injection of either HP lactate or pyruvate at 1 h post-surgery (2 groups: sham lactate and sham pyruvate). Overall,

30 mice ($n = 5$ per group) were included in this study. Localized ^1H MRS spectra were acquired continuously in the striatum of the left hemisphere of each mouse, except for the time required for shimming, proton imaging and ^{13}C MRS. Two time points were selected for the statistical comparison of the neurochemical profile: 75 and 110 min post-reperfusion/surgery. For the ^1H MRS comparison, the MCAO 2 h lactate and MCAO 2 h pyruvate groups were merged since they only received the bolus injection after both comparison time points.

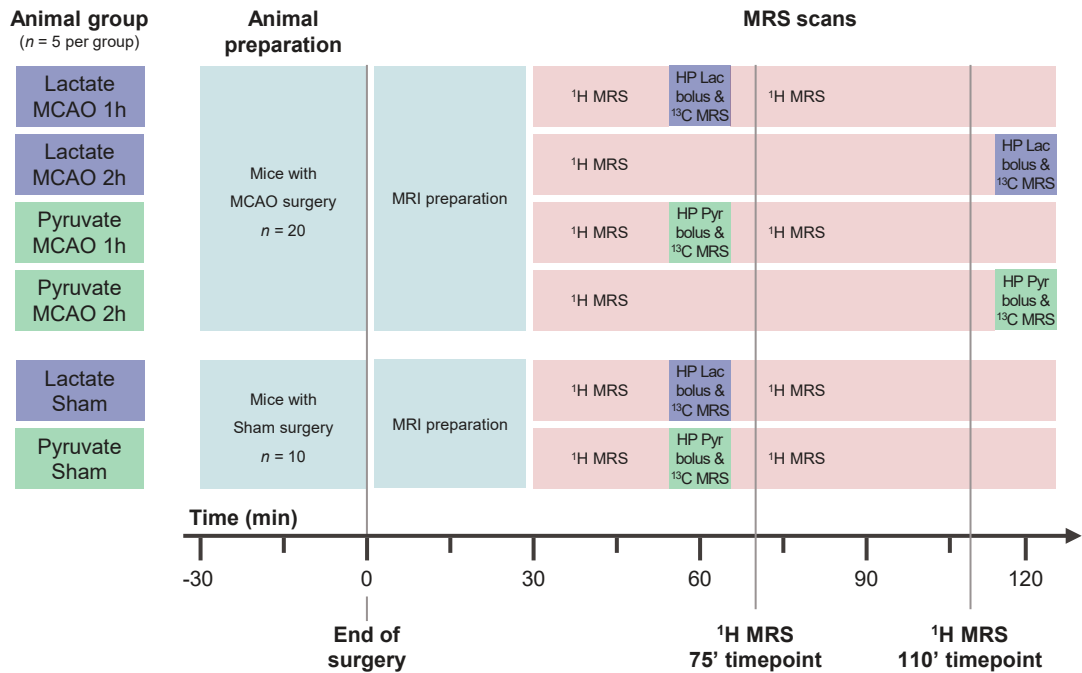


Figure 2.1: Outline of the experimental design for the HP ^{13}C and ^1H MRS experiments. This study includes six groups in total: sham mice with injection of either HP [$1\text{-}^{13}\text{C}$] lactate or HP [$1\text{-}^{13}\text{C}$] pyruvate at 1 h post-surgery; MCAO mice with HP [$1\text{-}^{13}\text{C}$] lactate injection at either 1 h or 2 h post-reperfusion; MCAO mice with HP [$1\text{-}^{13}\text{C}$] pyruvate injection at either 1 h or 2 h post-reperfusion. The ^1H MRS neurochemical profile of the left striatum is continuously measured in the remaining time, and compared between all groups at 75 min (the first ^1H MRS datapoint after ^{13}C HP MRS at 1 h for sham and MCAO 1 h groups) and at 110 min (the last ^1H MRS measurement before ^{13}C HP MRS for MCAO 2 h animals) post-reperfusion/surgery.

2.3.3 Transient middle cerebral artery occlusion (MCAO) model of stroke

Mice were kept under anesthesia with 1.5-2.0% isoflurane in 60% oxygen. Laser-Doppler flowmetry was used to monitor the regional cerebral blood flow (rCBF) through a flexible probe (Perimed AB, Sweden) glued to the skull at 1 mm posterior and 6 mm lateral from bregma.

Chapter 2. *In vivo* assessment of the metabolic impact of cerebral ischemia using MRS and hyperpolarized [1-¹³C] lactate and [1-¹³C] pyruvate

A lesion in the left striatum was induced by transient focal cerebral ischemia as previously described^{61,239}. In summary, the neck was incised and both left common and external carotid arteries were exposed and ligated. A silicone-coated nylon monofilament (Doccol Corp., Sharon, USA) was inserted through the common carotid artery into the internal carotid artery to obstruct the middle cerebral artery, as illustrated in Figure 2.2. The occluding filament was removed after 30 min to allow blood flow restoration. During occlusion, the left femoral vein was cannulated to allow the intravenous injection of the HP solution.

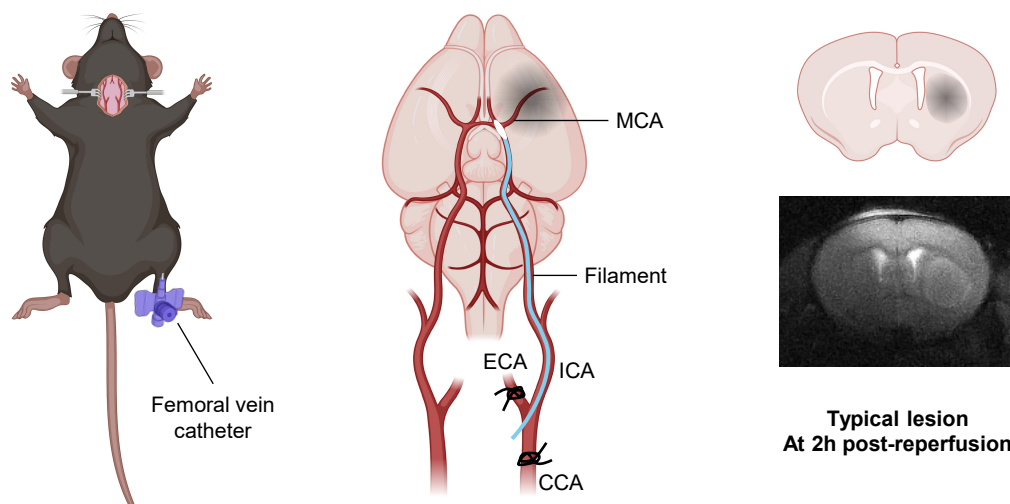


Figure 2.2: Illustration of the transient MCAO surgery procedure. A ventral midline neck incision is performed to expose and ligate both the left external carotid artery (ECA) and left common carotid artery (CCA). A silicone-coated is then inserted through the common carotid artery into the internal carotid artery (ICA) to occlude the left middle cerebral artery (MCA). The filament is removed after 30 minutes to allow reperfusion. This induces a focal ischemic lesion in the left striatum. During ischemia, the left femoral vein is cannulated for the subsequent injection of HP substrates.¹⁸

The intervention was considered successful if the rCBF remained below 20% of the baseline during occlusion and increased above 50% of the initial value within 10 min after reperfusion. Sham operated mice followed a similar surgical procedure without suture insertion or artery ligation.

2.3.4 Hyperpolarization

For HP lactate experiments, $16 \times 10\mu\text{L}$ frozen beads of 4.1 M sodium L-[1-¹³C] lactate (606022, Sigma Aldrich, Buchs, Switzerland) in H₂O:glycerol (1:1, v:v) doped with 25 mM of OX063 radical (Albeda Research, Denmark) were prepared.

For HP pyruvate experiments, $5 \times 5 \mu\text{L}$ frozen beads of neat $[1-^{13}\text{C}]$ pyruvic acid (Sigma Aldrich) doped with 21 mM of OX063 radical were prepared. To neutralize the acid upon dissolution, frozen beads of 10 M NaOH were added to the sample cup at a 1:1.44 (v:v) ratio.

The samples were loaded and hyperpolarized in a 7T/1K DNP polarizer¹⁸⁸. The liquid-state polarization measured in separate experiments was $(33.1 \pm 8.9)\%$ and $(59.0 \pm 5.0)\%$ for lactate and pyruvate¹³⁸, respectively.

2.3.5 Magnetic resonance measurements

All MR measurements were performed on a 9.4T/31cm horizontal actively shielded magnet (Magnex Scientific, Yarnton, UK), 500 mT m^{-1} strength and $5500 \text{ T m}^{-1} \text{ s}^{-1}$ slew rate shielded gradient coil set (RG120-250S, MRS Magnetics, Abingdon, UK), interfaced to a Varian INOVA spectrometer (Varian, Palo Alto, USA). The experimental setup is illustrated in Figure 2.3. Upon reperfusion, mice were transferred into the MRI scanner with a home-built ^1H quadrature/ ^{13}C single loop coil above the head (Figure 2.4), whose sensitivity profile was reported in a previous study²²⁸.

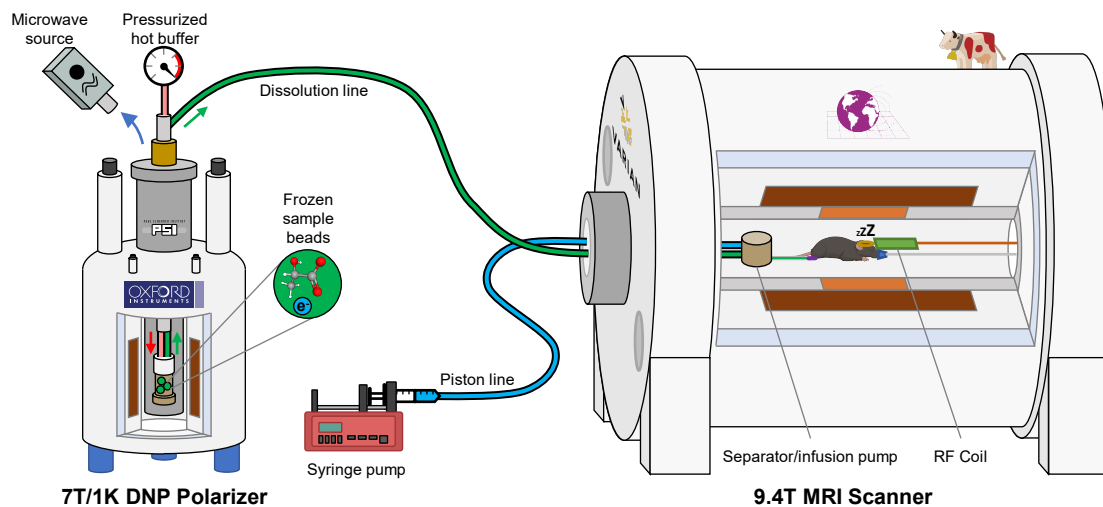


Figure 2.3: Sketch of the dDNP/MRI setup. The frozen sample beads are hyperpolarized in a 7T/1K DNP polarizer¹⁸⁸ by shining microwaves around 197 GHz. Upon polarization, the sample is melted by a hot solvent and pushed to the separator/infusion pump using pressurized helium gas. An automated separator/infusion pump injects the hyperpolarized substrate into the animal for the MRS acquisition.

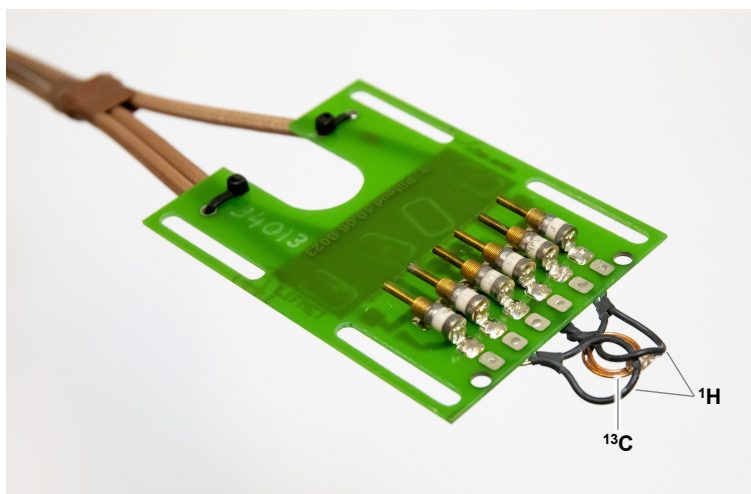


Figure 2.4: Mouse head ¹H quadrature/¹³C linear surface coil used for HP MRS acquisitions at 9.4T. The ¹³C loop is a 3 turn spiral (6/11 mm ID/OD) of \varnothing 0.8 mm enameled copper wire. ¹H element are 14 mm loops built with \varnothing 1 mm silver-plated copper wire.

2.3.6 ¹H imaging

Anatomical axial T_2W images were acquired with a fast spin-echo sequence (effective echo time $TE_{\text{eff}} = 52$ ms, $TR = 4000$ ms, 18×18 mm² FOV, 256×256 matrix) at the beginning of the MR scan to provide localization for the shimming voxels, as well as within 5 min of the HP injection and at the end of the scan protocol, approximately 2 h post-reperfusion to assess the evolution of the striatal lesion.

2.3.7 ¹H MRS

Localized proton spectroscopy was acquired on the same animals in which the hyperpolarized substrate was injected, except for one animal in each lactate group. Using the Fast, Automatic Shim Technique using Echo-planar Signal readout for Mapping Along Projections (FASTESTMAP) routine^{240,241}, static field inhomogeneity was corrected in a 2.0 mm \times 1.8 mm \times 2.0 mm voxel located in the striatum where the ischemic lesion was expected. ¹H MRS was performed using the SPin ECho, full Intensity Acquired Localized (SPECIAL) pulse sequence²⁴² ($TE = 2.8$ ms, $TR = 4000$ ms, 200 ms acquisition time, and 10×16 scans) and repeated continuously until 120 min post-reperfusion or post-surgery, except for the time required for shimming, HP ¹³C MRS and ¹H imaging. The absolute metabolite concentrations were quantified using LCModel V6.3²⁴³. Values with Cramer–Rao lower bounds (CRLB) above 40% were discarded from further analyses.

2.3.8 Hyperpolarized ^{13}C MRS

Using the FASTESTMAP routine^{240,241}, static field inhomogeneity was corrected in a $3.6\text{ mm} \times 6.9\text{ mm} \times 4.5\text{ mm}$ voxel within the brain to optimize the signal quality. At either 1 h or 2 h post-reperfusion in MCAO mice and 1 h post-surgery in sham-operated animals, either HP $[1-^{13}\text{C}]$ lactate or $[1-^{13}\text{C}]$ pyruvate was dissolved in 5 mL superheated D_2O or buffer solution (60 mM tris(hydroxymethyl)aminomethane (TRIS) and 0.3 mM ethylenediaminetetraacetic acid (EDTA) in D_2O at $\text{pD} = 7.6$), respectively. Approximately 2.5 mL of 80 mM solution was collected in the separator/infusion pump. A total of 450 μL , including 125 μL of dead volume was injected into the femoral vein through the automated protocol¹⁸⁸. ^{13}C MR spectra were then immediately acquired every 3 s with 30° four-segment B_1 -insensitive rotation²⁴⁴ (BIR-4) adiabatic pulses. The choice of the administered doses was based on the therapeutic doses reported by Berthet et al.⁶² and Yi et al.⁵⁷. Each mouse received only one bolus injection of either HP metabolites. The average doses received, as measured post-experiment, were $(1.08 \pm 0.19)\ \mu\text{mol g}^{-1}$ for HP lactate and $(1.12 \pm 0.13)\ \mu\text{mol g}^{-1}$ and for HP pyruvate.

2.4 Data processing

2.4.1 ^{13}C metabolite ratios

The signal from the first 120 s post-injection was summed, the metabolite peaks were fitted and the areas under the curve (AUC) were calculated using the Bayesian Data Analysis Software Package V4.01 (Washington University in St. Louis). The peak areas of $[1-^{13}\text{C}]$ lactate, $[1-^{13}\text{C}]$ alanine, $[1-^{13}\text{C}]$ pyruvate and $[^{13}\text{C}]$ bicarbonate were then used to compute the metabolite ratios. To reduce the variability between individuals, when relevant, the ratios were scaled to the HP infusate dose, namely by multiplying the ratio by the amount of HP pyruvate or lactate injected and dividing by the animal body weight. The infusate concentration was obtained via high-resolution NMR by comparing the signal intensity of the remaining solution to a reference $[1-^{13}\text{C}]$ acetate sample.

2.4.2 Kinetic modeling

The time course of $[1-^{13}\text{C}]$ lactate, $[1-^{13}\text{C}]$ alanine, $[1-^{13}\text{C}]$ pyruvate and $[^{13}\text{C}]$ bicarbonate signals were deduced by fitting each spectrum individually using the Bayesian Data-Analysis Software Package.

To quantify the apparent kinetic rates from the dynamic labeling pattern, multi-compartment models describing the metabolic kinetics post HP $[1-^{13}\text{C}]$ lactate or HP $[1-^{13}\text{C}]$ pyruvate bo-

Chapter 2. *In vivo* assessment of the metabolic impact of cerebral ischemia using MRS and hyperpolarized [1-¹³C] lactate and [1-¹³C] pyruvate

lus (Figures 2.6 and 2.7) injection were derived from their respective simplified schemes of cerebral transport and metabolism (Figure 2.5) and using the following assumptions:

- Each conversion or elimination step was modeled as a first-order chemical reaction.
- A single apparent lactate-to-pyruvate turnover step (lactate model) or pyruvate-to-lactate turnover step (pyruvate model) was used to describe both the transport of the substrate across the blood-brain barrier (BBB) and lactate dehydrogenase (LDH) exchange. The corresponding kinetic rate constant is rather related to the transport step, which is slower compared to LDH exchange^{236,245}.
- Although the LDH exchange is reversible, only the forward reaction was taken into account given that the bolus injection shifts the equilibrium towards downstream metabolites.
- Conversion of [1-¹³C] pyruvate up to [¹³C] bicarbonate was accounted in a single step since the intermediate product, ¹³CO₂, was not detected due to the limited bandwidth of RF pulses.
- Elimination steps were added to the end products.

The dynamic ¹³C MRS signal is a combination of the uptake of the precursor, metabolic conversion into downstream metabolites, as well as signal losses resulting from the longitudinal spin-lattice relaxation and repeated RF excitation. The time evolution of the downstream metabolites in the multisite models shown above can then be described using a set of differential equations.

Following an injection of HP lactate:

$$\frac{d}{dt} \begin{pmatrix} Pyr \\ Ala \\ Bic \end{pmatrix} (t) = \begin{pmatrix} -k_{PA} - k_{PB} - F - \frac{1}{T_1} & 0 & 0 & k_{LP} \\ k_{PA} & -k_{A, out} - F - \frac{1}{T_1} & 0 & 0 \\ k_{PB} & 0 & -k_{B, out} - F - \frac{1}{T_1} & 0 \end{pmatrix} \begin{pmatrix} Pyr \\ Ala \\ Bic \\ Lac \end{pmatrix} (t) \quad (2.1)$$

Where $Pyr(t)$, $Ala(t)$, $Bic(t)$ and $Lac(t)$ denote the time-varying signal amplitude of the corresponding HP ¹³C metabolites, k_X , $X \in \{LP, PA, PB, A\ out, B\ out\}$ the first-order kinetic rate constants for the conversion between the metabolites or their elimination, as summarized in Figure 2.6, T_1 is the longitudinal relaxation time constant, approximated to 15 s for all metabolites²⁴⁶, and F is the term accounting for the loss of magnetization resulting from the RF pulse:

$$F = -\frac{\ln(\cos(\alpha))}{TR} \quad (2.2)$$

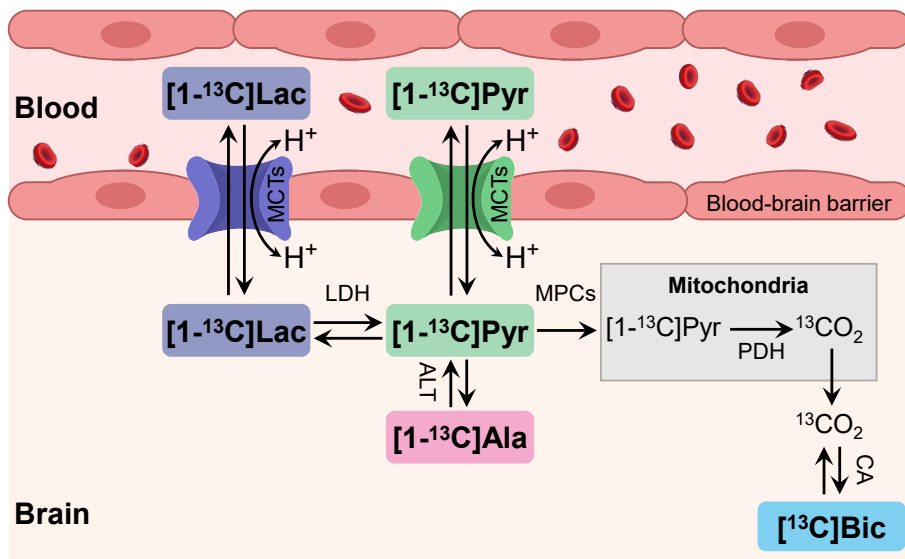


Figure 2.5: Simplified schematic of cerebral transport and metabolism of HP [1-¹³C] lactate and HP [1-¹³C] pyruvate. These substrates can cross the blood-brain barrier (BBB) via monocarboxylate transporters (MCTs). The intracellular [1-¹³C] lactate and [1-¹³C] pyruvate pools exchange via lactate dehydrogenase (LDH). [1-¹³C] pyruvate is either converted into [1-¹³C] alanine by alanine aminotransferase (ALT) or transported into the mitochondria via mitochondrial pyruvate carriers (MPCs), then oxidized by pyruvate dehydrogenase (PDH), producing ¹³CO₂ remaining in equilibrium with [¹³C] bicarbonate via carbonic anhydrase (CA).

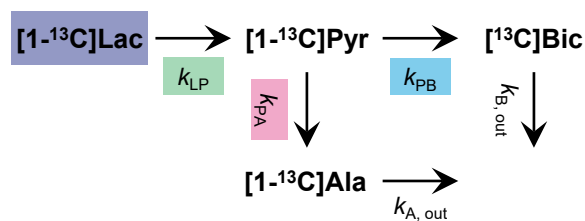


Figure 2.6: Mathematical kinetic model for the cerebral metabolism of HP [1-¹³C] lactate.

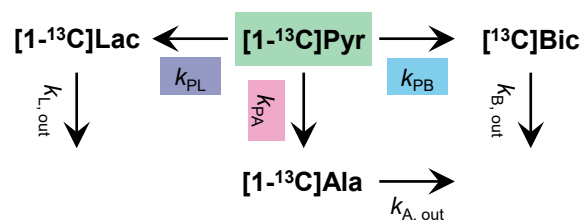


Figure 2.7: Mathematical kinetic model for the cerebral metabolism of HP [1-¹³C] pyruvate.

Chapter 2. *In vivo* assessment of the metabolic impact of cerebral ischemia using MRS and hyperpolarized [1-¹³C] lactate and [1-¹³C] pyruvate

Where $\alpha = 30^\circ$ is the flip angle of the RF pulse applied with a repetition time $TR = 3$ s.

By assuming a negligible contribution from endogenous ¹³C metabolites due to their low thermal polarization and natural abundance, the following initial conditions can be set:

$$\begin{pmatrix} Pyr \\ Ala \\ Bic \end{pmatrix} (t = 0) = \begin{pmatrix} 0 \\ 0 \\ 0 \end{pmatrix} \quad (2.3)$$

Similarly, the following set of differential equations is derived for the metabolism following an injection of HP pyruvate:

$$\frac{d}{dt} \begin{pmatrix} Lac \\ Ala \\ Bic \end{pmatrix} (t) = \begin{pmatrix} -k_{L, out} - F - \frac{1}{T_1} & 0 & 0 & k_{PL} \\ 0 & -k_{A, out} - F - \frac{1}{T_1} & 0 & k_{PA} \\ 0 & 0 & -k_{B, out} - F - \frac{1}{T_1} & k_{PB} \end{pmatrix} \begin{pmatrix} Lac \\ Ala \\ Bic \\ Pyr \end{pmatrix} (t) \quad (2.4)$$

with following initial conditions:

$$\begin{pmatrix} Lac \\ Ala \\ Bic \end{pmatrix} (t = 0) = \begin{pmatrix} 0 \\ 0 \\ 0 \end{pmatrix} \quad (2.5)$$

Where $Lac(t)$, $Ala(t)$, $Bic(t)$ and $Pyr(t)$ denote the time-varying signal amplitude of the corresponding HP ¹³C metabolites, k_X , $X \in \{PL, PA, PB, A\ out, B\ out, L\ out\}$ denote the first-order kinetic rate constants for the conversion or elimination of metabolites, as summarized in Figure 2.7.

The time course of the ¹³C signal intensity of the injected metabolite, either lactate or pyruvate, is fitted with a polynomial function and used as an input function for solving the set of differential equations. Then, apparent kinetic rate constants were determined by fitting each experimental ¹³C signal time course to their respective model using a trust-region least squares algorithm in a routine implemented in MATLAB R2021b (MathWorks, Natick, USA). Finally, to account for experimental variability, the kinetic rates corresponding to a metabolic step originating from the precursor metabolite were additionally scaled to the injected dose.

2.4.3 Statistical analysis

We performed statistical analyses using the MATLAB R2021b software (MathWorks, Natick, USA). One-way analysis of variance (One-way ANOVA) was used followed by Tukey-Kramer's test to correct for multiple comparison. A p value below 0.05 was considered statistically significant. All data are presented as mean \pm standard deviation unless otherwise stated.

2.5 Results

The anatomical T_2W images in Figure 2.8 illustrate the typical striatal lesion following 30 min transient ischemic stroke. Although slight morphological modifications are already noticeable at 1 h post-reperfusion, the lesion is only readily visible at 2 h post-reperfusion. As expected, there is no lesion in sham animals.

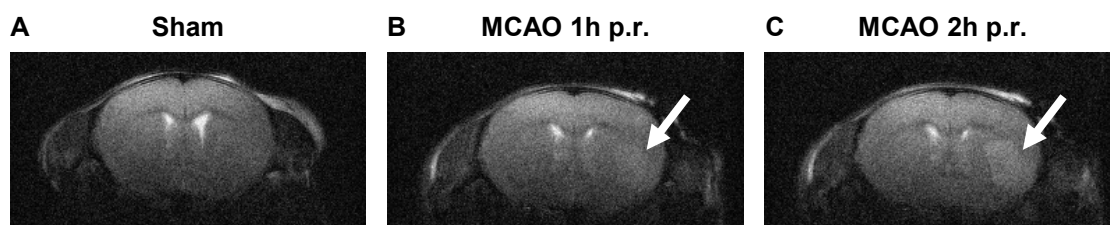


Figure 2.8: Representative axial T_2W slices acquired in the brain using a FSEMS sequence (4 averages). Arrows indicate the injured region resulting from the induced transient ischemic stroke. No lesion is observed in sham (A). Already slightly noticeable at 1 h post-reperfusion (p.r.) (B), the lesion becomes more clearly visible and delimited at 2 h post-reperfusion (C).

Representative dynamic cerebral HP ^{13}C MRS spectra acquired in sham and MCAO animals are shown in Figure 2.9. The infused HP $[1-^{13}C]$ lactate is converted into HP $[1-^{13}C]$ pyruvate, which is then further converted into either HP $[1-^{13}C]$ alanine or HP $[^{13}C]$ bicarbonate. The peak visible at 177.7 ppm is a known chemical impurity from the lactate stock solution and is therefore not a result of the mouse metabolism. The infused HP $[1-^{13}C]$ pyruvate is converted into HP $[1-^{13}C]$ lactate, $[1-^{13}C]$ alanine and HP $[^{13}C]$ bicarbonate. HP $[1-^{13}C]$ pyruvate hydrate is observed as well and represents about 8% of the $[1-^{13}C]$ pyruvate signal amplitude.

The averaged time courses of the individual HP ^{13}C metabolite signals are reported in Figure 2.10. Following HP $[1-^{13}C]$ lactate infusion, a lower labeling of the $[1-^{13}C]$ pyruvate pool is readily visible in all stroke animals compared to sham. The $[1-^{13}C]$ alanine and $[^{13}C]$ bicarbonate labeling are lower to a lesser extent. In experiments with HP $[1-^{13}C]$ pyruvate, a marked decrease in the labeling of $[1-^{13}C]$ alanine, as well as slightly lower $[1-^{13}C]$ lactate are observed after stroke compared to sham.

Using the metabolite ratio analysis (Figures 2.11 and 2.12) we observed that the metabolic conversions of both substrates in healthy animals were different from those of animals subjected to MCAO.

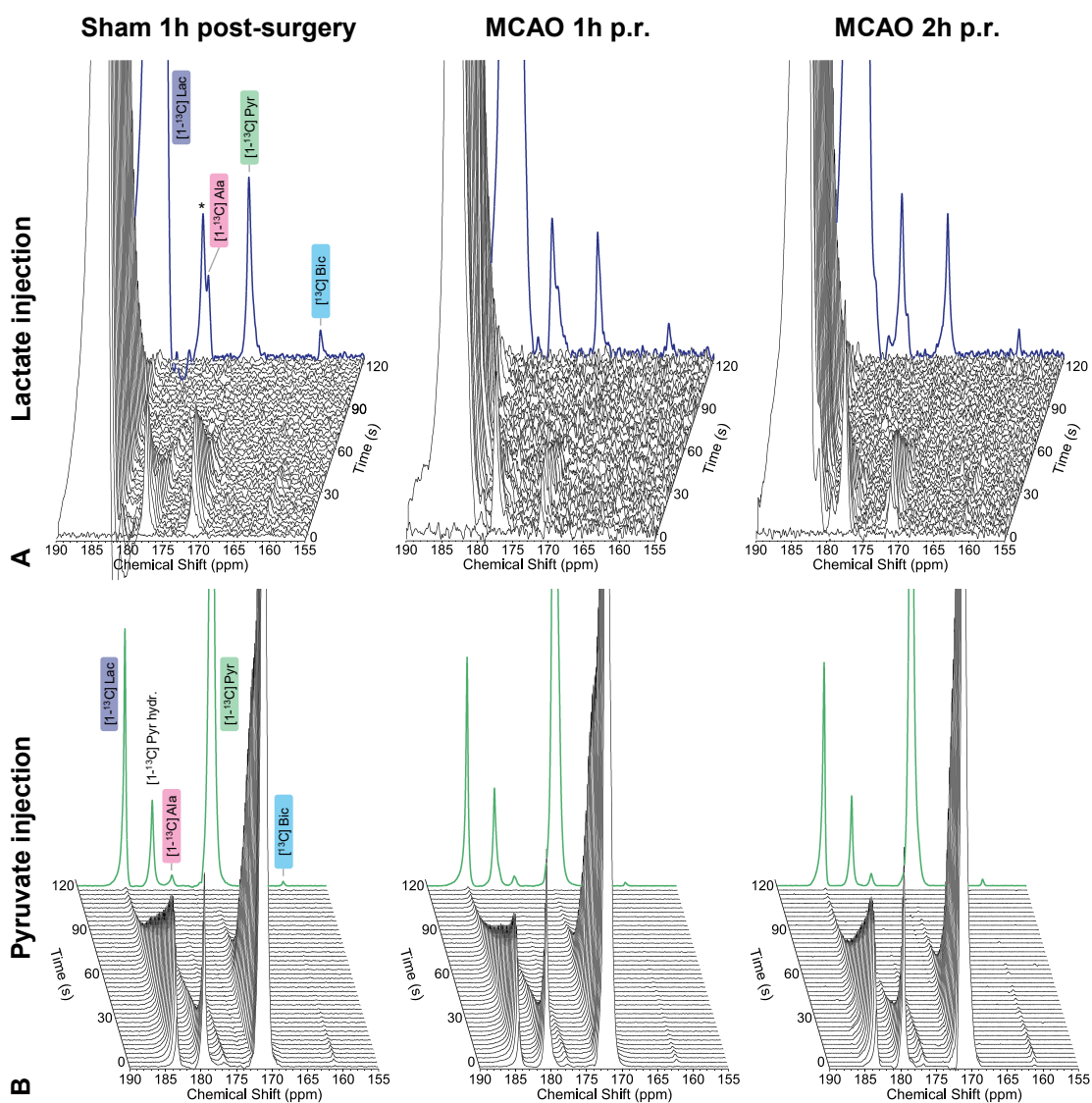


Figure 2.9: Representative dynamic ¹³C MRS acquired from healthy and stroke mice brains following infusion of (A) HP [1-¹³C] lactate (lb = 20 Hz) or (B) HP [1-¹³C] pyruvate (lb = 10 Hz). The bold colored spectra are the sum of the first 120 s post-infusion. (A) The peak at 177.7 ppm (*) is an impurity from the stock lactate solution.

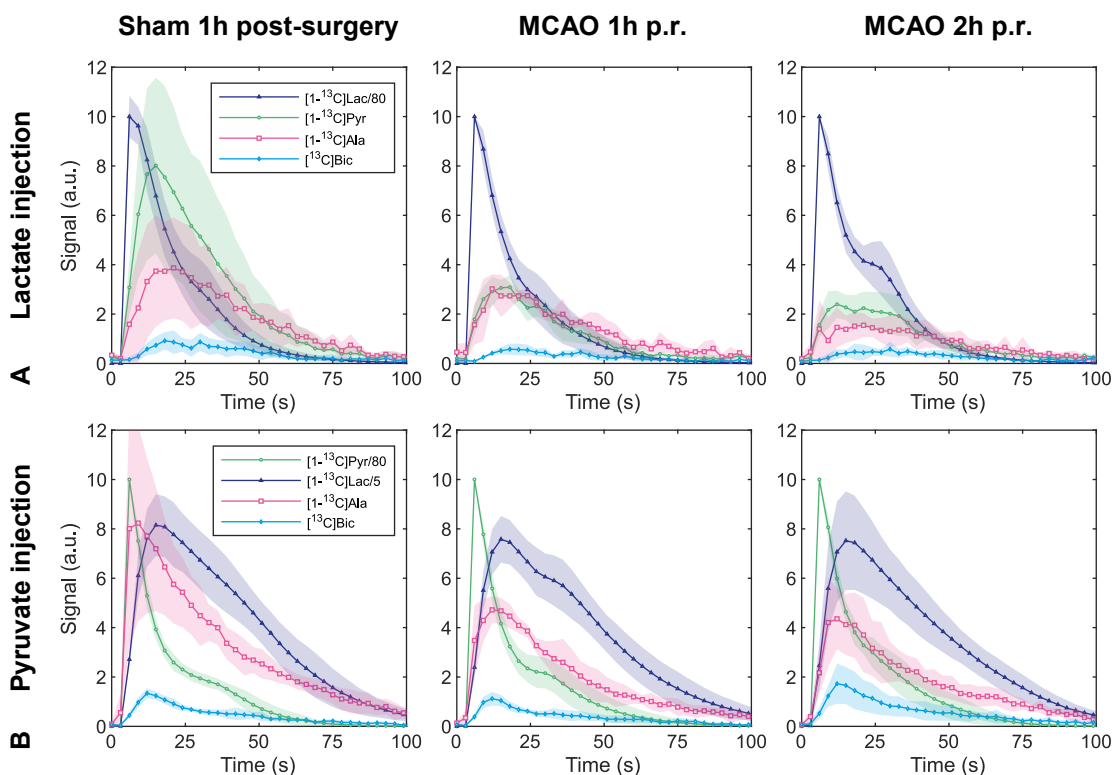


Figure 2.10: Averaged metabolic time courses across all experiments. For each individual experiment, the data were beforehand normalized to the highest signal intensity data point. The shaded areas represent the standard deviation around the mean. The lactate and pyruvate signals were scaled for display purposes as indicated in the legends.

Following lactate infusion, the pyruvate-to-lactate ratio (PLR) showed a trend towards lower values in MCAO 1 h animals compared to healthy animals (Figure 2.11A). After normalizing this ratio to the infusate dose to account for experimental variations (i.e. animal weight and actual substrate concentration as previously described²²⁸), the cPLR was found to be 38% lower in MCAO 1 h mice than in sham mice (Figure 2.11D). Further differences were found in the alanine labeling. In particular, the normalized alanine-to-lactate ratio (cALR) was 53% lower in the MCAO 2 h group than in the sham group, and 37% lower than in the MCAO 1 h group (Figure 2.11E). Furthermore, a trend towards a lower bicarbonate labeling was observed after stroke (cBLR, Figure 2.11F).

Following pyruvate infusion, MCAO 1 h mice showed a trend towards a lower lactate labeling than sham mice. The lactate-to-pyruvate ratio (LPR, Figure 2.12A) of the MCAO 2 h mice was 32% lower than that of sham mice, and 24% lower than that of MCAO 1 h mice. After normalizing the LPR to the actual pyruvate dose (cLPR, Figure 2.12D), the lactate labeling was found to be different between healthy and both groups of stroke animals; 18% lower in MCAO 1 h mice and 31% lower in MCAO 2 h mice. The alanine labeling was similar between

Chapter 2. *In vivo* assessment of the metabolic impact of cerebral ischemia using MRS and hyperpolarized [1-¹³C] lactate and [1-¹³C] pyruvate

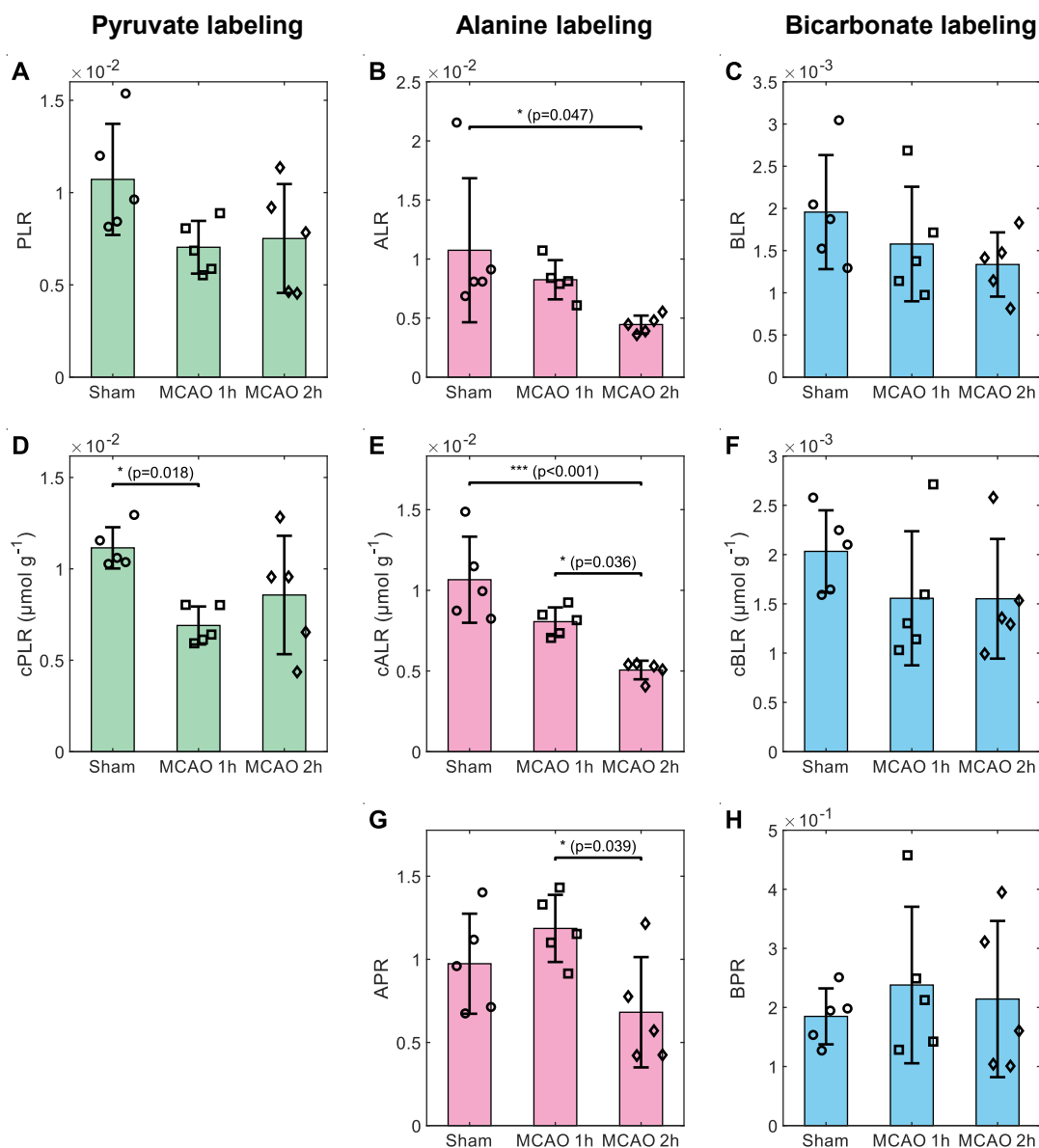


Figure 2.11: Metabolite ratios following injection of HP [1-¹³C] lactate in healthy sham and stroke MCAO animals. Data are displayed as the mean \pm standard deviation and overlaid with individual data points (circles for sham, squares for MCAO 1 h, diamonds for MCAO 2 h, and same for the next figures). Pyruvate-to-lactate ratio (PLR, **A**), alanine-to-lactate ratio (ALR, **B**), bicarbonate-to-lactate ratio (BLR, **C**). The same ratios corrected for the actual [1-¹³C] lactate dose injected (cPLR, cALR and cBLR, respectively, **D**, **E** and **F**). Alanine-to-pyruvate ratio (APR, **G**) and bicarbonate-to-pyruvate ratio (BPR, **H**). The cPLR was significantly lower in the MCAO 1 h group compared to sham (**D**). A trend towards decreasing alanine labeling (cALR) was observed after stroke (**E**), with a significant difference between MCAO 2 h and both sham and MCAO 1 h. The bicarbonate-to-lactate ratio (cBLR) tends to decrease after stroke (**F**).

both MCAO time points, and lower than sham by 42% in MCAO 1 h and by 48% in MCAO 2 h (cAPR, Figure 2.12E). As in HP lactate experiments, a slight trend towards a lower bicarbonate labeling was observed after stroke (cBPR, Figure 2.12F).

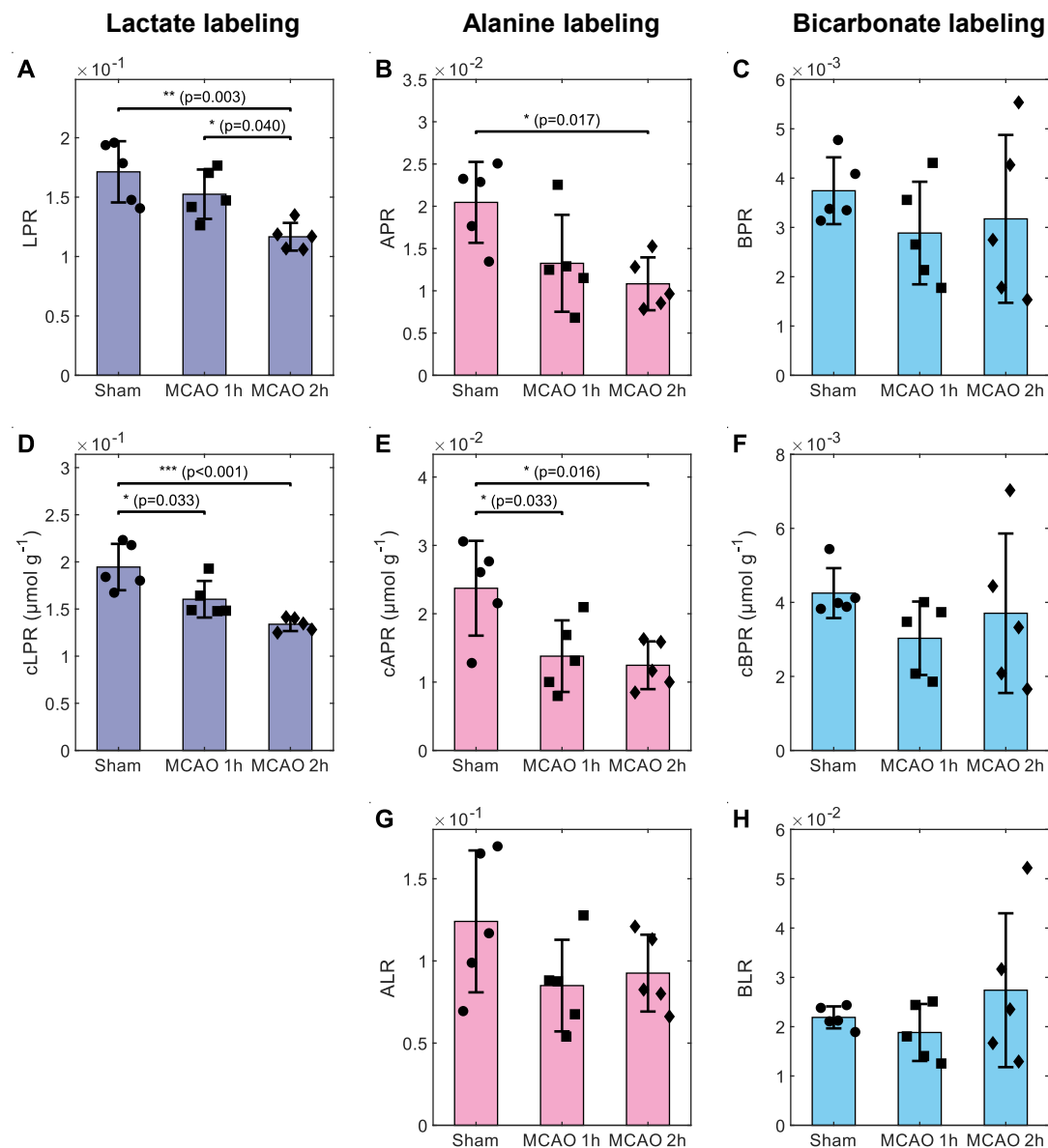


Figure 2.12: Metabolite ratios following injection of HP [¹⁻¹³C] pyruvate in healthy sham and stroke MCAO animals. Data are displayed as the mean ± standard deviation and overlaid with individual data points. Lactate-to-pyruvate ratio (LPR, **A**) Alanine-to-pyruvate ratio (APR, **B**) bicarbonate-to-pyruvate ratio (BPR, **C**). Metabolite ratios corrected for the actual [¹⁻¹³C] pyruvate dose injected (cLPR, cAPR, cBPR, respectively, **D**, **E** and **F**). Alanine-to-lactate ratio (ALR, **G**) and bicarbonate-to-lactate ratio (BLR, **H**). Both lactate and alanine labeling were lower in MCAO compared to sham (**D**, **E**).

Chapter 2. *In vivo* assessment of the metabolic impact of cerebral ischemia using MRS and hyperpolarized [1-¹³C] lactate and [1-¹³C] pyruvate

We then quantified the kinetics of HP [1-¹³C] pyruvate and HP [1-¹³C] lactate cerebral metabolism using mathematical modeling. In HP lactate experiments, the kinetic rate of lactate-to-pyruvate conversion was slower in stroke animals than in sham, both at 1 h (25%) and 2 h (34%) post-reperfusion (k_{LP} , Figure 2.13D). Furthermore, the kinetic rate of pyruvate-to-bicarbonate conversion (k_{PB} , Figure 2.13C) shows a trend towards higher values after stroke.

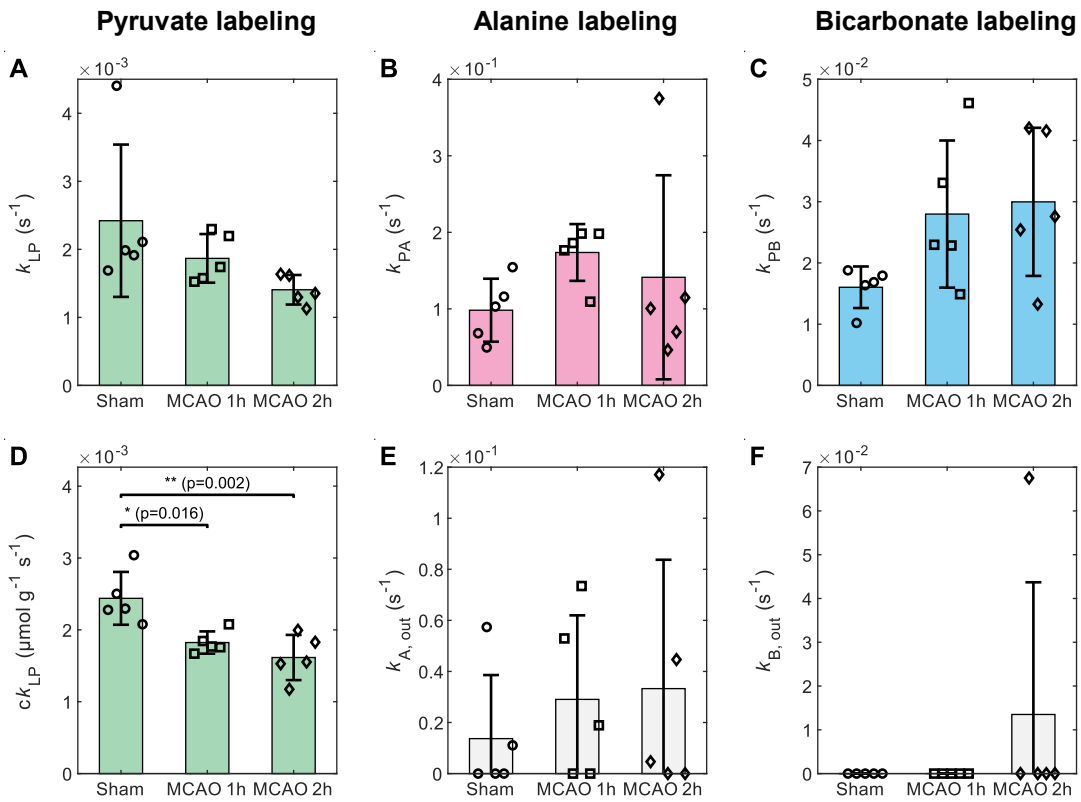


Figure 2.13: Kinetic rates following injection of HP [1-¹³C] lactate. Data are displayed as the mean \pm standard deviation and overlaid with individual data points (circles for sham, squares for MCAO 1 h, diamonds for MCAO 2 h, and same for next figure). Kinetic rate constants of lactate-to-pyruvate (k_{LP} , **A**), pyruvate-to-alanine (k_{PA} , **B**) and pyruvate-to-bicarbonate (k_{PB} , **C**) turnover. Lactate-to-pyruvate kinetic rate corrected for the actual dose of [1-¹³C] lactate injected ($c k_{LP}$, **D**). Kinetic rate constants for the elimination of alanine ($k_{A, out}$, **E**) and bicarbonate ($k_{B, out}$, **F**).

Similarly, the injections of HP pyruvate depicted a slower pyruvate-to-lactate labeling (k_{PL} , Figure 2.14D) after stroke, decreasing by 17% and 28% in MCAO 1 h and 2 h compared to sham, respectively.

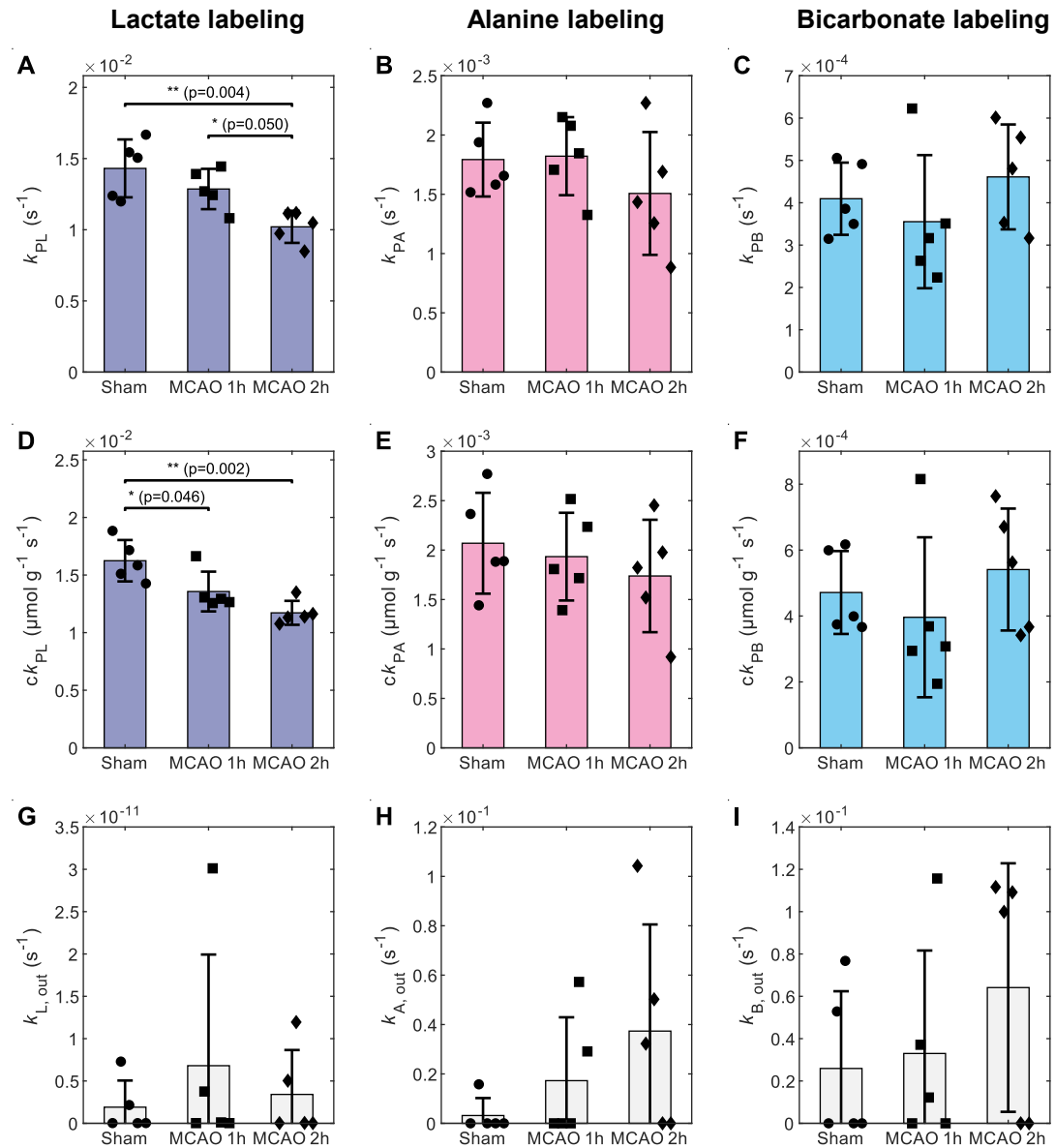


Figure 2.14: Kinetic rates following injection of HP [$1-^{13}C$] pyruvate. Data are displayed as the mean \pm standard deviation and overlaid with individual data points. Kinetic rate constants of pyruvate-to-lactate (k_{PL} , **A**), pyruvate-to-alanine (k_{PA} , **B**), pyruvate-to-bicarbonate (k_{PB} , **C**) turnover. Rate constants of the same metabolic steps corrected for the actual dose of [$1-^{13}C$] pyruvate injected (ck_{PL} , ck_{PA} , ck_{PB} , **D**, **E** and **F**, respectively). Kinetic rates for the elimination of lactate, alanine and bicarbonate ($k_{L, out}$, $k_{A, out}$ and $k_{B, out}$, **G**, **H** and **I** respectively).

Chapter 2. *In vivo* assessment of the metabolic impact of cerebral ischemia using MRS and hyperpolarized [1-¹³C] lactate and [1-¹³C] pyruvate

In Figure 2.15, we compare the forward kinetic rate constants against the metabolite ratios corresponding to the same labeling, similarly to Hill et al.²⁴⁷. In HP lactate experiments, a strong dependence is observed between all kinetic rates and ratio pairs (Pearson correlation coefficient: $r \approx 0.7$, Figure 2.15A-C), while the in HP pyruvate experiments, the dependence is very strong for the lactate labeling ($r = 0.97$, Figure 2.15D), and weak for remaining pairs.

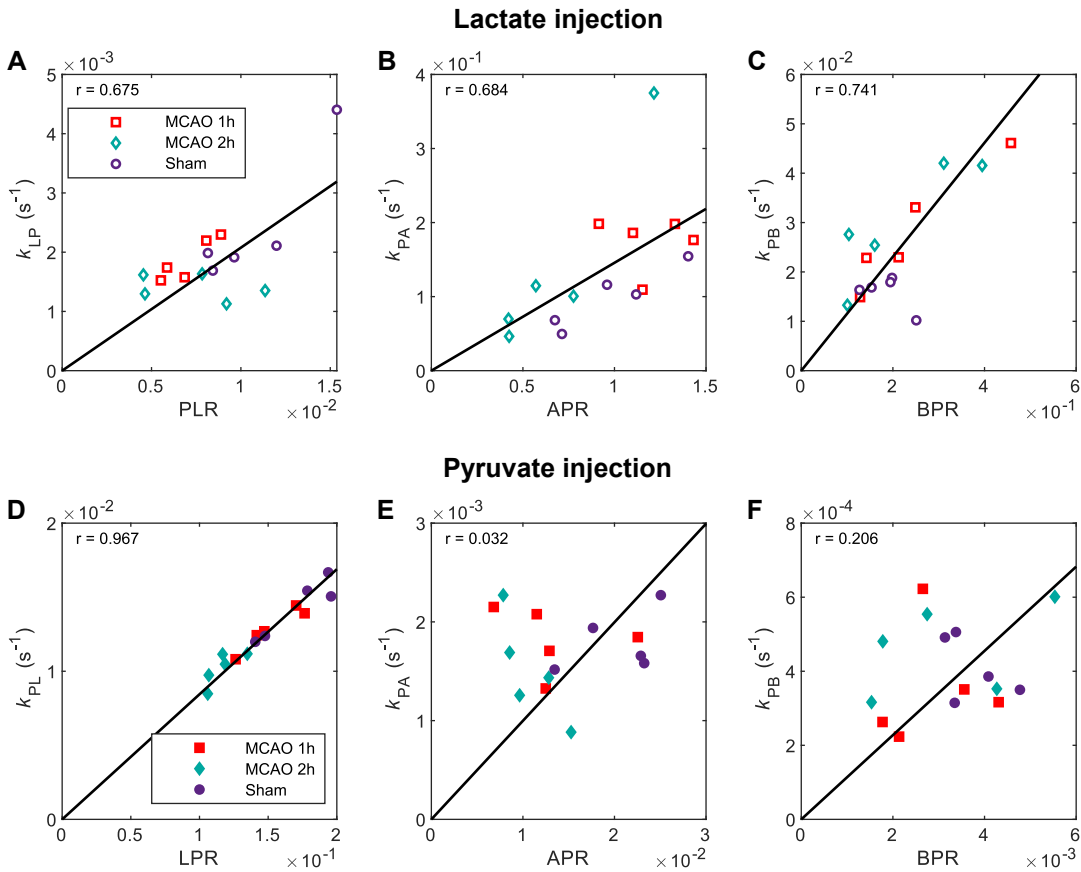


Figure 2.15: Correlation between kinetic rate constants and metabolite ratios, for HP [1-¹³C] lactate (A-C) and [1-¹³C] pyruvate (D-F) experiments. The bold curve represents the linear least squares fit. The Pearson correlation coefficient is displayed in the top-left corner of each plot.

The neurochemical profiles measured in the striatum at the left hemisphere (Figure 2.16) depicted noticeable changes in metabolite concentrations after MCAO. At the 75 min time point, which is shortly after the HP substrate bolus injection for ^{13}C MRS in the MCAO 1 h and sham groups, higher levels of lactate, as well as lower levels of macromolecules, glutamate and glutamine were observed after stroke compared to sham (Figure 2.17). Additional differences were observed at 110 min (Figure 2.18), with lower levels of taurine and NAA+NAAAG measured in stroke animals compared to sham. At both 75 min and 110 min time points, no significant differences were observed between both sham groups, injected with different substrates at 60 min, or between the three MCAO groups, receiving an injection of either lactate, pyruvate, or none of the two at 60 min. For all metabolites quantified, the neurochemical profile in the striatum measured immediately before and after the bolus injection was not substantially different (Figures 2.19 to 2.21).

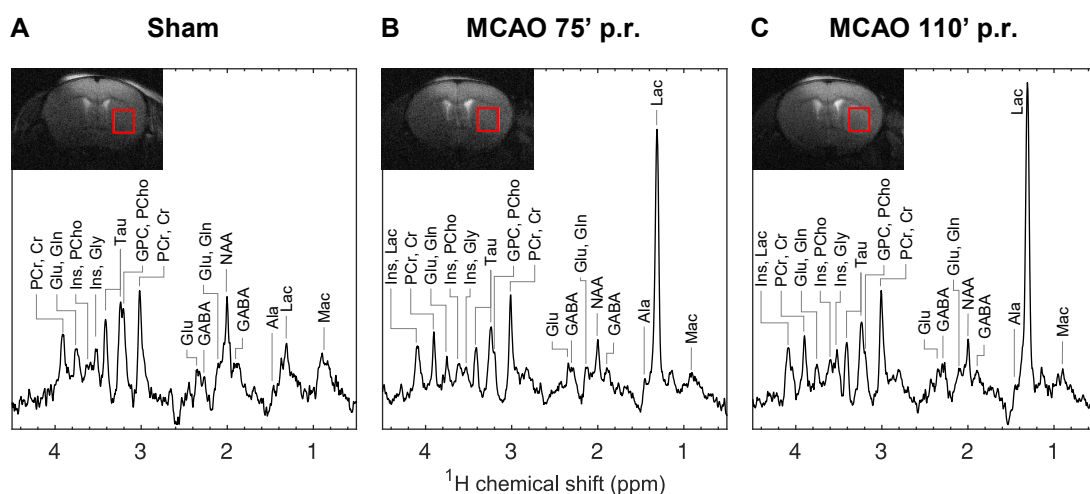


Figure 2.16: Representative ^1H MRS spectra (160 averages, 640 s of acquisition time for each point) and voxel position in the striatum of (A) a sham mouse 75 min post-surgery, and one MCAO mouse at (B) 75 min and (C) 110 min post-reperfusion. All animals received a bolus lactate injection at 60 min post-reperfusion/surgery. 5 Hz of line broadening was applied to each spectrum for visualization purposes. The red rectangles indicate the spectroscopy voxel within the striatum. Abbreviations: alanine (Ala), creatine (Cr), γ -aminobutyric acid (GABA), glutamine (Gln), glutamate (Glu), glycine (Gly), glycerophosphocholine (GPC), lactate (Lac), macromolecules (Mac), N-acetyl-aspartate (NAA), N-acetyl-aspartyl-glutamate (NAAAG), phosphocholine (PCho), phosphocreatine (PCr) and taurine (Tau).

¹H neurochemical profiles in the striatum at 75 min timepoint

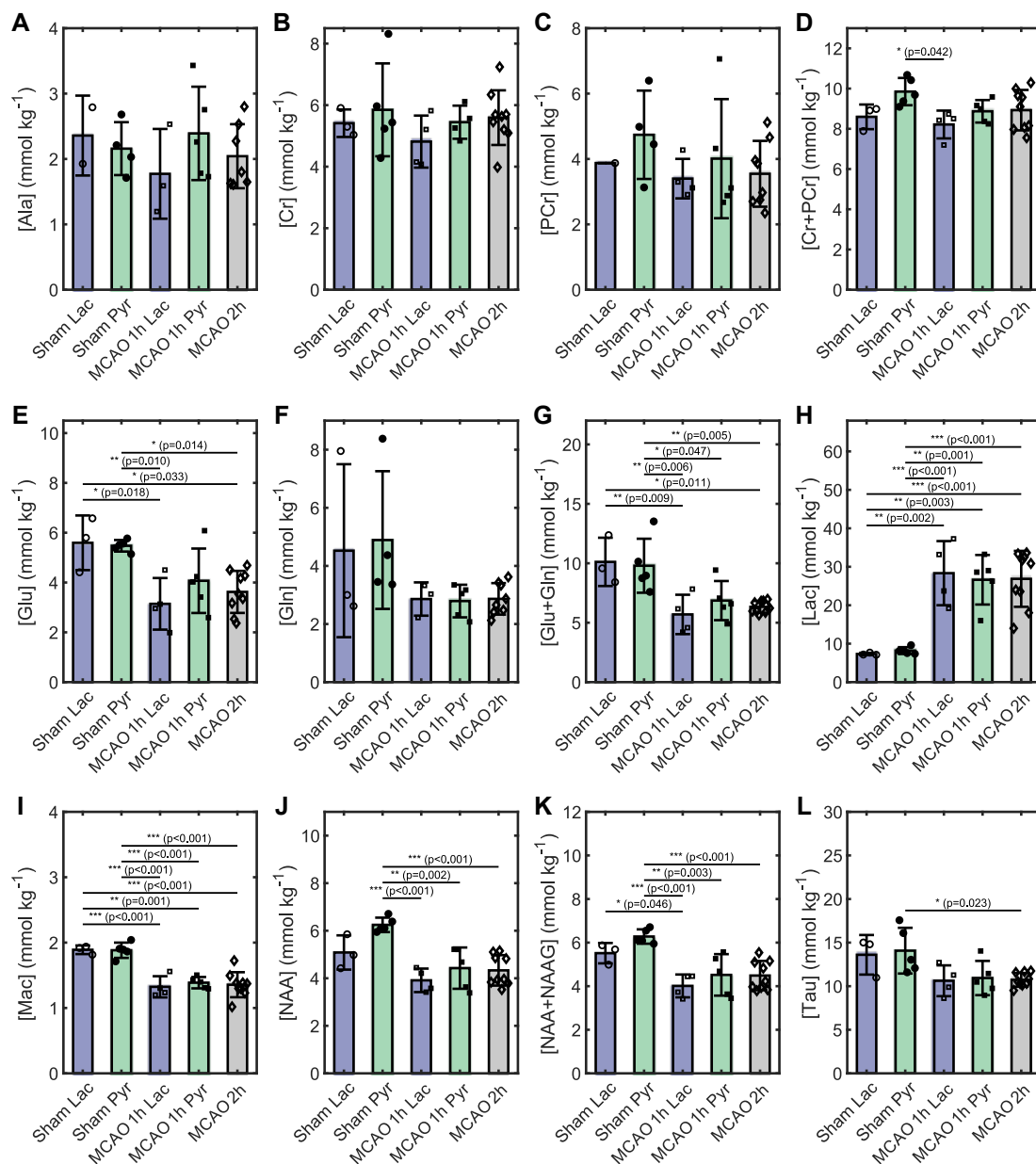


Figure 2.17: Metabolite concentrations of selected metabolites detected at 75 min post reperfusion i.e. about 15 minutes after the injection of either HP lactate or pyruvate in the sham and MCAO 1 h groups, whereas the MCAO 2 h group did not receive any injection yet. Data are displayed as the mean \pm standard deviation and overlaid with individual data points. Significant differences in many metabolites are depicted between sham and MCAO groups. However, no significant difference was depicted between both sham groups, or between the three MCAO groups.

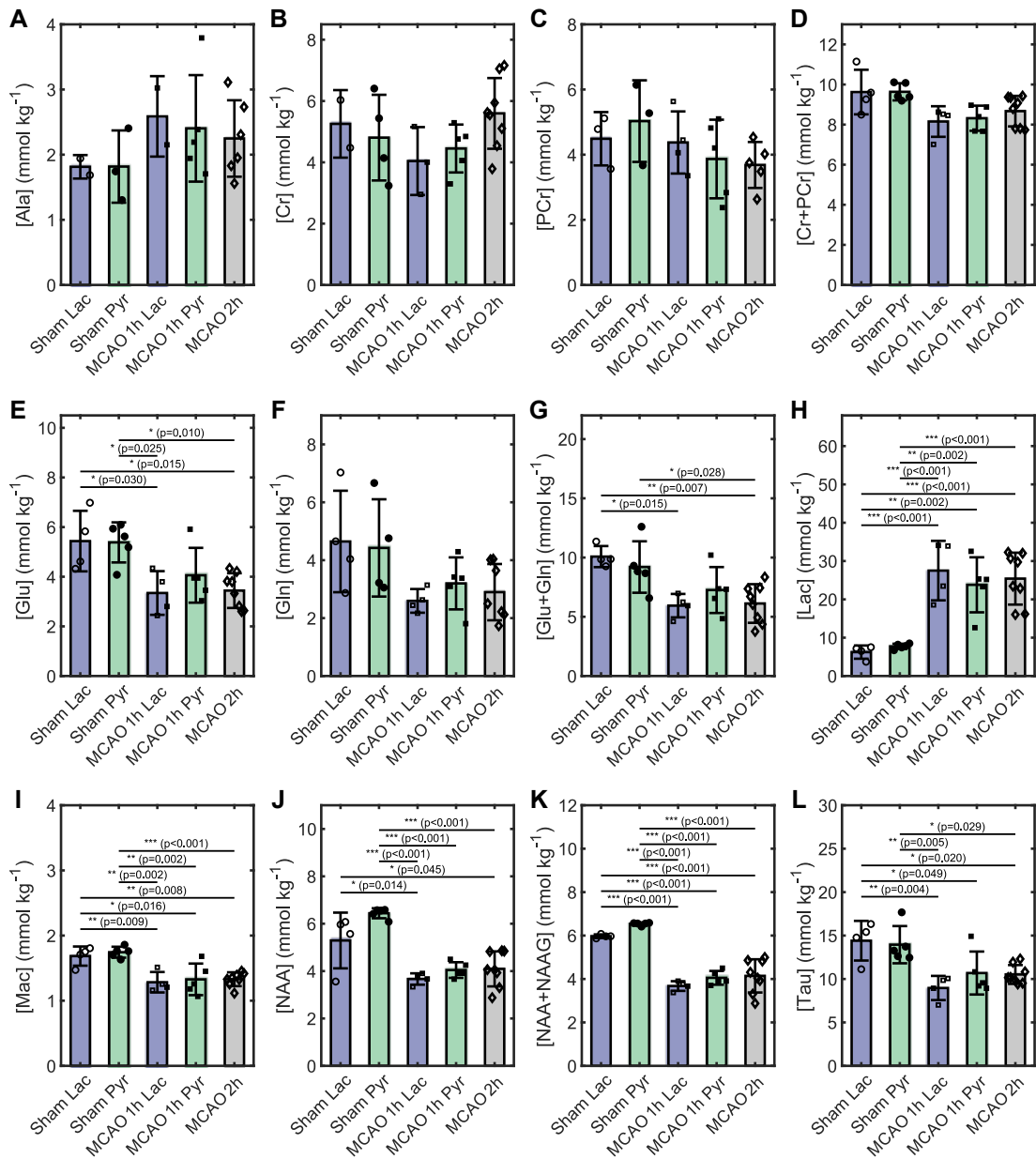
¹H neurochemical profiles in the striatum at 110 min timepoint

Figure 2.18: Metabolite concentrations of selected metabolites detected at 110 min post-reperfusion or post-surgery, therefore approximately 50 min after the injection of either HP lactate or pyruvate in the sham and MCAO 1 h groups. Data are displayed as the mean \pm standard deviation and overlaid with individual data points. Several differences are found between the sham and MCAO groups. No significant difference was depicted between both sham groups, or between the three MCAO groups.

Chapter 2. *In vivo* assessment of the metabolic impact of cerebral ischemia using MRS and hyperpolarized [1-¹³C] lactate and [1-¹³C] pyruvate

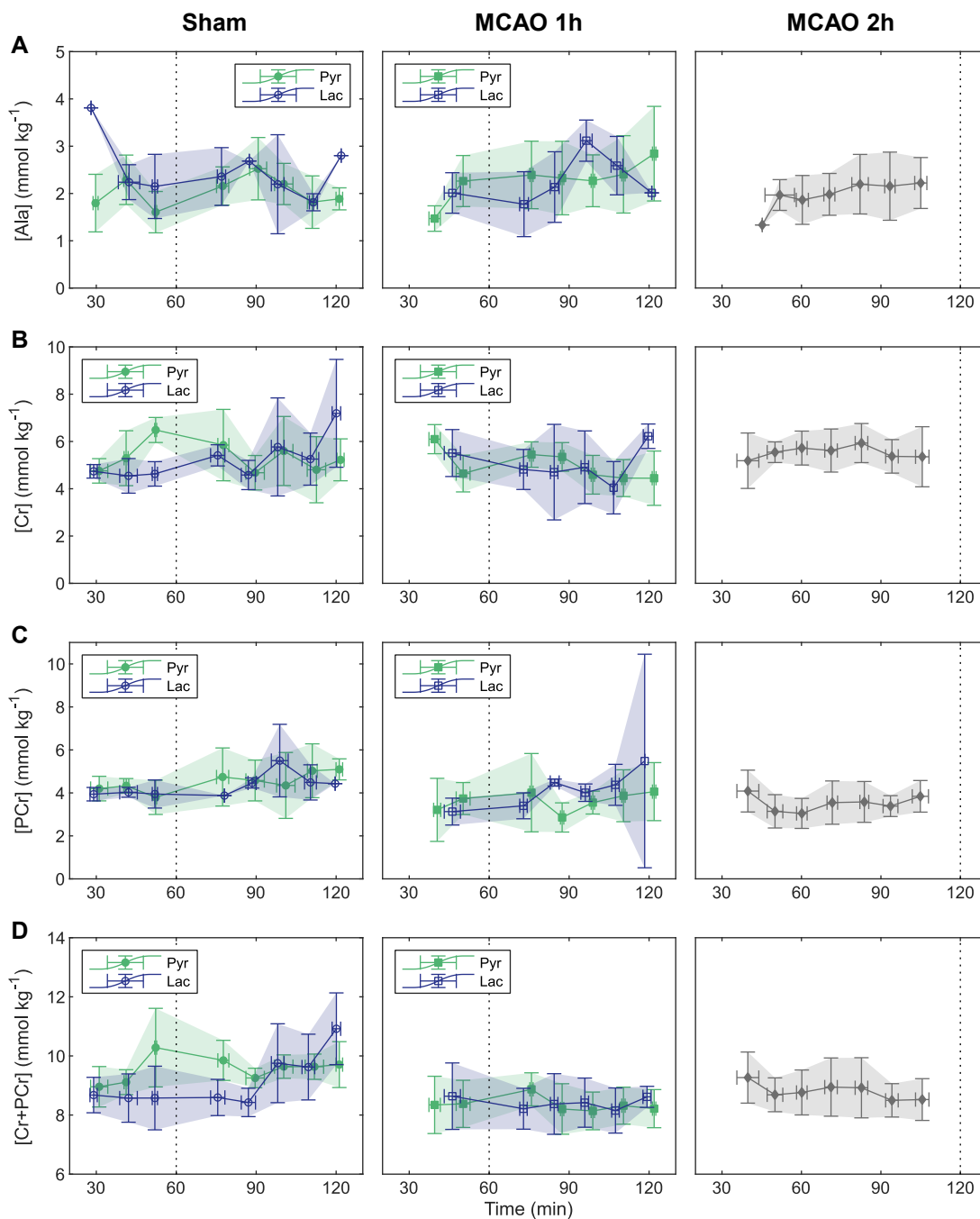


Figure 2.19: Time course of selected endogenous metabolites quantified in the striatum after sham surgery (left panel), and 30 min transient MCAO surgery (center and right panels). The blue data points are the groups receiving an injection of HP lactate, while the green data points are the groups receiving an injection of HP pyruvate. Vertical dotted lines indicate the times at which either HP lactate or HP pyruvate was injected for HP ¹³C MRS. The time zero indicates the beginning of reperfusion. Data are displayed as the mean ± standard deviation. Only data with a Cramer-Rao lower bounds (CRLB) below 40% in the LC-model quantification were included in the analysis.

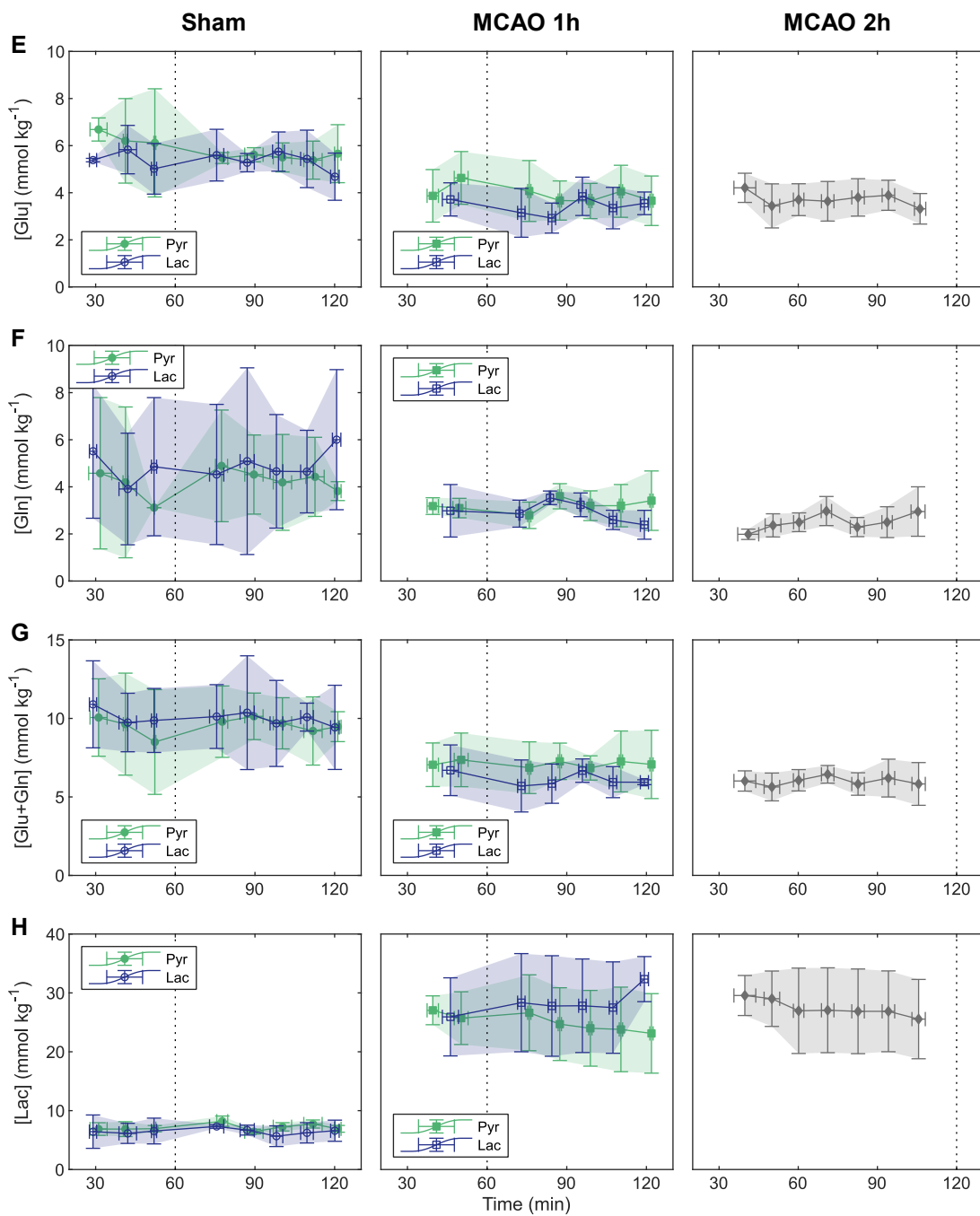


Figure 2.20: Time course of selected endogenous metabolites quantified in the striatum after sham surgery (left panel), and 30 min transient MCAO surgery (center and right panels).

Chapter 2. *In vivo* assessment of the metabolic impact of cerebral ischemia using MRS and hyperpolarized [1-¹³C] lactate and [1-¹³C] pyruvate

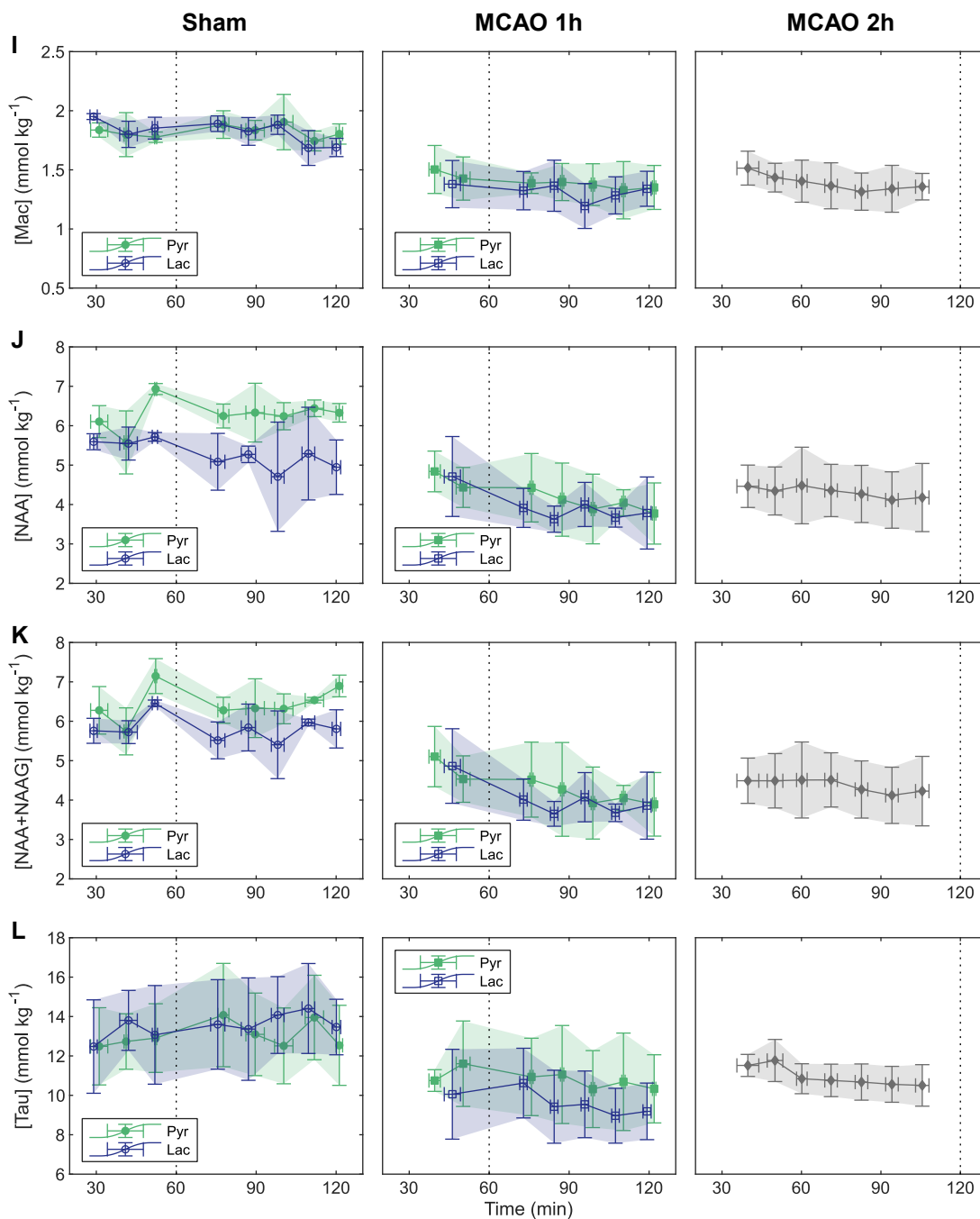


Figure 2.21: Time course of selected endogenous metabolites quantified in the striatum after sham surgery (left panel), and 30 min transient MCAO surgery (center and right panels).

2.6 Discussion

The transfer of HP ^{13}C labeling between pyruvate and lactate, starting from either $[1-^{13}\text{C}]$ pyruvate or $[1-^{13}\text{C}]$ lactate is a useful tool to assess *in vivo* metabolism. With the aim to provide a new platform for rapid molecular imaging without the use of ionizing radiation, this approach has rapidly translated from preclinical to clinical research²³¹. As HP $[1-^{13}\text{C}]$ lactate and $[1-^{13}\text{C}]$ pyruvate provide complementary views on the same metabolic pathway, our aim here was to compare their performance as metabolic contrasts while being used as neuroprotective agents in a transient mouse model of stroke. We analyzed the metabolite ratios and quantified the real time apparent kinetic rates of their cerebral metabolism after ischemic stroke.

We found a slower and lower interlabeling between lactate and pyruvate after stroke, both after HP $[1-^{13}\text{C}]$ lactate and $[1-^{13}\text{C}]$ pyruvate injections. This, suggests that either the transport of both of these monocarboxylates across the BBB or the LDH activity are decreased after stroke. Although it is known that the monocarboxylate transporter expression is increased after stroke²⁴⁸, the rise in the endogenous lactate concentration⁹³ could reduce the amount of HP lactate entering the brain, and/or reduce the conversion of HP pyruvate into lactate, which may explain the apparent lower and slower lactate-pyruvate interlabeling in the post-ischemic brain. Due to the larger endogenous lactate pool size compared to pyruvate, the metabolic conversion was one order of magnitude lower in $[1-^{13}\text{C}]$ lactate experiments (PLR and k_{LP}) compared to $[1-^{13}\text{C}]$ pyruvate measurements (LPR and k_{PL}).

Surprisingly, the labeling of pyruvate from lactate observed in stroke animals follows an opposite trend compared to a previous report²²⁸ in the same stroke model, while healthy animals depicted similar results in both studies (Figure 2.22). The only difference regarding the ^{13}C HP MRS acquisition is the different polarizing agent, which was switched from the nitroxyl TEMPOL to the trityl OX063 radical to boost the polarization level, while remaining parameters (MRI scanner, RF coil, MRS sequence, dDNP polarizer, dissolution system, dissolution buffer, anesthesia, veterinary surgeons, animal provider) remained strictly identical. Chapter 3 is focused on investigating this difference, and found that, even at the low dose of a polarizing agent, the catalytic antioxidant properties of TEMPOL act as a confounding factor and facilitate the conversion of lactate into pyruvate. Therefore, in this present study, using the more stable²⁴⁹ trityl radical OX063 instead enables us to focus on the inherent metabolic changes after stroke.

It is important to highlight that after a bolus of either substrate, the uptake is rate-limited by the transport across the BBB^{111,236,245}. Consequently, the HP substrate signal mostly originates from the blood, while downstream metabolite signals would be expected to arise from brain tissue. In HP $[1-^{13}\text{C}]$ pyruvate experiments, all the steps measured via ^{13}C MRS, which stem directly from pyruvate, are a combination of transport across the BBB and metabolism.

Chapter 2. *In vivo* assessment of the metabolic impact of cerebral ischemia using MRS and hyperpolarized [1-¹³C] lactate and [1-¹³C] pyruvate

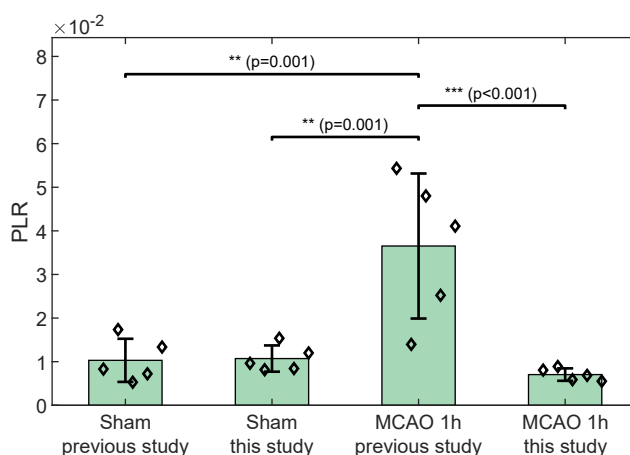


Figure 2.22: Comparison of the pyruvate labeling measured in HP [1-¹³C] lactate experiments to the previous study in the same animal model by Hyacinthe et al.²²⁸. A substantially different trend is observed in stroke animals, and will be further investigated in Chapter 3.

On the other hand, in HP [1-¹³C] lactate experiments, only the labeling of pyruvate is directly related to the lactate transport across the BBB, and the subsequent steps from pyruvate into alanine or bicarbonate represent intracellular processes. This distinction leads to interesting observations: in HP lactate experiments, the kinetic rate of pyruvate-to-bicarbonate conversion (k_{PB}) tends to be faster after stroke, while no such trend could be observed in HP pyruvate experiments although the same metabolic step is probed here, namely the conversion of [1-¹³C] pyruvate into acetyl-CoA and ¹³CO₂. Further metabolic contrasts were observed in the [1-¹³C] alanine labeling, which was lower after stroke compared to sham. However, it is likely that the alanine signal originates from soft peripheral tissues^{221,250,251} due to the low level of alanine aminotransferase in the brain²⁵².

Interestingly, in HP [1-¹³C] lactate experiments, the kinetic modeling analysis enabled a better distinction between healthy and stroke animals by taking into account the successive transport/enzymatic steps, unlike the metabolite ratio analysis. This is not the case in HP [1-¹³C] pyruvate measurements, where the lactate-to-pyruvate ratio and kinetic rate of pyruvate to lactate conversion are strongly correlated, and is equivalently analyzed with both approaches.

While both substrates require a similar dose to achieve neuroprotection, lactate has a substantially higher endogenous abundance, approximately 20 times higher than pyruvate in healthy animals²⁵³. In addition, the flux of lactate across the BBB is higher than for pyruvate²⁵⁴. As a result, lactate therapy remains closer to physiological conditions, reducing the risks of saturating the metabolic pathways.

Nonetheless, in both situations tested here, the infused dose was higher than the typical doses used in preclinical and clinical research. Therefore, we wanted to investigate whether these higher doses induced changes that would affect the absolute metabolite concentrations quantified by proton spectroscopy. Consistent with previous studies^{93,228,255,256}, the observed neurochemical profiles evolved rapidly after stroke, and striking changes in metabolite concentrations were readily observed after reperfusion, particularly the typical higher lactate concentration within the lesion. Based on the proton spectra, neither the therapeutic bolus of pyruvate nor that of lactate induced additional changes in the metabolites pool size in the striatum of healthy or ischemic brains, suggesting that even when applied at a higher dose, they do not substantially alter the metabolism in the infarct core. It is important to note that the ¹H spectroscopy was collected in a voxel located within the ischemic core area, while the HP ¹³C MRS was detected in the whole brain using the surface coil profile to limit the detection area. As a consequence, it is not possible to directly relate the results between both modalities. The 2 hours time window of the ¹H MRS is not long enough to assess the evolution of the endogenous lactate concentration over time²²⁸.

2.7 Conclusion

In this chapter, we demonstrated the feasibility of quantifying the global cerebral metabolic kinetics of HP [1-¹³C] lactate and HP [1-¹³C] pyruvate while being used at therapeutic doses in a mouse model of ischemia-reperfusion. Both substrates reported distinct global cerebral transport and metabolism between the ischemic and healthy brains. Major changes are taking place in the first two hours after reperfusion, reflecting the metabolic reprogramming set in motion to meet the energetic demands after blood flow is restored in the acute phase of stroke. Although HP lactate metabolism is more challenging to measure due to a lower polarization and magnitude of the conversion into downstream metabolites compared to HP pyruvate, it achieved similar kinetic contrasts. Unlike HP pyruvate, measuring the metabolism of HP lactate offers the ability to probe subsequent steps, to distinguish between the uptake and metabolism within brain tissues. On the biological side, lactate administered as a therapy remains more physiological than pyruvate, and presents more established neuroprotective effects, currently undergoing phase 2 clinical trials for acute ischemic stroke. Overall, while pyruvate is a better imaging probe, lactate is more advantageous on the therapeutic side.

The global measurements performed in this study assessed the metabolism of the whole brain, without distinction between healthy tissue, potentially salvageable penumbra and core of the focal ischemic injury. Despite this limitation, the present study sets the ground for further investigations to fully exploit the potential of HP pyruvate and HP lactate as metabolic contrasts for stroke theranostics.

Chapter 2. *In vivo* assessment of the metabolic impact of cerebral ischemia using MRS and hyperpolarized [1-¹³C] lactate and [1-¹³C] pyruvate

Further improvements of the measurement sensitivity and the use of localization techniques, which will be the focus of the next chapters, would allow us to more precisely map the metabolic conversions. In addition, a deeper understanding of the differences in how the brain uses these two neuroprotective agents may also contribute to a better understanding of their mechanisms of action.

3 Influence of DNP polarizing agents on biochemical processes: TEMPOL in transient ischemic stroke

3.1 Abstract

Hyperpolarization of ^{13}C by dissolution dynamic nuclear polarization (dDNP) boosts the sensitivity of magnetic resonance spectroscopy (MRS), making possible the monitoring *in vivo* and in real time of the biochemical reactions of exogenously infused ^{13}C -labeled metabolic tracers.

The preparation of the hyperpolarized substrate requires the use of free radicals as polarizing agents. Although added at very low doses, these radicals are not biologically inert. Among the observations of the previous chapter, a lower labeling of pyruvate after a bolus injection of HP lactate was found in stroke mice compared to healthy animals. Surprisingly, this is opposite to a previous study conducted on the same animal model. Between both studies, the main difference is the polarizing agent, which was changed from the nitroxyl radical TEMPOL to the trityl radical OX063 to boost the polarization.

Here, we demonstrate that the presence of the nitroxyl radical TEMPOL influences significantly the cerebral metabolic readouts of a hyperpolarized [$1\text{-}^{13}\text{C}$] lactate bolus injection in a mouse model of ischemic stroke with reperfusion. Thus, the choice of the polarizing agent in the design of dDNP hyperpolarized MRS experiments is of great importance, and should be carefully taken into account to prevent or consider significant effects that could act as confounding factors.

This chapter is adapted from the following manuscript: **Lê Thanh Phong**, Buscemi Lara, Lepore Mario, Mishkovsky Mor, Hyacinthe Jean-Noël, Hirt Lorenz. *Influence of DNP Polarizing Agents on Biochemical Processes: TEMPOL in Transient Ischemic Stroke*, ACS Chemical Neuroscience, 2023. doi:10.1021/acscemneuro.3c00137

This study was conceived by MM, HL and HJN. BL and LM performed the stroke surgery. I acquired all experimental data. BL and myself analyzed and interpreted the data. All authors contributed to drafting and revising the manuscript.

3.2 Introduction

Hyperpolarization of ^{13}C labeled small molecules temporarily increases the nuclear spin polarization by up to five orders of magnitude. Among the different hyperpolarization techniques designed to enhance nuclear magnetization, dynamic nuclear polarization (DNP)¹³³ is the most versatile one. The DNP process involves the transfer of polarization from unpaired electron spins to neighboring nuclear spins through dipolar interaction, making it possible to hyperpolarize a large variety of substrates. As discussed in Section 1.4.4.3, in a typical DNP sample, unpaired electron spins (also called polarizing agents) in the form of free radicals are homogeneously mixed with the labeled substrate of interest as frozen glassy beads. In practice, only tens of millimolar of polarizing agent are needed to hyperpolarize molar of the substrate. A large variety of radicals has been proposed since the introduction of DNP²⁵⁷, including non-persistent UV-induced radicals^{177,180} and stable free radicals, the latter being widely used in biological investigations.

In fact, the choice of polarizing agent has a great influence on the maximal polarization levels that can be achieved, as it influences the mechanism by which the DNP process occurs. As a rule, when directly polarizing low gyromagnetic ratio nuclei (such as ^{13}C), narrow electron spin resonance (ESR) line radicals (e.g. Trityl or BDPA) are preferable, and high polarization levels can be reached within several hours. On the other hand, broad ESR line radicals (e.g. nitroxyl) usually provide better performance for high gyromagnetic ratio nuclei and especially for ^1H . Nevertheless, recent efforts for optimizing and accelerating the preparation of hyperpolarized (HP) samples while using the ubiquitous and accessible nitroxyl radicals showed that the use of microwave modulation¹⁴⁹ with or without the combination of cross-polarization^{151,152} schemes may lead to very competitive polarization even on ^{13}C -labeled compounds¹⁸⁶.

The advent of the dissolution DNP protocol allowed the preparation of biocompatible solutions of HP metabolic substrates. Consequently, it paved the way for novel magnetic resonance spectroscopy (MRS) applications, by enabling *in vivo* acquisitions of biochemical reactions of exogenously infused solutions of HP ^{13}C -labeled tracers in real time.

Altered metabolism is a common feature of many neurological disorders, motivating extensive efforts to develop and apply HP ^{13}C MRS for neuroimaging^{214,220,258}. Early on, proton MRS was used to report the evolution of the neurochemical profile of endogenous metabolites like lactate after ischemic brain injury²⁵⁹. Interestingly, while hypoxia produces large amounts of lactate due to reduced blood supply^{88,259}, it has been demonstrated that the administration of exogenous lactate at reperfusion protects against ischemia-induced cell death and disability^{62,63}.

Chapter 3. Influence of DNP polarizing agents on biochemical processes: TEMPOL in transient ischemic stroke

In the context of advancing hyperpolarized MR neuroimaging and, in particular, the development of theranostic probes for ischemic stroke, the focus was, as a first step, on the implementation of HP [1-¹³C] lactate as a probe for interrogating cerebral metabolism²³⁶. It was demonstrated that after transient hypoxia-ischemia injury, hyperpolarized [1-¹³C] lactate administered at a beneficial dose^{62,63} rapidly reaches the brain and gets converted into pyruvate and CO₂²²⁸. It is important to highlight that in these studies the polarizing agent of choice was the widely available and affordable nitroxyl radical 4-hydroxy-2,2,6,6-tetramethylpiperidine-1-oxyl (TEMPOL). Although small amounts of TEMPOL are necessary for the DNP process, and its millimolar concentration is decreased upon the dilution with the dissolution solvent, even at these low doses, it may not be biologically inactive. Indeed, TEMPOL is a radical scavenger whose antioxidant activity has been used for a long time to prevent the adverse consequences of oxidative stress and inflammation in a number of pathological conditions²⁶⁰. In particular, TEMPOL has been shown to provide neuroprotection when administered before or after reperfusion in animal models of global and focal cerebral ischemia^{261–265}.

In the context of this thesis, the polarizing agent was changed from TEMPOL to the trityl radical OX063 to double the liquid-state polarization. A substantial sensitivity improvement was achieved, enabling the metabolic time course of all downstream metabolites to be quantified to allow detecting dynamic contrasts via kinetic modeling (Chapter 2). Interestingly, a decreased pyruvate labeling was observed in stroke animals compared to healthy mice, which is opposite to the previous study on the same animal model by Hyacinthe et al.²²⁸. Further verification is required to isolate the origin of this surprising change.

Hence, the aim of the present chapter was to investigate whether the presence of TEMPOL influences the cerebral metabolic readouts of an HP [1-¹³C] lactate bolus injection in a mouse model of ischemic stroke with reperfusion. In the dDNP protocol, the polarizing agent was the trityl radical OX063, which has not been reported for neuroprotection and produces higher ¹³C polarization²⁶⁶ in metabolic precursors. Then, the metabolic readouts of the injection of HP [1-¹³C] lactate polarized with the trityl radical were compared to that of a similar bolus spiked with the nitroxyl radical TEMPOL.

3.3 Methods

The experimental procedure is similar to the procedure reported in Section 2.3. The HP MRS datasets from the MCAO 1 h group presented in Section 2.5 are reused in the present chapter. The present part adds the measurements of the MCAO + TEMPOL group.

3.3.1 Animal experimentation

All experiments involving mice were conducted according to Federal and local ethical guidelines and were approved by the local regulatory authorities (Service de la Consommation et des Affaires Vétérinaires, Canton de Vaud, Switzerland), license numbers VD2017.5 and VD2017.6. Male C57BL/6J mice (6 to 10 weeks, Charles River, France) were maintained in an animal facility with controlled humidity and temperature, a 12 h light/dark cycle and free access to food and water.

3.3.2 Transient middle cerebral artery occlusion (MCAO) model of stroke

A lesion in the left striatum was induced by transient 30 min focal cerebral ischemia as previously described^{61,239}. In summary, mice were kept under anesthesia with 1.5-2.0% isoflurane in 60% oxygen and laser-Doppler flowmetry was used to monitor the regional cerebral blood flow (rCBF) through a flexible probe (Perimed AB, Sweden) glued to the skull at 1 mm posterior and 6 mm lateral from bregma. The neck was incised and both left common and external carotid arteries were exposed and ligated. A silicone-coated nylon monofilament (Docol Corp., Sharon, USA) was inserted through the common carotid artery into the internal carotid artery to obstruct the left middle cerebral artery (MCA). The occluding filament was removed after 30 min to restore the blood flow. The intervention was considered successful if the rCBF remained below 20% of the baseline during occlusion and increased above 50% of the initial value within 10 min after the filament retraction. The left femoral vein was cannulated during occlusion to allow the intravenous injection of the HP solution.

3.3.3 Hyperpolarization

A preparation of 4.1 M sodium L-[1-¹³C] lactate (606022, Sigma Aldrich, Buchs, Switzerland) in water:glycerol (1:1, v:v) was doped with 25 mM of OX063 radical (Albeda Research, Copenhagen, Denmark). 160 μ L of mixture was frozen into 10 μ L beads and hyperpolarized in a 7T/1K DNP polarizer¹⁸⁸. In separate experiments, a liquid-state polarization of $(33.1 \pm 8.9)\%$ was measured in a 9.4T MRI scanner at the time of injection.

3.3.4 Magnetic resonance measurements

MR measurements were performed on a 9.4T/31cm horizontal actively shielded magnet (Magnex Scientific, Yarnton, UK) connected to a Varian INOVA spectrometer (Varian, Palo Alto, USA).

Chapter 3. Influence of DNP polarizing agents on biochemical processes: TEMPOL in transient ischemic stroke

Upon reperfusion, mice were transferred into the MRI scanner with a ^1H quadrature/ ^{13}C linear surface coil above the head, whose sensitivity profile was described in a previous study²²⁸. Using the FASTESTMAP routine²⁴¹, static field inhomogeneity was corrected in a $3.6\text{ mm} \times 6.9\text{ mm} \times 4.5\text{ mm}$ voxel within the brain to optimize the signal quality.

Anatomical axial T_2 weighted (T_2W) images were acquired with a fast spin-echo sequence (effective echo time $\text{TE}_{\text{eff}} = 52\text{ ms}$, $\text{TR} = 4000\text{ ms}$, $18\text{ mm} \times 9\text{ mm}$ FOV, 256×128 matrix) at the beginning of the MR scan to provide localization for the shimming voxels, as well as within 5 min of the HP injection and at 2 h post-reperfusion to assess the evolution of the striatal lesion.

At 1 h post-reperfusion, the lactate sample was dissolved in 5 mL superheated D_2O , pushed to a separator/infusion pump and injected through an automated protocol¹⁸⁸. The injection volume was set to 450 μL , including 125 μL of dead volume, to reach a therapeutic dose of HP [$1\text{-}^{13}\text{C}$] lactate. In average, the dose delivered was $(1.07 \pm 0.14)\ \mu\text{mol g}^{-1}$, which corresponds to $(121 \pm 16)\text{ mg kg}^{-1}$ of sodium lactate. Immediately, global ^{13}C HP MRS was triggered and acquired every 3 s with 30° BIR-4 adiabatic pulses. The spatial localization was provided by the coil's sensitivity profile²²⁸.

3.3.5 Animal groups

Two animal groups were scanned: MCAO ($n = 5$), and MCAO+TEMPOL ($n = 5$). In the latter, a dose of 22 nmol g^{-1} (3.8 mg kg^{-1}) of 4-hydroxy-2,2,6,6-tetramethylpiperidine-1-oxyl (TEMPOL, Sigma Aldrich, Buchs, Switzerland) was co-injected with the HP lactate bolus by adding it to the separator/infusion pump where both substances are mixed between the injection and dissolution. The TEMPOL dose was identical as when previously used as the polarizing agent²²⁸.

3.3.6 Determination of the injected dose

250 μL of the remaining solution in the infusion pump was mixed with an equal volume of 80.0 mM [$1\text{-}^{13}\text{C}$] acetate solution in D_2O , and doped with 1 mM of Gd-DO3A-butrol (Gadobutrol, Gadovist, Bayer AG, Zürich, Switzerland) to reduce the ^{13}C T_1 . 1D ^{13}C high-resolution NMR was performed on a 400 MHz spectrometer (Avance NEO, Bruker BioSpin, Fällanden, Switzerland). The integral of the [$1\text{-}^{13}\text{C}$] lactate and [$1\text{-}^{13}\text{C}$] acetate peaks were compared to determine the concentration of the lactate solution.

3.3.7 ^{13}C MRS data processing

The signal from the first 120 s post-injection was summed, then the area under the curve (AUC) of the metabolite peaks was fitted using the Bayesian Data-Analysis Software Package V4.01 (Washington University in St. Louis). The peak areas of [$1\text{-}^{13}\text{C}$] lactate, [$1\text{-}^{13}\text{C}$] alanine, [$1\text{-}^{13}\text{C}$] pyruvate, [^{13}C] bicarbonate were then used to compute the metabolite ratios. Across the experimental data of this study, the concentration of the lactate solution and weight of the animals were homogeneous.

3.3.8 Statistical analysis

Mann-Whitney U-test analyses were performed using MATLAB R2021b (MathWorks, Natick, USA). A p -value below 0.05 was considered statistically significant. All data are presented as mean \pm standard deviation unless otherwise stated.

3.4 Results and discussion

The middle cerebral artery occlusion (MCAO) transient stroke procedure induces a focal ischemic lesion in the left striatum, as visible in hypersignal in representative T_2W axial images (Figure 3.1). Although it is only very slightly visible at 1 h post-reperfusion, the timepoint at which HP lactate is injected, the lesion boundaries become substantially more contrasted at 2 h post-reperfusion.

DNP requires the use of free radicals as polarizing agents. While they are filtered out in clinical investigations, this is generally not the case in preclinical studies. Despite their low concentration in the sample after dissolution, they could still potentially interfere with the biochemical processes that are being probed. Here we show that the *in vivo* administration of the nitroxyl radical TEMPOL, even at the low dose used as polarizing agent, significantly altered the cerebral metabolic response to an HP [$1\text{-}^{13}\text{C}$] lactate bolus injection following transient hypoxia-ischemia.

As expected, immediately after the infusion of HP [$1\text{-}^{13}\text{C}$] lactate at 1 h post-reperfusion, [$1\text{-}^{13}\text{C}$] pyruvate, [$1\text{-}^{13}\text{C}$] alanine and [^{13}C] bicarbonate were detected in the brain compartment (Figures 3.1 and 3.2). However, the metabolite ratios, computed from the sum of the MRS signals acquired in the first 120 s post-infusion, reported distinct outputs between mice after MCAO receiving HP [$1\text{-}^{13}\text{C}$] lactate polarized with trityl radical (to be referred to as MCAO group) and mice after MCAO receiving the same bolus of HP [$1\text{-}^{13}\text{C}$] lactate but with the addition of TEMPOL (to be referred to as MCAO+TEMPOL group, Figure 3.3).

Chapter 3. Influence of DNP polarizing agents on biochemical processes: TEMPOL in transient ischemic stroke

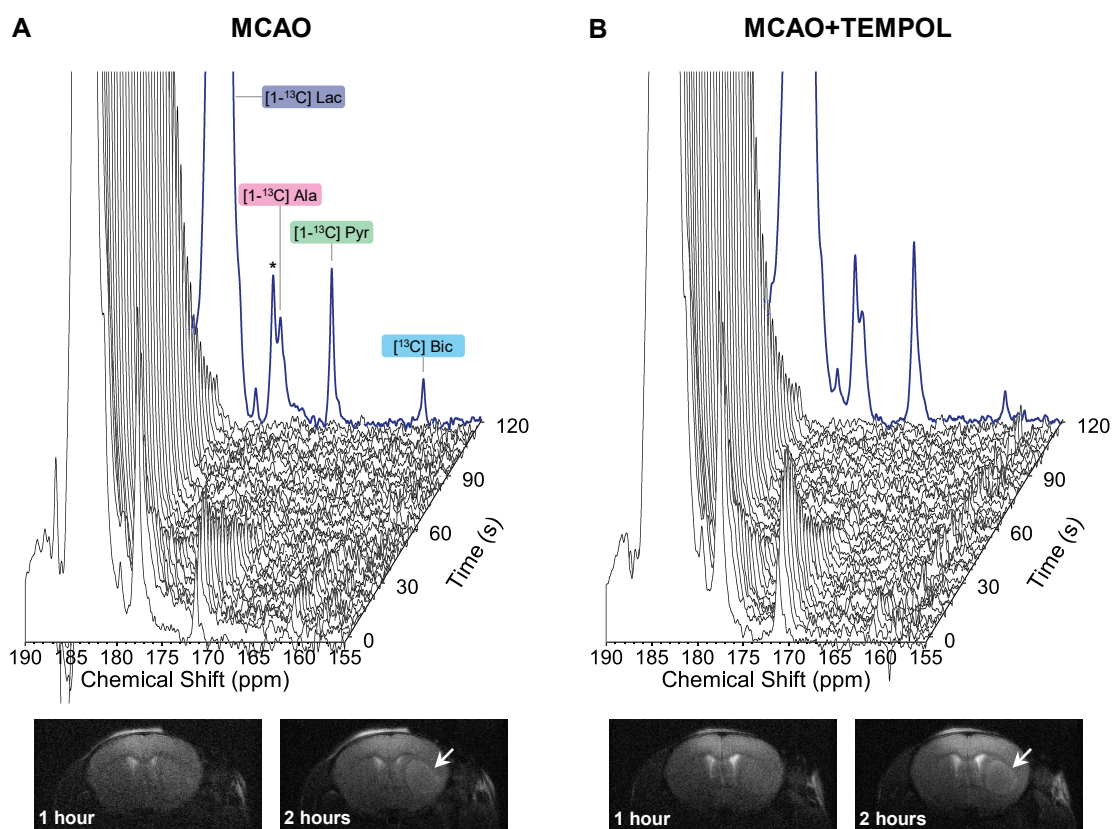


Figure 3.1: Representative dynamic cerebral ^{13}C MRS acquired after a bolus infusion of $[1-^{13}\text{C}]$ lactate (20 Hz line broadening). The summed signal from the first 120 s post-infusion is plotted in blue. The vertical scale was normalized to the height of the summed HP lactate peak. In both groups (**A-B**), the HP $[1-^{13}\text{C}]$ lactate (183.5 ppm) was converted into $[1-^{13}\text{C}]$ pyruvate (171.1 ppm), $[1-^{13}\text{C}]$ alanine (176.7 ppm) and $[^{13}\text{C}]$ bicarbonate (161.2 ppm). The signal observed at 177.7 ppm (*), partially overlapping with the alanine peak, is an impurity from the stock lactate solution. Bottom: representative axial T_2W images of the brain acquired at 1 h and 2 h post-reperfusion. In both groups (**A-B**), the striatal lesion was slightly visible at 1 h post-reperfusion and clearly contrasted at 2 h post-reperfusion (white arrows).

While the pyruvate-to-lactate ratio (PLR, Figure 3.3A) of the MCAO group $((7.0 \pm 1.4) \times 10^{-3})$ was lower than that of the group which received the co-injection of TEMPOL $((1.07 \pm 0.21) \times 10^{-2})$, the alanine-to-lactate ratio (ALR, Figure 3.3B) was lower in the MCAO+TEMPOL group $((5.3 \pm 1.0) \times 10^{-3})$ compared to the MCAO group $((8.2 \pm 1.7) \times 10^{-3})$. The alanine-to-pyruvate ratio (APR, Figure 3.3D) was significantly lower in the MCAO+TEMPOL group $((5.1 \pm 1.1) \times 10^{-1})$ compared to the MCAO group (1.19 ± 0.20) . Finally, no changes were observed in the lactate-to-bicarbonate conversion (BLR, Figure 3.3C). By polarizing ^{13}C using OX063 we were able to double the initial polarization compared to our previous results with TEMPOL²²⁸. The increased sensitivity enabled an accurate quantification of $[^{13}\text{C}]$ bicarbonate signals.

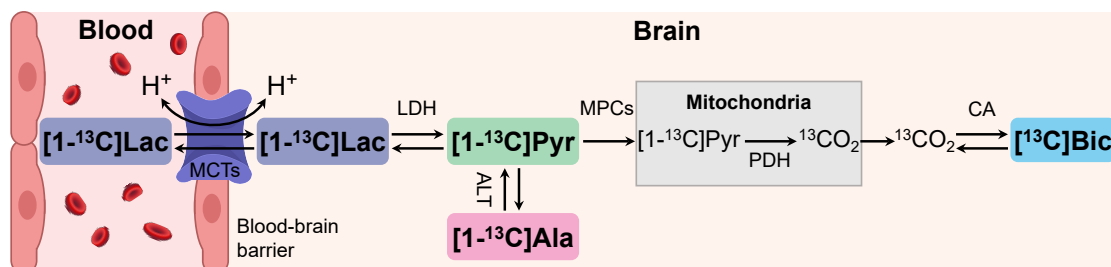


Figure 3.2: Simplified schematics of cerebral [1-¹³C] lactate metabolism. [1-¹³C] lactate can cross the blood-brain barrier (BBB) via monocarboxylate transporters (MCTs). The intracellular [1-¹³C] lactate and [1-¹³C] pyruvate pools are exchanged via lactate dehydrogenase (LDH). [1-¹³C] pyruvate is either converted into [1-¹³C] alanine by alanine aminotransferase (ALT) or transported into the mitochondria via mitochondrial pyruvate carriers (MPCs), then oxidized by pyruvate dehydrogenase (PDH), producing ¹³CO₂ remaining in equilibrium with [¹³C] bicarbonate via carbonic anhydrase (CA).

The blood flow deficit during ischemic stroke results in oxygen and glucose depletion in the affected brain region, giving rise to excitotoxicity and ionic imbalance, nitrosative and oxidative stress, as well as apoptotic cell death¹³. The generation of toxic free radicals is even exacerbated after the restoration of blood flow, in what is known as reperfusion injury. During cerebral ischemia, the superoxide anion (O₂⁻), which is mainly generated in mitochondria as a result of one-electron reduction of oxygen, is produced at such high levels that ability of the natural scavenger enzyme superoxide dismutase (SOD) to dispose of it is overwhelmed.

TEMPOL is a cell- and BBB-permeable compound with SOD-mimic activity that can react successively with hydroperoxyl and superoxide radicals to decompose them into H₂O₂ and O₂, while consuming H⁺, acting as a self-replenishing antioxidant agent^{267,268} (Figure 3.4A). Our results highlight different PLR between both groups of MCAO animals, being higher in those that were co-injected with TEMPOL (Figure 3.3A). This difference could be related to the consumption of H⁺ in the TEMPOL-mediated decomposition of reactive oxygen species, which could indirectly enhance the conversion of lactate into pyruvate by favoring a more efficient uptake of the exogenous HP [1-¹³C] lactate via the lactate/H⁺ monocarboxylate transporter (MCT) import and/or by favoring a displacement of the LDH equilibrium towards the production of [1-¹³C] pyruvate, NADH and H⁺ (Figures 3.2 and 3.4B).

Chapter 3. Influence of DNP polarizing agents on biochemical processes: TEMPOL in transient ischemic stroke

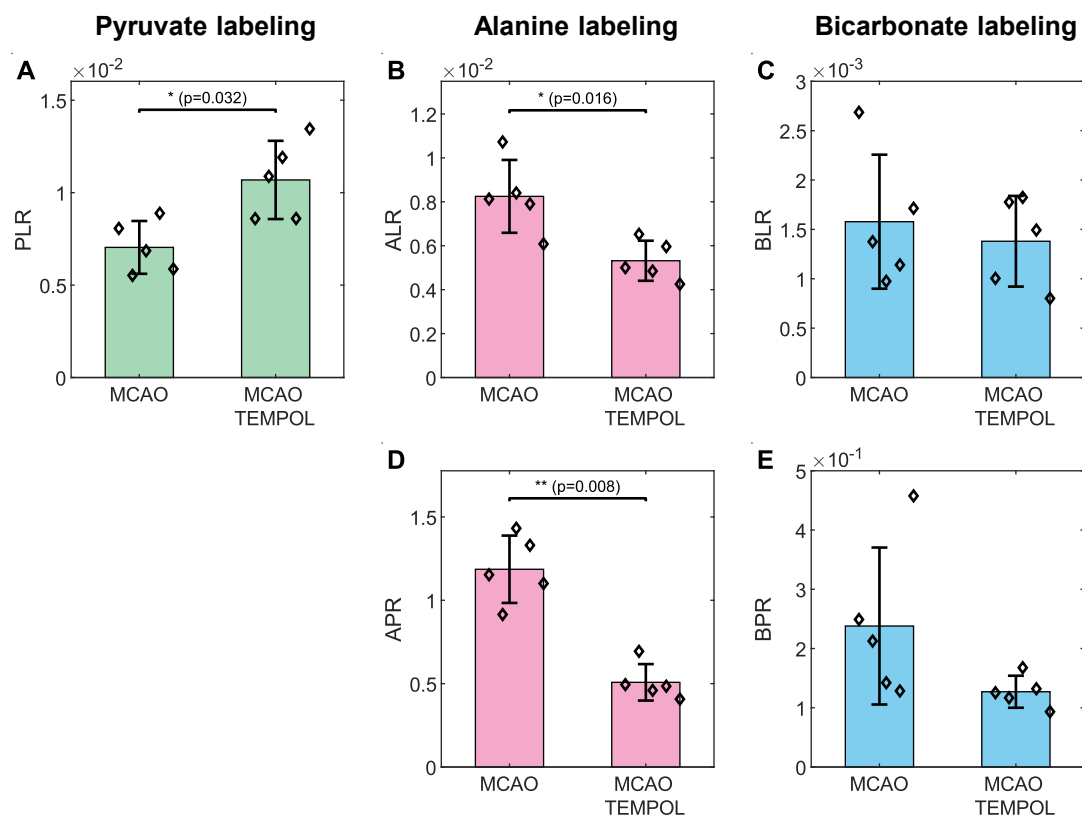
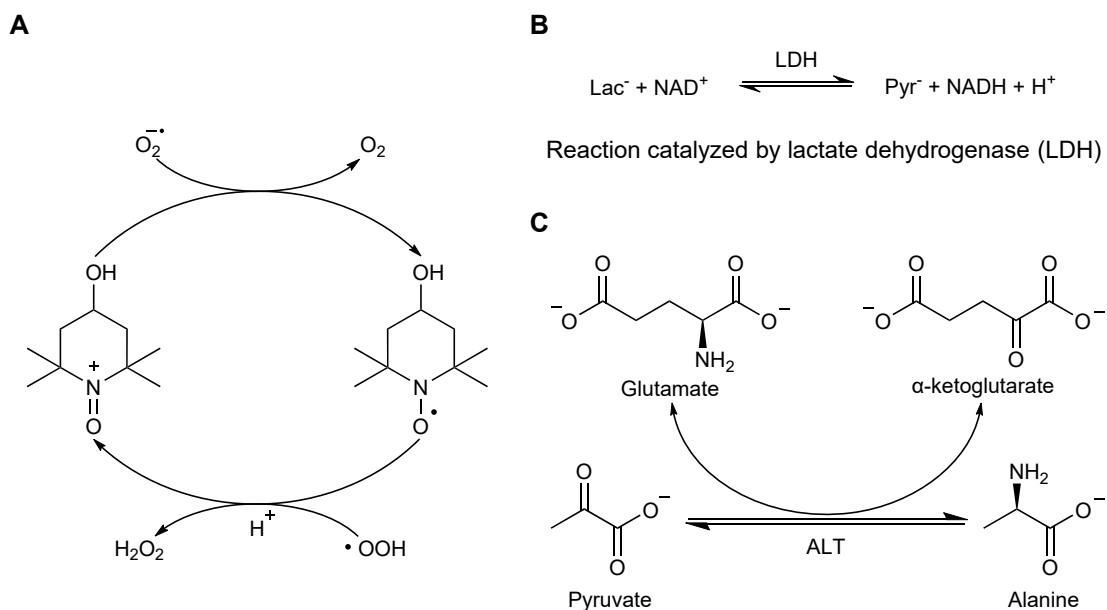


Figure 3.3: Metabolite ratios measured following injection of HP [1-¹³C] lactate. Data are displayed as the mean \pm standard deviation and overlaid with individual data points (black diamonds). Pyruvate-to-lactate ratio (PLR, **A**), alanine-to-lactate ratio (ALR, **B**), bicarbonate-to-lactate ratio (BLR, **C**). Alanine-to-pyruvate ratio (APR, **D**) and bicarbonate-to-pyruvate ratio (BPR, **E**). The PLR was significantly lower in the MCAO group compared to MCAO+TEMPOL group (**A**). A lower alanine labeling (ALR) was observed in MCAO+TEMPOL compared to MCAO (**B**). No changes were observed in the bicarbonate-to-lactate ratio (BLR, **C**).

The dose of TEMPOL used in our experiments (3.8 mg kg^{-1}) is about 5 to 50 times lower than that reported to protect at reperfusion^{261,262,265}. Nevertheless, since TEMPOL antioxidant properties stem from a catalytic reaction, small amounts of the nitroxyl radical could be sufficient to appreciate a biological effect. In contrast, trityl radicals are typically more stable²⁴⁹ due to the electron delocalization conferred by their molecular structure. Although they react with the superoxide radical²⁶⁹, the low dosage and non-catalytic reaction are unlikely to substantially affect the experiment outcome.

Earlier experiments using HP [1-¹³C] pyruvate to study cerebral metabolism reported that [1-¹³C] alanine rather originates from peripheral tissues than from the brain^{221,251}. It is probable that the change in ALR after stroke is related to muscles around the skull, close to the coil, whose metabolism was affected by the common carotid artery ligation during



Superoxide dismutase-like activity of TEMPOL Reaction catalyzed by alanine aminotransferase (ALT)

Figure 3.4: Schematic representations of the chemical reactions potentially involved in the interpretation of the measured ^{13}C NMR signals, with or without TEMPOL. **(A)** Superoxide dismutase-like catalytic activity of TEMPOL, converting hydroperoxyl and superoxide radicals into H_2O_2 and O_2 ; **(B)** Lactate-pyruvate exchange catalyzed by lactate dehydrogenase (LDH); **(C)** Pyruvate-alanine exchange catalyzed by alanine aminotransferase (ALT).

surgery. However, the cerebral concentration of alanine has been reported to be steadily elevated during ischemia, an effect attenuated by TEMPOL²⁶⁴. In the same study, TEMPOL decreased extracellular glutamate release, reduced the ischemic lesion size and improved neurobehavioral outcomes. In the ischemic tissue, neural cells respond to oxygen and glucose deficits by rapidly depolarizing and massively releasing glutamate. This glutamate can be taken up by astrocytes, where it can be converted into alanine by ALT using pyruvate as a co-substrate²⁷⁰. The conversion of pyruvate to alanine by ALT requiring glutamate, (Figure 3.4C), the decrease that we observed in $[1-^{13}\text{C}]$ alanine labeling (Figure 3.3B and D) could be thus related to the effect of TEMPOL in decreasing the availability of glutamate to be consumed for the transamination reaction of $[1-^{13}\text{C}]$ pyruvate.

3.5 Conclusion

In conclusion, the administration of TEMPOL at the dose commonly used as a polarizing agent for DNP results in a significantly different cerebral metabolic response to HP [1-¹³C] lactate following transient ischemic stroke. Our results highlight that the boost in sensitivity afforded by hyperpolarized ¹³C MRS made feasible the detection of the metabolic interference of TEMPOL.

Additionally, they show that care should be taken when choosing the polarizing agent in DNP hyperpolarization experiments, as certain biologically active reagents like TEMPOL can meddle with the biochemical processes of interest. Even if used in small doses, they may have significant effects that could act as confounding factors. This could be important not only for *in vivo* preclinical research as shown in here, but it could also have some impact on new, recently developed uses of DNP HP techniques like the ¹³C hyperpolarization via cross-polarization^{151,152} from DNP-polarized ¹H spins, which is being applied to metabolomics studies, and which so far prefers nitroxyl radicals to achieve this cross-polarization²⁷¹.

4 Design and performance of a fluid path compatible dDNP/LOD-ESR probe

4.1 Abstract

Dissolution Dynamic Nuclear Polarization (dDNP) was invented almost twenty years ago. Ever since, hardware advancement has observed 2 trends: the quest for DNP at higher field and, more recently, the development of cryogen free polarizers. Despite the DNP community is slowly migrating towards “dry” systems, many “wet” polarizers are still in use. Traditional DNP polarizers can use up to 100 L of liquid helium per week, but are less sensitive to air contamination and have higher cooling power. These two characteristics make them very versatile when it comes to new methods development.

In this chapter we retrofitted a 5T/1.15K “wet” DNP polarizer with the aim of improving dissolution, cryogenic and DNP performance. We designed, built, and tested a new DNP probe that is compatible with the fluid path (FP) technology and a Longitudinal Detected Electron Spin Resonance (LOD-ESR) probe to investigate radical properties at real DNP conditions.

The new hardware increased the maximum achievable polarization and the buildup rate constant of a [1-¹³C] pyruvic acid-trityl sample by a factor 1.5, as well as their repeatability. The new measurement capabilities also allowed to characterize and optimize the ESR properties of [1-¹³C] lactate DNP samples, increasing the liquid state polarization by a factor 2.5.

Finally, the increased liquid He holding time together with the possibility to constantly keep the sample space at low pressure upon sample loading and dissolution allowed us to save about 20 L of liquid He per week.

This chapter is adapted from the following manuscript: **Lê Thanh Phong**, Hyacinthe Jean-Noël, Capozzi Andrea. *How to improve the efficiency of a traditional dissolution dynamic nuclear polarization (dDNP) apparatus: Design and performance of a fluid path compatible dDNP/LOD-ESR probe.* Journal of Magnetic Resonance, 338:107197, 2022. doi:10.1016/j.jmr.2022.107197

This study was conceived by CA and HJN. I designed the hardware and analyzed experimental data in collaboration with CA. The thermodynamic model was built and simulated by CA. I performed all experiments and drafted the manuscript. CA and HJN revised the manuscript.

4.2 Introduction

In recent years, hyperpolarized Magnetic Resonance (MR) has become a well-established branch of MR thanks to the unprecedented sensitivity gain it can give access to^{205,272–281}.

Among the different hyperpolarization techniques targeting the liquid state, dissolution Dynamic Nuclear Polarization (dDNP) is probably the one requiring the most expensive and technically demanding hardware²⁸². Invented in 2003 by Ardenkjaer-Larsen and co-workers¹³³, dDNP produces solutions of hyperpolarized nuclei by suddenly dissolving solid frozen samples prepared by DNP¹⁴². Being the polarization transferred to the nuclei of interest from unpaired electron spins via microwave irradiation, operating at low temperatures (1–1.5 K) and high magnetic field (3.35–7 T)^{144,185,187} is a key requirement for this technique. Indeed, the electrons' Boltzmann polarization sets the theoretical limit that the nuclear spins can achieve.

These experimental conditions are provided by the so-called “dDNP polarizer”. In its most general definition, it is a cold-bore magnet equipped with a source/waveguide apparatus able to shine microwaves at the appropriate frequency onto the magnet isocenter, and a dissolution system that instantly melts and extracts the hyperpolarized sample. Most importantly, liquid He is used to cool the sample down to the target temperature. Traditional dDNP polarizers^{144,188,189}, based on a “wet cryostat”, require the provision of liquid He from an external source, can use up to 100 L of the cryogenic fluid per week. Liquid He is a non-renewable expensive commodity, and not all facilities are equipped with recovery systems. Therefore, the dDNP community, inspired by the clinical and commercially available SPINlab™ (GE Healthcare, Chicago, Illinois, USA)¹⁹², is progressively moving towards cryogen-free systems able to recondense the boiled off He gas in a closed loop by using a cryocooler^{139,193,194}. These systems are excellent “workhorses” for application experiments and have the clear advantage of low running costs and absence of cryogenics to handle. Moreover, they are often equipped with a dissolution apparatus based on the fluid path (FP) technology to minimize the heat load during the process^{139,192,194}. Indeed, the FP allows to efficiently melt the hyperpolarized sample without repressurizing the sample space and having to introduce an external dissolution wand.

Nevertheless, cryogen-free systems have three main disadvantages: a high upfront investment, a limited cooling power (few Watts), as well as substantially higher sensitivity to air contamination. On the other hand, “wet cryostat”-based dDNP polarizers are still used on a daily basis by several groups^{200,283–285}. These systems, being more robust and offering higher cooling power, are very flexible and versatile when it comes to methods developments. The old generation of dDNP polarizers was designed between 10 and 20 years ago^{133,188,189}.

In this chapter, with the purpose of improving the cryogenic and polarization performance of an existing wet 5T/1.15K DNP polarizer¹⁸⁸, we detail the cost-effective implementation of a new DNP probe compatible with a custom fluid path system (CFP)^{200–202,282}. Furthermore, we show how the new design allows to easily complement the apparatus with a home-built LOD-ESR spectrometer with the purpose of investigating the radical properties at real DNP experimental conditions^{201,286}, which will be used to characterize and optimize the formulation of [1-¹³C] lactate DNP samples in water-glycerol matrices using gadolinium doping¹⁶² to achieve better DNP enhancements.

4.3 Methods

4.3.1 Original setup

The DNP polarizer being upgraded (Figure 4.1, Vanderklink Sarl, La Tour-de-Peilz, Switzerland) is similar in design and working principle to the prototype developed by Comment et al.¹⁸⁸ in 2007. It is based on a vertical unshielded 89 mm wide bore magnet (Bruker Spectrospin, Fällanden, Switzerland) set to a field strength of 5 T corresponding to an ESR frequency of around 140 GHz. The magnet bore accommodates a double-walled 316L stainless-steel cryostat equipped with two copper radiation shields and a tail section of 50/80 mm ID/OD (Leiden Cryogenics B.V., Leiden, Netherlands). The cryostat inner vacuum chamber (IVC) hosts the variable temperature insert (VTI) to condense and control the helium flow. The latter mounts, at the top of the tail, a 316L stainless-steel gas/liquid He phase separator used to refill, with minimal perturbation, the $\varnothing 36.5$ mm sample space.

Although the cryostat is of the continuous flow type, it is generally operated in batch mode to achieve lower temperature. Firstly, it is filled with liquid helium from a 100 L external dewar (RH100, Air Liquide, Paris, France) via a rigid transfer line (CryoVac, Troisdorf, Germany) ending inside the phase separator. Then, the phase separator is isolated from the sample space by closing two needle valves, and the He bath is pumped on by a 253 m³ h⁻¹ roots pump (Ruvac WAU 251, Leybold, Cologne, Germany) backed by a 65 m³ h⁻¹ rotatory pump (Trivac D65B, Leybold). This procedure enables one to reach a helium bath temperature of (1.15 ± 0.05) K.

Two peculiarities characterize the original dDNP polarizer design by Comment et al.¹⁸⁸: the sample insertion and dissolution happen at atmospheric pressure, and the waveguide has to be removed upon insertion of the dissolution wand.



Figure 4.1: Picture of the dDNP setup upgraded in this chapter. The 5T/1.15K DNP polarizer is composed of a liquid-helium VTI inserted into a wide-bore NMR magnet ramped up to a magnetic field strength of 5 T. All vacuum pumps are installed behind the polarizer. Liquid helium is drawn from an external 100 L storage tank. Part of the liquid-state polarization measurements are performed in the benchtop $^1\text{H}/^{19}\text{F}/^{13}\text{C}/^{129}\text{Xe}$ 1.05 T (44.77 MHz ^1H frequency) NMR spectrometer in the foreground, while the remaining experiments are performed in the 14.1T MRI scanner located behind the filter panel.

Chapter 4. Design and performance of a fluid path compatible dDNP/LOD-ESR probe

Figure 4.2 shows all parts of the original design that have been replaced in this study: the “DNP probe” (or main insert) including the brass microwave cavity, the NMR coil with its stainless steel outer conductor coaxial cable, the brass baffles to cut thermal convection and radiation; the fiber glass “sample stick” for sample insertion into the polarizer; the gold-plated stainless steel “removable waveguide”, slid inside the sample stick to carry the microwaves onto the sample space; the carbon fiber dissolution wand to be inserted instead of the waveguide to instantly transform the solid frozen sample into an injectable hyperpolarized solution.

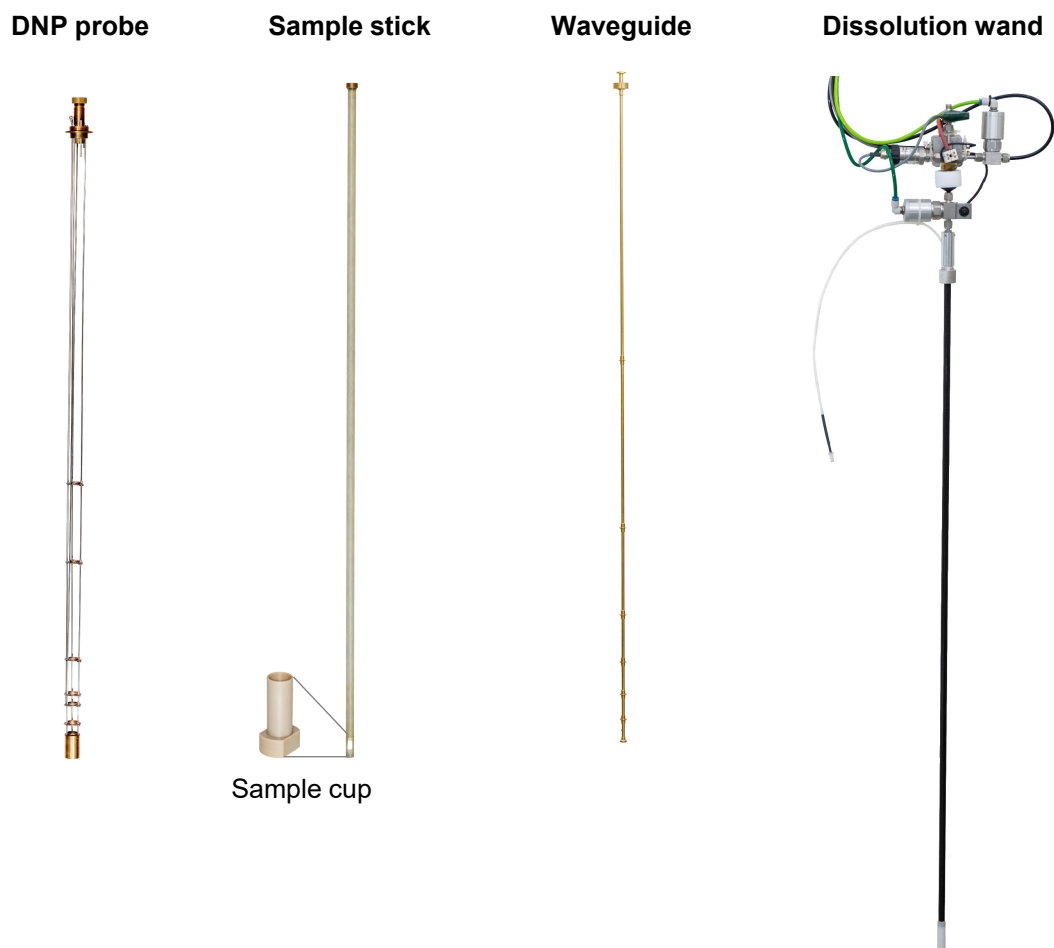


Figure 4.2: Components of the dDNP polarizer based on the design by Comment et al.¹⁸⁸ that we replaced in this study: the “DNP probe” (or main insert) that includes the microwave cavity, the NMR coil with its coax cable, the baffles to cut thermal conductivity mounted on three stainless steel rods; the “sample cup”; the fiberglass “sample stick” for sample insertion into the polarizer; the removable “waveguide” to shine microwaves onto the sample; the “dissolution wand” to be introduced inside the sample stick after repressurization of the cryostat and removal of the waveguide to instantly transform the solid frozen sample into an injectable hyperpolarized solution.

4.3.2 Custom Fluid Path (CFP)

The CFP presented previously^{194,200–202,282} has been adapted to the length of the retrofitted polarizer (Figure 4.3, the different components are reported in bold in the text). The red arrow pointing down indicates the input for the superheated buffer; the green arrow pointing right indicates the output for the hyperpolarized solution.

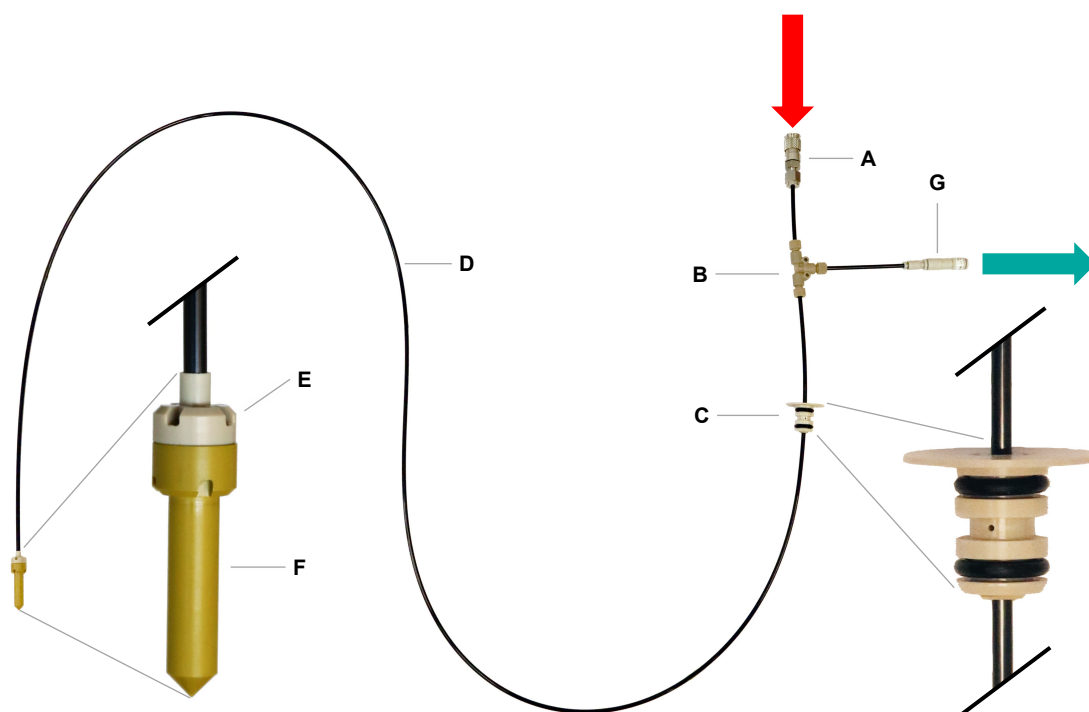


Figure 4.3: The figure shows the Custom Fluid Path (CFP) used in this study. The device is composed by a “quick connect” (A); a “flow separator” (B); a “dynamic sealing” (C); “coaxial capillaries” (D), whose only the outer 1/8" one is shown; a “vial top-part” (E), a “vial bottom-part” (F) and a “one-way valve” (G). To adapt the CFP to this polarizer the coaxial capillary length was increased to 1500 mm with respect to the original study²⁰⁰. The red and blue arrows indicate the inlet and outlet, respectively.

The superheated buffer reaches the sample flowing through a 1.60/1.90 mm ID/OD natural color PEEK inner capillary -not shown- (Zeus Inc., Orangeburg, NC, USA); the hyperpolarized solution is ejected from the polarizer flowing in between the inner capillary and a 2.40/3.18 mm ID/OD black color PEEK outer capillary (D, Zeus Inc., Orangeburg, NC, USA). The stainless steel “quick connect” (A, SS-QM2-B-200, Swagelok, Solon, OH, USA) allows coupling of the CFP to the “dissolution head” boiler (see Appendix A.2). The PEEK “flow separator” (B, P-713, IDEX Health & Science, Lake Forest, IL, USA) splits the dissolution buffer from the hyperpolarized solution. The home-built PEEK (C, Ketron 1000, Mitsubishi Chemical Advanced Materials, Tielt, Belgium) “dynamic sealing” allows to move the sample vial inside the polarizer downwards for insertion and upwards for dissolution/extraction while keeping the sample

space at low pressure. The home-built vial is reusable and made of a PEEK “vial top-part” (**E**, Ketron 1000, Mitsubishi Chemical Advanced Materials), laser welded (Leister Technologies, Kaegiswil, Switzerland) to the outer capillary, and a PAI “vial bottom-part” (**F**, Duratron T4203, Mitsubishi Chemical Advanced Materials) containing the sample (500 μ L of geometrical volume). The two parts are made leak tight to superfluid He by compressing a 8 \times 1 mm 95 Shore A PTFE O-ring (Kremer GmbH, Wächtersbach, Germany) to be replaced before each new loading. The “one-way valve” (**G**, AKH04-00, SMC, Tokyo, Japan) at the outlet prevents air cryo-pumping when the vial is at low temperature inside the polarizer. A detailed description of the assembling procedure and functioning principle of the CFP was provided in the work by Capozzi et al.²⁰⁰.

4.3.3 CFP compatible DNP probe

A new DNP probe was designed to accommodate the CFP into the polarizer (Figure 4.4, the different components are reported in bold in the text).

The probe is built around a 1320 mm long 316L stainless steel 12.0/13.0 mm ID/OD tube (**B**, Interallloy AG, Schinznach-Bad, Switzerland) inside which the CFP slides to reach the magnet isocenter. Although thinner tubes were commercially available, a 0.5 mm wall thickness was selected for better mechanical rigidity. An “air lock compartment”, composed of a vial 316L stainless steel “loading chamber” (**G**) and an ISO-KF 16 gate valve (**H**, Vatlock 01224-KA06, VAT, Haag, Switzerland), is attached to the top of the sample tube as a buffer volume between the room and the low-pressure sample space.

A home-built 316L stainless steel ISO-KF 40 flange seals the probe to the VTI and provides hermetic RF (**C**, feedthrough SMA connector, SF-2991-6002, Amphenol SV Microwave, West Palm Beach, USA) and microwave (**A**, circular 4.6 mm to rectangular WR-06 transition, Elmika, Vilnius, Lithuania) interfaces. Polished brass baffles (**I**) are brazed along the stainless-steel tube to reduce thermal convection and radiation and to provide mechanical support to the 4.6/5.0 mm ID/OD circular 316L stainless-steel waveguide (**E**, Interallloy AG, Schinznach-Bad, Switzerland) and the semi-rigid coaxial cable with stainless steel outer conductor (**D**, .141SS-W-P-50, Jyebao, Taiwan). The waveguide is interfaced to the microwave source (VCOM-06/140/1/50-DD, ELVA-1, Tallinn, Estonia) with a 90° WR-06 E-plane bend (Elmika, Vilnius, Lithuania).

The 13.2 cm³ copper cavity (**F**) is polished to reduce microwave absorption. The cavity wall is angled at 45° at the waveguide output to reflect the microwaves onto the DNP sample. A copper pseudo-Alderman-Grant (AG) coil (**J**, 8 mm ID \times 16 mm window height, 800 μ L inner volume) supported by a PTFE coil former (not shown), is inserted into the cavity for solid-state NMR detection. The coil is remotely tuned and matched outside of the cryostat with a coaxial

cable (RG_223_/U, Huber+Suhner, Herisau, Switzerland) and a matching network with two piston trimmer capacitors (V1949, Knowles-Voltronics, Itasca, USA).

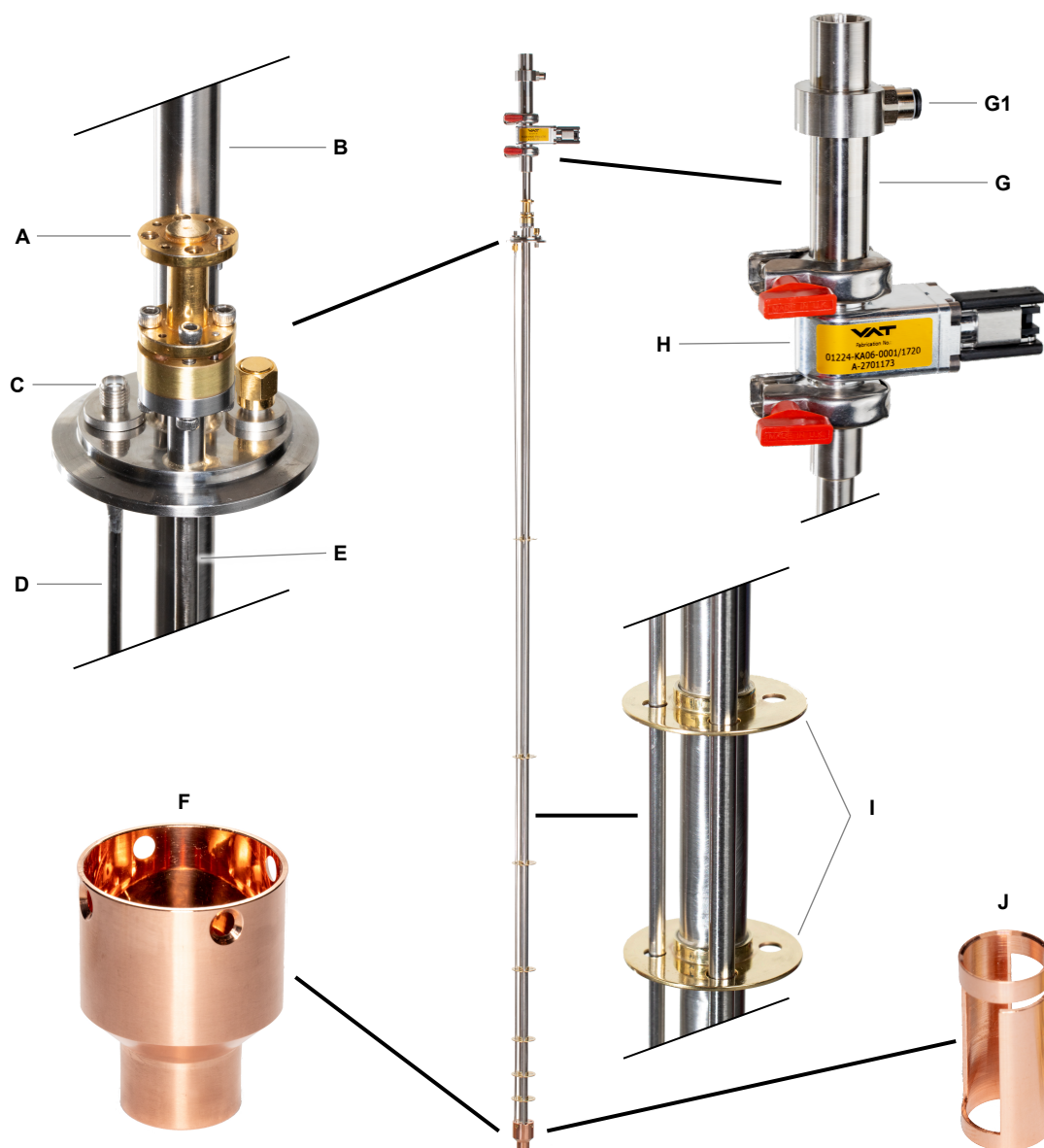


Figure 4.4: The figure shows the new DNP probe. The most important parts are zoomed in (follow straight black lines) to better picture the main components: rectangular WR-06 to circular 4.6 mm microwave transition (A); stainless-steel sample loading tube (B); feedthrough SMA connector (C); rigid coax cable (D); stainless-steel waveguide (E); copper microwave cavity (F); loading chamber (G) with He gas port (G1); gate valve (H); brass baffles (I), pseudo-Alderman-Grant copper coil (J).

Chapter 4. Design and performance of a fluid path compatible dDNP/LOD-ESR probe

A dedicated “CFP pressure-test station” (Appendix A.1) was built to provide pressurized helium for leak-testing^{192,201}, and compressed air for drying the CFP after dissolution.

Loading of the CFP inside the polarizer is similar to what was earlier described^{200,201}: the CFP is first connected to the pressure-test station He gas stem, and the pressure regulator set to provide a tiny flow; after pipetting the liquid sample inside the bottom part of the vial and connecting it to the top part, the vial is immersed in liquid nitrogen to flash-freeze the sample solution; the helium flow removes air from the CFP, then its output is closed with a stopcock valve; to test for leaks, the He gas pressure inside the CFP is increased to 4 bar, and the CFP inlet closed. If after 5 min the pressure gauge indicator steadily shows 4 bar, the CFP is considered ready for loading inside the polarizer. At this point, the dynamic sealing is moved down to touch the vial, a mild flow applied to the He gas port (**G1**), and the vial moved inside the loading chamber that is then closed at the top with the dynamic sealing. Finally, the He gas stream is closed, the gate valve opened, and the vial pushed down to reach the NMR coil at the bottom of the DNP probe. During all these operations, the sample space is already cold and continuously pumped, with its pressure that increases from 1 to 10 mbar, at the most.

4.3.3.1 LOD-ESR setup

To measure the radical properties at DNP conditions, Longitudinal Detected Electron Spin Resonance (LOD-ESR) was implemented similarly to previous works^{201,286}.

The LOD-ESR probe (Figure 4.5, the different components are reported in bold in the text) is built around a CFP outer capillary (**B**) and a dynamic sealing (**C**) such that a similar loading procedure of the sample inside the polarizer can be followed (a leak test is not performed in this case). A PEEK (Ketrion 1000, Mitsubishi Chemical Advanced Materials) coil former (**E**) is permanently screwed to the vial top part (**D**). The bottom portion of the coil former has a 7.5 mm outer diameter, small enough to enter the NMR coil of the DNP probe. The sample cup (**F**), which slides and locks inside the coil former, can be loaded with up to 120 μL of sample.

The detection coil is a 600-turn copper wire split solenoid made of 0.1 mm enameled copper wire. The number of turns was maximized with respect to the available space to increase the induced voltage, therefore optimize the detection sensitivity of the measurement²⁸⁶. A 3 mm gap allows the microwaves to reach the sample (cut-off dimension at 140 GHz is 1 mm). The two ends of the detection coil are routed inside the coil former and soldered to a twisted pair of silver-plated copper wires that runs upwards through the black capillary to carry the signal out of the polarizer. Electrical connections are provided at the outer end of the probe (**A**).

The signal is measured using a three stages 106 dB gain differential amplifier (Appendix A.3) and NI USB-6002 (National Instruments, Austin, USA) 16-bit analog-to-digital acquisition

card. To reduce noise pickup, signals are transmitted as a differential pair using BNC Twinax cables between the probe, differential amplifier and acquisition card. Furthermore, all ground loops in the LOD-ESR setup were eliminated: the acquisition card is grounded to the cryostat, powered using a floating DC source, and galvanically separated from the computer using a USB digital isolator (ADuM4160, Analog Devices, Norwood, USA). A voltage controlled variable attenuator (138-142 GHz frequency range, ≈ 2 dB insertion loss, P/N VCVA-06 and ADL-10/100, ELVA-1, Tallinn, Estonia) is inserted between the output of the microwave source and the probe to allow modulation of the output power at a specific frequency to feed the digital lock-in²⁰¹.

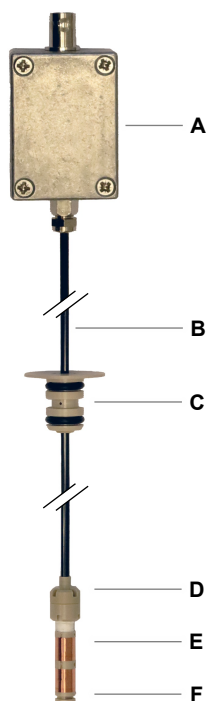


Figure 4.5: We report here the LOD-ESR probe designed for this study and compatible with the DNP probe with no need for any modification of the NMR part. The probe is composed by the following elements: a leak-tight connection box that transforms the twisted pair carrying the signal to BNC Twinax connector (A); a CFP 1/8" outer capillary (B) with its dynamic sealing (C) and laser welded vial top-part (D); a coil former supporting a 600-turn spit solenoid (E); a sample cup (F).

For electron spin–lattice relaxation time (T_{1e}) measurements the output power was modulated at 0.1 Hz between 0 mW and 35 mW. The rate was low enough to record the full time evolution of the electron spins during saturation and relaxation²⁰¹ (Figure 4.6A). The signal was averaged 256 times to measure each sample. Extraction of the T_{1e} was performed by fitting the relaxation curve data to the equation representing the signal S evolution as a function of time:

$$S(t) = A \left(e^{-\frac{t}{T_{1e}}} - e^{-\frac{t}{\tau}} \right) \quad (4.1)$$

where A is a free parameter that represents the highest signal intensity, and τ is the characteristic time constant of the probe. The latter measured 20.6 ms, upon excitation of the set-up with a squared wave²⁰¹. For radical spectrum recording, the microwave frequency was increased from 139.8 GHz to 140.0 GHz in steps of 1.25 MHz and the output power modulated at 4.8 Hz between 0 mW and 35 mW (Figure 4.6B). For each frequency step the demodulated signal was integrated for 20 s in the time domain, equivalent to setting the low pass filter of the lock-in to 0.05 Hz.

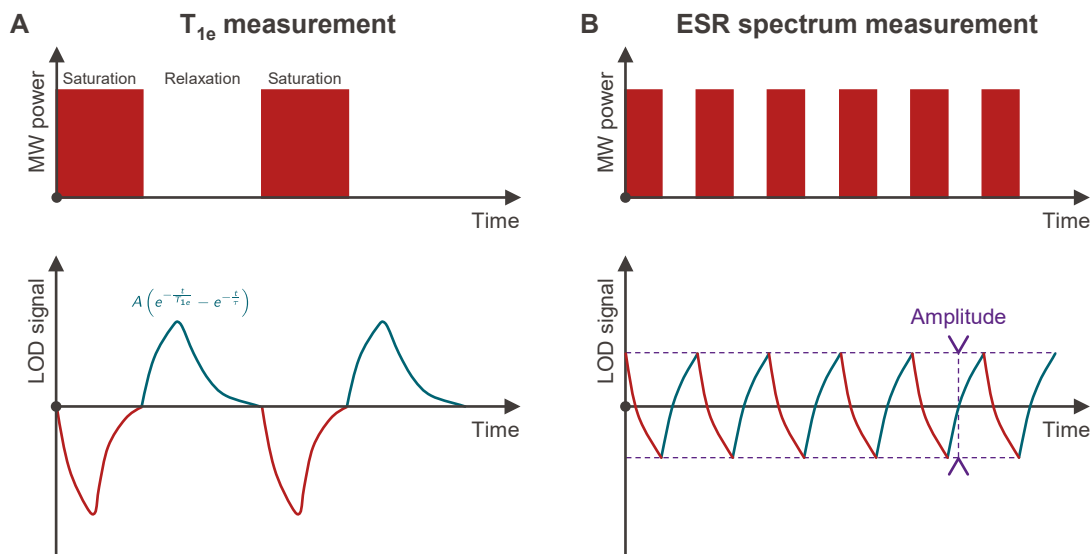


Figure 4.6: Schematic representation of the LOD-ESR signal evolution. **(A)** In T_{1e} measurements, the microwave power modulation rate is slow enough to record the full time evolution of the electron spins during both saturation and relaxation. **(B)** The microwave power is modulated at a higher rate to make the LOD-ESR signal oscillate. The steady-state amplitude is related to the proportion of spin packets resonating at a given microwave frequency.

4.3.3.2 Estimation of cryogenic performance

To compare the cryogenic performance of the two DNP probes, the liquid helium hold time was measured at routinely used DNP conditions, i.e. sample space cooled down to 1.15 K with a sample inside subjected to microwave irradiation. Before each measurement, the polarizer was operated for at least half a day to cooldown the radiation shields of the cryostat to 200 K (outer shield) and 100 K (inner shield). Then, a DNP sample was inserted, the helium was filled to the maximum capacity of the polarizer (550 mm above the sample location, approx. 1300 mL of usable liquid helium). The hold-time measurement started, after filling liquid He, once the vacuum pumps lowered the temperature in the sample space below 1.16 K and the microwave irradiation was started at full power (60 mW). The measurement was considered concluded when the temperature into the sample space suddenly dropped below 1.12 K,

indication of no residual liquid He inside the sample space. The temperature sensor used was a ruthenium oxide (RuO₂) resistor (10 kΩ at room temperature, RX-103A, Lake Shore Cryotronics, Westerville, USA). Using the same strategy, the holding time measurements for the two probes were repeated at 4.2 K, keeping the sample space at atmospheric pressure.

4.3.3.3 A simple thermal model for heat conduction

We built a simple model for heat conduction only, to help interpreting the cryogenic performance data. The thermal conductivity κ (unit W m⁻¹ K⁻¹) relates to the facility with which heat can diffuse into a material. The Fourier's law, in its most general form, yields the quantity of heat diffusing through a unit surface during a unit of time $\frac{d\vec{q}}{dt}$ within a material subjected to a temperature gradient²⁸⁷ $\vec{\nabla}T$:

$$\frac{d\vec{q}}{dt} = -\kappa\vec{\nabla}T \quad (4.2)$$

If the cross section A of the material is constant across its length L , then the problem can be simplified to 1-dimension, and the heat flowing across 2 surfaces distant dx per unit time writes.

$$\frac{dQ}{dt}dx = -A\kappa\frac{dT}{dx} \quad (4.3)$$

With $\frac{dQ}{dt} = -A\kappa\frac{dq}{dt}$. Considering that the thermal conductivity can be temperature dependent and that the ends temperatures, T_{high} and T_{low} are constant, we finally obtain the expression for the power transmitted across the material:

$$\frac{dQ}{dt} = -\frac{A}{L} \int_{T_{\text{high}}}^{T_{\text{low}}} \kappa(T) dT \quad (4.4)$$

To evaluate the difference in heat conduction between the two DNP probes, equation 4.4 was numerically integratedⁱ using MATLAB (MathWorks, Natick, Massachusetts, USA). For all calculations, T_{high} and T_{low} were set to 295 K and 1.15 K, respectively; the cross section of each component was calculated according to the geometry (Table 4.1). The temperature dependent thermal conductivity for the different materials was obtained interpolating data tables from^{287,289}. Since the transported heat per unit time depends on the length of the conductor, the calculation for each component was ran for 2 values of L : 1200 mm (distance

ⁱMATLAB code provided in Supplementary data of Lê et al.²⁸⁸.

Chapter 4. Design and performance of a fluid path compatible dDNP/LOD-ESR probe

between the cryostat isocenter and the ISO-KF 40 flange and corresponding to an almost empty cryostat) and 1200–550 mm (corresponding to a full cryostat).

Table 4.1: Specifications of the dDNP probe components used in the heat conduction simulations.

Component name	Quantity	Material	OD (mm)	ID (mm)	Cross sec. (mm ²)	Heat cond. (mW)	Heat cond. (%)
Mounting rod	3	Stainless steel 316L	3.0	0.0	7.07	52.9	71.6
Wave guide	1	Stainless steel 316L	6.0	5.6	3.64	9.1	12.3
Sample stick	1	Fiber glass	16.0	14.0	47.12	4.3	5.8
Coax cable shield	1	Stainless steel 304L	3.6	3.0	3.11	7.7	10.4
Old probe	6	Miscellaneous				73.9	100

Component name	Quantity	Material	OD (mm)	ID (mm)	Cross sec. (mm ²)	Heat cond. (mW)	Heat cond. (%)
Loading tube	1	Stainless steel 316L	13.0	12.0	19.63	48.90	82.7
Wave guide	1	Stainless steel 316L	5.0	4.6	3.01	7.50	12.6
CFP outer capillary	1	PEEK	3.2	2.4	3.52	0.11	0.2
CFP inner capillary	1	PEEK	1.8	1.6	0.53	0.02	0.0
Coax cable shield	1	Stainless steel 304L	3.2	3.0	0.97	2.50	4.2
New probe	5	Miscellaneous				59.1	100

4.3.4 DNP of [1-¹³C] pyruvate

4.3.4.1 Sample preparation

For all measurements with HP [1-¹³C] pyruvate, the samples were [1-¹³C] pyruvic acid (Sigma Aldrich, Buchs, Switzerland) doped with 15 mM of AH111501 trityl radical (Albeda Research, Copenhagen, Denmark). LOD-ESR experiments were performed on 100 μ L samples (full cup), while DNP experiments were performed on 5 μ L samples as this provided ample signal for liquid-state measurements and reduces the consumption of expensive chemicals and polarizing agents. Samples were prepared fresh before each experiment.

4.3.4.2 Solid-state DNP measurements

Solid-state DNP performance was investigated for the two probes in separate experiments. In both cases, 5 μ L of sample was loaded inside the sample cup/vial together with NaOH at stoichiometric ratio (7.2 μ L of 10 M NaOH in H₂O) to neutralize the pyruvic acid upon dissolution.

A Cameleon 3 NMR spectrometer (RS2D, Mundolsheim, France) coupled to a 100 W RF amplifier (5-200 MHz, BT00100-Gamma, Tomco, Stepney, Australia) was used with both probes to monitor the solid-state NMR signal.

Firstly, a microwave frequency sweep from 139.8 to 140.0 GHz, in steps of 10 MHz, was performed to measure the DNP enhancement profile of the sample and determine optimal irradiation condition ($n = 1$). For each frequency step, the sample was hyperpolarized with 55 mW microwave power and the NMR signal was acquired with a 30° hard pulse after 10 min. Before each polarization interval, microwaves were switched off and the polarization destroyed with $1000 \times 10^\circ$ hard pulses.

Secondly, working at 139.86 GHz, a microwave power sweep was performed to investigate power density differences between both probes ($n = 1$). The power was increased from 1 mW to 3 mW in steps of 1 mW, from 5 mW to 60 mW in steps of 5 mW and a final step at 63 mW which is the maximal power output at this frequency.

Finally, at optimal DNP condition (i.e. 55 mW and 139.86 GHz for the new probe, and 63 mW and 139.86 GHz for the old one), the samples were hyperpolarized and monitored with a hard 5° pulse every 120 s to measure the buildup curves ($n = 3$). The experiments lasted from 3 to 3.5 h, more than three times the buildup time constant (i.e. at least 95% of the polarization plateau, result of a mono-exponential curve fit).

To assess the NMR sensitivity, the signal-to-noise ratio (SNR) in the last 20 min (10 data points) was averaged and normalized to the sample volume.

Maximum solid-state polarization was back calculated from the liquid-state value assuming a pyruvate low field T_1 of 60 s and a time interval between the end of the dissolution and beginning of the liquid-state acquisition of 7 s for the original probe and 8.5 s for the new one (see next paragraph).

4.3.4.3 Liquid-state polarization measurements

After shining microwaves at optimal conditions for as long as 3 buildup time constants, each sample was dissolved and transferred to a 14.1T/26cm horizontal bore magnet (Magnex Scientific, Oxford, United Kingdom), interfaced to a BioSpec Avance NEO spectrometer (Bruker BioSpin, Ettlingen, Germany) to measure its liquid-state polarization and relaxation time. To dissolve the samples, 5.5 mL of buffer solution (40 mM tris(hydroxymethyl)aminomethane (TRIS) and 0.3 mM ethylenediaminetetraacetic acid (EDTA) in D_2O balanced to pD = 7.6) was heated to 170–180 °C (12 bar of vapor pressure) and pushed with helium gas over a 6 m long, 2.0/3.0 mm ID/OD PTFE tube into a separator/infusion pump¹⁸⁸ placed in the isocenter of the horizontal magnet.

Prior to release the superheated buffer, for the old DNP probe, the dissolution procedure entailed to repressurize the sample space, to remove the waveguide, to lift the sample stick in

order to raise the sample cup above the liquid He level, and finally to insert the dissolution wand to be docked on top of the sample cup¹⁸⁸.

For the new DNP probe, the “dissolution head” was removed from the dissolution wand and placed at a fixed position on top of the polarizer (Appendix A.2). In this case, the dissolution procedure simply entailed to pull the CFP upwards by 10 cm and connect it to the dissolution headⁱ.

Using the dissolution stick, the liquid was pushed during 3.5 s with a pressure of 6.0 bar, while the CFP required 5.0 s and 9.0 bar due to the higher flow resistance due to the smaller inner capillary.

After the transfer, the (2.5 ± 0.2) mL of HP solution was left to settle for 3.5 s inside the separator/infusion pump. Then the ^{13}C NMR signal was acquired with 10° hard pulses every 3 s for 60 times using a solenoid coil^{187,206}. The decay of the HP NMR signal was fitted with a mono-exponential function to determine the ^{13}C T_1 at 14.1 T.

To measure the thermal equilibrium signal, 5 μL of 0.5 M Gd-DO3A-butrol (Gadobutrol, Gadovist, Bayer) was added to the solution collected inside the separator/infusion pump, achieving a 1 mM concentration to shorten the spin-lattice relaxation time T_1 while negligibly affecting the spin-spin relaxation time T_2 . The thermal NMR signal was acquired with 10° hard pulses, TR = 5 s and 1024 averages. The liquid-state DNP enhancement was calculated from the ratio between the HP and thermal NMR signals ($n = 3$ for each probe).

4.3.4.4 Characterization of [1- ^{13}C] pyruvate T_1

A solution of 100 mM sodium [1- ^{13}C] pyruvate in a 40 mM TRIS and 0.3 mM EDTA buffer solution in D_2O was prepared, and the pD was adjusted to 7.6. Measurements of the longitudinal relaxation time of the labeled carbon was performed as a function of the temperature between 20 and 50 $^\circ\text{C}$ with an inversion-recovery sequence on a Bruker Avance III HD 600 MHz (14.1 T) NMR spectrometer with a 5 mm CryoProbe Prodigy BBO.

4.3.5 Optimization of [1- ^{13}C] lactate DNP sample formulation

4.3.5.1 Sample preparation

A stock solution with 4.4 M sodium [1- ^{13}C] lactate (Sigma Aldrich, Buchs, Switzerland) and 20 mM OX063 trityl radical (Albeda Research, Copenhagen, Denmark) in H_2O :glycerol (1:1,

ⁱVideos attached as Supplementary Material in Lê et al.²⁸⁸.

v:v) was prepared. It was then split into five aliquots doped with Gd-DO3A-butrol (Gadobutrol, Gadovist®, Bayer) to a final concentration of 0.0, 0.5, 1.0, 2.0 and 4.0 mM.

4.3.5.2 Solid-state characterization

The lactate samples with increasing gadolinium doping were characterized with LOD-ESR to measure their respective T_{1e} and ESR spectrum.

Each ESR spectrum was acquired with 201 frequency steps from 139.75 to 140.00 GHz. The microwave power was modulated using a 4.8 Hz square wave between 0 and 35 mW. This value takes the insertion loss of the voltage-controlled attenuator into account. The signal was processed by a digital lock-in in LabVIEW (National Instruments, Austin, USA) as described above. At each frequency step, the measurement was let to stabilize for 10 s, before averaging the amplitude of the demodulated signal during 20 s.

T_{1e} measurements were performed with the microwave source set to 139.87 GHz and 35 mW. The attenuator was left open during 2 s to saturate a certain portion of the ESR spectrum. After closing the attenuator, the signal evolution across the detection coil induced by the electron spins was measured during 6 s. This procedure was repeated for 256 averages.

Microwave frequency sweeps were performed every 10 MHz from 139.75 to 140.00 GHz (26 steps) similarly to description in Section 4.3.4.2 to determine the DNP enhancement profile of each sample. In a brief, for each frequency step, the sample was hyperpolarized during 10 min with 55 mW microwave power, after which the NMR signal was acquired with a 30° hard pulse, then destroyed with a thousand 10° hard pulses.

4.3.5.3 Liquid-state polarization measurements

The lactate samples with 0.0 mM and 1.0 mM of Gd-DO3A-butrol were hyperpolarized during 3 h with 60 mW microwave power at the optimal frequencies determined in the sweeps, the positive peak at 139.84 GHz and negative peak at 139.92 GHz for the 0.0 and 1.0 mM samples, respectively. The buildup of the solid-state NMR signal was measured every 120 s with a 2.5° hard pulse. The samples were then dissolved in 5.5 mL superheated D₂O and transferred to the 14.1T MRI scanner to measure their liquid-state polarization as described in Section 4.3.4.2. 8.5 s after dissolution, the hyperpolarized signal was acquired every 3 s with a 10° hard pulse until 180 s. The decay of the HP NMR signal was fitted with a mono-exponential function to determine the liquid-state T_1 of [1-¹³C] lactate at 14.1 T.

To measure the thermal equilibrium signal, 5 μL of 0.5 M Gd-DO3A-butrol was added to the (2.5 ± 0.2) mL solution collected inside the separator/infusion pump to reduce the ¹³C

longitudinal relaxation time of lactate. The thermal NMR signal was acquired with the same pulse 10° hard pulses, $TR = 5$ s and 1024 averages. The liquid-state DNP enhancement was calculated from the ratio between the HP and thermal NMR signals ($n = 3$ for each sample composition).

4.3.6 Statistical analysis

For each comparison metric, a one-way analysis of variance (ANOVA) in OriginPro 2019b (OriginLab, Northampton, USA) was used to compare the statistical difference between means. A p -value below 0.05 was considered significant. All values are expressed as mean \pm standard deviation.

4.4 Results and discussion

4.4.1 Cryogenic performance

Figure 4.7A shows the polarizer's holding time when equipped with the original DNP probe (blue line) and the new one (red line). While the old design allows to keep the sample immersed in liquid He for 4 h, the CFP design prolongs this time to 5.5 h, providing a 37.5% improvement. An increased holding time is very advantageous when long acquisitions are required (e.g. measurement of a DNP spectrum), especially for polarizers not equipped with an automatic He filling system.

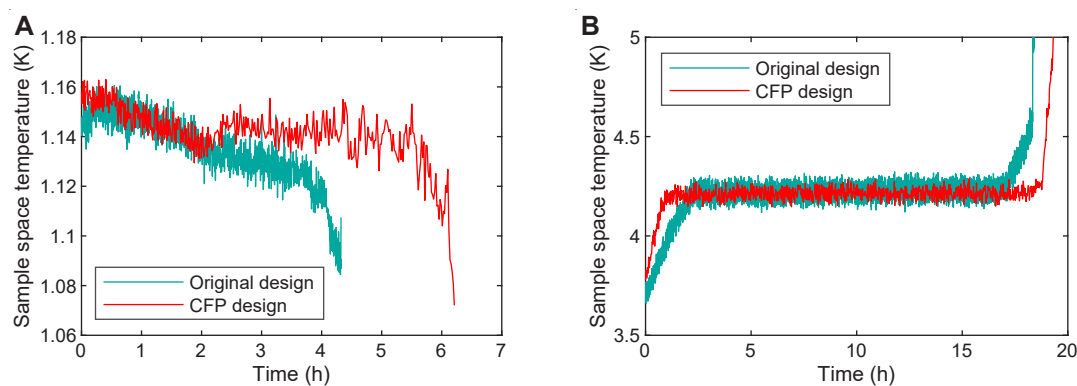


Figure 4.7: Temperature evolution as a function of time of the polarizer sample space when equipped with the original DNP probe (blue line) and the CFP compatible one (red line) at **(A)** 1.15 K and **(B)** 4.2 K.

In both cases, the temperature decreases slightly as a function of time because the sample space pressure, and thus the temperature, is affected by the liquid He level inside the cryostat. Less He means less boil off, therefore a lower achievable pressure for a given pumping power.

The sudden temperature drop at the end of the measurement is caused by the absence of liquid He in the cryostat. The latter is followed by a transitory drastic reduction of the pressure. Right after, the temperature rises (data not shown). Provided that the cryostat can be filled with maximum 1300 mL of liquid He, the original design boils off on average 325 mLh^{-1} , while the CFP compatible one only 236 mLh^{-1} . Therefore, the original design has a liquid He consumption excess of 89 mLh^{-1} .

Although our model for conduction accounts for a 25% difference in heat transfer (Figure 4.8, see also Table 4.1 and simulation code in Lê et al.²⁸⁸), this can only partially justify the prolonged holding time at 1.15 K of the new DNP probe. The original design transfers heat at a rate of 0.136 Js^{-1} , while the CFP compatible one at 0.109 Js^{-1} . The rate difference of 0.027 Js^{-1} decreases to 0.015 Js^{-1} when the cryostat is almost empty. Assuming an average consumption of 0.021 Js^{-1} , this means that the original design every hour transfers 76 J more than the new one. Therefore, only because of heat conduction, being the liquid He latent heat 21 kJ kg^{-1} and liquid He density 0.125 kgL^{-1} , the original probe boils off 30 mL of He more per hour than the CFP compatible one. This is a third of the value experimentally measured.

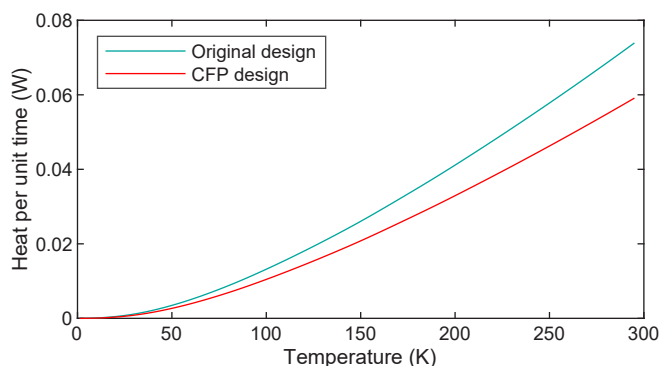


Figure 4.8: Calculation of heat transfer due to conduction for the original DNP probe (blue line) and the CFP compatible one (red line) when the cryostat is almost empty. The heat conduction difference between the two probes is 25%.

An explanation could be that the two designs establish different convective pathways for the boiled off He gas. In general, a laminar flow for the evaporated gas is favorable to reduce heat transfer via convection²⁹⁰. This is most likely what happens inside the new probe 12 mm ID loading tube. Differently, the original design, because of the removable waveguide and sample stick, is characterized by discontinuities in the surface of the radiation shields. These discontinuities can create turbulences in the flow of He gas and thus increased heat transfer via convection. This explanation is confirmed by the cryostat holding time measured at 4.2K. At these conditions where the He boil off is less severe, the original DNP probe design allowed to keep the cryostat at 4.2 K for 15 h, while the new design for 18 h (Figure 4.7B). This 20% improvement is close to what we calculated in our heat conduction model.

In the analysis above we assumed a constant liquid He evaporation rate for the two probes. Nevertheless, looking at Figure 4.7, this is true only when the old probe is inside the cryostat. In that case, the latter boils off He at a rate of 325 mLh^{-1} , during the 4 h of holding time. Differently, when the CFP compatible probe is inside, the cryostat shows the same consumption rate for the first 2 h, and a decreased rate of 189 mLh^{-1} for the remaining 3.5 h. The rate change happens when the liquid He level drops below the 4th baffle (half of the full capacity), counting from the top (see Figure 4.4). The heat conduction through the probe can justify only part of the boil-off rate. According to the simulations, this contribution ranges from 194 mLh^{-1} to 105 mLh^{-1} for the old probe, and from 155 mLh^{-1} to 84 mLh^{-1} for the new one, depending on the He level.

The other contributions come from heat conduction through the VTI and the inner wall of the cryostat, convection of the boiled off He, and radiation. A quantitative analysis of the sum of these phenomena is beyond the scope of this work. Qualitatively, we can imagine that when the He level drops, the other phenomena are attenuated, and the less efficient heat conduction of the new probe becomes more relevant. Most likely, being the last three baffles closer than the first three baffles, convection pathways are “broken” when the liquid He level drops below the 4th baffle.

In addition to the longer holding time to each He filling, the fact that the CFP compatible probe allows to exchange samples without repressurizing the polarizer sample space further reduces the He consumption during repeated experiments. Working at the system maximum capability, these improvements together allowed to save approximately 20 L of liquid He per week.

4.4.2 DNP spectrum and LOD-ESR results

In Figure 4.9A we report the ^{13}C DNP spectrum of the sample (blue dots). $[1-^{13}\text{C}]$ pyruvic acid doped with 20 mM of AH111501 trityl achieves its maximum polarization for a microwave frequency value of 139.86 GHz. The positive maximum DNP enhancement is slightly higher than the negative one, as already reported in previous studies for a similar sample without addition of Gd^{3+} compounds^{162,192,266}.

The DNP spectrum nicely overlaps with the LOD-ESR one, entailing that the DNP mechanism behind is thermal mixing and/or cross effect^{145,146,291,292}. The latter rely on triple spin flips of one ^{13}C and two electron spins separated in energy by one nuclear Larmor frequency. Therefore, DNP can happen only for microwave frequencies where electron spins resonate. Microwave frequency modulation did not yield any further improvement implying that the spin system is optimal for direct DNP. Indeed, a trityl $T_{1e} = (651 \pm 10) \text{ ms}$ is long enough, with

respect to spectral diffusion, for efficient saturation of the ESR line by using monochromatic irradiation²⁹³.

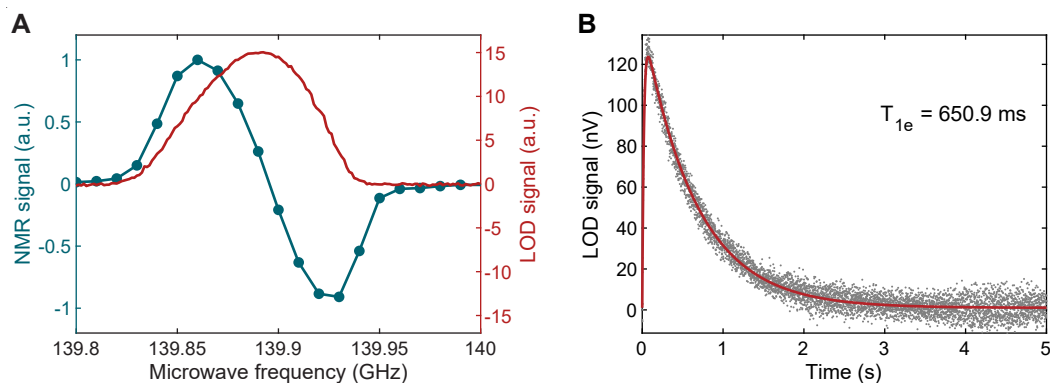


Figure 4.9: [^{13}C] pyruvic acid NMR signal as a function of the microwave frequency (blue dots with eye-guiding line) superimposed to trityl AH111501 LOD-ESR spectrum (red line) both measured at 1.15 K and 5 T; vertical axis according to color (A). Evolution of the radical signal as a function of time after switching off the microwaves (gray dots); the data were fitted as explained in Methods to extract the electron T_{1e} (red line) (B).

4.4.3 Solid-state polarization and microwave power density

Replacing the original probe with the CFP compatible one has a strong effect on the DNP performance (Figure 4.10). The back calculated solid-state polarization value increases by a factor 1.52 from $(24.6 \pm 3.0)\%$ to $(38.3 \pm 1.9)\%$. This value is in good agreement with the maximum achievable polarization (approx. 55%) that the same sample can achieve on a 5 T SPINlab, considering the different working temperature of the two machines (0.80 K vs 1.15 K).

The volume normalized SNR improved by a factor 1.45 (Figure 4.10C). Therefore, within the experimental errors, the NMR sensitivity of the two probes remains the same, despite the less efficient impedance matching scheme (i.e. remote tuning and matching network) of the new probe compared to the original one (i.e. local tuning and matching network)^{188,206}. This behavior is due to the superior filling factor of the pseudo-Alderman-Grant coil (800 μL volume) compared to the original saddle coil (3800 μL), that must accommodate the 16 mm wide sample stick. Moreover, a remote tuning and matching network is more versatile when multinuclear capability is required, being the cryogenic part of the probe the same.

The buildup time constant decreased by a factor 1.42 from (3920 ± 297) s to (2745 ± 63) s, with a standard deviation smaller by a factor 5 (Figure 4.10D). Most likely, the latter is due to the fixed microwave source-waveguide assembly that characterizes the new DNP probe that is not disconnected/reconnected at each dissolution/new sample loading.

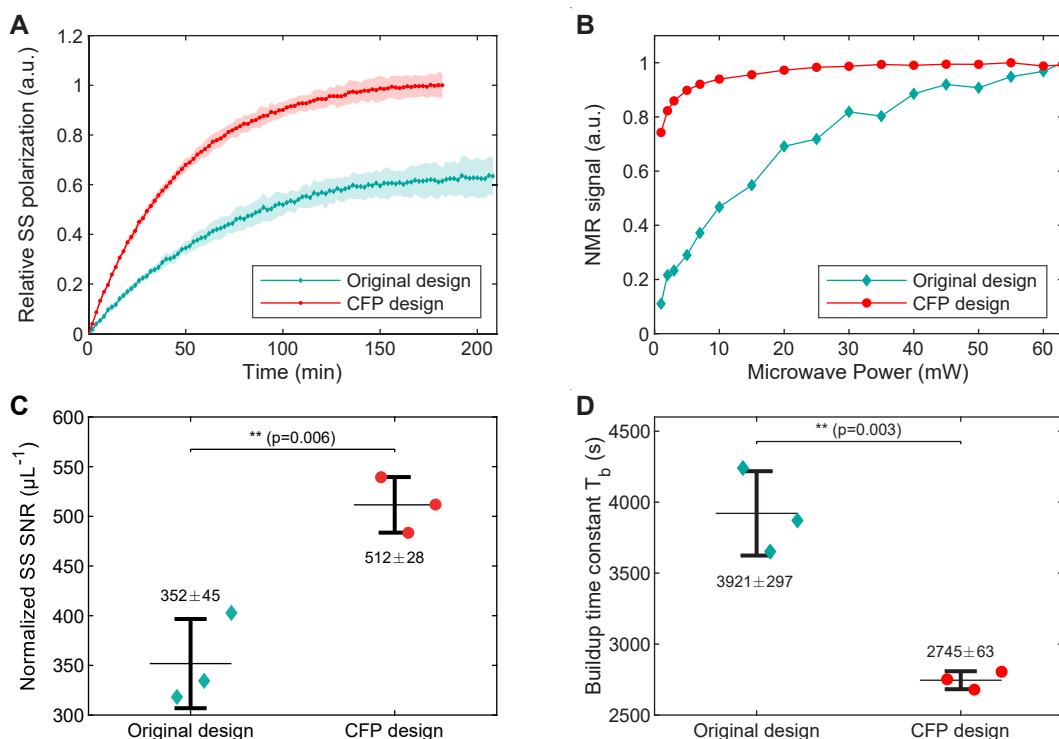


Figure 4.10: Example of ^{13}C DNP solid-state build measured when shining microwaves at best conditions with original probe (blue diamonds) and the new probe (red circles); on both curves, the lighter-colored areas represent the error measured as standard deviation of three measurements. The signal intensity was normalized with respect to the highest value; the two plateaus correspond to back calculated values of $(24.6 \pm 3.0)\%$ to $(38.3 \pm 1.9)\%$ for the old and new design, respectively ($n = 3$ for each case) (A). ^{13}C DNP microwave power sweep measured at 139.86 GHz when using the original probe (blue diamonds) and the new one (red dots); the lines connecting the data points help guiding the eyes (B). Sample volume normalized SNR measured in correspondence of the polarization plateau ($n = 3$) for the original probe (blue diamonds) and the new probe (red dots); the mean, standard deviation and p -value are reported (C). Buildup time constant resulting from the fit of polarization curves ($n = 3$) for the original probe (blue diamonds) and the new probe (red dots); the mean, standard deviation and p -value are reported (D).

The superior polarization speed and level are a consequence of the higher microwave power density at the sample position in the new probe. Indeed, the reduced size of the microwave cavity (13.2 cm^3 vs 23.4 cm^3) allows to achieve maximum DNP enhancement already for a microwave power output of 25 mW with an onset of sample heating for 55 mW (Figure 4.10B). Differently, in the original probe even at maximum output power of the microwave source (e.g. 63 mW) the DNP enhancement is still growing. This behavior is usually related to insufficient microwave power and consequent poor saturation of the radical ESR line^{293,294}.

We would like to specify that we did not attempt to measure the sample ^{13}C NMR signal at thermal equilibrium at 5 T and 1.15 K. When trityl radical is involved, the $[1-^{13}\text{C}]$ pyruvic acid T_1 value is several tens of hour, implying that one duly performed measurement would run over 2 or 3 days. This is costly and inconvenient in the absence of an automatic liquid He filling system. The polarization values in the solid-state were back calculated from the liquid-state ones (see Methods).

4.4.4 Dissolution and liquid-state polarization

After dissolution and transfer, the measured liquid-state $[1-^{13}\text{C}]$ pyruvic acid polarization increased from $(21.9 \pm 2.7)\%$ to $(33.3 \pm 1.6)\%$, when using the CFP compatible probe (Figure 4.11A-B). Despite the final ^{13}C concentration being the same (i.e. 20 mM), the T_1 increases from $(42.0 \pm 0.5) \text{ s}$ to $(46.7 \pm 1.7) \text{ s}$, when dissolving the sample from the new probe (Figure 4.11C). We ascribe this behavior to a temperature effect. From T_1 inversion recovery measurements at 14.1 T of a sodium $[1-^{13}\text{C}]$ pyruvate solution, we estimated that the relaxation time evolves as a function of the temperature T as $T_1(T) = (0.877 \cdot T + 21.4) \text{ s}$ between 20 and 50°C (Figure 4.12). As the temperature increases, the correlation time for rotational motion is shortened which reduces the relaxivity caused by intermolecular dipolar relaxation of small molecules²⁹⁵.

Therefore, we estimate that, at the time of acquisition, the hyperpolarized solution obtained using the original probe has a temperature of 23.5°C , while the one using the CFP probe has a temperature of 28.8°C . These temperature values are in good agreement with the reading of a T-type (copper/constantan) thermocouple placed inside the separator/infusion pump used to collect the hyperpolarized solution inside the bore of the MRI scanner.

Finally, it is worth stressing the fact that using a CFP dissolution system simplifies this procedure and makes it less user dependent, because it avoids any repressurization and subsequent opening of the polarizer sample space to the room environment.

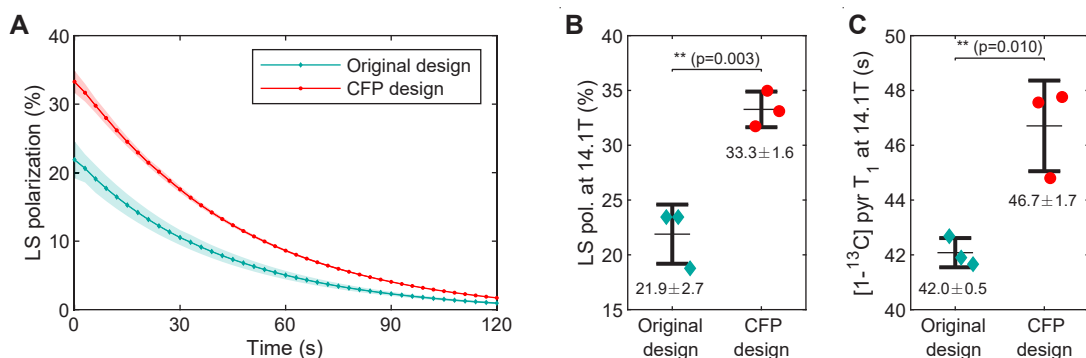


Figure 4.11: Example of hyperpolarized $[1-^{13}\text{C}]$ pyruvate relaxation curve measured in the 14.1T horizontal MRI scanner after dissolution from the original probe (blue diamonds) and the new probe (red circles) after dissolution (A). Repeated measurements ($n = 3$) for $[1-^{13}\text{C}]$ pyruvic acid liquid-state polarization after dissolution and pH neutralization from the original probe (blue diamonds) and the new probe (red dots); the mean, standard deviation and p -value are reported (B). Repeated measurements ($n = 3$) for $[1-^{13}\text{C}]$ pyruvate liquid-state T_1 after dissolution and pH neutralization from the original probe (blue diamonds) and the new probe (red dots); the mean, standard deviation and p -value are reported (C).

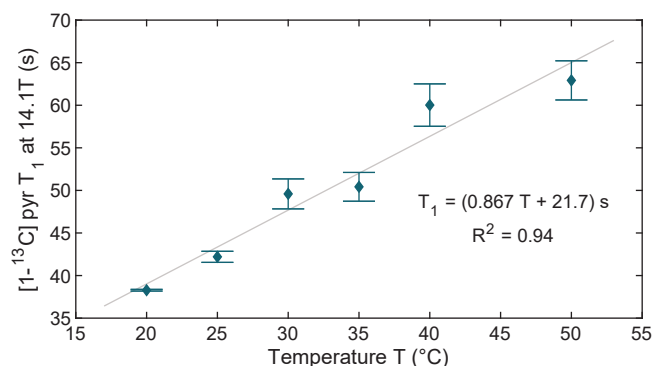


Figure 4.12: T_1 measurements as a function of temperature at 14.1 T for 100 mM sodium $[1-^{13}\text{C}]$ pyruvate in a 40 mM TRIS buffer solution in D_2O adjusted to $\text{pD} = 7.6$. The gray line is the linear fit of the measured data points.

4.4.5 Characterization and optimization of [1-¹³C] lactate DNP samples

[1-¹³C] lactate trityl samples in a water-glycerol matrix were characterized at different gadolinium doping concentrations (Figure 4.13), and the measured properties are summarized in Table 4.2.

A long T_{1e} of 2001 ms was observed in the sample without gadolinium, which resulted in a weak LOD signal (Figure 4.13A). With increasing gadolinium concentration, a faster radical relaxation as well as a narrower ESR linewidth down to 50 MHz were observed (Figure 4.13A-B). Although the exact reasons for the latter are unclear, a contributing factor could be the less efficient ESR saturation at the spectrum edges due to the shorter T_{1e} causing more inefficient spectral diffusion¹⁶². As briefly discussed in Section 1.4.4.3, the moderate T_{1e} and ESR linewidth reduction can lead to a better DNP enhancement. The DNP enhancement profile narrows with increasing gadolinium doping, and one can observe that only the undoped sample shows a higher DNP enhancement on the positive peak, whereas all gadolinium-doped samples were polarizing better on the negative peak (Figure 4.13C), similarly to previous reports^{162,266}.

Table 4.2: Solid-state parameters measured at increasing Gd-DO3A-butrol concentrations in a sample with 4.4 M sodium [1-¹³C] lactate and 20 mM OX063 in H₂O:glycerol (1:1, v:v) at 5 T and 1.15 K.

[Gd-DO3A-butrol] (mM)	T_{1e} (ms)	ESR FWHM (MHz)	DNP maxima delta (MHz)	ϵ_+/ϵ_-
0.0	2001	123.0	90	1.128
0.5	639	65.0	70	0.995
1.0	392	58.8	70	0.932
2.0	232	51.3	50	0.952
4.0	135	48.8	50	0.806

With 0.5 mM Gd-DO3A-butrol, the T_{1e} was reduced from 2001 to 639 ms, which is comparable to the [1-¹³C] pyruvic acid trityl sample previously measured (Figure 4.9B). Increasing the gadolinium doping to 1.0 mM decreases the T_{1e} of 392 ms, which is close to the optimal value previously reported¹⁶² for ¹³C samples in a water-glycerol matrix at 7 T and 1.2 K. This was therefore selected for the liquid-state polarization measurements.

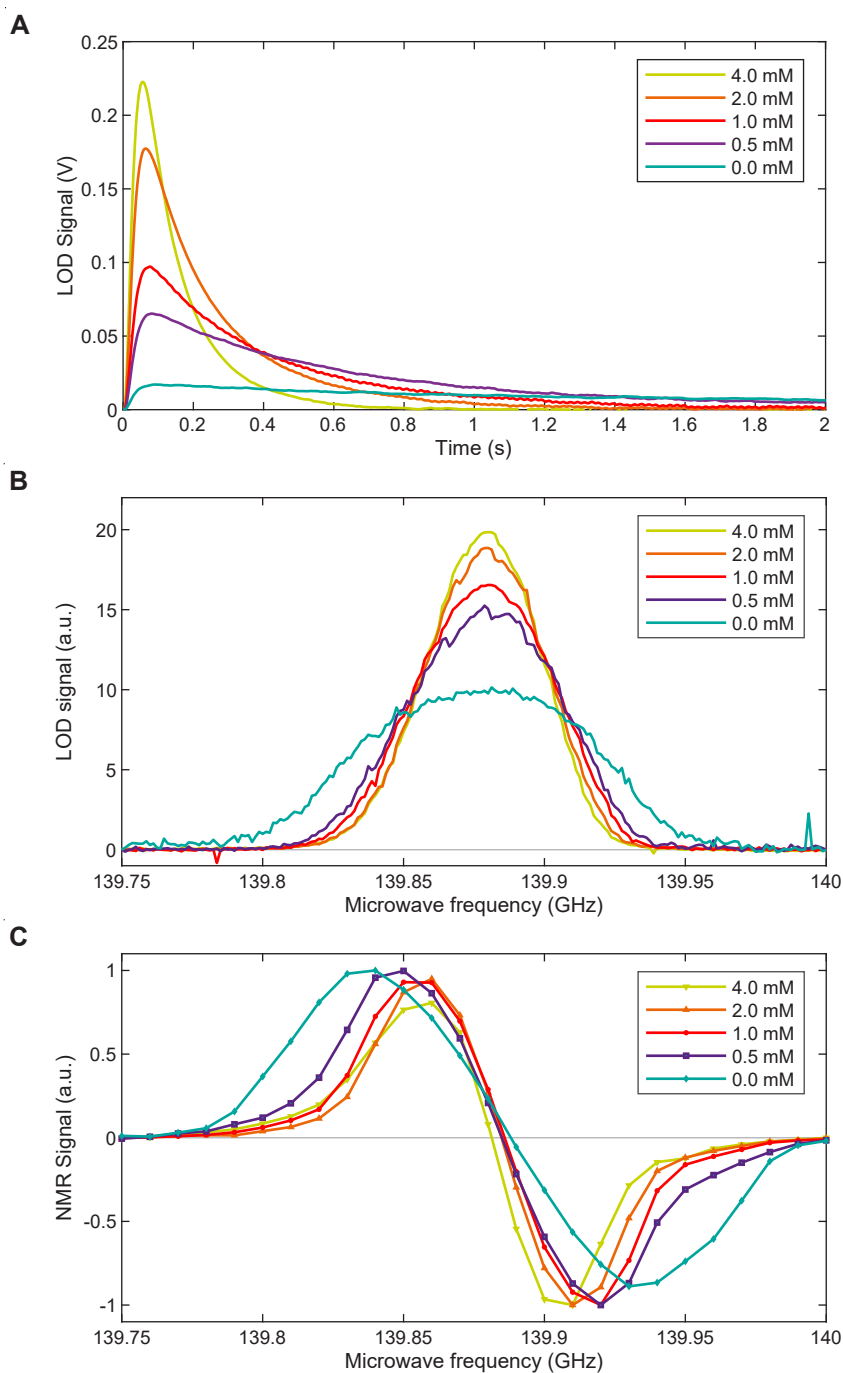


Figure 4.13: Effect of adding Gd-DO3A-butrol to a 4.4 M sodium [$1-^{13}\text{C}$] lactate sample in H_2O :glycerol (1:1, v:v) doped with 20 mM OX063 radical, at 5 T and 1.15 K. **(A)** T_{1e} measurements. The voltage is scaled to the value measured after the 106 dB differential amplifier. **(B)** ESR spectra with integral value normalized to 1. **(C)** DNP microwave sweeps. The largest signal of each curve is normalized to 1.

[1- ^{13}C] lactate DNP samples with 0 mM and 1 mM Gd-DO3A-butrol were hyperpolarized at 5T/1.15K. The lactate sample with 1 mM Gd-DO3A-butrol achieved faster and higher polarization (Figure 4.14A), with a longer buildup time constant by 28% (Figure 4.14B).

Gadolinium doping provided a higher liquid-state polarization of (27.0 ± 1.7)% compared to (10.9 ± 1.8)% at baseline (Figure 4.15B). After dissolution, the gadolinium was sufficiently diluted to avoid affecting the solution state T_1 of lactate (Figure 4.15C). The back-calculated solid-state polarization at the time of dissolution were (12.6 ± 2.1)% and (31.1 ± 2.0)% for the baseline and optimized samples, respectively, assuming a low-field relaxation time of 60 s.

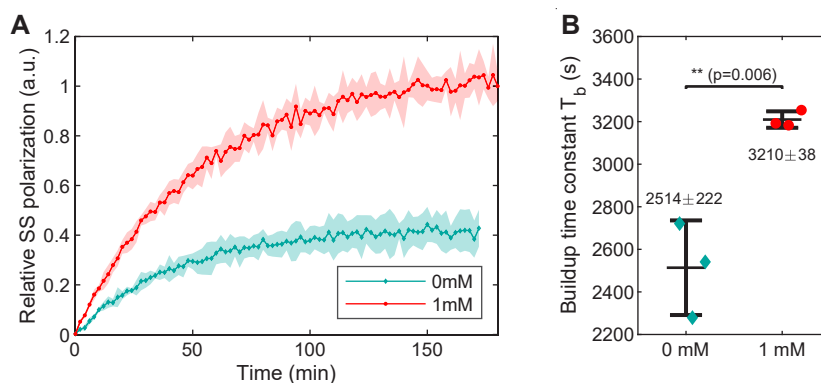


Figure 4.14: (A) Solid-state NMR buildup signal of 4.4 M sodium [1- ^{13}C] lactate and 20 mM OX063 in H_2O :glycerol (1:1, v:v) with either 0 mM or 1 mM of Gd-DO3A-butrol. The buildup curve of each sample was rescaled to the liquid-state polarization, assuming negligible dissolution and transfer losses. The data points depict the average polarization buildup from three separate experiments, while the shaded area represents the standard deviation. (B) Buildup time constants deduced by a mono-exponential fit of the SS NMR signal evolution.

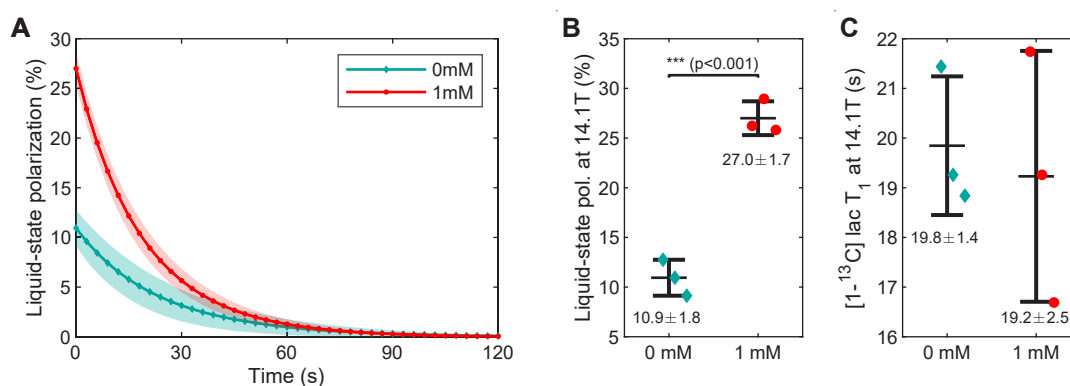


Figure 4.15: (A) Decay of the liquid-state polarization of sodium [1- ^{13}C] lactate at 14.1 T following dissolution and transfer, for the samples with either 0 mM or 1 mM of Gd-DO3A-butrol. The data points are the average of three experiments while the shaded area depicts the standard deviation across them (B) Initial liquid-state polarization of both [1- ^{13}C] lactate samples. (C) Liquid-state ^{13}C T_1 of the hyperpolarized lactate solutions at 14.1 T.

4.5 Conclusion

In this chapter we retrofitted a 5 T “wet” DNP polarizer. We designed, built, and tested a new DNP probe compatible with the fluid path technology. The new design allowed to increase the liquid He holding time on a single experiment from 4 h to 5.5 h and to save 20 L of liquid He during a working week. The CFP, being a sample holder and a dissolution system at the same time, allowed to reduce the size of the microwave cavity. The increased microwave power density at the sample site improved the maximum achievable DNP enhancement and buildup rate constant by a factor of 1.5. This yielded, at the time of acquisition, a liquid state polarization as high as 33% on [1-¹³C] pyruvic acid doped with trityl.

Furthermore, the new probe can also accommodate a LOD-ESR probe for investigating the radical properties at real DNP conditions with no need to modify or replace any part of the NMR hardware. Guided by in-situ LOD-ESR, the sample formulation for [1-¹³C] lactate was optimized through gadolinium doping^{162,163,266} to increase the liquid-state polarization by a factor of 2.5.

In overall, this upgrade provides a precious sensitivity boost for our next *in vivo* acquisitions. The design can be implemented to most “wet” DNP polarizers, by adapting the sample tube length, and the flange/baffles diameter to the specific cryostat. Finally, it adds relevant measurement capabilities to enable deeper investigations of various DNP sample properties, for example to study the impact of different solvents on the ESR properties for ¹²⁹Xe DNP at 5 T²⁹⁶, or to assess the influence of glassing matrix deuteration on ⁶Li DNP samples at 7 T²⁹⁷. Deeper insights into the ESR properties, in particular about spectral diffusion, could be achieved by adding a second microwave source and waveguide on the empty quadrant of the probe to enable pump-probe electron-electron double resonance (ELDOR) experiments.

5 Highly versatile dDNP: implementation of a multi-sample/multi-nucleus cryogenic probe with parallel NMR detection

5.1 Abstract

Low throughput is one of dDNP main shortcomings. Especially for clinical and preclinical applications, where direct ^{13}C nuclei polarization is usually pursued, it takes hours to generate one single hyperpolarized (HP) sample. Therefore, being able to hyperpolarize more samples at once represents a clear advantage and can expand the range and complexity of the applications.

In this chapter, we present the design and performance of a highly versatile and customizable dDNP cryogenic probe, herein adapted to a 5 T “wet” preclinical polarizer, that can not only accommodate up to three samples at once, but it is also capable of monitoring the solid-state spin dynamics of each sample separately, regardless of the kind of radical used and the nuclear species of interest. Within 30 min, the system was able to dispense three HP solutions with high repeatability across the channels ($(30.0 \pm 1.2)\%$ carbon polarization for $[1-^{13}\text{C}]$ pyruvic acid doped with trityl radical). Moreover, we tested multi-nucleus NMR capability by polarizing and monitoring simultaneously ^{13}C , ^1H and ^{129}Xe . Finally, we implemented simultaneous $[1-^{13}\text{C}]$ lactate/ $[1-^{13}\text{C}]$ pyruvate polarization, and back-to-back dissolution/injection in a healthy mouse model to perform multiple-substrate HP MRS at 14.1 T.

This chapter is adapted from the following paper: **Lê Thanh Phong**, Hyacinthe Jean-Noël, Capozzi Andrea. *Multi-sample/multi-nucleus parallel polarization and monitoring enabled by a fluid path technology compatible cryogenic probe for dissolution dynamic nuclear polarization*. Scientific Reports, 13:7962, 2023. doi:10.1038/s41598-023-34958-3

This study was conceived by CA and HJN. CA and myself designed the hardware, analyzed and interpreted experimental data. I performed all experiments. All authors prepared the manuscript.

5.2 Introduction

Hyperpolarization via dDNP was invented in 2003 by Ardenkjær-Larsen et al.¹³³ to enhance, by several orders of magnitude, the NMR signal of biomolecules relevant to the investigation of fundamental physiological processes such as aberrant glycolytic metabolism in cancer tissues, fatty acids cardiac metabolism, and organs perfusion^{280,298,299}.

Although all NMR active nuclear spins can be hyperpolarized via dDNP^{135,154,202,300,301}, during the last two decades, the technique has proved itself as the most effective and versatile key of access to ¹³C MRI/S with second short time resolution²⁸⁰. The latter unleashed a new range of applications aimed at investigating several enzymatic pathways and other physiological properties in real time for preclinical^{272,298,302} and clinical studies^{141,273,275,303}.

Unfortunately, this unprecedented MR signal enhancement does not come without a price. One main shortcoming of dDNP is the low throughput it achieves. As described in Section 1.4.4, the polarization transfer from the electron spins, added to the sample in form of stable or labile radicals, to the nuclear spins is performed at a sub-liquid helium temperature and high magnetic field, by means of microwave irradiation close to the radical's ESR¹⁴². These physical conditions, needed to reach close to unity electron spin polarization, extend the buildup time of X-nuclei polarization to the range of hours.

Concurrently, applications as the study of the pharmacodynamics of an anti-cancer tracer³⁰⁴, examination of the heart metabolism after infarction³⁰⁵, multiple compounds injection for the combined investigation of physiological processes^{306–308}, are few examples that greatly benefit from the possibility to produce, inject and monitor the fate of different hyperpolarized solutions within minutes.

Cross-polarization schemes from hyperpolarized protons¹⁵² can decrease the polarization time of X-nuclei to tens of minutes. Originally, the high B_1 requirements limited the efficiency of this approach to small samples, but optimized cross-polarization RF pulse sequences^{309,310}, and coils³¹¹ could lift these limitations. Nevertheless, even if DNP can be quickly achieved, the sample turnover remains time consuming and cumbersome, particularly in the context of *in vivo* preclinical or clinical HP MR. Therefore, across the years, dDNP polarizers with multi-sample capability have been developed^{189,198}, in particular employing the Fluid Path (FP) technology^{192,194}, because of its versatility and reduced cryogenic heat load.

Usually, in dDNP “one size does not fit all”. Sample preparation and polarization conditions must be optimized for different substrates, nuclear species, and radicals. Hyperpolarizing more samples with different formulations is a non-trivial task, especially if different radicals are involved. When using radicals traditionally employed in dDNP (e.g. nitroxyl and trityl), thermal mixing or cross effect are the dominant polarization transfer mechanisms²⁸². In this

case the appearance of the DNP spectrum is strongly dependent on the ESR properties of the radical rather than the Larmor frequency of the nuclei³¹²⁻³¹⁴. If the radicals used have very different **g**-tensors, the DNP spectra for a given nucleus/radical pair can be far apart precluding the possibility to polarize simultaneously the samples.

Hence, possible advanced applications that involve the polarization of different nuclei or simply different ¹³C labelled substrates would benefit greatly from selective NMR detection.

In this chapter, we detail the design and performance of a highly versatile and customizable dDNP cryogenic probe, herein adapted to a 5T “wet” preclinical polarizer²⁸⁸, that, employing a Custom Fluid Path (CFP)^{200,315}, can not only co-polarize up to three samples, but it is also capable of monitoring the solid-state dynamic of each of them separately, thanks to dedicated pseudo-Alderman-Grant (AG) coils and multi-nucleus parallel NMR acquisition on three distinct channels. We tested the system for the generation of three HP solutions of the same substrate (i.e. [1-¹³C] pyruvic acid) within a short time interval; for the simultaneous polarization and monitoring of ¹H, ¹³C and ¹²⁹Xe; and for [1-¹³C] lactate/[1-¹³C] pyruvate polarization and back-to-back dissolution and injection in a healthy mouse model to perform multi-substrate HP MRS at 14.1 T.

5.3 Methods

5.3.1 Multi-sample DNP probe design and NMR setup

In Figure 5.1, we report 3D drawings of the multi-sample dDNP cryogenic probe adapted to our 5 T “wet” polarizer, whose design, functioning principle, retrofit and performance were described in Chapter 4. All main components are indicated by capital letters.

Inspired by the SPINlab™ seminal paper¹⁹² and the preclinical polarizer by Cheng et al.¹⁹⁴, sample handling is managed using the FP technology: the presence of a dynamic sealing and an air-lock compartment allows to keep the dDNP polarizer constantly at low pressure during loading, polarization and dissolution. This feature is crucial when working with more than one sample because it allows their individual operation. Differently, we employ CFPs that allow more flexibility in terms of reusability and nature (i.e. liquid or solid) of the compound of interest upon loading^{200,202,288,315}. The 1470 mm long cryogenic probe is built around a 316L stainless steel 3-arms manifold (**H**) composed by a 58.3/68.0 mm ID/OD tube with 3 ISO-KF16 half-nipples welded on it at a 30° angle (**G**). The manifold is hermetically closed at the top by a stainless-steel flange (**C**) pressing on two 55 × 2 mm NBR O-rings. The top flange holds the microwave inlet to the waveguide (**B**) and three hermetic SMA connectors (**D**, SF-2991-6002, Amphenol SV Microwave, West Palm Beach, USA). Each ISO-KF16 half-nipple is connected to an air-lock compartment composed by an ISO-KF16 gate valve (**L**, Vatlock 01224-KA06, VAT,

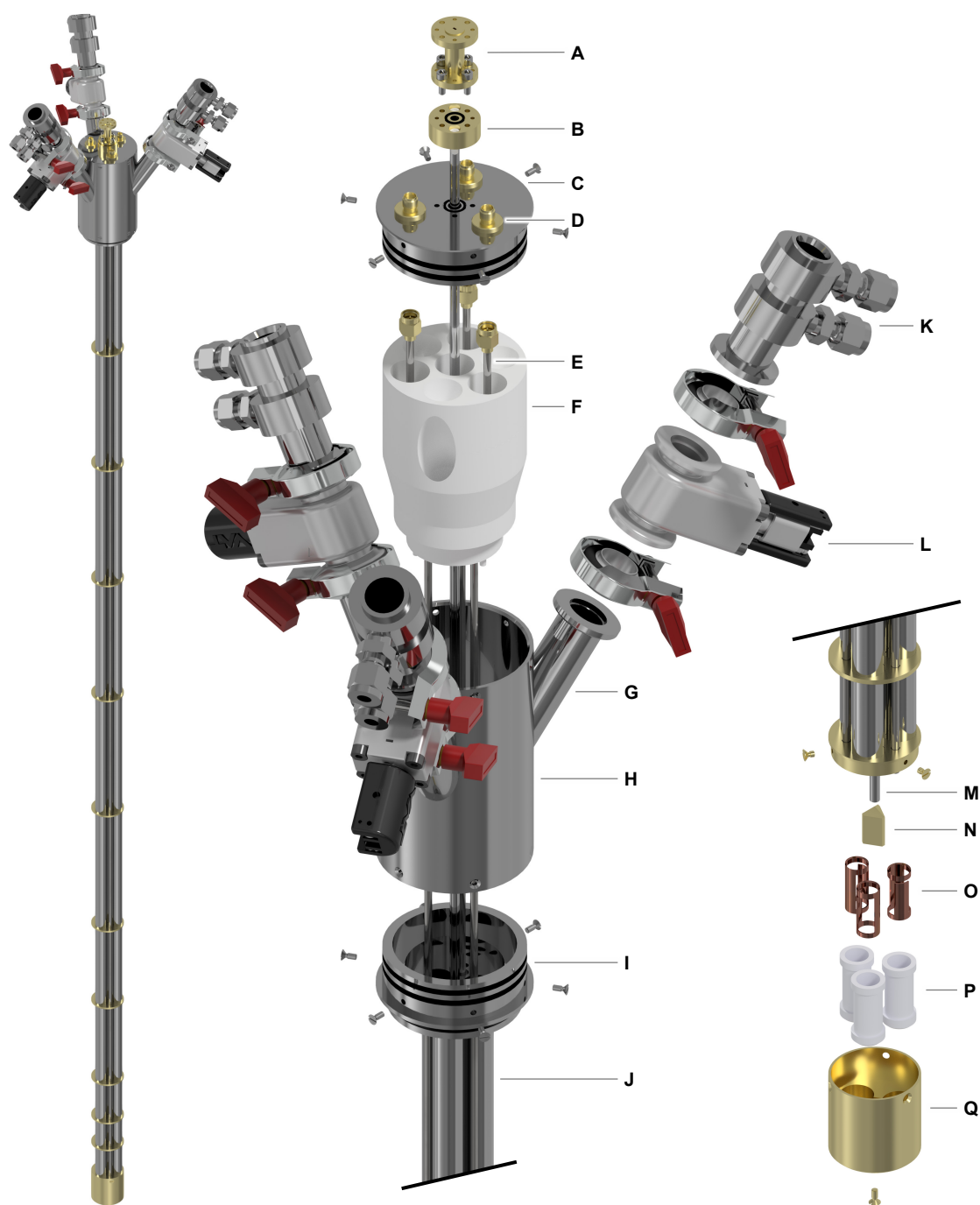


Figure 5.1: Multi-sample dDNP cryogenic probe designed to accommodate three custom fluid paths (CFPs). The main components are indicated by capital letters: WR-06 to circular 3.6 mm microwave transition (A); waveguide flange (B); top flange (C); SMA feedthrough connector (D); semi-rigid 0.141" stainless-steel coaxial cable (E); 3D-printed guide (F); ISO-KF16 half nipple (G); 3-arms manifold (H); ISO-KF40 flange (I); 12.6/13.0 mm stainless-steel sample loading tube (J); loading chamber (K); ISO-KF16 gate valve (L); circular 3.6/4.0 mm stainless-steel waveguide (M); gold-plated tetrahedral microwave reflector (N); pseudo-Aldermann-Grant NMR coils, one for each sample (O); PTFE coil formers (P); gold-plated microwave cavity (Q).

Chapter 5. Highly versatile dDNP: implementation of a multi-sample/multi-nucleus cryogenic probe with parallel NMR detection

Haag, Switzerland) and a 316L stainless-steel loading chamber (**K**) with two hermetically glued (Araldite®, Huntsman, The Woodlands, USA) Swagelok connectors (SS-6M0-1-2W, Swagelok, Solon, USA) to pump on the dynamic sealing (top connector) during sample operation below the gate valve, and to flush the chamber's volume with He gas (bottom connector) during sample operation above the gate valve. A custom-made ISO-KF40 316L stainless-steel flange (**I**) hermetically closes the bottom part of the manifold with two 55 × 2 mm NBR O-rings and seals the cryogenic probe to the polarizer Variable Temperature Insert (VTI, not shown). A 3D printed structure (**F**), placed inside the manifold, provides support and alignment for the 3.6/4.0 mm ID/OD circular 316L stainless-steel waveguide (**M**, Interlloy AG, Schinznach-Bad, Switzerland), the three semi-rigid coaxial cables with stainless steel outer conductor (**E**, .141SS-W-P-50, Jyebao, Taiwan) and, most importantly, guides each CFP inside one of the three 1225 mm long 316L stainless steel 12.6/13.0 mm ID/OD sample tubes (**J**, Interlloy AG, Schinznach-Bad, Switzerland) upon sample insertion. The tubes are welded to the bottom of the ISO-KF40 flange.

Below the ISO-KF40 flange, brazed gold-plated baffles offer mechanical support to the sample tubes, the coaxial cables and the waveguide, and reduce heat transfer via convection and radiation. The top of a gold-plated microwave cavity (**Q**) is brazed to the lower end of the sample tubes. Differently, the centrally mounted waveguide and the three coaxial cables enter the cavity and terminate, respectively, close to a microwave reflector (**N**) and three copper pseudo-AG NMR coils (**O**) placed inside three PTFE coil formers (**P**) for electrical insulation.

A single microwave source (VCOM-06/140/1/50-DD, ELVA-1, Tallinn, Estonia) is interfaced to the waveguide with a circular 3.6 mm to rectangular WR-06 transition (**A**, Elmika, Vilnius, Lithuania), a 90° WR-06 E-plane bend (Elmika, Vilnius, Lithuania, not shown), and a 150 mm WR-6 straight waveguide (ELVA-1, Tallinn, Estonia, not shown).

To better understand the logic behind the microwave delivery scheme and NMR coils decoupling, we show detailed section views of the fully assembled microwave cavity in Figure 5.2. The different elements are indicated as in Figure 5.1. The reflector (**N**) is shaped as a tetrahedron whose top vertex is concentric to the waveguide (**M**); the bottom face is screwed onto the bottom of the cavity (**Q**) and the other three faces form a 45° angle with the vertical axis. In this way, the microwave beam splits in three portions that invest perpendicularly each sample through one opening of the pseudo-AG coil (**O**). Each coil is remotely tuned and matched outside of the VTI with a coaxial cable and a tuning/matching network with two 1.5–250 pF piston trimmer capacitors (V1949, Knowles-Voltronics, Itasca, USA). The inside of the microwave cavity makes a tight fit around the coil formers (**P**). These metallic “wells” not only act as cavity reducers increasing the microwave energy density around the samples, but also shield the B_1 of the pseudo-AG coils avoiding cross talking across channels.

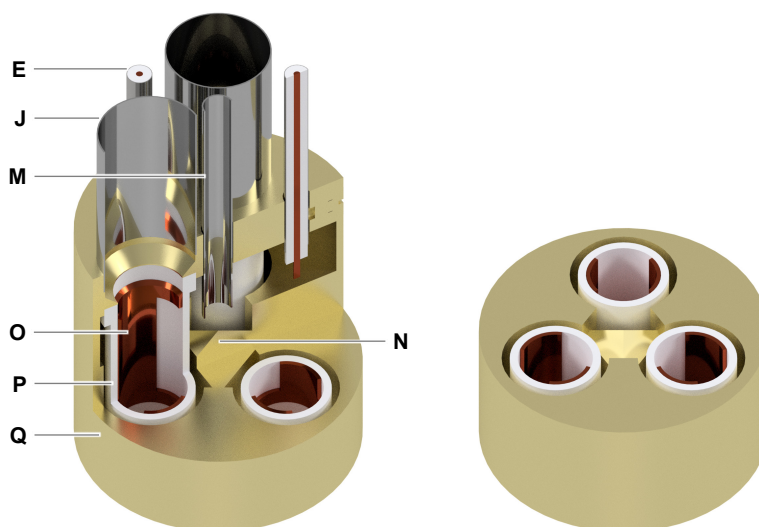


Figure 5.2: Detailed section views of the fully assembled microwave cavity. The main components are indicated by capital letters: semi-rigid 0.141" stainless-steel coaxial cable (E); 12.6/13.0 mm stainless-steel sample loading tube (J); circular 3.6/4.0 mm stainless-steel waveguide (M); gold-plated tetrahedral microwave reflector (N); pseudo-Aldermann-Grant NMR coils, one for each sample (O); PTFE coil formers (P); gold-plated microwave cavity (Q).

The three NMR circuits are interfaced to a 3Tx/3Rx NMR console (Gecko Cameleon 4, RS2D, Mundolsheim, France) via passive Tx/Rx switches and custom-designed low-noise (26.2 dB gain and 0.39 dB noise figure at 55 MHz) preamplifiers based on PGA-103+ (Mini-Circuits, Brooklyn NY, USA). Details about the preamplifiers design are reported in Appendix B. RF power is provided by two RF power amplifier modules embedded inside the NMR console (5-310 MHz, 300 W, BTM00300-GammaS, Tomco, Stepney, Australia), and one external amplifier (5-200 MHz, 100 W, BT00100-Gamma, Tomco). To allow parallel NMR acquisition on the three channels for polarization buildup monitoring, microwave frequency sweep, and microwave power sweep, the existing sequences²⁸⁸ were modified, and a new plugin for online data processing and visualization implemented. In case of homonuclear experiments three identical tuning/matching networks were used and each pair of power amplifier output/preamplifier gain was carefully adjusted to provide the same B_1^+ and signal amplification across the channels. Using parallel transmission and reception NMR channels, the excitation pulses were sent on the three samples at the same time, then their respective signal was simultaneously detected. During heteronuclear experiments, specific tuning/matching networks were used to cover the needed frequency range. The three samples were measured sequentially with a short delay (< 1 ms) because of the single local oscillator (LO) architecture of the spectrometer.

5.3.2 dDNP of [1-¹³C] pyruvic acid

Consistency among the three channels, in terms of polarization in the solid state and after dissolution, was investigated using [1-¹³C] pyruvic acid (Sigma Aldrich, Buchs, Switzerland) doped with 15 mM of OX063 trityl radical (Albeda Research, Copenhagen, Denmark), hereafter referred as PA-sample. 5 μ L of PA-sample was loaded into three different CFPs, together with NaOH at stoichiometric ratio (7.2 μ L of 10 M NaOH in H₂O), as earlier described in Chapter 4. The CFPs were inserted one by one inside the polarizer.

Once the working base temperature was steadily reached, the ¹³C NMR signal (Larmor frequency of 53.43 MHz) was simultaneously measured on the three channels as a function of the microwave frequency (from 139.8 to 140.0 GHz in steps of 10 MHz). This experiment, repeated only once ($n = 1$), allowed to obtain the so-called ¹³C DNP sweep from the three sample slots simultaneously. For each frequency step, the samples were exposed to microwave irradiation for 10 min. The power was kept constant at 55 mW across the microwave frequency span. At the end of each irradiation period, the NMR signal from each slot was acquired using a 30° hard pulse and then destroyed sending a comb of 1000 \times 10° hard pulses, while switching off the microwaves to avoid any repolarization.

NMR signal enhancement as a function of microwave power (i.e. a microwave power sweep) was performed at a microwave frequency of 139.87 GHz to investigate power density differences between the three sample slots ($n = 1$). The power was increased from 1 mW to 3 mW in steps of 1 mW and from 5 mW to 60 mW in steps of 5 mW. The final step was set at 63 mW, which is the maximal power output of the microwave source at this frequency. Before each new power step, the polarization of each sample was destroyed by sending a train of 1000 \times 10° hard pulses.

From the DNP microwave frequency and power sweeps, we could find the microwave parameters providing the best NMR signal enhancement. These two values (i.e. 139.87 GHz and 60 mW) were used to investigate differences in the amplitude and the dynamics of the NMR signal enhancement across the channels. The NMR signal dynamic was simultaneously acquired on each sample using a 5° hard pulse ($n = 2$). This procedure was repeated every 120 s to follow the polarization buildup curve. The experiment lasted at least 2.5 h, more than four times the buildup time constant (i.e. at least 98% of the polarization plateau, result of a mono-exponential curve fit).

After polarization, the three samples were dissolved back-to-back with a 15 min interval between consecutive samples. Each HP solution was automatically transferred to a 1.05 T benchtop NMR spectrometer (Spinsolve ¹³C/¹²⁹Xe Ultra, Magritek, Aachen, Germany) to measure its liquid-state polarization and relaxation time. Each PA-sample was melted using 5.5 mL of buffer solution (40 mM tris(hydroxymethyl)aminomethane (TRIS) and 0.3 mM

ethylenediaminetetraacetic acid (EDTA) in D₂O balanced to pD = 7.6) pre-pressurized at 4 bar with He gas, heated up to 180 °C (12 bar vapor pressure) and pushed for 2.5 s with He gas at 8.0 bar over a 2.0 m long, 2.0/3.0 mm ID/OD PTFE tube into a separator/infusion pump¹⁸⁸, placed on top of the benchtop spectrometer (see Appendix A.2 for details about the dissolution device). After a settling time of 0.5 s, approx. 750 µL of solution was injected into a 5 mm NMR tube already placed inside the spectrometer. The acquisition started 6 s after the beginning of the injection and was performed sending 1° pulses every 3 s for 60 times. The decay of the HP NMR signal was fitted with a mono-exponential function to measure the ¹³C *T*₁ of [1-¹³C] pyruvate at 1.05 T. It is important to notice that the NMR solid-state signal on three channels was continuously acquired until the last CFP was removed from the sample space to evaluate possible perturbations of the polarization level of the sample(s) still not involved in the dissolution procedure and cross-talking between the coils.

Upon measurement of the thermal equilibrium signal, 2 µL of 0.5 M Gd-DO3A-butrol (Gadovist®, Bayer, Leverkusen, Germany) was added to the solution collected inside each NMR tube to reduce the ¹³C relaxation time of pyruvate. The thermal NMR signal was averaged for 1024 times using 90° hard pulses every 3 s. The liquid-state DNP enhancement was calculated from the ratio between the HP and thermal NMR signals and rescaled for the difference in the flip angle of the pulses (*n* = 2 for each slot).

The maximum solid-state polarization was back calculated from the liquid-state value using the [1-¹³C] pyruvate *T*₁ measured at 1.05 T and taking into account a delay of 9 s (2.5 s push time + 0.5 s settling time in the separator/infusion pump + 1 s push time into the NMR tube + 5 s settling time in the NMR tube) between dissolution and onset of the liquid-state acquisition.

5.3.3 Evaluation of cryogenic performance

To compare the cryogenic performance of the multi-sample CFP compatible dDNP cryogenic probe to its single-sample equivalent (Chapter 4), sample space temperature and pressure were measured over time after insertion of the CFPs in two different experiments: monitoring of the above-mentioned parameters during simultaneous DNP sweeps of three samples until depletion of all liquid He inside the cryostat (*n* = 1); monitoring of the above-mentioned parameters during solid-state polarization of three samples and back-to-back dissolutions until no sample was left inside the cryostat (*n* = 1). Prior to each experiment, the polarizer VTI was cooled down and used for half a day to lower the temperature of the two cryostat's radiation shields to 200 K (outer shield) and 100 K (inner shield). Then the VTI was filled completely with 1300 mL of liquid He, and the sample space pumped on by a 253 m³ h⁻¹ roots pump (Ruvac WAU 251, Leybold, Cologne, Germany) backed by a 65 m³ h⁻¹ vane pump

Chapter 5. Highly versatile dDNP: implementation of a multi-sample/multi-nucleus cryogenic probe with parallel NMR detection

(Trivac D65B, Leybold, Cologne, Germany). Measurements started when the sample space pressure dropped below 1 mbar. The temperature sensor used was a ruthenium oxide (RuO_2) resistor (10 k Ω at room temperature, RX-103A, Lake Shore Cryotronics, Westerville, USA). The pressure sensor used was a capacitive gauge (CTR100 230301, Oerlikon Laybold Vacuum, Köln, Germany).

5.3.4 Simultaneous DNP monitoring and optimization of samples prepared with different nuclei and radicals

The ability to co-polarize and simultaneously monitor the NMR signal dynamic of samples containing different target nuclei during a DNP experiment was tested on ^{13}C , ^{129}Xe and ^1H using the following preparations:

- ^{13}C as target nucleus: 20 μL of 4.4 M sodium-L-[1- ^{13}C] lactate (Sigma Aldrich, Buchs, Switzerland) doped with 20 mM OX063 (Albeda Research, Copenhagen, Denmark), 1 mM Gd-DO3A-butrol (Gadovist®, Bayer, Leverkusen, Germany) and dissolved in H_2O :glycerol 1:1 (v:v), hereafter referred as Lac-sample, previously optimized in Chapter 4. This sample was also dissolved and transferred inside the benchtop NMR spectrometer to measure its liquid-state polarization ($n = 3$) as described in the former paragraph.
- ^1H as target nucleus: 50 μL of UV-light irradiated 27.8 M H_2O in glycerol- d_8 :pyruvic acid 3:2 (v:v), hereafter referred as H_2O -sample. The detailed sample preparation was described in a former publication²⁰²; all chemicals were purchased from Sigma Aldrich, Buchs, Switzerland.
- ^{129}Xe as target nucleus: 200 μL of 2.85 M ^{129}Xe and 30 mM 2,2,6,6-Tetramethyl-piperidin-1-oxyl (TEMPO) dissolved in melting isobutanol, hereafter referred as Xe-sample. The detailed sample preparation was described in a former publication¹⁵⁴; all chemicals were purchased from Sigma Aldrich, Buchs, Switzerland.

Each sample was loaded inside a different CFP and inserted into the polarizer. The NMR circuits were all matched to 50 Ω and slot 1, slot 2 and slot 3 tuned to the Larmor frequency of ^{13}C (53.43 MHz), ^1H (212.48 MHz) and ^{129}Xe (58.78 MHz), respectively. Microwave frequency sweeps were performed as previously described, but the frequency span was increased to 139.80-140.15 GHz. Willing to co-polarize samples containing different radicals, the influence of microwave frequency modulation was also investigated, and three more sweeps, with 20, 40 and 60 MHz of frequency modulation peak-to-peak amplitude at 1 kHz modulation rate, were performed. Finally, the polarization buildup at optimal microwave irradiation for the three samples was monitored acquiring the NMR signal by means of a 2.5° hard pulse on each

channel. Since the local oscillator of the NMR spectrometer can generate one frequency at a time upon demodulation of the received signal, a delay of 330 μ s across the three channels was introduced in the NMR sequence. This scheme was repeated every 120 s to follow the growth of the NMR signal of the samples.

5.3.5 Sequential *in vivo* cerebral HP-MRS

We tested the ability to perform co-polarization of different compounds and back-to-back dissolution/injection in a preclinical environment using [1- 13 C] pyruvate and [1- 13 C] lactate to perform multi-substrate HP MRS in a healthy mouse model.

Animal experiments were conducted according to federal and cantonal ethical guidelines and approved by the local regulatory authorities (Service de la Consommation et des Affaires Vétérinaires, Canton de Vaud, Switzerland), licence number VD2017.6 and complied with the ARRIVE guidelines. Male C57BL/6J mice (10 weeks, Charles River, France) were maintained in a temperature- and humidity- controlled animal facility, a 12 h light/dark cycle and free access to food and water.

In Figure 5.3 we report a sketch of the experimental setup. The multi-sample dDNP probe was loaded with two CFPs. One contained 65 μ L of Lac-sample and the other 20 μ L of PA-sample. Therefore, only the buildup in slot 1 and slot 2 was monitored via NMR. The samples were exposed to microwave irradiation for up to 3 h (139.86 GHz and 63 mW).

In the meantime, a healthy C57BL6/J male mouse (25.1 g) was anesthetized with 2% isoflurane in 60% oxygen, and a catheter placed in the left femoral vein to inject the HP solutions. The mouse was immobilized with a stereotaxic device, and a 1 H quadrature/ 13 C linear surface coil was placed above the head (Figure 5.4). Two separator/infusion pumps¹⁸⁸ were simultaneously connected to the catheter using a flangeless T-junction (P-712, IDEX Health & Science, Lake Forest, IL, USA) and prefilling the 125 μ L of dead volume with a phosphate-buffered saline (PBS) solution. In this way, the animal did not need to be handled between injections. Each separator/infusion pump was driven in turn using a syringe pump (NE-1010, New Era Pump Systems, Farmingdale, NY, USA) programmed to inject 450 μ L through the catheter, including the dead volume. MR experiments were performed in a 14.1T/26cm pumped horizontal bore magnet (Magnex Scientific, Yarnton, UK) interfaced to a BioSpec Avance NEO MRI console (Bruker BioSpin, Ettlingen, Germany). Prior to 13 C MRS, field map-based shimming was used to optimize B_0 homogeneity in the mouse brain.

Once the whole setup was in place and the animal ready for injection, the Lac-sample was dissolved first using 5.5 mL of D₂O pre-pressurized at 4 bar with He gas, heated up to 180 °C (12 bar vapor pressure) and pushed for 5 s with He gas at 10 bar over a 6 m long, 2.0/3.0 mm ID/OD

Chapter 5. Highly versatile dDNP: implementation of a multi-sample/multi-nucleus cryogenic probe with parallel NMR detection

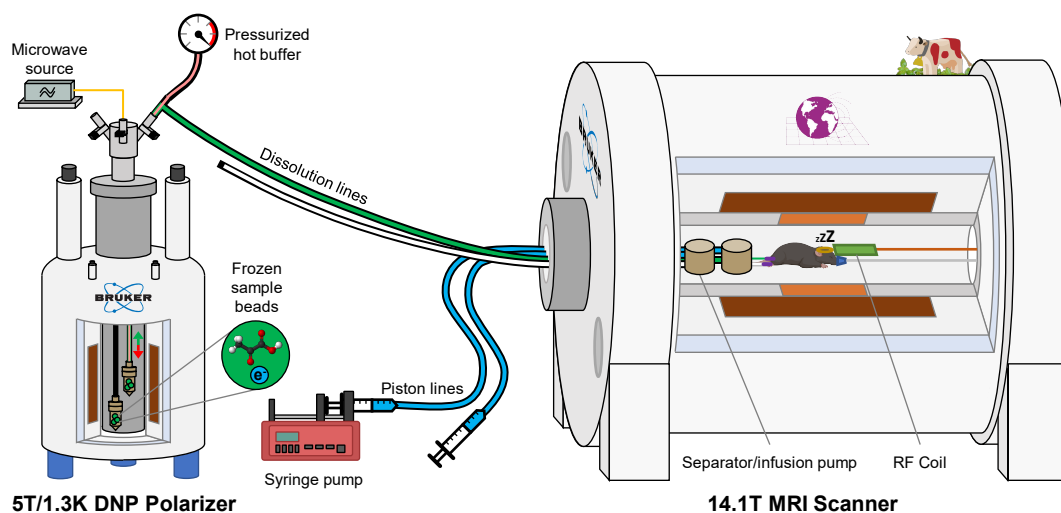


Figure 5.3: Setup for multiple injections into a healthy mouse. The “wet” 5T/1.3K DNP polarizer is equipped with a multi-sample cryogenic probe loaded with two CFPs. Two separate dissolution lines transfer the HP solutions to two distinct separator/infusion pumps placed inside the MRI scanner. One syringe pump drives the injection of the HP solutions into the rat, pushing on separate water-filled piston lines.

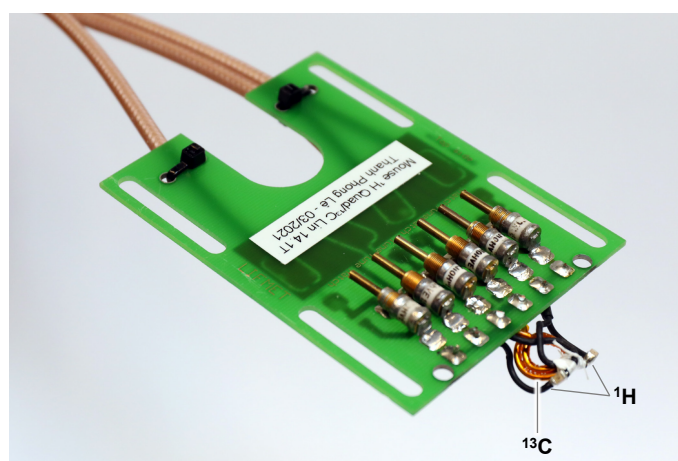


Figure 5.4: Picture of the mouse head ^1H quadrature/ ^{13}C linear surface coil used for HP MRS acquisitions at 14.1 T. The ^{13}C loop is a 2-turn spiral (8/14 mm ID/OD) of \varnothing 1.5 mm enameled copper wire. ^1H element are \varnothing 14 mm loops built with \varnothing 1 mm silver-plated copper wire.

PTFE tube to transfer the lactate HP solution to one separator/infusion pump. A 325 μL bolus of 80 mM HP [$1\text{-}^{13}\text{C}$] lactate was intravenously injected into the mouse at a rate of $650\ \mu\text{L s}^{-1}$. Immediately, unlocalized cerebral ^{13}C MRS was acquired using 30° BIR-4 pulses every 3 s during 3 min. 15 minutes after the first dissolution, the PA-sample was similarly dissolved in a buffer solution (60 mM TRIS and 0.3 mM EDTA in D_2O balanced to $\text{pD} = 7.6$) and transferred to the second separator/infusion pump. A 325 μL bolus of 80 mM HP [$1\text{-}^{13}\text{C}$] pyruvate was injected and measured as the previous sample.

5.3.6 Statistical analysis

When experiments were repeated more than once, numerical results are reported as mean \pm standard deviation.

5.4 Results and discussion

5.4.1 Cryogenic, DNP and NMR performance of the multi-sample probe

In Figures 5.5 and 5.6, we summarize the performance of the multi-sample dDNP probe in terms of cryogenics, homogeneity of the microwave irradiation and Tx/Rx equivalence across the three NMR channels. For this purpose, we loaded each slot with 5 μL of PA-sample. As described in the previous chapter, the dDNP system works in batch mode¹⁸⁸, i.e. the VTI is filled to its maximum capacity with liquid He and then the temperature is lowered by reducing the pressure of the sample space.

The maximum liquid He holding time (Figure 5.5A) was measured during parallel microwave frequency sweeps (Figure 5.5B). The sample space was stable between 1.35 K and 1.30 K over 300 min (5 h). After this time, the sudden temperature drop and subsequent temperature increase indicated the absence of any residual cryogenic liquid inside the sample space. Correspondingly, the pressure decreased from 1.2 mbar to 0.7 mbar. During the first 210 min (duration of the microwave frequency sweep), we could appreciate pressure spikes spaced by 10 min due to the train of RF pulses used to destroy the DNP signal after each microwave frequency step. We could not see the same pattern on the temperature curve because of higher background noise of temperature sensor with respect to the pressure sensor.

The single slot CFP compatible dDNP probe that we described in Chapter 4 allowed us to work at 1.15 K with a liquid He holding time of 6 h. For the same cooling power of the VTI, the increased heat transfer generated by the multi-sample probe is due to the extra building material rather than the three samples themselves. Indeed, as previously demonstrated, the

Chapter 5. Highly versatile dDNP: implementation of a multi-sample/multi-nucleus cryogenic probe with parallel NMR detection

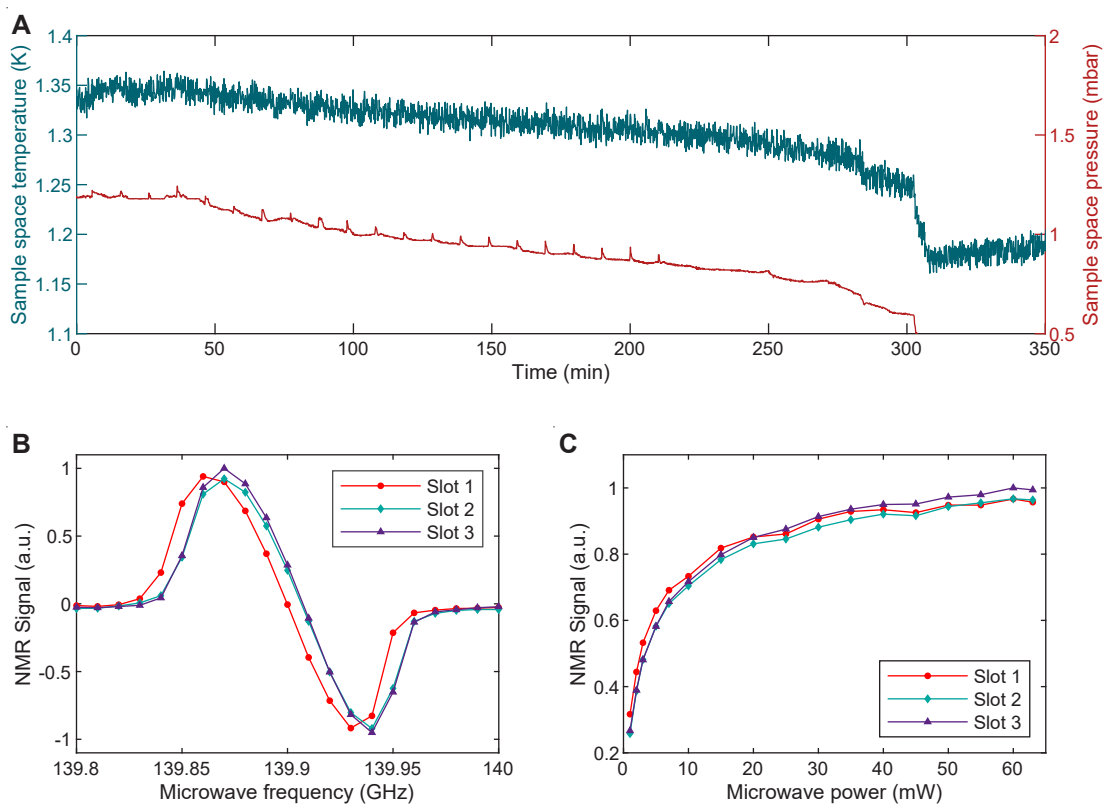


Figure 5.5: Temperature and pressure behaviour inside the polarizer sample space during the microwave frequency sweep (A). Microwave frequency sweeps at 5 T and (1.325 ± 0.025) K measured simultaneously on three equal volume ($5 \mu\text{L}$) PA-samples with a microwave power output of 55 mW; the NMR signal intensity of the curves was normalized according to the highest value measured across the three slots. The lines connecting the data points help guiding the eyes (B). Microwave power sweeps measured at 139.87 GHz for the same samples; the NMR signal intensity was normalized to the highest value of all curves. The lines connecting the data points help guiding the eyes (C).

stainless steel sample loading tube and the semi-rigid coaxial cable account for 86% of the total thermal conductivity, while the CFP for less than 1%.

Signal intensity-wise, the microwave sweeps from the three slots looked alike (in Figure 5.5B, signals were normalized to the highest one, but the DNP spectrum in slot 1 was shifted downfield by 10 MHz with the maximum DNP enhancement appearing at 139.86 GHz instead of 139.87 GHz. Most likely, this is due to a magnetic field difference across the slots of 71.4 ppm (i.e. 0.35 mT). Indeed, upon charging the magnet, the cryoshims were adjusted placing a sample aligned along the vertical axis of the polarizer. Despite this small offset, the maximum available microwave power of the source, together with the presence of a tetrahedral mirror placed in front of the bottom part of the waveguide, was enough to saturate the DNP enhancement when working at 139.87 GHz (Figure 5.5C). Although compared to only 20 mW used

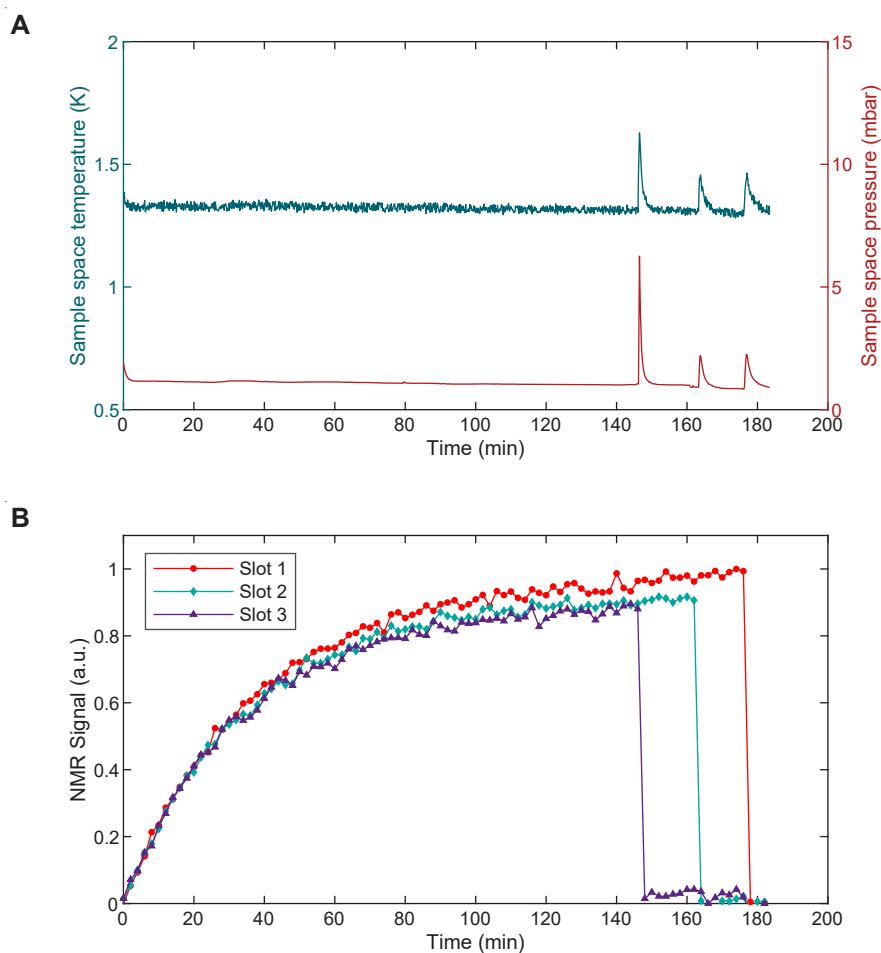


Figure 5.6: Monitoring of the cryogenic (A) and NMR behaviour (B) upon microwave irradiation at constant frequency (139.87 GHz) and constant power (63 mW) and subsequent back-to-back dissolutions. The NMR signal of the curves was normalized according to the highest value measured across the slots.

for the single-sample dDNP probe (Chapter 4), a threefold amount of power was required to obtain the maximum available enhancement, the power sweeps showed an even distribution of the microwaves across the slots.

This behaviour was confirmed by simultaneously monitoring the NMR signal dynamic of the three PA-samples upon irradiation at constant microwave frequency (i.e. 139.87 GHz) and power (63 mW). In Figure 5.6B we show how, within 10% discrepancy, for each time point, the NMR signals measured from the three slots evolved together during 150 min of microwave irradiation. During this time period, the sample space temperature and pressure remained between 1.30–1.35 K and 1.0–1.2 mbar, until the first dissolution from slot 3 was performed. At this point, these two parameters increase to 1.6 K and 6.5 mbar, respectively, because of the heat load brought by the superheated buffer flowing through the CFP (Figure 5.6A). The

dissolutions from slot 2 and slot 1 followed delayed by 15 min each and showed a similar behaviour. Concerning the behaviour of the system, four aspects are noteworthy:

- After each dissolution, the cryogenic system recovered after 5 min, going back to baseline temperature and pressure values (Figure 5.6A).
- The temperature and pressure jump inside the sample space due to the passage of hot buffer through the CFP in one slot did not decrease the NMR signal in the other slots (Figure 5.6B).
- The NMR signal from the slot interested by the dissolution suddenly dropped below 4% of the pre-dissolution signal intensity (Figure 5.7) confirming the absence of pronounced cross talking between the three AG coils.
- The second and third dissolutions generated a less pronounced temperature/pressure jump because of the lower liquid He level left after the first event (Figure 5.6A).

5.4.2 Solid-state and liquid-state polarization of pyruvic acid

In a separate set of experiments ($n = 2$) we measured the solid-state and liquid-state polarization obtained on the same kind of samples (i.e. three slots loaded with a PA-sample). We summarize our findings in Figure 5.8.

After 100 min, all samples reached at least 95% of the maximum achievable signal (Figure 5.8A) with a polarization time constant of (1762 ± 47) s, (1932 ± 58) s, (1944 ± 16) s for slot 1, slot 2 and slot 3, respectively (Figure 5.8B). While the buildup time constant in slots 2 and 3 was, within experimental errors, the same, the one from slot 1 was approximately 200 s shorter. Being the last point of the microwave power sweep very similar for all slots, we ascribe this discrepancy to the irradiation frequency being 10 MHz lower than the optimal value for slot 1. Indeed, it was earlier demonstrated that buildup time constants decrease moving the microwave frequency to the left/right of the positive/negative maximum of the DNP spectrum¹⁸⁵. Most importantly, the buildup was considerably shorter compared to what we measured earlier using the single-sample dDNP probe (Chapter 4). In that case, $[1-^{13}\text{C}]$ pyruvic acid doped with 15 mM trityl showed a buildup time constant of (2745 ± 63) s. The latter is justified by the lower base temperature (1.15 K vs. 1.35 K) that could be reached using the single-sample DNP probe. Indeed, as shown in the work from Filibian et al.³¹⁶, the buildup time constants (T_b) scale nicely with the relation $T_b^{-1} = T^2$, where T is the temperature of the He bath.

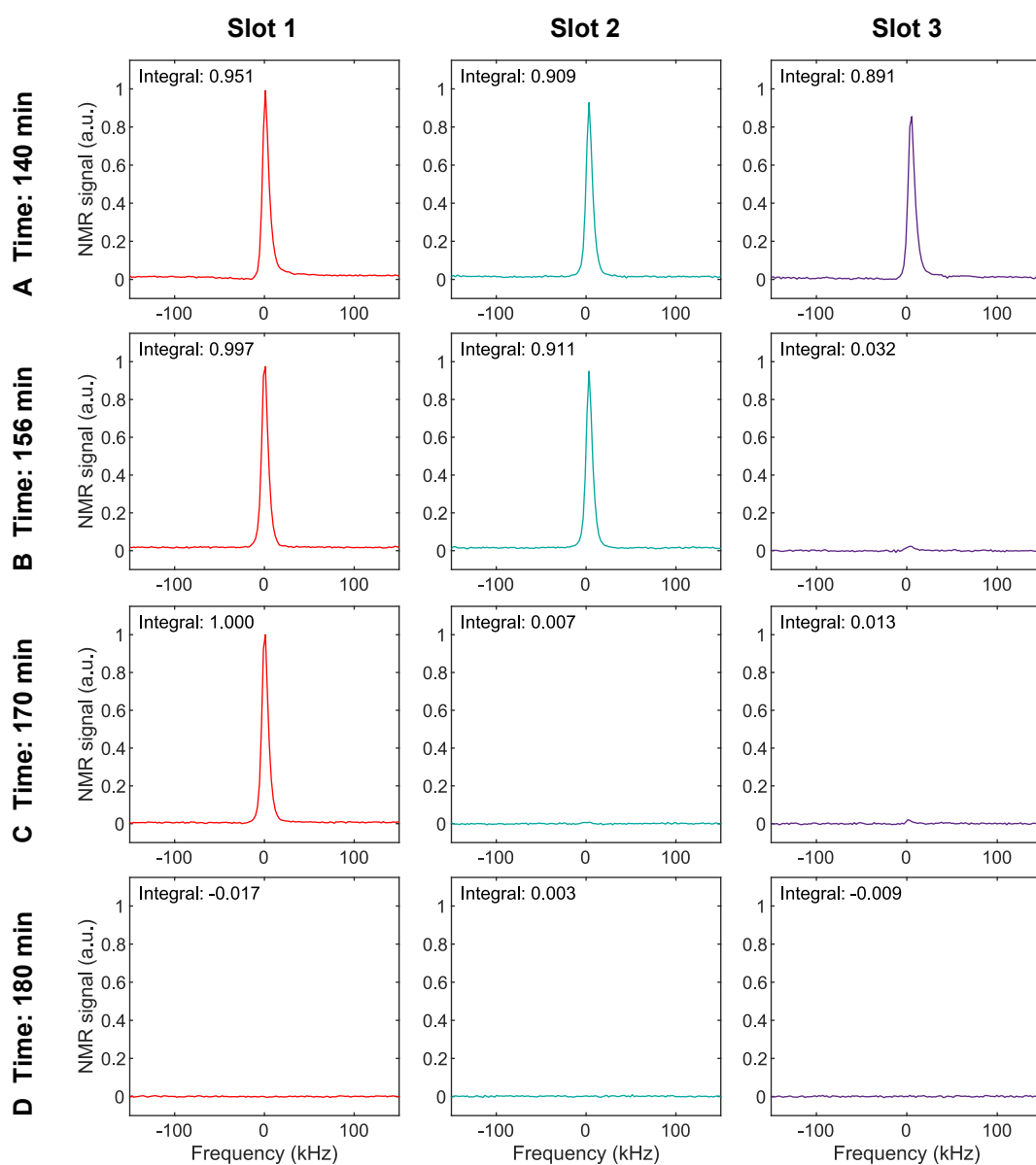


Figure 5.7: Investigation of cross talk between the three slots during a homonuclear experiment. The first row (**A**) displays the spectra acquired at 140 min after the start of the experiment. The NMR signal intensity is similar within 7% discrepancy across the slots. After dissolving the sample in slot 3 (**B**, at 156 min), a signal equivalent to 3.6% of the signal prior to dissolution is observed in that slot. This residual NMR signal is likely detected from the samples in slots 1 and 2. After the second dissolution (**C**, at 170 min), a similar residual signal is observed in slots 2 and 3. No NMR signal is observed following the dissolution of all samples (**D**, 180 min timepoint).

Chapter 5. Highly versatile dDNP: implementation of a multi-sample/multi-nucleus cryogenic probe with parallel NMR detection

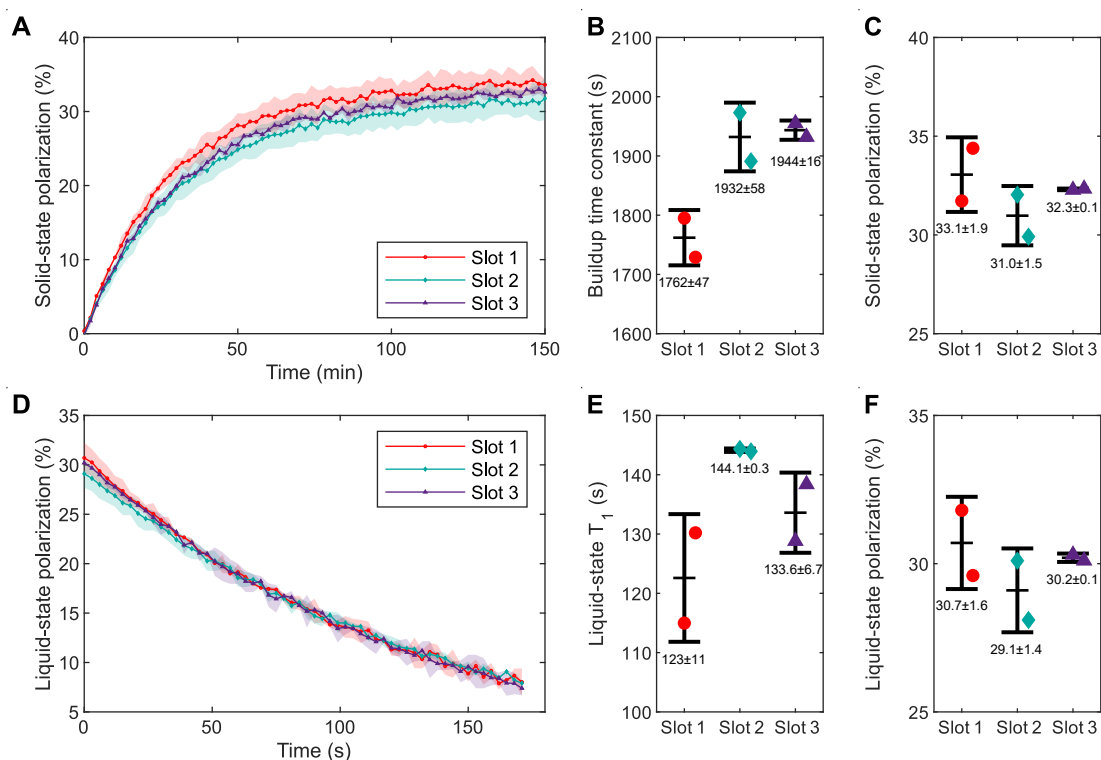


Figure 5.8: Summary of the dDNP performance of the multi-sample probe when loaded with three PA-samples ($n = 2$): solid-state polarization dynamics during microwave irradiation inside the polarizer (A); fitted mono-exponential buildup time constant (B); back-calculated maximum solid-state polarization from liquid-state value (C); liquid-state polarization dynamics after dissolution inside the benchtop NMR spectrometer (D); fitted mono-exponential relaxation time constant (E); calculated liquid-state polarization upon injection of the HP solution inside the benchtop NMR spectrometer from thermal equilibrium value (F). Numerical results are expressed as mean \pm standard deviation. Shaded areas represent the standard deviation between measurements.

After dissolution and relaxation inside the benchtop spectrometer (Figure 5.8D), we calculated an average liquid-state polarization of $(30.0 \pm 1.2)\%$ (Figure 5.8F). With a relative error as small as 4% over six dissolutions, the system demonstrates high repeatability and equal dDNP performance across the channels. Again, compared to the single-slot probe (Chapter 4), the slightly lower maximum achievable polarization can be justified by the difference in base temperature. The ^{13}C solid-state polarization value of $(32.1 \pm 1.4)\%$ (Figure 5.8C) was back calculated assuming a relaxation time during transfer of 130 s (Figure 5.8E).

5.4.3 Solid-state polarization and monitoring of different nuclei

We deliberately chose an extreme case where we tried to co-polarize and monitor the Lac-sample ([1- ^{13}C] lactate + trityl), the Xe-sample (^{129}Xe + TEMPO) and the H₂O-sample (^1H + lactyl radical).

Figure 5.9A shows how monochromatic (i.e. no frequency modulation) microwave sweeps of the three samples have poor overlap, with the maximum of the Xe-sample appearing at 140.05 GHz and the maxima for the other two samples around 139.85 GHz, where the Xe-sample DNP is very far from optimal. Instead of programming the microwave source to swiftly change the output frequency, as it happens for instance in ELDOR experiments³¹⁷, we decided to explore the effect of microwave frequency modulation. The latter increases the breadth of the DNP spectrum, and the larger the modulation amplitude, the further apart the positive and negative DNP maxima move^{149,201}.

In Figure 5.9B-D we report the effect of increasing modulation amplitude on the DNP spectra. At 139.94 GHz, when driving the frequency output with a sine wave oscillating by 60 MHz peak-to-peak amplitude, not only the Xe-sample polarization increased by a factor of 2, but also, its positive peak became almost coincident with the negative one of the Lac-sample. At the same time, the H₂O-sample could still be polarized at 50% of its maximum value. Therefore, we used this microwave irradiation setting to simultaneously monitor the buildup of all samples (Figure 5.9E). Shining microwaves for 3 h they all reached the maximum available polarization.

5.4.4 Sequential *in vivo* cerebral HP MRS

In HP MR, [1- ^{13}C] pyruvate is widely recognized as the golden standard to assess real-time metabolism *in vivo* through its conversion to lactate, bicarbonate and alanine²⁹⁹. Nevertheless, lactate is another promising molecule, despite the less straightforward sample formulation²³⁴. Differently from pyruvate, it can be injected at physiological concentration with known neuroprotective effects²²⁸, it easily crosses the blood-brain barrier²³⁶, and allows detecting the secondary conversions to alanine and bicarbonate through pyruvate providing a better understanding of the lactate dehydrogenase activity^{234,318}.

Therefore, to test the capability of our system to produce injectable HP solutions containing physiologically interesting metabolites with a rate much shorter compared to the usual ^{13}C DNP buildup time, we chose to perform two [1- ^{13}C] lactate/[1- ^{13}C] pyruvate back-to-back injections into a healthy mouse.

Chapter 5. Highly versatile dDNP: implementation of a multi-sample/multi-nucleus cryogenic probe with parallel NMR detection

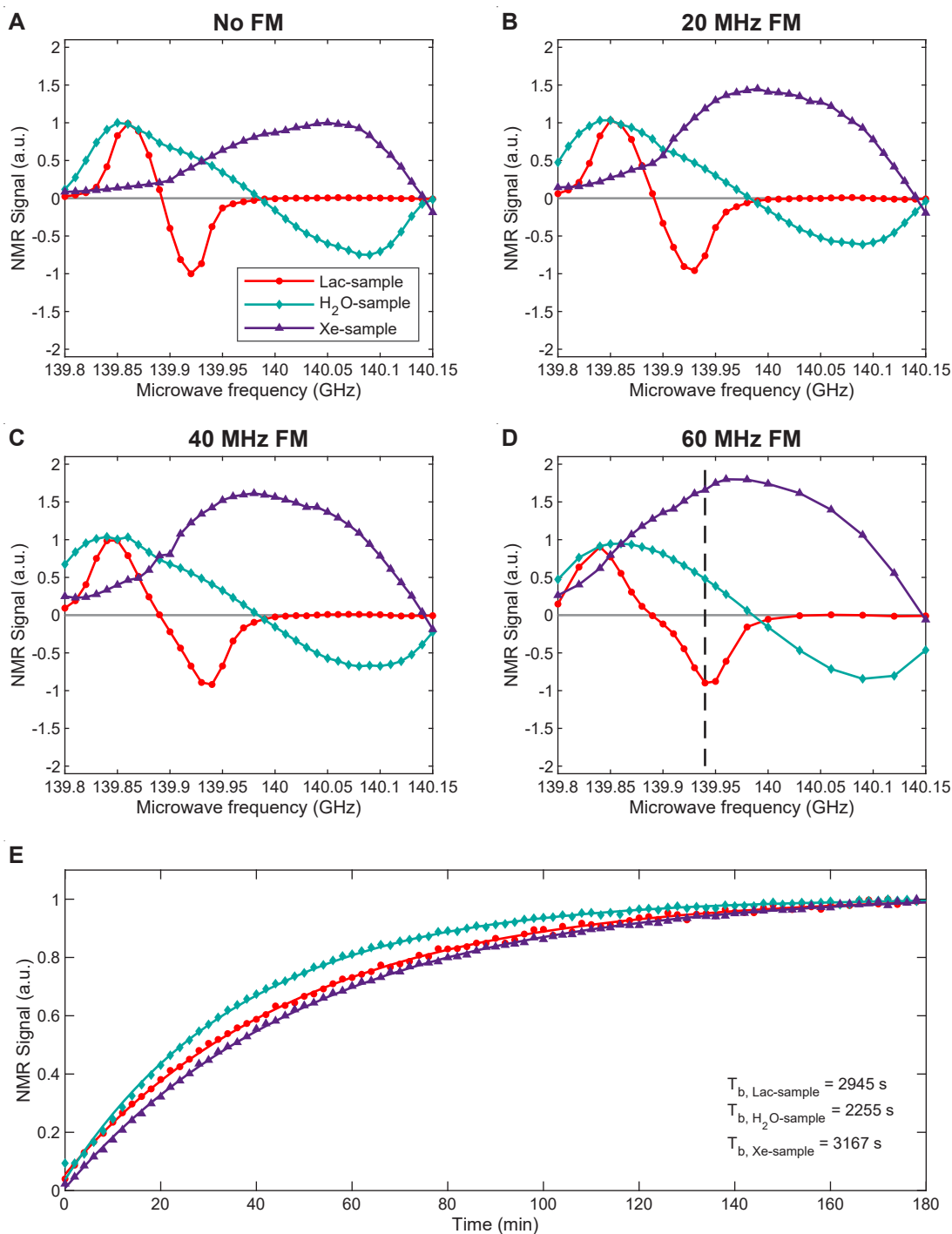


Figure 5.9: Lac-sample, H₂O-sample and Xe-sample simultaneous DNP microwave frequency sweep without (A) and with 20 MHz (B), 40 MHz (C) and 60 MHz (D) of frequency modulation amplitude. Lac-sample, H₂O-sample and Xe-sample simultaneous polarization buildup monitoring shining microwaves at 139.94 GHz with 60 MHz frequency modulation amplitude and 63 mW output power (E). The dashed line in (D) indicates the microwave irradiation frequency used in (E). The intensity of each sweep in (A) was normalized to 1. The signal intensity of the sweeps in (B, C, D) was normalized with respect to (A).

To have the same ^{13}C nuclei final concentration after dissolution, the Lac-sample volume was 3.25 times larger than the PA-sample. Despite the slightly different DNP spectrum, both samples showed optimal DNP at 139.86 GHz (Figure 5.10). The slightly higher radical content compensated for the slower spin diffusion due to lower ^{13}C concentration¹⁵⁶, and the Lac-sample built-up polarization approximately at the same rate as the PA-sample (Figure 5.11A). In a separate set of experiments, the $[1-^{13}\text{C}]$ lactate liquid-state polarization measured inside the benchtop spectrometer was $(24.3 \pm 1.5)\%$ ($n = 3$).

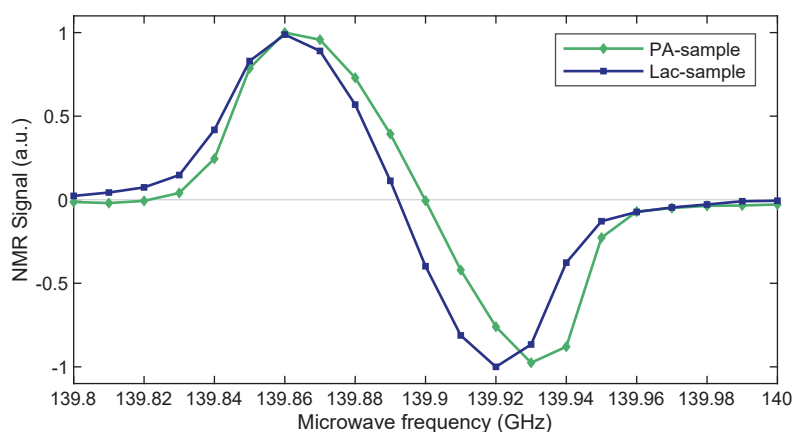


Figure 5.10: Microwave frequency sweep of the Lac-sample and PA-sample measured simultaneously using the multi-sample DNP probe. Both samples have maximum enhancement at 139.86 GHz. The spectral breadth of the Lac-sample is narrower because of the presence of Gd^{3+} in its formulation.

The Lac-sample was dissolved first and infused into the mouse to monitor its cerebral metabolism into pyruvate, alanine and bicarbonate (Figure 5.11B). 15 minutes later, the pyruvate sample was similarly dissolved and its cerebral conversion into lactate, alanine and bicarbonate was successfully monitored (Figure 5.11C). The maximal SNR in single spectra, without applying any line broadening, was 402 and 313 for pyruvate and lactate, respectively, which is consistent with the difference in liquid-state polarization level of the two samples. Nevertheless, the SNR of downstream metabolites were substantially smaller after injecting lactate compared to pyruvate. The latter was due to lower label exchange (Chapter 2) between HP lactate to endogenous pyruvate with respect to HP pyruvate to endogenous lactate because of the difference in pool size of the two metabolites^{234,253}.

Chapter 5. Highly versatile dDNP: implementation of a multi-sample/multi-nucleus cryogenic probe with parallel NMR detection

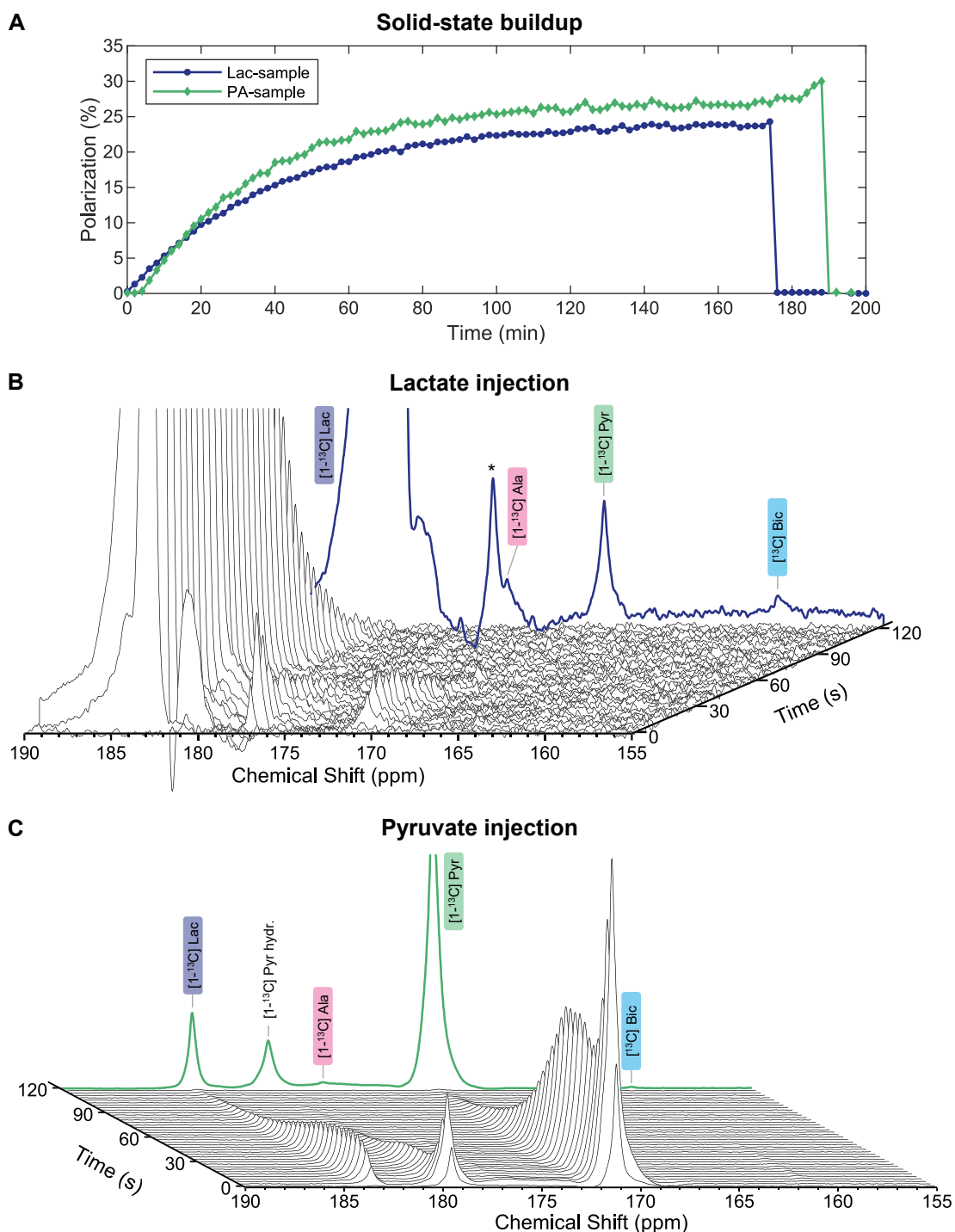


Figure 5.11: Solid-state NMR signal of the PA-sample (green) and Lac-sample (blue) simultaneously hyperpolarized and dissolved within 15 minutes from each other; the curves were scaled to the liquid-state polarization measured in separate experiments (A). Unlocalized cerebral ^{13}C -MRS to investigate the metabolism of HP lactate, which metabolizes into pyruvate, alanine and bicarbonate; the bold blue line represents the sum of individual spectra measured in the first 120 s post-injection; the peak marked with a (*) is an impurity of the stock lactate solution (B). Unlocalized cerebral ^{13}C -MRS to probe the metabolism of HP pyruvate, which metabolizes into lactate, alanine and bicarbonate; the bold green line represents the sum of signals 120 s post-injection (C). In (B-C) a line broadening of 20 Hz was applied.

5.5 Conclusion and perspectives

Regardless of their formulation, being able to optimize and/or monitor the DNP performance of more samples at once represents a powerful tool to improve and expand the scope of applications that entail multi HP compound injections. In this chapter, we have detailed the design and performance of a versatile multi-sample dDNP probe. Benefiting from the compactness of the CFP, three samples, each with its own dedicated NMR coil, could be incorporated despite the narrow $\varnothing 36.5$ mm VTI. This probe has the unique characteristic of selective NMR capability across three sample slots, and we proved its employment in a preclinical application.

We were able to produce three pyruvate HP solutions within 30 min from the first dissolution, and the delay was mainly caused by the time needed for the buffer to heat-up rather than for the cryogenic system to recover. Indeed, after each dissolution, the system was able to go back to its base working temperature within 5 min. Therefore, injections with a shorter delay could be obtained by improving the heat transfer from the heating element to the solvent, or by using many dissolution heads in parallel.

The working base temperature was 15% higher compared to the similarly built single-sample probe (Chapter 4). This decreased the maximum achievable polarization of pyruvate accordingly. If for a wet system the increased thermal conductivity was, after all, negligible, this aspect will deserve extra care in case of implementation of the dDNP into a cryogen-free system¹⁹⁴. In that case, providing a better thermal anchoring of the probe to the radiation shields of the polarizer will improve the base temperature, as well as cutting specific patterns along the stainless-steel sample tubes or using a thinner coaxial cable to reduce thermal conductivity.

Despite the larger microwave cavity compared to the single-sample probe, a sufficient microwave power density was still achieved to saturate the DNP enhancement. Microwave losses could be reduced by electroplating the stainless-steel waveguide with a better electrical conductor, such as gold or copper^{195,196}.

Finally, we showed how microwave frequency modulation can be an easy to implement and versatile tool to find the microwave irradiation “sweet spot”, when trying to simultaneously polarize samples with very different formulations.

6 Improving the spatiotemporal efficiency of spectrally resolved ^{13}C MRI to probe the dynamic metabolic interplay in a mouse model of stroke

6.1 Abstract

Distinct global metabolic dynamics of the HP neuroprotective agents [$1\text{-}^{13}\text{C}$] lactate and [$1\text{-}^{13}\text{C}$] pyruvate were previously depicted between the ischemic and healthy mice brains. This could reflect the evolving metabolic reprogramming to adapt to the energetic demands in the acute phase of stroke. The ischemic lesion being inhomogeneous, adding the ability to unravel the specific regional patterns of the metabolic response to a stroke insult could provide new information to help understanding the fate of these therapeutic molecules, and would be essential for having a relevant diagnostic component in a theranostic approach for stroke.

The transition from global MRS measurements to dynamic MR spectroscopic imaging represents primarily a technical challenge, requiring substantial upgrades of our acquisition tools and strategies. For measurements in the mouse brain, a $^1\text{H}/^{13}\text{C}$ volume coil was designed to achieve uniform RF excitation throughout the brain to facilitate the application of imaging strategies and kinetic modeling of dynamic metabolite signals, while a ^{13}C receive-only surface coil ensures highly sensitive detection. In parallel, a model-based MR spectroscopic imaging scheme, the IDEAL spiral CSI sequence, was implemented on a 14.1T MRI scanner. A highly efficient HP MR signal sampling is achieved with this sparse acquisition scheme, which not only allows economical usage of the nonrenewable hyperpolarized signal, but also allows short acquisition times to achieve a high temporal resolution to resolve dynamic features.

Together with the upgraded dDNP polarizer, these MR tools enabled dynamic HP MRSI in the mouse brain at high spatiotemporal resolution. In a proof-of-concept experiment, the regional pattern of the cerebral metabolic response to a neuroprotective bolus of HP [$1\text{-}^{13}\text{C}$] pyruvate was mapped in a stroke mouse. We identified a distinct metabolism within the ischemic core, with a higher and faster lactate labeling compared to healthy tissues.

Part of the content of this chapter was presented in: **Lê Thanh Phong**, Buscemi Lara, Lepore Mario, Capozzi Andrea, Hirt Lorenz, Mishkovsky Mor, Hyacinthe Jean-Noël. *Development and application of dynamic MRSI of an HP neuroprotective agent in an MCAO mouse model of ischemic stroke at 14.1 T*. Proceedings of ISMRM & ISMRT Annual Meeting & Exhibition, Toronto (CA), June 3-8 2023

My contribution to this chapter is in its entirety. I designed, built and characterized the RF cross-coil setup, implemented the dynamic MRSI sequence and reconstruction, performed all *in vitro* and *in vivo* experiments. I analyzed and interpreted the results together with all coauthors. The animal surgery and monitoring were performed by Mario Lepore.

6.2 Introduction

Dissolution dynamic nuclear polarization (dDNP) provides an unprecedented sensitivity to magnetic resonance for spectroscopy or imaging. DNP systems operating at high magnetic field (greater than or equal to 5 T) and sub-liquid helium temperature can routinely yield a liquid-state nuclear polarization exceeding 50% for pyruvate^{138,139,194}, as well as on other metabolic substrates, for example glucose¹⁶². Nonetheless, while achieving a polarization close to unity is one part of the challenge, an efficient acquisition of the short-lived hyperpolarized signal to probe the metabolic or physiological processes of interest is key.

Preclinical stroke research is most widely applied in mice and rats, especially for their similar brain vasculature compared to the human^{319,320}. On a broad scope, studying the effect of neuroprotective agents such as lactate or pyruvate entails not only their role as metabolic substrates but also as signaling molecules. For the latter, mice are usually preferred than rats because they are much easier to genetically engineer for studying the role of specific genes in the neuroprotective processes. From the perspective of MRI acquisitions, the mouse brain is more difficult to image, in particular due to the four-fold¹ smaller volume compared to the rat brain, which requires voxel volumes to be reduced in order to resolve brain regions with the same level of detail, resulting in proportionally lower signals.

In our study of the metabolic contrasts of hyperpolarized neuroprotective agents, namely [1-¹³C] lactate and [1-¹³C] pyruvate (Chapter 2), distinct global dynamic metabolic contrasts were observed between healthy and stroke animals. Nevertheless, the ischemic brain is composed of several distinct regions evolving over time: the infarcted core, ischemic penumbra, and surrounding healthy tissues. MR spectroscopic imaging (MRSI) could disentangle specific regional metabolic patterns resulting from a stroke injury and provide crucial insights to improve our understanding of the biological mechanisms intervening after stroke. More importantly, volumetric-resolved measurements are critical to exploit the potential of these HP neuroprotectants as molecular imaging contrast agents in a theranostic approach for stroke. The transition from dynamic global MRS measurements to the investigation of both the regional and dynamic metabolic patterns of these tracers necessitates the implementation of efficient MRSI sampling strategies, in order to parsimoniously use the nonrenewable hyperpolarized signal, compensate for partitioning the MR signal into small voxels, as well as minimizing the measurement duration to accurately track the temporal evolution of these processes.

Our previous measurements of the metabolism of HP neuroprotective agents at a therapeutic dose in the mouse brain (Chapters 2, 3 and 5, as well as Hyacinthe et al.²²⁸) were all performed using a linear ¹³C surface coil. They are widely used in single-voxel or non-selective

¹About $\approx 415 \text{ mm}^3$ and $\approx 1765 \text{ mm}^3$ in the adult mouse³²¹ and rat³²², respectively.

Chapter 6. Improving the spatiotemporal efficiency of spectrally resolved ^{13}C MRI to probe the dynamic metabolic interplay in a mouse model of stroke

spectroscopy, since their small size and proximity to the region of interest yields a high sensitivity. In our application, the latter is highly required due to the weak downstream metabolite signals resulting from the impeded delivery through the blood-brain barrier (BBB) of the neuroprotectants that we investigate^{236,245}. However, the non-homogeneous RF excitation profile of surface coils complicates the use of most imaging sequences and leads to a difficult quantification of the dynamics of tracers metabolism. Indeed, the RF-induced depolarization, which is a parameter of the kinetic models (Section 2.4.2), would be spatially dependent. The usual approach³²³ to achieve both uniform RF excitation and high receive sensitivity is to use a volume transmit-coil and separate anatomically shaped receive-coils, also known as a cross-coil or transmit-only/receive-only (TORO) setup.

In this chapter, we present the implementation of high-resolution dynamic MRSI acquisitions for metabolic imaging of HP neuroprotective tracers in the mouse brain. To achieve this goal, we developed and characterized an RF cross-coil setup that offers highly sensitive surface detection capabilities, along with uniform RF volume excitation to achieve efficient imaging and accurate kinetic analysis of metabolites signals. In parallel, we selected, implemented, and tested an efficient acquisition strategy to achieve dynamic and multislice HP ^{13}C MRSI. Finally, in a proof-of-concept experiment, these developments are applied *in vivo* to perform dynamic HP cerebral metabolic imaging in a mouse model of transient ischemic stroke. While our interest lies in investigating the metabolism of several HP neuroprotective agents, we initially conducted imaging experiments with hyperpolarized [1- ^{13}C] pyruvate, as it produces higher downstream metabolite signals that are easier to detect (Chapter 2).

Instead of making our developments on the same platform previously used (7T/1K DNP polarizer and 9.4T MRI scanner, Chapters 2 and 3) to facilitate the comparison between global and localized measurement results, we transitioned to a 14.1T MRI scanner, which is more technically capable and suitable for MRSI developments. Recently upgraded to a state-of-the-art spectrometer console, it provides support for multichannel RF coil arrays, better gradient performance¹, better software capabilities for MR sequence design particularly with non-Cartesian k -space trajectories, and shimming based on 3D B_0 field maps. This MRI scanner is coupled to the 5T/1.15K DNP polarizer upgraded in Chapters 4 and 5 towards better DNP performance and throughput.

6.2.1 MRSI acquisition schemes

Due to the rapidly and irreversibly decaying longitudinal magnetization, measurements with HP probes require specific acquisition schemes. In addition, the transient nature of the

¹1000 mTm^{-1} peak strength and 6450 $\text{Tm}^{-1}\text{s}^{-1}$ slew rate compared to 500 mTm^{-1} and 5500 $\text{Tm}^{-1}\text{s}^{-1}$ on the 9.4T MRI scanner.

metabolic response to the HP substrate requires time-resolved measurements to properly describe their dynamics. Over the years, many methods for HP metabolic imaging have been developed with various combinations²¹⁶ of schemes for spectral encoding, spatial encoding, RF excitation, and contrast scheme, and can be broadly classified as follows^{217,324}:

- **Spectroscopic imaging methods** provide a continuous NMR spectrum for each voxel and do not require any prior knowledge.

Free induction decay chemical shift imaging³²⁵ (FID-CSI) is the simplest method. It consists in 2D or 3D spatial phase-encoding followed by FID readout providing the spectral encoding. It achieves both large spectral bandwidth, high spectral resolution, and robustness against static field inhomogeneity. However, since each k -point needs to be individually acquired, it uses the magnetization inefficiently and requires long acquisition times, therefore FID-CSI is generally limited to single time point acquisitions, or dynamic imaging with a coarse spatial resolution.

Rapid spectroscopic imaging techniques accomplish simultaneous spectral and spatial encoding by traversing the k -space at distinct echo times. For each k -point, the spectrum can be obtained using a Fourier transform along the echo time dimension³²⁶. The gradient spatial encoding scheme can be achieved with any trajectory, for example, echo-planar³²⁷, spiral^{328,329}, radial³³⁰, or concentric rings³³¹. Although this type of acquisition scheme greatly reduces the measurement time, this comes at the cost of a limited spectral bandwidth and coarse spectral resolution.

- **Model-based imaging methods** encode spectral and spatial information by acquiring images at shifted echo times similarly to rapid spectroscopic imaging techniques. However, using prior knowledge of the resonance frequencies of the metabolites, fewer echo time steps are required in the reconstruction by using model-based approaches³³², which we will further discuss later in detail in Section 6.2.2. These schemes can typically be applied in the presence of a few well-separated resonances. B_0 inhomogeneity can be accounted for via ^1H static field maps. However, artifacts can occur if it varies during the acquisition.
- **Metabolite-selective imaging methods** decouple the spectral and spatial encoding by selectively exciting individual metabolites using a spectral-spatial (SPSP) pulse³³³, followed by a rapid imaging readout, for example echo planar³³⁴ or spiral³³⁵. These methods are only applicable to spectra with well-separated resonances. Compared to model-based methods, they provide a similar³³⁶ SNR when consuming an equal amount of HP magnetization. However, they can be easily adjusted to excite the metabolites differently, with smaller flip angles on injected substrates to spare their magnetization, and larger ones on downstream metabolites to improve their SNR³³⁷. The narrow

passband, by design, of the SPSP RF pulses makes these schemes sensitive to center frequency errors and static field inhomogeneity.

- **Refocused imaging methods** provide an efficient use of nuclear magnetization for molecules with a long³³⁸ spin-spin relaxation time (T_2), which is the case for $[1-^{13}\text{C}]$ pyruvate and $[1-^{13}\text{C}]$ lactate³³⁹ whose T_2 are in the order of seconds under physiological conditions³⁴⁰. Compared to gradient-echo type methods, which spoil the remaining magnetization at the end of each cycle, refocused methods maintain the residual transverse magnetization using a refocusing pulse between successive cycles. In addition, at the end of each pulse train, the remaining steady-state transverse magnetization can be stored back to the longitudinal direction³⁴¹.

Such methods are known as steady-state free precession (SSFP) sequences. Among them, balanced SSFP (bSSFP), which refocuses all imaging gradients within one cycle, offers the highest SNR efficiency³⁴². In the context of MRSI, the intrinsic frequency response of bSSFP can be applied to image one metabolite at a time by placing within the bandpass region, and undesired metabolites in the stopbands^{177,343}. Particularly for the imaging of numerous resonant frequencies, spectrally selective pulses can be used to improve the specificity of the acquisition³⁴⁴. The RF pulses may be deliberately applied off-resonance to shorten both their duration and the repetition time, in order to achieve a better spatiotemporal resolution³⁴⁵. Another variant is the combination of bSSFP with a sparse multi-echo (model-based) approach³⁴⁶.

- **Spatiotemporal encoding** (SPEN)^{347,348} encodes both spatial and spectral information simultaneously using one gradient axis by applying frequency-swept RF excitation in combination with an encoding gradient, resulting in the progressive excitation of the spins depending on both their chemical shift and spatial coordinate. The application of a readout gradient decodes spatial information into the time domain, while the spin density and spectral information reside in the signal amplitude and phase, respectively. Combined with a conventional k -space readout to encode additional spatial dimensions, SPEN achieves the acquisition of single-shot spectroscopic images with a sub-second temporal resolution^{349,350}.

Our specific application focuses on imaging the hyperpolarized neuroprotective agents $[1-^{13}\text{C}]$ lactate and $[1-^{13}\text{C}]$ pyruvate in a mouse model of stroke, and requires both high spatial and temporal resolution to properly resolve the stroke lesion as well as the metabolic dynamics. Both substrates and their downstream metabolites have well-defined and separated chemical shift displacements, making them suitable for model-based or metabolite-selective acquisition schemes. As a result of the project timeline, the RF coil being developed in parallel to the imaging sequence, the use of either refocused or spatiotemporal encoding pulse sequences

would have been difficult with the inhomogeneous transmit field profile achievable with the available transmit-receive surface coil, although this can be taken into account using additional compensation schemes^{351,352}. Given these constraints and requirements, we opted for a model-based method which typically requires a shorter acquisition time compared to spectroscopic imaging methods²¹⁵.

6.2.2 IDEAL spiral CSI

The IDEAL spiral CSI acquisition scheme³⁵³ is a model-based MRSI sequence that provides efficient spectral-spatial encoding.

The spectral encoding is based on the Iterative Decomposition of water and fat with Echo Asymmetry and Least-squares estimation³³² (IDEAL) principle. Extending the Dixon-type fat-water separation principle³⁵⁴ to an arbitrary number of resonances, it relies on the acquisition of multiple images with shifted echo times such that the signal from metabolites with distinct resonant frequencies will be acquired with a different relative phase in the image series. Using prior knowledge of their chemical shifts, either assumed or measured with MRS, the map of individual metabolites can be reconstructed by least-squares fitting^{355,356}.

Efficient²¹⁵ spatial encoding is achieved with a single-shot center-out spiral to sample the full k -space³⁵⁷, yielding an efficient usage of the nonrenewable hyperpolarized signal. Contrary to an EPI readout, the spiral trajectory may start at the k -space origin, allowing a very short time delay between the RF excitation and start of acquisition to minimize T_2^* signal decay and maximizing the SNR efficiency³⁵⁸. Spiral readout trajectories are also relatively immune to motion³⁵⁹ and flow³⁶⁰ artifacts. 3D volumetric images can typically be obtained either by adding an additional phase encoding³⁶¹, or readout gradient^{362,363}.

Nevertheless, the performance of the IDEAL spiral CSI scheme may be severely impaired in presence of gradient trajectory imperfections and off-resonance effects due to static field inhomogeneity which will induce blurring and reduce the effective resolution^{215,324}.

The steps to achieve single-slice MRSI via the IDEAL spiral CSI scheme are schematically illustrated in Figure 6.1 and are described below:

1. First, to provide prior knowledge for the chemical-shift reconstruction, a spectrum of the slice is acquired. A slice-selective pulse α_1 is applied, typically a sinc-shaped, or calculated via the Shinnar-Le Roux algorithm³⁶⁴, then the free induction decay signal is measured. The remaining transverse magnetization is further destroyed by a gradient spoiler.

2. Secondly, a spiral-encoded image is acquired following a slice-selective pulse α_2 . The tip angle may be different from α_1 , however the pulse bandwidth must be identical to make sure that the same slice is measured. Here, the spiral trajectory starts at the origin of the k -space and evolves outwards under the constraints of a maximum gradient frequency close to the k -space center, then switching to the constraints of a maximum gradient slew rate and amplitude as the trajectory evolves outwards. Following the acquisition, the remaining transverse magnetization is then destroyed by a gradient spoiler.
3. Thirdly, the acquisition of the spiral-encoded image (2) is repeated in rapid succession for a total of N_E images. Typically, the echo timeⁱ is set to the minimal value TE_0 for the first readout, and is increased by an increment ΔTE in the following images of this series. Therefore $TE = TE_0 + (m - 1) \cdot \Delta TE$, $m = 1 \dots N_E$. TE_0 depends on the RF pulse length, as well as the duration of the slice-rephasing lobe.

The procedure (1)-(3) is performed for each of N_S slices, then is repeated at a time interval TR for each of the N_R repetitionsⁱⁱ.

6.2.2.1 Spectroscopic image reconstruction

The reconstruction of IDEAL spiral CSI images entails two main steps, as described by Wiesinger et al.³⁵³. For each slice out of N_S slices and N_R repetitions, the chemical-shift reconstruction deduces single-metabolite frequency-domain data from the train of shifted-echo images. Then, for each metabolite, the individual frequency-domain image is reconstructed into the spatial domain. The spectroscopic image reconstruction is detailed below and summarized in Figure 6.2.

6.2.2.2 Chemical-shift reconstruction

For each slice, one spectrum and N_E spiral images with echo times shifted by ΔTE were acquired within each repetition.

First, the slice-selective spectrum is computed from the free induction decay signal to determine the resonant frequencies ω_q , $q = \{1..N_M\}$, of each of the N_M metabolites.

Let $TE_m = TE_0 + (m - 1) \cdot \Delta TE$, $m = 1 \dots N_E$, be the echo time for the m^{th} spiral image defined as the time interval between the effective center of the RF pulse and the first data sampling

ⁱIn fact, this is not an echo in the strict sense, due to the absence of RF or gradient refocusing of spin magnetization. The echo time is here defined as the time interval between the effective center of the RF pulse and the acquisition of the k -space center, which is the first acquisition point of the spiral.

ⁱⁱHere, we define one repetition as the acquisition of one spectrum and N_E echo images for each of the N_S slices, therefore N_S spectra and $N_S \times N_E$ spiral images are acquired per repetition.

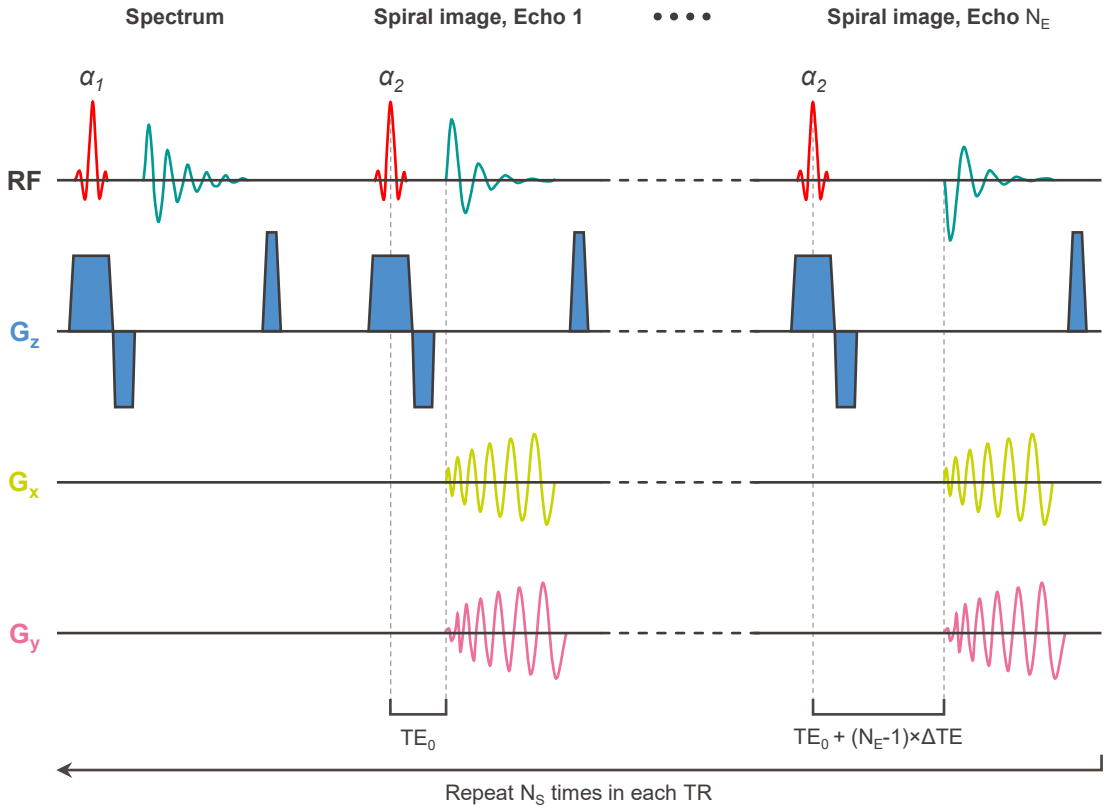


Figure 6.1: Schematic representation of the IDEAL spiral CSI sequence, for the acquisition of an axial (xy) slice. The sequence starts with a spectrum acquisition, using a slice selective RF pulse α_1 . In rapid succession, N_E spiral-encoded images are acquired following a slice-selective RF pulse α_2 and variable echo time $TE = TE_0 + (m - 1) \cdot \Delta TE$, $m = 1 \dots N_E$. Following each spectrum or image, a gradient spoiler destroys the remaining transverse magnetization. This scheme is repeated for all N_S slices within each repetition.

point. $y_{m,n}$, $n = 1 \dots N_{Sp}$, is the n^{th} measured data point at location k_n (in spatial frequency domain) out of N_{Sp} sampling points for the m^{th} image. Due to the echo time shifting, the time interval $\tau_{m,n}$ between the excitation and acquisition of the point k_n is shifted between each image: $\tau_{m,n} = TE_m + t_n$, where t_n is a time interval between the start of the spiral and the acquisition of k_n . t_n is incremented by the acquisition dwell time.

Let \mathbf{r}_p be a set of discretized spatial positions of our slice. The measured signal can then be expressed as the combination of the signal from each metabolite q at the spatial positions \mathbf{r}_p :

$$y_{m,n} = \sum_q e^{i\omega_q \tau_{m,n}} \sum_p \underbrace{e^{i\mathbf{k}_n \mathbf{r}_p}}_{F_{n,p}} x_q(\mathbf{r}_p) \quad (6.1)$$

The first exponential is a time-evolution term representing the signal precession at the resonant frequency ω_q of the metabolite q in the rotating frame. $F_{n,p}$ is the encoding component

Chapter 6. Improving the spatiotemporal efficiency of spectrally resolved ^{13}C MRI to probe the dynamic metabolic interplay in a mouse model of stroke

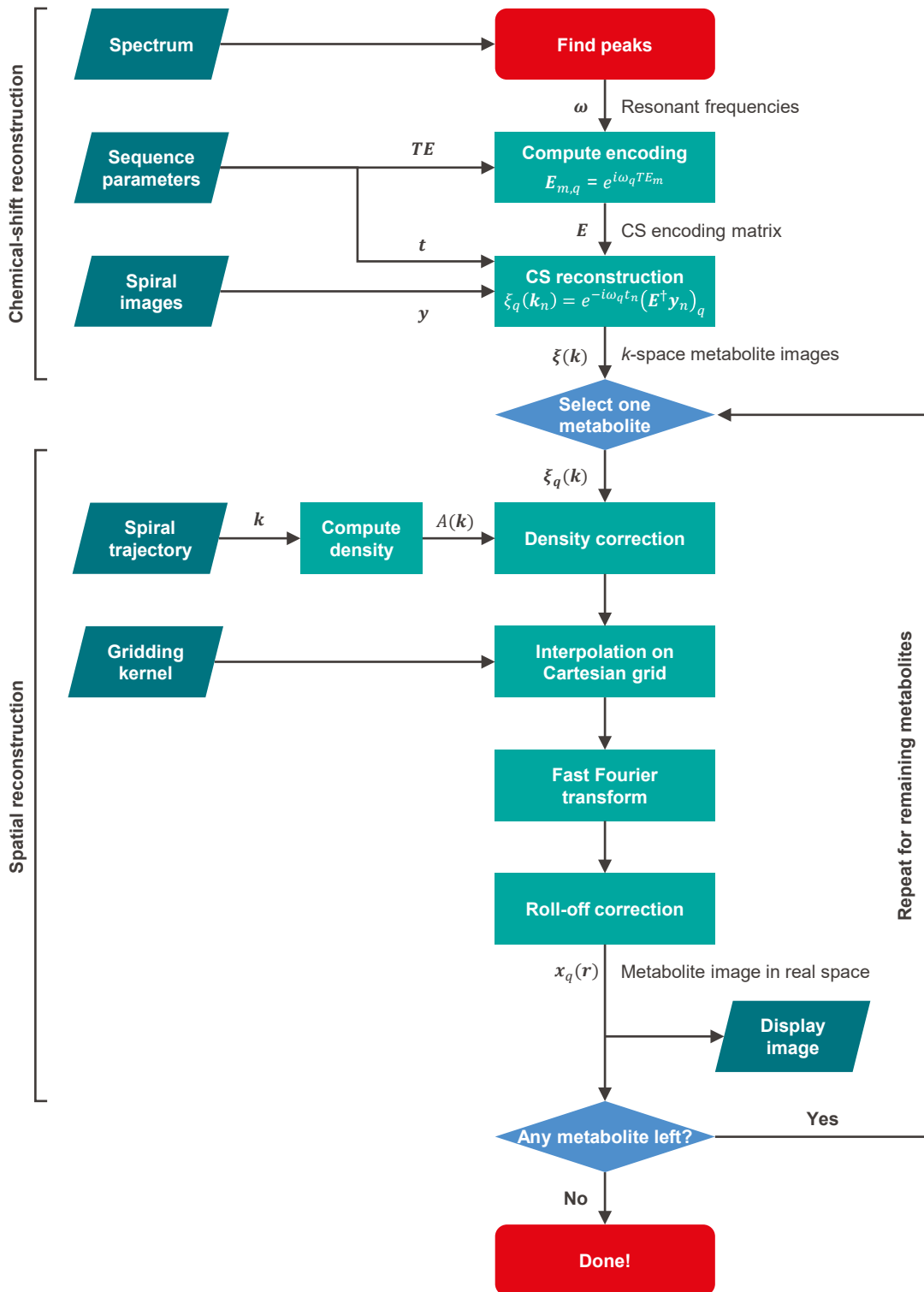


Figure 6.2: Flowchart of the spectroscopic image reconstruction, for a single slice and repetition.

giving the signal contribution from the spatial position \mathbf{r}_p to the k -point \mathbf{k}_n . $x_q(\mathbf{r}_p)$ denotes the signal intensity of the metabolite q at position \mathbf{r}_p . Summing the contributions of the metabolite q over all positions p and using $\tau_{m,n} = TE_m + t_n$ to split the time evolution in the echo time and acquisition time, one get:

$$y_{m,n} = \sum_q E_{m,q} e^{i\omega_q t_n} \xi_q(\mathbf{k}_n) \quad (6.2)$$

with the chemical-shift encoding matrix components $E_{m,q} = e^{i\omega_q TE_m}$ and the k -space contributions of the q^{th} metabolite $\xi_q(\mathbf{k}_n) = \sum_p F_{n,p} x_q(\mathbf{r}_p)$.

The chemical shift encoding matrix \mathbf{E} can be built from the sequence parameters and frequencies found in the slice-selective spectrum. Then, the chemical shift reconstruction is achieved by inverting the equation 6.2 to determine the k -space data for each metabolite:

$$\xi_q(\mathbf{k}_n) = e^{-i\omega_q t_n} (\mathbf{E}^\dagger \mathbf{y}_n)_q \quad (6.3)$$

Where \mathbf{E}^\dagger is the Moore-Penrose pseudo-inverseⁱ of \mathbf{E} .

The performance of the chemical-shift reconstruction depends on the condition number of the matrix \mathbf{E} , which would result in large noise amplification if it is ill-conditioned. The number of distinct echo times N_E needs to be equal or greater³⁵⁵ to the number of spectral components N_M , i.e., $N_E \geq N_M$. The optimal choice of echo time increment ΔTE can be determined by maximizing the effective number of signal averages (NSA)³⁶⁵:

$$NSA_q = \frac{1}{(\mathbf{E}^H \mathbf{E})_{q,q}^{-1}} \quad (6.4)$$

Where the CS encoding element similar to the one above additionally takes into account the transverse magnetization decay set to $T_2^* = 20$ ms in the simulations:

$$E_{m,q} = e^{i\omega_q TE_m} e^{-\frac{TE_m}{T_2^*}} \quad (6.5)$$

6.2.2.3 Spatial reconstruction

The chemical shift reconstruction described above provides the images $\xi_q(\mathbf{k})$ of individual metabolites q in the frequency domain. It remains to transform these into images \mathbf{x}_q in the spatial domain. Since they are encoded on a non-Cartesian grid using a spiral readout, a traditional fast Fourier transform cannot be directly applied. Many methods exist to re-

ⁱThe Moore-Penrose pseudo inverse is a generalization of the matrix inverse when the matrix may not be invertible. It finds the closest solution, in the least square sense, $\mathbf{A}^\dagger \mathbf{b} = \mathbf{x}$ to the system of linear equations $\mathbf{A}\mathbf{x} = \mathbf{b}$.

Chapter 6. Improving the spatiotemporal efficiency of spectrally resolved ^{13}C MRI to probe the dynamic metabolic interplay in a mouse model of stroke

construct non-Cartesian k -space datasets. Here, we opted for the regridding (or gridding) algorithm^{366,367} whose principles are as follows:

Firstly, the spiral readout scheme performs a non-uniform density encoding, with a higher sampling density at the k -space center compared to its periphery. Therefore, the contribution of each sampled point must be corrected accordingly. Using a Voronoi diagram, the area around each sampling point is computed³⁶⁸ then multiplied to the sampled value.

Secondly, the sampled data are interpolated onto a Cartesian grid. Each data point is convoluted and distributed on the frequency-domain grid. Ideally, the convolution would be an infinite sinc function³⁶⁷ because its Fourier transform is a boxcar function, which would therefore not affect the spatial domain image. Unfortunately, this is not feasible as it would require arrays of infinite dimensions. Instead, a smaller gridding kernel is used for the convolution, generally using the Kaiser-Bessel kernel^{369,370} providing the best image quality. To reduce interpolation artifacts, the gridding process is performed on an oversampled grid, for example, by doubling the number of data points in every direction. The data resampled onto the Cartesian grid undergoes a fast Fourier transform to reconstruct the spatial image. Since the Fourier transform of any other kernel than an infinite sinc is not a rectangular function, the spatial image must be deapodized, in a so-called roll-off correction.

6.3 Methods

6.3.1 MRI system

MR experiments were performed on a 14.1T/26cm pumped horizontal bore magnet (MagneX Scientific, Yarnton, UK), 1000 mT m^{-1} strength and 6450 $\text{T m}^{-1} \text{s}^{-1}$ slew rate shielded gradient set (BFG240-120-S12B, Resonance Research, Billerica, USA), interfaced to a BioSpec Avance NEO MRI console (Bruker BioSpin, Ettlingen, Germany) and running ParaVision 360 V3.2. Two $^1\text{H}/^{19}\text{F}$ and one X-nucleus (up to the frequency of ^{31}P) channels are available, each with a dedicated 1 kW broadband (15-650 MHz) RF amplifier and preamplifier module with an integrated active Tx/Rx switch. Additionally, four separate channels are available for receive-only coil arrays.

6.3.2 RF coils and animal setup

6.3.2.1 Design considerations

As mentioned in Section 6.2, the combined use of a ^{13}C volume transmit-coil with ^{13}C surface receive-coils is the favored approach to simultaneously achieve a high detection sensitivity and an uniform excitation profile, therefore facilitating the use of MRSI sequences as well as the dynamic signal analysis. In addition, a ^1H coil, typically integrated into the X-nuclei transmit-coil, is needed for the measurement preparation and standard anatomical imaging.

In the context of MRI, most volume coils, regardless of the operating frequency or dimensions, are built with a so-called birdcage design³⁷¹, which achieves a good B_1 field homogeneity, power efficiency, SNR, as well as a low power deposition. Unfortunately, birdcage coils are complex in design and may be difficult to manufacture. Instead, inspired by the work of Garbow et al.³⁷², we opted for a simpler solution, by building a pair of $^1\text{H}/^{13}\text{C}$ saddle coils. Although they achieve lower RF performances compared to birdcage coils³⁷³, this is unlikely to limit our applications, since the selected MRSI acquisition scheme only uses small flip angles at a low duty cycle.

Regarding the ^{13}C receive-only coil, we opted to include two receive loops to achieve better brain coverage compared to the single-loop linear coil used previously. While a phase array with more elements, typically in a 2×2 arrangement for small rodent brains, could enable accelerated image acquisition, the implementation of such a design would be difficult given the small mouse brain size. Moreover, while two receive elements can be easily geometrically decoupled and connected to conventional $50\ \Omega$ input impedance preamplifiers, the decoupling of phase arrays above two elements typically requires low-input impedance preamplifiers³⁷⁴, which are a scarce commodity in the MR community, and not readily available for the required frequency (150 MHz, ^{13}C at 14.1 T). This would therefore require either a custom order from a commercial supplier or designing custom circuits³⁷⁵, which both did not fit in the project timeline.

6.3.2.2 ^{13}C receive-only surface coil

The surface receive-only coil (Figure 6.3) is composed of two loop elements covering an area of $15 \times 25 \text{ mm}^2$ over the surface of a $\varnothing 16 \text{ mm}$ cylinder. The receive-element size was adjusted to provide full brain coverage, but not beyond. Each loop element is made of two turns of $\varnothing 1 \text{ mm}$ solid enameled copper wire (CUL 1,0, Block, Verden, Germany) wound around a 3D printed nylon PA12 coil former. The overlap was carefully adjusted to achieve a geometrical decoupling better than 30 dB.

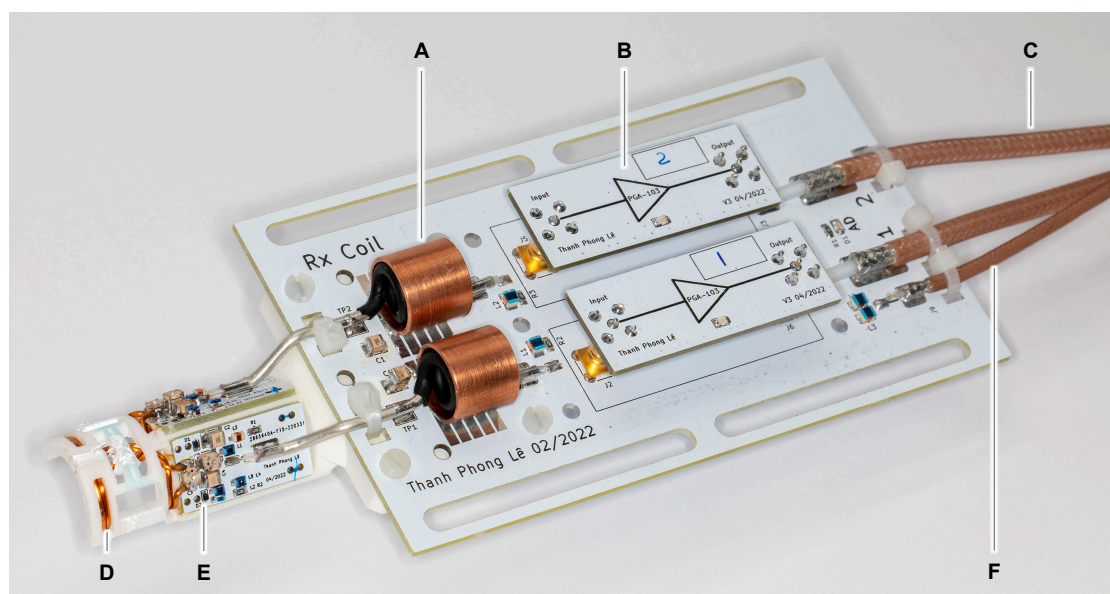


Figure 6.3: ^{13}C surface receive-only array for the mouse brain. This coil has two actively detuned loops covering a $15 \text{ mm} \times 25 \text{ mm}$ surface on curved surface with 8 mm radius. If required, a small tube (not shown) filled with water can be attached on the arc above both receive elements to assist with the positioning of the receive-coil. Balun (A); Preamplifier (B); RF cable for Rx signal (C); Loop element (D); Tuning, matching and active detuning circuit (E); Cable for active detuning current (F).

Each loop element was connected to a printed circuit board (Figure 6.4) for impedance matching and active detuning. Two stacks of a ceramic trimmer capacitor (Thin-Trim 9402-0, $0.5\text{-}2.5 \text{ pF}$, Johanson, Boonton, NJ, USA) onto a non-magnetic fixed-value porcelain capacitor (100B Series, American Technical Caramics, Huntington Station, NY, USA)¹ are used for tuning and matching (C1-C2 and C3-C4 in Figure 6.4). During transmission, each loop element is actively detuned by shifting the resonance frequency using two PIN diodes (D1 and D2, SMP1321-079LE, Skyworks, Irvine, California, USA) that connect a parallel capacitor (C5) when they are forwardly biased with about 50 mA supplied as a DC bias through the coaxial line (J1).

¹For a given capacitance value, stacking a small half-turn trimmer onto a fixed-value capacitor provides a substantially higher Q-factor compared to a larger half-turn trimmer capacitor.

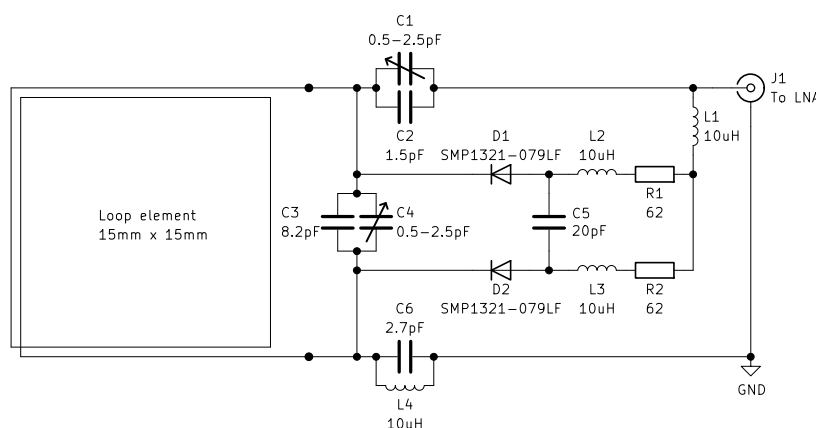


Figure 6.4: Simplified electrical diagram for one receive element. This circuit is connected to the preamplifier through a solenoid balun tuned to ^{13}C frequency to reduce common-mode currents. During transmission, the coil is detuned by applying a positive +5 V bias on J1 to forwardly bias both diodes D1 and D2 with 50 mA current each.

Each loop element is connected to an in-house made low-noise amplifier (24.9 dB gain, 0.53 dB noise figure at 150 MHz, based on PGA-103+, Minicircuits, Brooklyn, New York, USA), described and characterized in Appendix B, through a solenoid balun made of a semi-rigid coaxial cable (EZ_86_CT, Huber+Suhner, Herisau, Switzerland) looped inside a shielded copper tube and bridged with fixed-value capacitors. The preamplifier was placed parallel to the static field to reduce the Hall effect³⁷⁶.

At 150.75 MHz, the unloaded/loaded Q-factors measured using return loss measurements³⁷⁷ are 302/244 and 300/242 for the left and right loops, respectively, using a 15 mL centrifuge tube (16 mm OD) filled with 9 g L^{-1} NaCl in H_2O at 25°C as a load.

6.3.2.3 $^1\text{H}/^{13}\text{C}$ volume coil

The volume coil (Figure 6.5) has a $\varnothing 40\text{ mm}$ opening and is composed of two independent series saddle coils with a 120° aperture. The coils are arranged such that their respective B_1^+ are orthogonal to minimize mutual interactions. Both saddle coils are made of $\varnothing 1\text{ mm}$ single-stranded silver-plated copper wire (0.3% Ag, Kabeltronik, Denkendorf, Germany) wound around a 3D printed nylon PA12 coil former. The inner coil ($\varnothing 43\text{ mm} \times 35\text{ mm}$) is tuned to ^1H frequency (599.42 MHz) and provides a vertical linearly polarized B_1^+ field. The outer coil ($\varnothing 48\text{ mm} \times 40\text{ mm}$) is tuned to ^{13}C (150.75 MHz) and provides a horizontal linear B_1^+ field.

The impedance matching circuits are placed on a printed circuit board at the bottom of the coil, which also serves as a mechanical support to attach the coil assembly to the holder. An electrical diagram of the coils is found in Figure 6.6.

Chapter 6. Improving the spatiotemporal efficiency of spectrally resolved ^{13}C MRI to probe the dynamic metabolic interplay in a mouse model of stroke

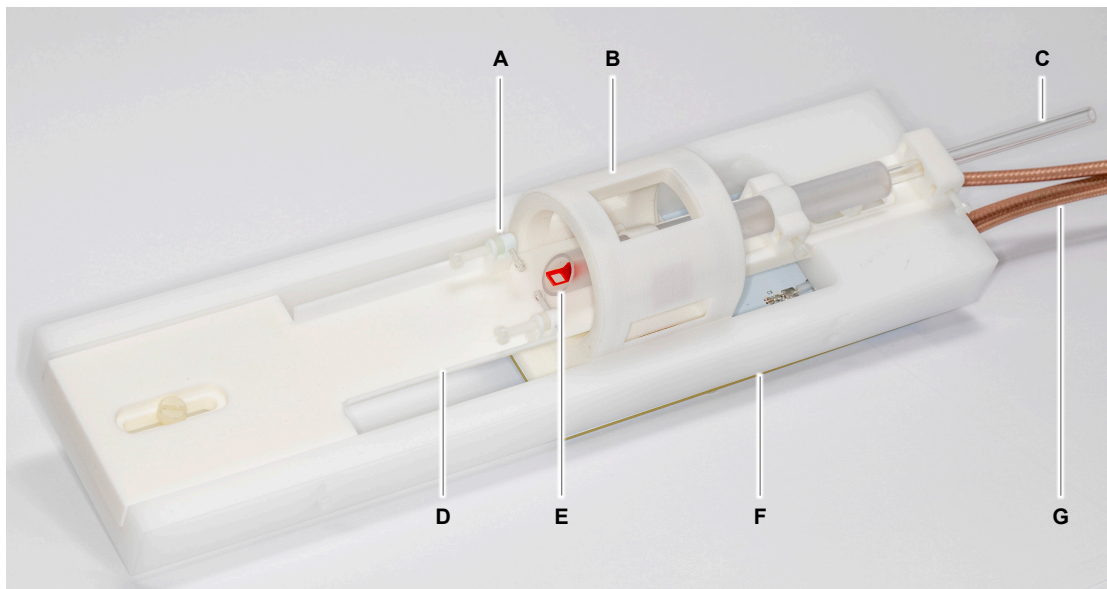


Figure 6.5: $^1\text{H}/^{13}\text{C}$ volume coil with integrated mouse holder and fixation device. Ear bar (A); ^1H and ^{13}C saddle coils housing (B); Animal ventilation inlet (C); Mouse bed (D); Bite bar and nose cone (E); Tuning, matching and active detuning board (F, below); RF and active detuning cables (G)

To avoid the buildup of standing waves between the lumped elements and achieve a proper resonant frequency with reasonable capacitor values, the ^{13}C coil was segmented once between the two loops, while the ^1H saddle coil was divided into 9 segments to keep each segment shorter than $\lambda/10$. Each coil was tuned and matched using non-magnetic fixed-value porcelain capacitors (100B Series, American Technical Ceramics, Huntington Station, NY, USA) and PTFE trimmer capacitors (C1-C4 in Figure 6.6, NMKJ10HVE, 0.5-9.0 pF, Knowles-Voltronics, Cazenovia, NY, USA). The PIN diode D1 on the ^{13}C coil is forward biased with 120 mA via J3 during transmission, and reverse biased during reception (MA4P1250NM-1072T, MACOM, Lowell, MA, USA) to detune the coil. The volume coil is attached to a dedicated base machined out of polyoxymethylene and a 3D printed mouse bed with a set of screws, which can be released to slide the coil along the bed in order to facilitate the animal positioning. The mouse head is immobilized by means of a bite bar, a pair of ear bars, and a nose cone.

All coils are interfaced to the magnet leg with RG_400_U coaxial cables (Huber+Suhner, Herisau, Switzerland) for RF, and K_02252_D-08 (Huber+Suhner) for the active detuning lines. The MRI console provides both the active detuning currents (tuned: +5 V, max 500 mA; detuned: -36 V, max -50 mA), as well as the bias voltages to power the preamplifiers (+10 V, max 200 mA per receive channel).

Chapter 6. Improving the spatiotemporal efficiency of spectrally resolved ^{13}C MRI to probe the dynamic metabolic interplay in a mouse model of stroke

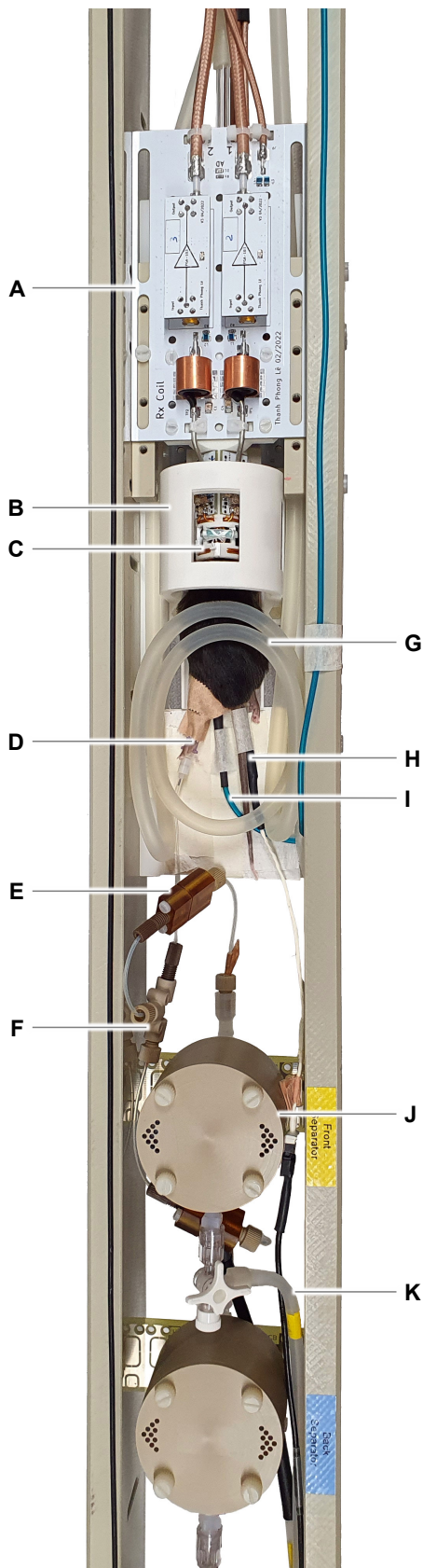


Figure 6.7: Setup for HP MRS(I) measurements in mice with up to two injections of HP substrates. ^{13}C Rx coil board (A); $^1\text{H}/^{13}\text{C}$ volume coil (B); ^{13}C Rx coil elements (C); Femoral vein catheter (D); One-way valve (E); Flow combiner for double-injection experiments (F); Water-heating hose (G); Thermometer (H); Tube for respiration monitor (I); Separator/infusion pump (J); Piston line (K).

6.3.3 RF coil characterization

The cross-coil setup was placed at the isocenter of the MRI scanner and loaded with a 14/16 mm ID/OD syringe filled with 400 mM [$1\text{-}^{13}\text{C}$] acetate and 10 mM Gd-DO3A-butrol in H_2O . The transmit power of the ^{13}C volume coil was calibrated using the MRI scanner automated protocol. Then, two ^{13}C gradient echo images 1 and 2 were acquired with nominal flip angles $\alpha_1 = 60^\circ$ and $\alpha_2 = 120^\circ$ in a 5 mm axial slice at the isocenter of the magnet, using $\text{TR} = 3.5$ s, $\text{TE} = 1.94$ ms, $20\text{ mm} \times 20\text{ mm}$ FOV, 20×20 matrix, 128 averages.

Following reconstruction of both images, the effective flip angle for each voxel was calculated using the double-angle method³⁷⁸:

$$\alpha_{1,\text{eff}} = \cos^{-1}\left(\frac{I_2}{2I_1}\right) \quad (6.6)$$

where $\alpha_{1,\text{eff}}$ is the effective flip angle for the nominal flip angle α_1 in the voxel with intensities I_1 and I_2 in the images 1 and 2, respectively.

Receive sensitivity maps were computed for combined and individual images from the receive array by normalizing the intensity of image 1 by the transmit field map for each voxel:

$$S = \frac{I_1}{\sin(\alpha_{1,\text{eff}})} \quad (6.7)$$

Finally, the homogeneity of these quantities was quantified using their coefficient of variation (ratio of the standard deviation to the mean) in a $10\text{ mm} \times 6\text{ mm}$ elliptic region of interest (ROI), corresponding to the approximate dimensions of the largest axial cross-section of the mouse brain.

For comparison purposes, the transmit field and sensitivity of the ^1H quadrature/ ^{13}C linear ($\varnothing 14/11$ mm) surface coil previously used in Chapter 5 was mapped with identical measurements.

6.3.4 Implementation of the IDEAL spiral CSI method

The vendor-provided global spectroscopy and spiral imaging methods SINGLEPULSE and SPIRAL, respectively, were modified and merged into a single method to achieve the slice-selective MRS followed by a train of shifted echo time Archimedean spiral-encoded images described in Section 6.2.2. The method was implemented such that the acquisition of multiple slices could be achieved in rapid succession. Dynamic shimming was implemented as well to allow optimizing the static field within each slice. However, this capability was not used for the experiments presented below as it did not show substantial improvements in earlier tests.

Chapter 6. Improving the spatiotemporal efficiency of spectrally resolved ^{13}C MRI to probe the dynamic metabolic interplay in a mouse model of stroke

The online image processing was deactivated. Offline image reconstruction was implemented in MATLAB R2021b, using the algorithm described in Section 6.2.2.1. The signal from either coil channels were reconstructed independently and further combined using the sum of squares method³⁷⁹. In our measurements, the metabolite frequencies did not substantially drift over the timecourse of the experiment, and were therefore kept identical for all repetitions.

The effective number of spatial averages (NSA) as a function of the echo time increment was computed for a series of 7 images using equation 6.4 and plotted on Figure 6.8. For the five metabolites observed following an injection of $[1-^{13}\text{C}]$ pyruvate, as observed in Chapter 2, the mean NSA would be maximal for $\Delta TE = 0.255$ ms (Figure 6.8A). However, from earlier results (Figure 5.11), only small $[1-^{13}\text{C}]$ alanine and $[^{13}\text{C}]$ bicarbonate signals are expected to be detected at 14.1 T, thus it is unlikely that they will be imaged. Therefore, only $[1-^{13}\text{C}]$ pyruvate, $[1-^{13}\text{C}]$ pyruvate hydrate and $[1-^{13}\text{C}]$ lactate were considered for the optimization of ΔTE , yielding an optimum at 0.230 ms (Figure 6.8B).

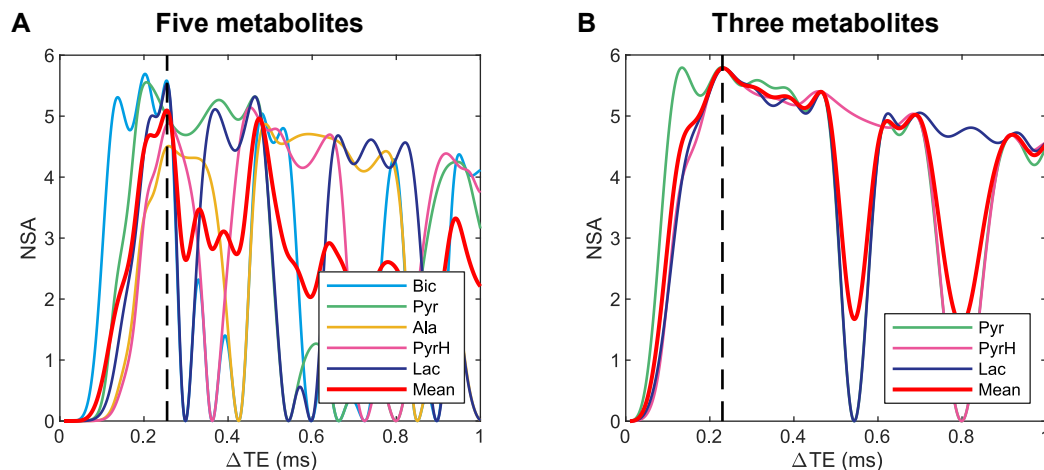


Figure 6.8: Effective number of spatial averages (NSA) for series with 7 images as a function of the echo time increment (ΔTE), for images containing (A) $[^{13}\text{C}]$ bicarbonate (161.1 ppm), $[1-^{13}\text{C}]$ pyruvate (171.1 ppm), $[1-^{13}\text{C}]$ alanine (176.7 ppm), $[1-^{13}\text{C}]$ pyruvate hydrate (179.4 ppm) and $[1-^{13}\text{C}]$ lactate (183.3 ppm), or (B) only $[1-^{13}\text{C}]$ pyruvate, $[1-^{13}\text{C}]$ pyruvate hydrate and $[1-^{13}\text{C}]$ lactate. The value maximizing the average NSA is 0.255 ms and 0.230 ms, respectively.

6.3.5 *In vitro* MRSI

The MRSI protocol was tested using a thermally-polarized multi-compartment phantom composed of a 14/16 mm ID/OD syringe filled with D_2O , in which four 5 mm NMR tubes were inserted. Each tube was filled with a different water solution of either sodium $[1-^{13}\text{C}]$ acetate 0.4 M, $[1-^{13}\text{C}]$ glycine 0.4 M, $[^{13}\text{C}]$ urea 0.4 M or both sodium $[1-^{13}\text{C}]$ acetate 0.2 M and $[1-$

^{13}C] glycine 0.2 M. Gd-DO3A-butrol (Gadovist®, Bayer, Leverkusen, Germany) was added to each solution to a final concentration of 10 mM to reduce the ^{13}C T_1 and shorten the repetition time.

Three 4 mm axial slices were acquired using the IDEAL spiral CSI sequence. For each slice, a slice-selective spectrum was acquired to provide prior information to the chemical shift image reconstruction with a 5° Shinnar–Le Roux (0.21 ms pulse length, 4200 Hz bandwidth) RF pulse followed by a 90 ms FID acquisition with 2048 points (22727 Hz or 150.8 ppm spectral bandwidth). 7 spiral images with minimum echo time $TE_0 = 1.196$ ms and increment $\Delta TE = 0.23$ ms were then acquired successively, each using a 10° Shinnar–Le Roux RF pulse (0.21 ms pulse length, 4200 Hz bandwidth), followed by a single-shot 20.65 ms spiral readout with 2065 points to obtain a 20 mm \times 20 mm FOV and 20 \times 20 image matrix (Figure 6.9). The spectra and spiral images from all slices were acquired in rapid succession and repeated every $TR = 2000$ ms. The transmission and reception working frequencies were set to 177.3 ppm, between $[1-^{13}\text{C}]$ glycine and $[1-^{13}\text{C}]$ acetate.

The measurement was averaged 256 times to achieve sufficient signal on the thermally-polarized phantom. ^{13}C MRSI images corresponding to each metabolite were then superimposed to ^1H images. Note that here, ΔTE was set to the same value as for *in vivo* experiments rather than to an optimal value for the phantom substrates.

To deduce the effective in-plane resolution, the spatial point spread function (PSF) of the spiral acquisition with the parameters listed above and corresponding trajectory (Figure 6.9) is simulated for a single 1 mm \times 1 mm pixel centered in the FOV, without and with the assumption of a 20 ms T_2^* decay.

6.3.6 *In vivo* MRSI

A 20 μL $[1-^{13}\text{C}]$ pyruvic acid sample doped with 15 mM of OX063 trityl radical (Albeda Research, Copenhagen, Denmark) was prepared and hyperpolarized during 150 min using the triple DNP probe as described in Section 5.3.

In the meantime, transient MCAO ischemic stroke was surgically induced in one C57BL6/J male mouse (8 weeks old, 25.9 g body weight) as described in Section 2.3.3. Following successful reperfusion, the animal was installed into the RF cross-coil setup, and loaded into the 14.1T MRI scanner.

The B_0 field homogeneity was optimized in the mouse brain using Paravision field map-based shimming procedures, yielding an estimated 42 Hz water linewidth in the brain volume. At 1.5 h post-reperfusion, the $[1-^{13}\text{C}]$ pyruvic acid sample was melted in a superheated buffer solution (60 mM tris(hydroxymethyl)aminomethane (TRIS) and 0.3 mM ethylenediaminete-

Chapter 6. Improving the spatiotemporal efficiency of spectrally resolved ^{13}C MRI to probe the dynamic metabolic interplay in a mouse model of stroke

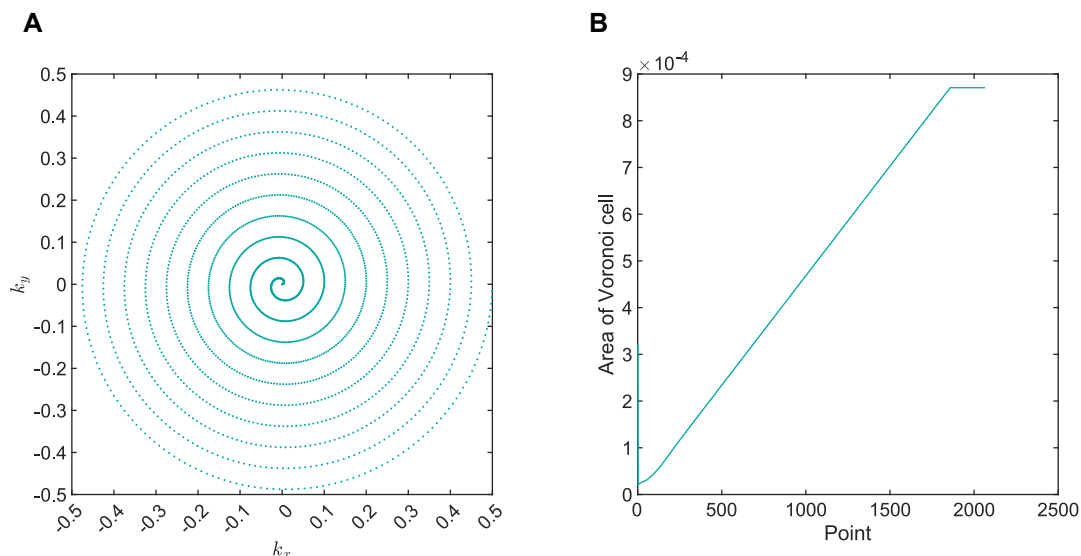


Figure 6.9: (A) k -space trajectory of the spiral readout for a final 20×20 matrix size. 2065 points are acquired in 20.65 ms. The maximum gradient frequency was set to 500 Hz. The maximal gradient strength is 143 mT m^{-1} . (B) Area in reciprocal space associated to each of the k -points, normalized to unity. In the last turn (points with no outer neighbor), the area was kept constant. The density is the inverse of the area of these regions.

traacetic acid (EDTA) in D_2O at pD 7.6 and 180°C), neutralized with NaOH, and transferred to a separator/infusion pump. Then, a therapeutic $325 \mu\text{l}$ bolus of 80 mM $[1-^{13}\text{C}]$ pyruvate was injected into the femoral vein of the mouse, corresponding to a dose of $1.04 \mu\text{mol g}^{-1}$. The $[1-^{13}\text{C}]$ pyruvate polarization at the time of injection was about 30%, as measured in separate pilot experiments.

The acquisition was automatically started 1 s after the beginning of the infusion, and dynamic imaging was performed using the IDEAL spiral CSI sequence described above, using the same sequence parameters as in Section 6.3.5, except that the measurements were repeated 60 times with $\text{TR} = 2 \text{ s}$ without averaging. The working frequency was centered between $[1-^{13}\text{C}]$ lactate and $[1-^{13}\text{C}]$ pyruvate at 177.3 ppm. Lactate could be imaged up to 60 s post-injection.

6.3.7 MRSI data analysis

Dynamic MRSI images were reconstructed as described above then overlaid on corresponding ^1H anatomical images. Within the brain region, the lactate-to-pyruvate ratio (LPR) was calculated voxel-wise for each pair of lactate-pyruvate image. In both images of individual time points as well as the averaged time course of the HP measurement, brain masks were applied to both the left and right hemispheres to quantify and compare the metabolites signal intensity within either side of the brain.

6.4 Results

6.4.1 RF coil characterization

The B_1^+ profile of the RF cross-coil setup, normalized to the nominal flip angle, is displayed in Figure 6.10A. Since the signal was detected using the receive-coil array, the transmit field map is not reliable in the lower region of the phantom due to the restricted coverage. Within a 10 mm × 6 mm elliptic region of interest corresponding to the largest axial cross-section of the mouse brain (grey contour in Figure 6.10), the coefficient of variation of B_1^+ was 3.0%. The reference power, which is the power at the coil plug required to achieve a 90° 1 ms hard pulse was 7.9 W, which translates into a B_1^+ efficiency of $8.2 \mu\text{TW}^{-\frac{1}{2}}$.

Receive sensitivity maps are reported on Figure 6.10B for the combined array and Figure 6.10C-D for individual loops. The sensitivity profile is sufficient to cover a 10 mm × 6 mm ellipse, roughly the mouse brain, however with a coefficient of variation of 21.3%.

For comparison, the 11 mm ^{13}C linear Tx/Rx surface coil, used for the measurements presented in Chapter 5), has a coefficient of variation of 13.8% and 38.3% on the transmit field and receive sensitivity, respectively (Figure 6.11), as well as an average SNR in the ROI lower by 23% compared to the volume-transmit/surface-receive RF cross-coil setup.

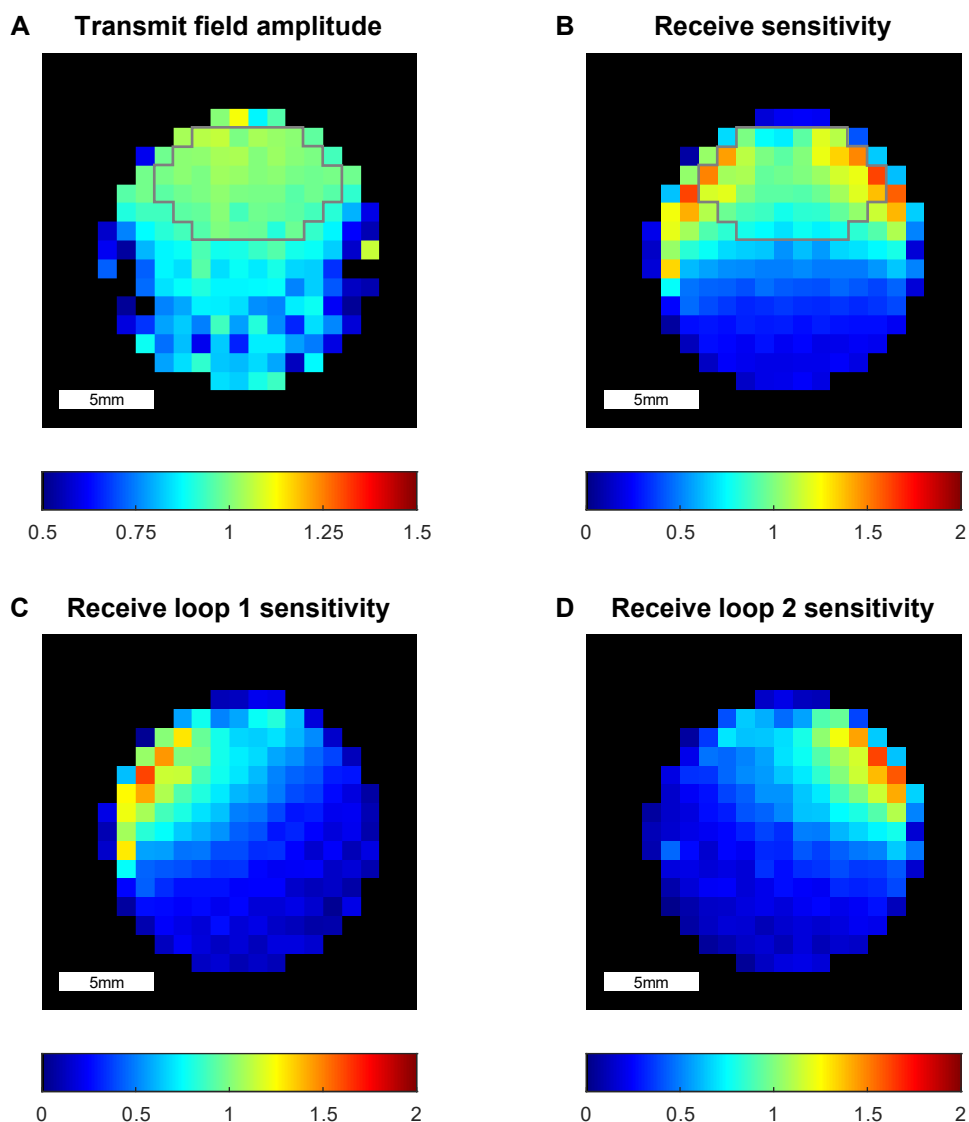


Figure 6.10: (A) ^{13}C transmit field amplitude map of the ^{13}C volume coil, measured in a 5 mm slice longitudinally centered with respect to the Tx and Rx coils. The transmit field map was normalized to the nominal flip angle. (B) Sensitivity map of the mouse head 2-loop ^{13}C receive-coil, following combination of both channels and correction of the signal intensity for the effective flip angle. The gray contour delimits the 10 mm \times 6 mm ellipse in which the B_1^+ amplitude and sensitivity homogeneity were characterized. (C-D) Sensitivity map of each ^{13}C receive loop. All sensitivity maps were set to the same scale, normalized to the value at the center of the ROI.

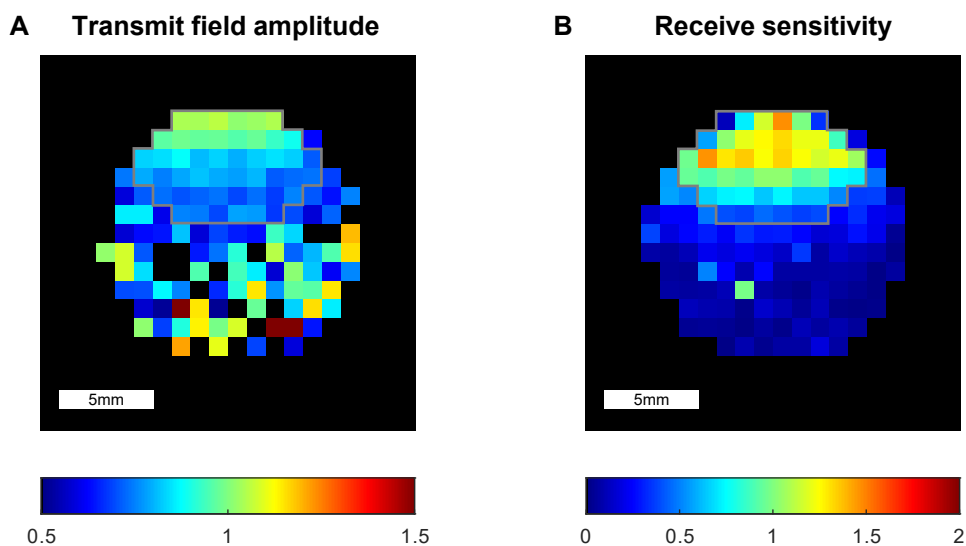


Figure 6.11: Characterization of the $\varnothing 11$ mm ^{13}C linear surface coil: B_1^+ amplitude (A) and receive sensitivity (B). The gray contour delimits a region of interest corresponding to the mouse brain cross section.

6.4.2 *In vitro* MRSI

Figure 6.12 depicts a ^{13}C spectroscopic image acquired in a multi-compartment phantom using the multislice IDEAL spiral CSI sequence. ^{13}C images were superimposed on a ^1H image, confirming that a proper spatial localization was achieved.

Although the [^{13}C] urea compartment had an equivalent concentration than the [$1\text{-}^{13}\text{C}$] acetate and [$1\text{-}^{13}\text{C}$] glycine compartments, the signal detected was substantially lower due to the distance to the receive-coil elements.

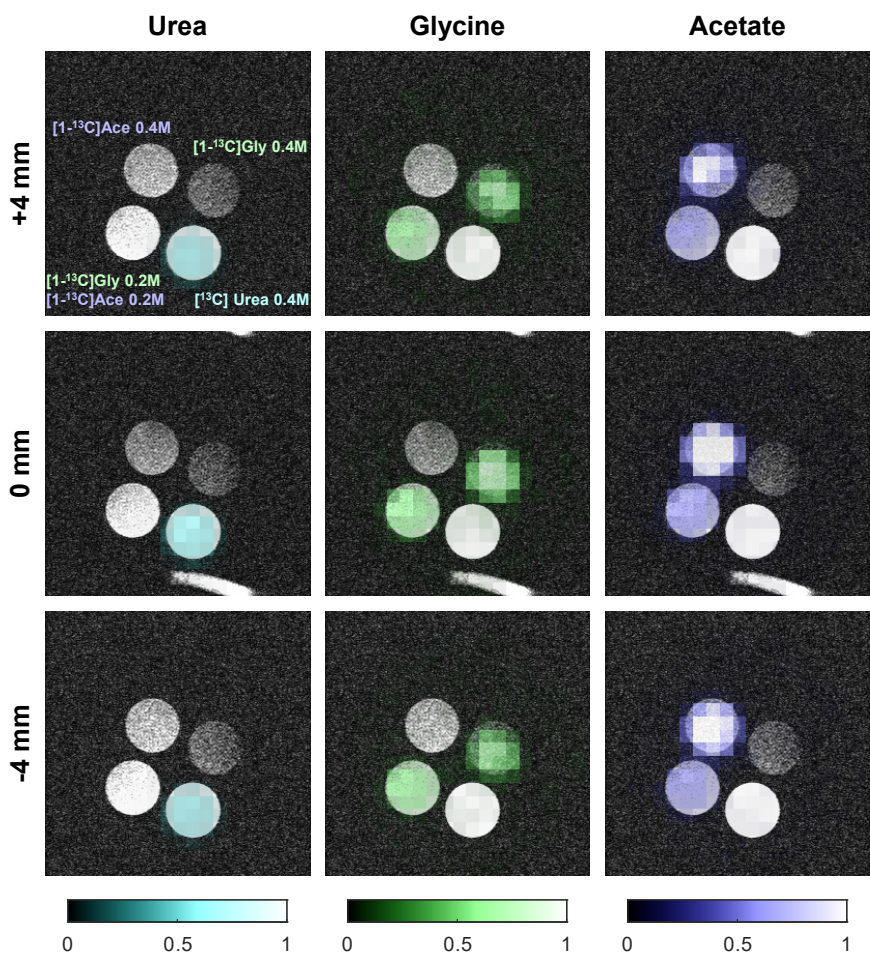


Figure 6.12: Multislice MRSI acquired in a phantom using the IDEAL spiral CSI sequence. In clockwise order from the uppermost compartment, the tubes contain water solutions of sodium $[1-^{13}\text{C}]$ acetate 0.4 M, $[1-^{13}\text{C}]$ glycine 0.4 M, $[^{13}\text{C}]$ urea 0.4 M, both sodium $[1-^{13}\text{C}]$ acetate 0.2 M and $[1-^{13}\text{C}]$ glycine 0.2 M. Gd-DO3A-butrol 10 mM was added to each tube to reduce the ^{13}C longitudinal relaxation time.

From simulations of the point spread function of the spiral acquisition, the effective in-plane resolution is 1.44 mm (measured at the FWHM of the PSF profile) for the nominal 1 mm spatial resolution, (Figure 6.13A-B). After assuming a typical T_2^* decay of 20 ms, which acts as a natural apodisation, the PSF is broadened to 1.56 mm at the FWHM (Figure 6.13C-D), and to 1.61 mm after adding a frequency offset of 5 Hz to account for the typical static field inhomogeneity observed in our experiments (Figure 6.13E-F).

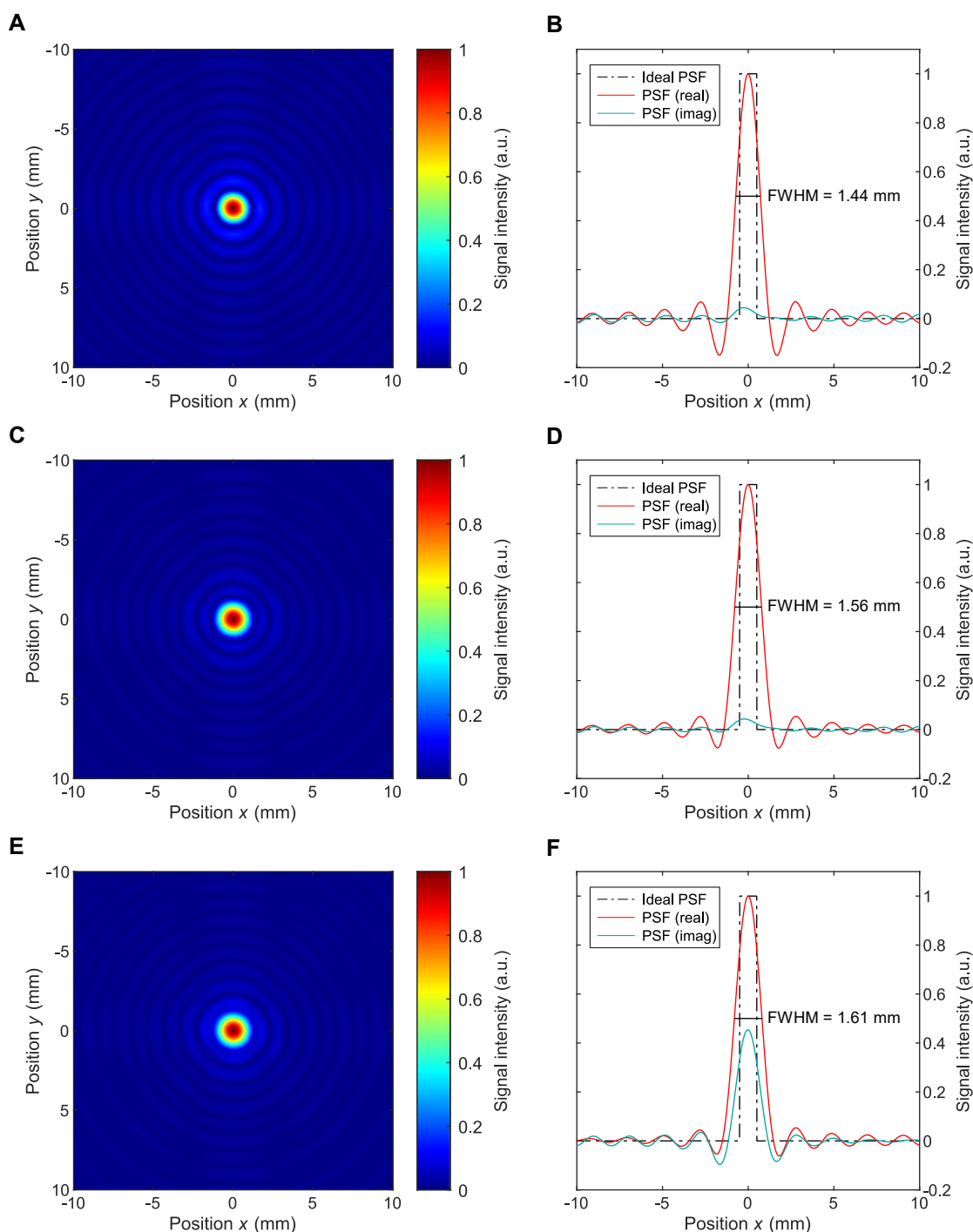


Figure 6.13: Spatial point spread function **(A)** of the spiral acquisition with a final 20×20 matrix and $20 \text{ mm} \times 20 \text{ mm}$ field of view, simulated for a single $1 \text{ mm} \times 1 \text{ mm}$ pixel centered in the FOV. **(B)** Profile of the PSF, the effective resolution is 1.44 mm for a nominal 1 mm pixel width. The maximum peak-to-peak amplitude of the side lobes is 21.9% of the maximum signal intensity. **(C-D)** Spatial PSF and PSF profile simulated while assuming a T_2^* decay of 20 ms , decreasing the side lobes amplitude to 12.9% . **(E-F)** Spatial PSF and PSF profile assuming a T_2^* decay of 20 ms and 5 Hz off-resonance frequency.

6.4.3 *In vivo* MRSI

Following the surgically-induced stroke, ^1H images acquired in the mouse brain depicted an ischemic lesion located in the striatum, on the right-hand side of the anterior slice (Figure 6.14). The three images displayed are located in the middle of the three 4 mm axial slices considered for ^{13}C MRS and MRSI. The static field inhomogeneity, computed from the B_0 maps as the standard deviation of the water frequency within the brain volume, was 42.4 Hz which corresponds to 10.7 Hz in ^{13}C frequency.

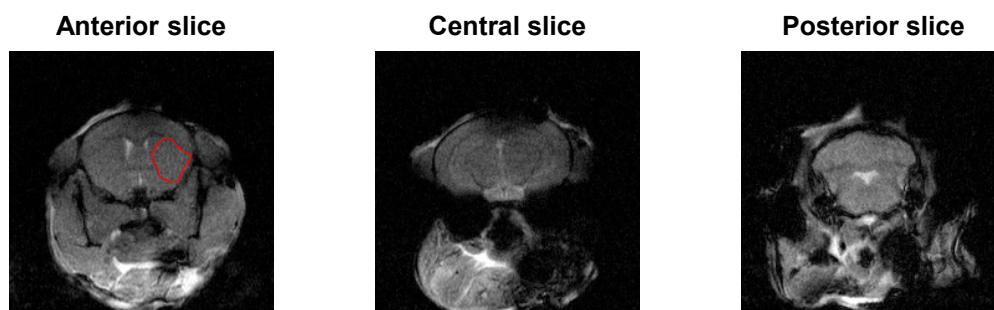


Figure 6.14: Axial proton images representing the slices in which dynamic slice-selective MR spectra and spectroscopic images were acquired. The surgically-induced ischemic lesion is located on the right-hand side of the anterior slice and highlighted in red.

Dynamic slice-selective spectra (Figure 6.15) acquired prior to spiral-encoded images depict the arrival of pyruvate and its conversion into lactate. The metabolite resonance frequencies were deduced from these spectra and used as prior knowledge for the image chemical-shift reconstruction. Within the anterior slice, multiple pyruvate and pyruvate hydrate peaks, around 171 ppm and 179 ppm respectively, are observed, while lactate resonates at a single frequency. In these measurements, neither alanine nor bicarbonate was detected.

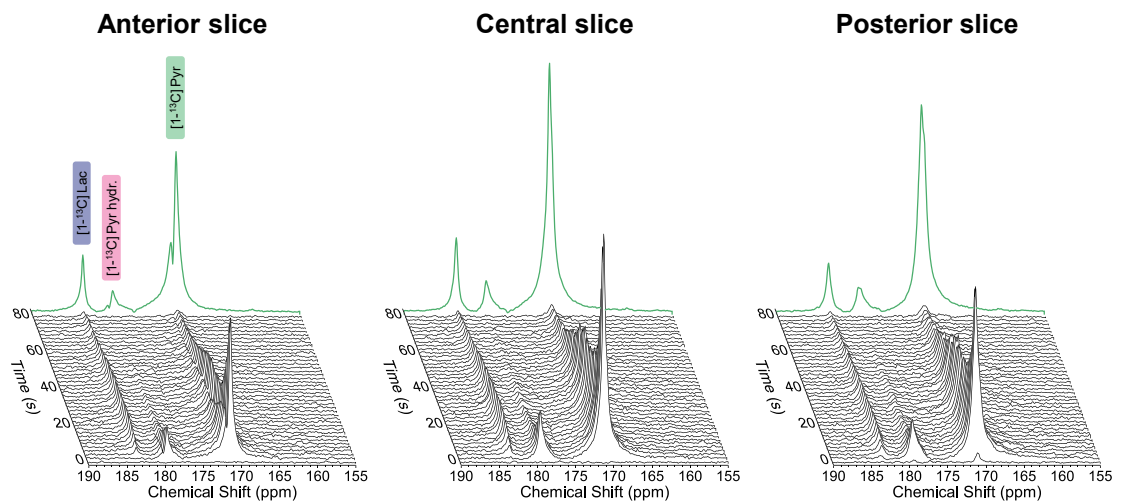


Figure 6.15: Dynamic slice-selective cerebral ^{13}C MRS acquired after a bolus infusion of $[1-^{13}\text{C}]$ pyruvate in a stroke mouse. A 25 Hz line broadening is applied to the signals, and the magnitude component is displayed. The green curve represents the summed signal. The same vertical scale was applied to all three slices. HP $[1-^{13}\text{C}]$ pyruvate (171.1 ppm), was converted into $[1-^{13}\text{C}]$ lactate (183.3 ppm). No $[1-^{13}\text{C}]$ alanine nor $[^{13}\text{C}]$ bicarbonate signal could be observed in these experiments. In the anterior slice, multiple peaks are found for pyruvate and pyruvate hydrate, which is likely the result of distinct compartments and static field B_0 inhomogeneity.

Dynamic ^{13}C spectroscopic images were acquired in an MCAO mouse following a bolus injection of HP $[1-^{13}\text{C}]$ pyruvate within three 4 mm axial slices (Figures 6.16, 6.17 and 6.18). They depict the rapid influx of both pyruvate and pyruvate hydrate followed by slower labeling of lactate. Pyruvate and pyruvate hydrate signals were detected both inside the brain and in surrounding tissues, while lactate was predominantly detected within the brain.

For each slice, the pyruvate and lactate signals as well as their ratios were quantified at each time point on either side of the brain (Figures 6.19 and 6.20). The signal of both metabolites was systematically lower in the ipsilateral hemisphere. In the anterior slice, the LPR increases earlier and faster on the lesion side compared to contralateral tissues, while a comparable dynamic is observed on both sides in remaining slices.

Chapter 6. Improving the spatiotemporal efficiency of spectrally resolved ^{13}C MRI to probe the dynamic metabolic interplay in a mouse model of stroke

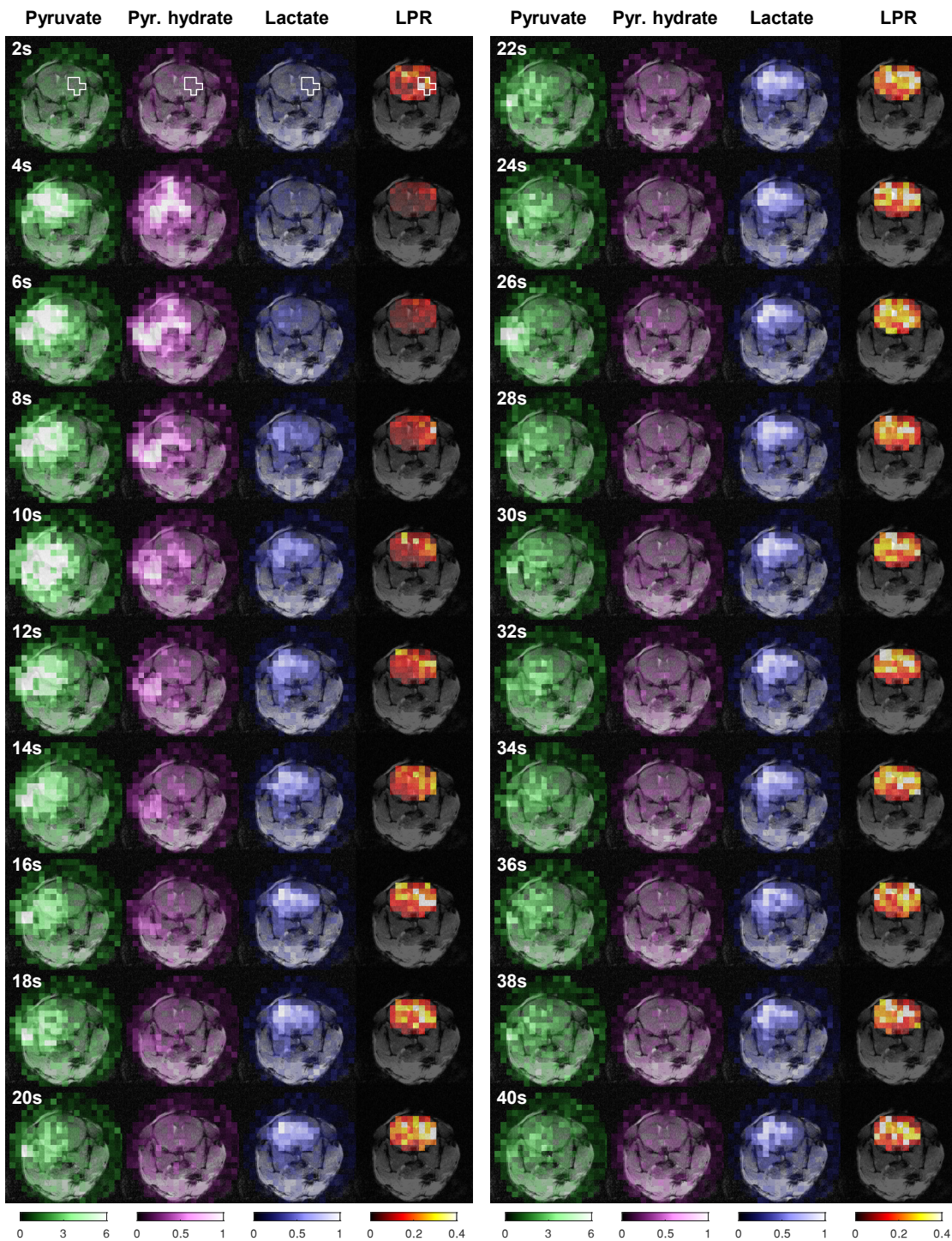


Figure 6.16: Anterior slice of the dynamic MRSI acquired in an MCAO transient stroke mouse after a bolus injection of HP [1- ^{13}C] pyruvate overlaid on anatomical ^1H images. A rapid influx of pyruvate and pyruvate hydrate is observed in the first repetitions before a slower and more diffuse labeling of lactate. No zero-filling, filtering or masking was applied on metabolite images. The voxel-wise lactate-to-pyruvate ratio (LPR) is reported within the brain region.

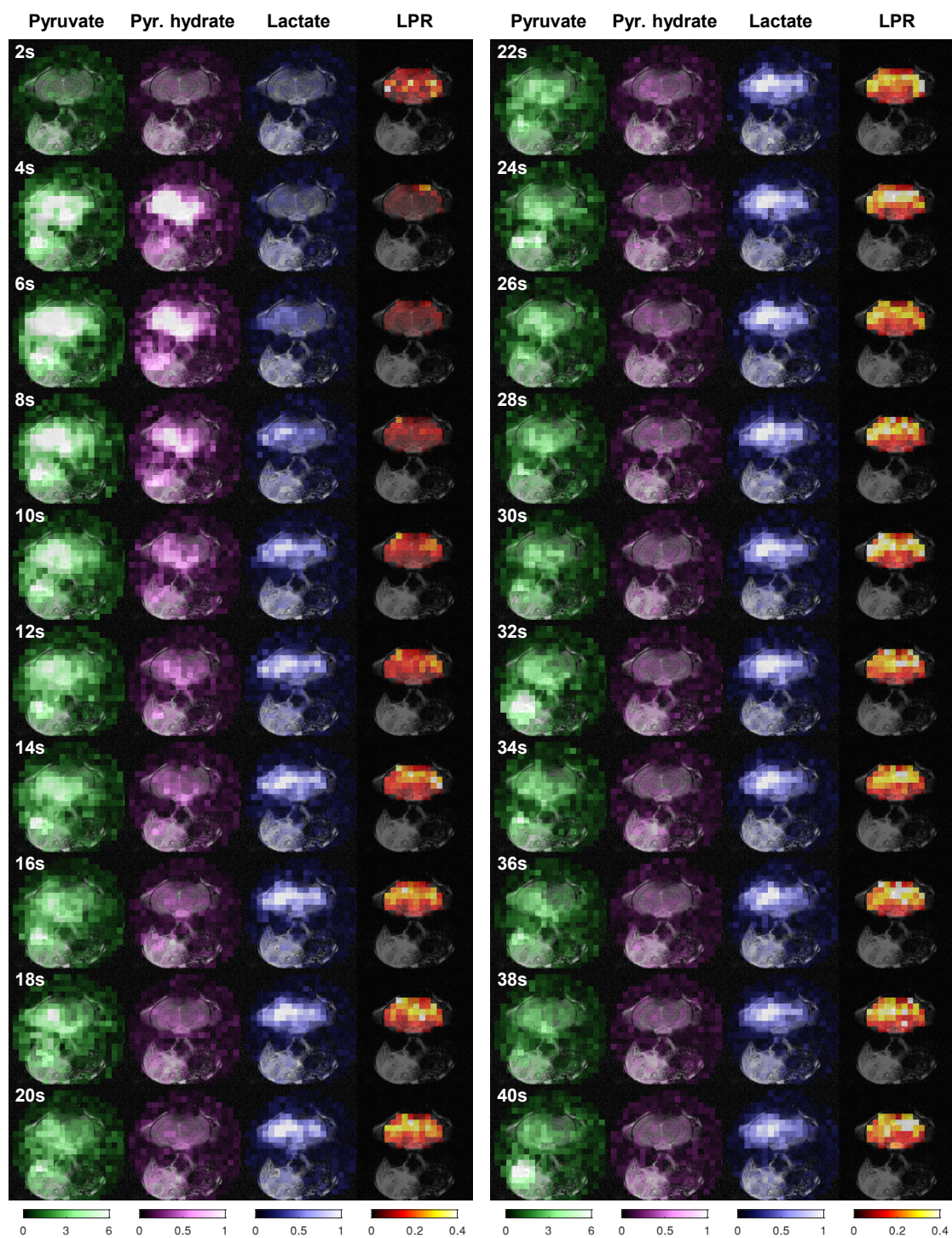


Figure 6.17: Central slice of the dynamic HP MRSI acquired in an MCAO mouse.

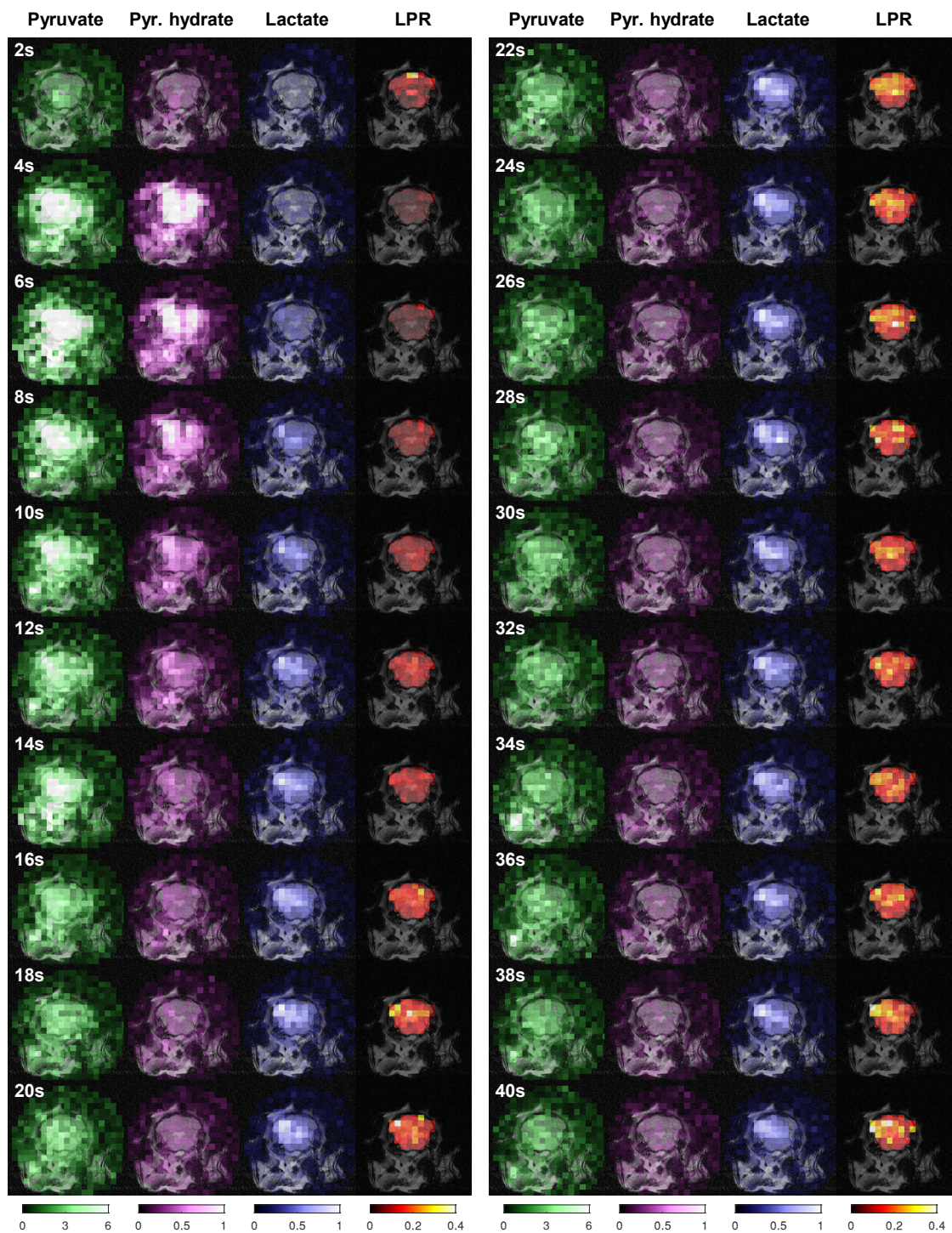


Figure 6.18: Posterior slice of the dynamic HP MRSI acquired in an MCAO mouse.

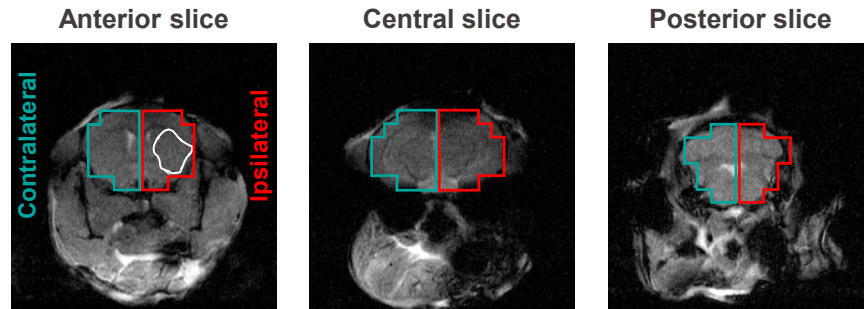


Figure 6.19: Regions of interest for comparing the metabolites signals between either brain sides. The contour of the stroke lesion is marked in white.

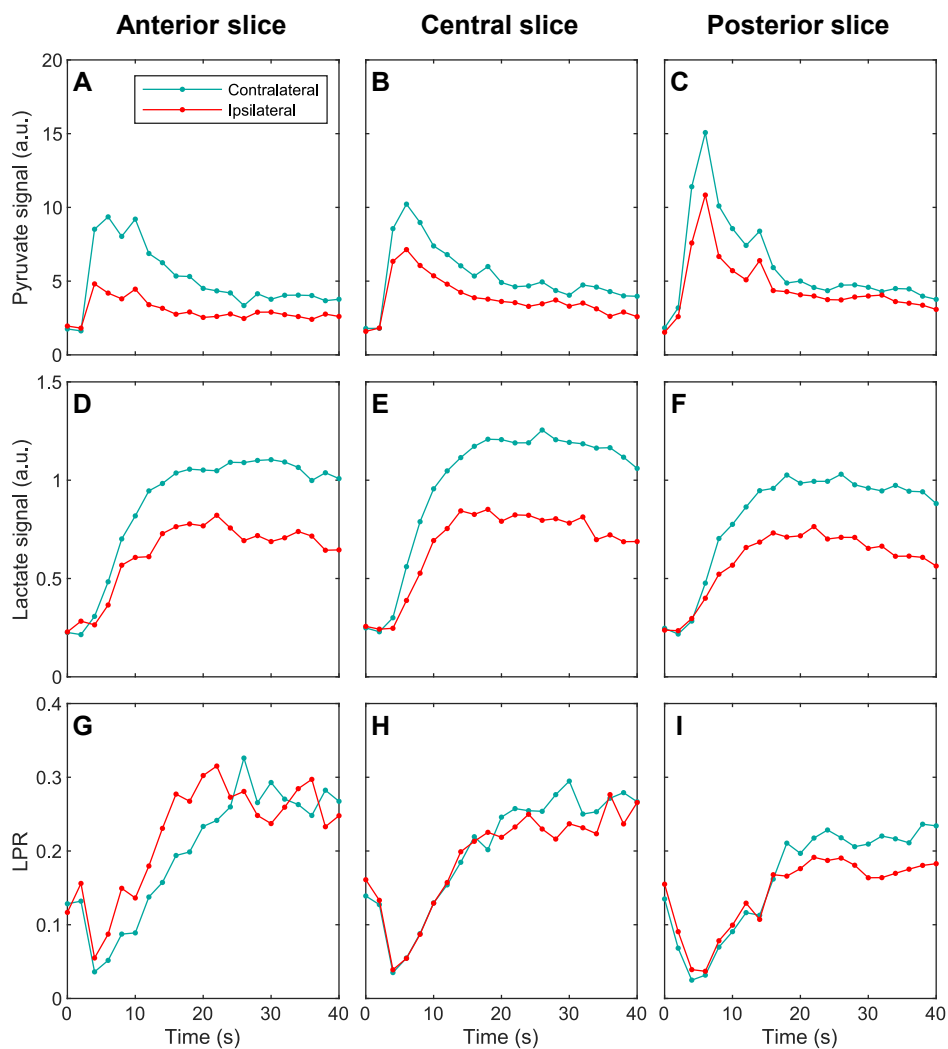


Figure 6.20: Time course of $[1-^{13}\text{C}]$ pyruvate and $[1-^{13}\text{C}]$ lactate signals and their ratio on either brain sides and within each slice. In overall, lower signals are observed in the ipsilateral hemisphere (A-F). In the anterior slice, where the lesion is located, the LPR rises earlier and faster in the ipsilateral compared to the contralateral side (G). Remaining slices measure similar dynamics on either brain sides (H-I).

Chapter 6. Improving the spatiotemporal efficiency of spectrally resolved ^{13}C MRI to probe the dynamic metabolic interplay in a mouse model of stroke

Time-averaged metabolite and ratio maps are reported in Figure 6.21. Quantified signals and ratios on either side of the brain are reported in Figure 6.22. In general, higher signals of both lactate and pyruvate are observed in the contralateral brain hemisphere. A higher LPR is found in the ipsilateral striatum, which is located on the right-hand side of the anterior slice, while the remaining slices show a comparable LPR on both brain sides.

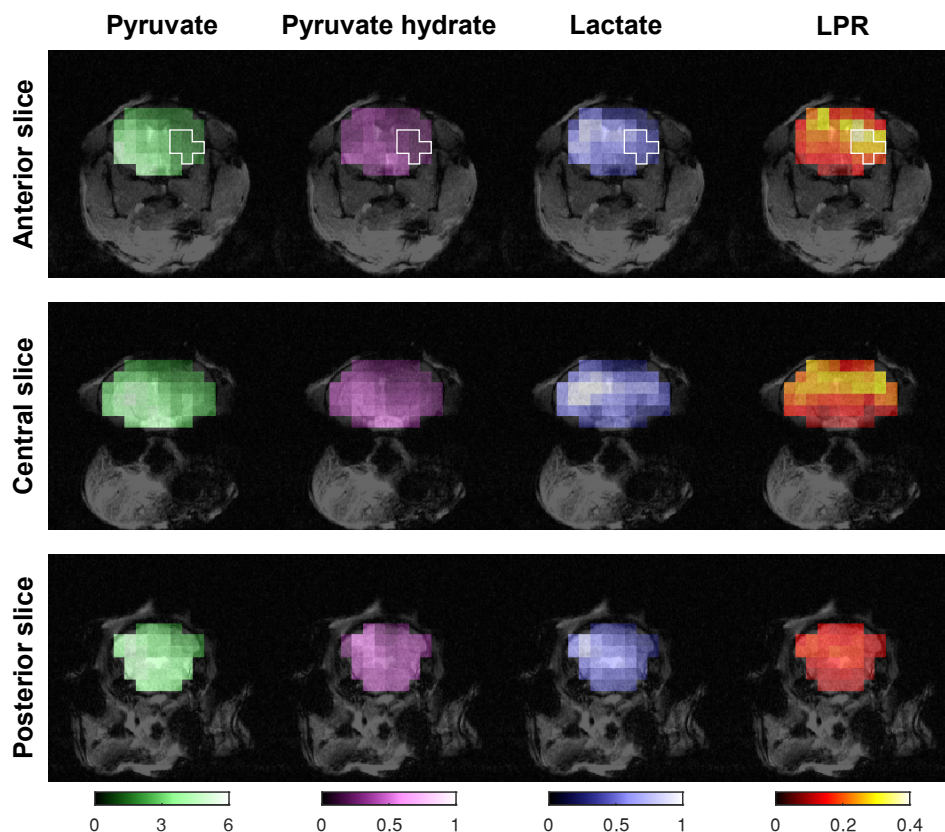


Figure 6.21: $[1-^{13}\text{C}]$ pyruvate, $[1-^{13}\text{C}]$ pyruvate hydrate, $[1-^{13}\text{C}]$ lactate and lactate-to-pyruvate ratio (LPR) maps averaged over the repetitions 3 to 21, 4 s to 40 s post-injection. In the anterior slice, a higher LPR is observed in the region of the striatum affected by transient ischemia, while remaining slices display a comparable LPR on either side of the brain.

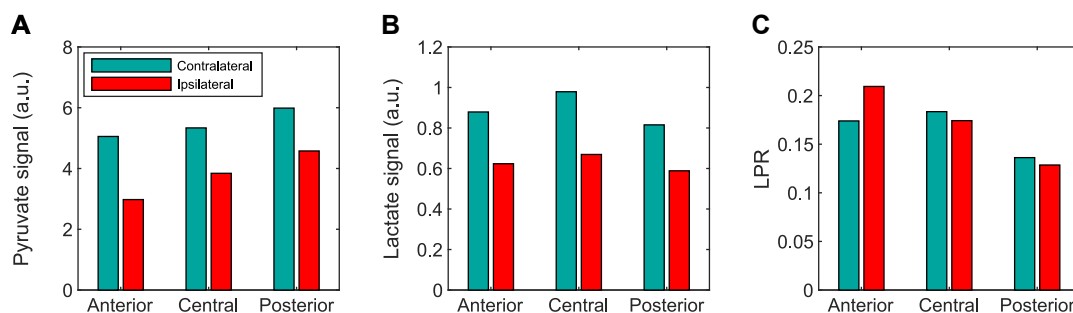


Figure 6.22: Average signals and ratios quantified within either side of the brain for each slice over the repetitions 3 to 21 of the dynamic acquisition. (A-B) In overall, both lactate and pyruvate signal intensities are lower in the ipsilateral hemisphere compared to the contralateral hemisphere. (C) In the anterior slice, where the ischemic lesion is located, a higher LPR is detected in the ipsilateral side, while the remaining slices containing no lesion display a similar LPR on either side.

6.5 Discussion

This chapter discusses the upgrade of several aspects of our HP MRI setup, and focused on enabling dynamic metabolic imaging in the mouse brain to overcome the technical limitations of our previous global MRS measurements (Chapters 2 and 3). In this part of the project, the acquisition sensitivity and efficiency were boosted by the implementation of an advanced RF cross-coil setup and MRSI sequence. Together with substantial improvements of the dDNP polarizer leading to a better liquid-state polarization (Chapters 4 and 5), we successfully imaged the dynamic metabolic response of the mouse brain after stroke-reperfusion to a bolus of HP [1- ^{13}C] pyruvate, highlighting new metabolic contrasts between ischemic and healthy tissues.

The studies presented in Chapters 2-5 used dual-frequency surface coils³⁸⁰. While they are optimal for both global and single-voxel spectroscopy, they do not provide a homogeneous excitation and reception profile, rendering them less suitable for MRSI. Here, we conceived a specific $^1\text{H}/^{13}\text{C}$ RF cross-coil setup for the mouse brain to provide both better coverage and sensitivity. A transmit $^1\text{H}/^{13}\text{C}$ volume coil achieved a homogeneous ^{13}C excitation profile, while a 2-loop receive-only ^{13}C surface coil was used to acquire the MR signal throughout the brain with high sensitivity. In MR acquisitions of small samples such as the mouse brain, the sample noise contribution is typically smaller than the thermal noise contribution of room-temperature loop elements and receiver chain^{323,381}. Therefore, particular attention was required in the receive-coil design to achieve the highest sensitivity. Here, the physical size of the impedance matching circuit was minimized to reduce the length of electrical traces, and the loop elements were soldered directly to tuning capacitors to reduce the number of solder joints that account for a substantial proportion of circuit losses³⁸². A substantially more

Chapter 6. Improving the spatiotemporal efficiency of spectrally resolved ^{13}C MRI to probe the dynamic metabolic interplay in a mouse model of stroke

efficient receive path is achieved by placing the preamplifiers on the coil itself. Compared to the case of a Tx/Rx coil using the stack of preamplifiers provided by the spectrometer manufacturer, this removes 3.5 m of cables and a Tx/Rx switch, lowering the noise figure of the receive chain by an estimatedⁱ 1.45 dB. In other words, this increases the SNR by 40%. A substantially better sensitivity could be achieved with cryogenically-cooled RF receive elements and preamplifiers, particularly for X-nuclei applications, because the proportion between coil and sample losses increases as the frequency decreases. For mouse brain coils, a typical sensitivity gain of 4-fold at 100 MHz³⁸³ (^{13}C at 9.4 T), 2-fold at 200 MHz³⁸⁴ (^1H at 4.7 T), 2.5-fold at 400 MHz³⁸⁵ (^1H at 9.4 T) have been reported. However, cryogenic coils require substantial technical infrastructure and constraints that are out of the scope of this work.

The receive sensitivity profile was evaluated in a homogeneous phantom, depicting a coverage equivalent to the largest mouse brain cross-section. With two larger receive elements, a broader and more homogeneous coverage was achieved compared to the linear ^{13}C coil previously used for global MRS at 14.1 T (Chapter 5). Specifically, the new coil enables the deepest brain regions to be imaged, with an average SNR higher by 29% in the axial brain cross-section. Nevertheless, the sensitivity was inhomogeneous in the immediate vicinity of the receive elements, which could be optimized in future revisions of the coil using electromagnetic simulations. This does not affect the analysis of the voxel-wise metabolite ratios, since the maps of all metabolites are similarly affected by the inhomogeneous sensitivity profile. The measurements show as well that the sensitivity drops beyond the brain volume, which helps to attenuate noise and signals from undesired tissues that could contaminate the acquired image.

The IDEAL spiral CSI sequence was implemented on our MRI scanner. Thanks to the efficient spectral and k -space encoding scheme, thus sparing the non-replenishable hyperpolarized signals, fast and dynamic MRSI acquisitions were enabled. The acquisition scheme was tested on a multi-compartment phantom, and confirmed that a proper chemical shift separation and spatial localization were achieved. In particular, these results suggest that the small gradient requirements of these acquisitions (15% of the peak gradient strength and 12% of the maximum slew rate) did not lead to substantial gradient linearity or dynamic imperfections that would require additional corrections of the k -space trajectory in the image reconstruction.

ⁱFrom the coil to the provided preamplifier, there are 1.5 m of RG_400_/U from the coil to the magnet front end, 0.5 m of RG_223_/U to the interface adapter box, 1.0 m of RG316 to the coil plug, and 1.5 m of RG_223_/U to the stack of preamplifiers. At 150 MHz, they cause 0.25 dB, 0.07 dB, 0.31 dB and 0.22 dB of insertion loss, respectively. Additionally, there are five connector interfaces with 0.025 dB of insertion loss each. The provided preamplifier module with integrated Tx/Rx switch (HPLNA XBB31P 2HP 600, Bruker Biospin P/N Z111093) has a 1.0 dB noise figure, which is higher than the 0.53 dB noise figure of our custom preamplifier.

With the upgraded DNP polarizer (Chapters 4 and 5), the RF coil with better coverage and sensitivity, as well as the efficient MRSI sequence, effective tools were available to successfully achieve MRSI with a 10.4 μL effective (4 μL nominal) voxel volume in the mouse brain every 2 s. Here, we successfully imaged the dynamic cerebral metabolic response to a bolus of HP [1- ^{13}C] pyruvate following stroke up to one minute post-injection.

In both dynamic and averaged images, the overall signal intensity of both pyruvate and lactate were lower within the ipsilateral hemisphere compared to the contralateral one. This could be the result of a decreased blood perfusion due to the surgical procedure, similarly to a previous report³⁸⁶. This did not seem to affect the metabolic profile of healthy tissues, as within the central and posterior slices, both the magnitude and dynamics of the lactate-to-pyruvate ratio remained similar on either side of the brain. However, a distinct metabolic response is observed in the anterior slice, with a higher and faster LPR buildup in the ischemic injury region compared to contralateral tissues, similarly to previous reports²²⁶. This metabolic contrast could potentially indicate post-stroke metabolic reprogramming, such as higher pyruvate uptake due to increased monocarboxylate transporter expression²⁴⁸, or a higher LDH activity after ischemia³⁸⁷.

In the presented approach, spectroscopic images were acquired following slice-selective pulses and therefore suffer from chemical shift displacement errors in the longitudinal direction. With a 4200 Hz pulse bandwidth centered between lactate and pyruvate that resonate 12.2 ppm (1840 Hz) apart, it can be deduced that the effective lactate and pyruvate slices were shifted by 0.88 mm on either side of the 4 mm slices. This could be reduced by either increasing both the RF pulse bandwidth and slice-selection gradient strength, or by using a global excitation followed by a 3D encoding scheme (Appendix C).

Although several downstream metabolites (i.e. lactate, alanine and bicarbonate) could be detected in global MRS measurements (Chapter 5), the MRSI protocol only achieved a limited dynamic range: only lactate could be imaged after an injection of HP pyruvate since the low conversion into remaining downstream metabolites, specifically bicarbonate, did not yield sufficient signal for imaging purposes. As a result of these limitations, we did not attempt to image the metabolism of HP [1- ^{13}C] lactate using the IDEAL spiral CSI sequence, due to the low conversion of HP lactate into downstream metabolites, which would then provide an insufficient MR signal. Indeed, the pyruvate-to-lactate ratio following an HP lactate injection is similar to the bicarbonate-to-pyruvate ratio following an HP pyruvate injection (Chapter 2).

To improve sensitivity to low concentration metabolites, we designed an acquisition sequence with metabolite-specific excitation and stack-of-spiral readout (Appendix C). Although this allowed the application of a larger flip angle on downstream metabolites to increase their MR signal, the sensitivity still remained insufficient to image the conversion of HP lactate

Chapter 6. Improving the spatiotemporal efficiency of spectrally resolved ^{13}C MRI to probe the dynamic metabolic interplay in a mouse model of stroke

into pyruvate, as well as the production of bicarbonate from HP pyruvate. For such cases, an acquisition scheme providing greater efficiency, such as bSSFP, is likely required.

Our measurements face several inherent challenges of hyperpolarized MRS(I) at ultra-high field. First, at higher magnetic field strengths, the longitudinal relaxation time of carbonyl ^{13}C nuclei, composing most dDNP substrates, drastically decreases^{134,209,388} as the chemical shift anisotropy relaxation scales with the square of the static field strength³⁸⁹. This limits our time window for imaging to about one minute post-injection. Second, higher field strengths exacerbate static field inhomogeneity³⁹⁰ which induces image blurring³⁹¹ in the spiral acquisitions. In our measurements, multiple resonance frequencies were observed for the injected substrate, pyruvate (-hydrate), while the downstream metabolite lactate only resonated at a single frequency. This likely indicates that a fraction of the signal originates from peripheral soft tissues or blood vessels that experience a slightly different static field. In these measurements, the static field homogeneity was optimized only in the brain region. A larger shimming volume, which considers the whole sensitivity volume of the receive-coil, could avoid these multiple resonant frequencies and improve the chemical shift reconstruction. Furthermore, the static field maps could be taken into account into the spiral reconstruction to reduce off-resonance-induced blurring³⁹².

Tables 6.1 and 6.2 list the imaging parameters of studies reported in peer-reviewed journals performing dynamic or single time point HP MRSI in the mouse or rat brain following an injection of HP (ethyl-) pyruvate. Despite the physical challenges, our measurements, with a 10.4 μL effective (4 μL nominal) voxel volume and 2 s time resolution, achieve spatial and temporal resolution similar to the best dynamic HP MRSI studies previously reported in the small rodent brain (Table 6.1). Similarly to our measurements, none of these dynamic or single time point studies achieved sufficient sensitivity to image downstream metabolites other than lactate in the mouse brain.

Table 6.1: Non-exhaustive list of dynamic ¹³C HP MRSI studies in mice or rat brain

Reference	Year	Substrate(s)	Imaged downstream metabolites	MRSI sequence	Nominal voxel size (mm ³)	Nominal voxel volume (μL)	Matrix size	FOV (mm ³)	Temporal resolution (s)	B ₀ (T)	Animal
Present work	2023	[1- ¹³ C] pyr	[1- ¹³ C] lac	Multislice IDEAL spiral CSI	1 × 1 × 4	4.0	20 × 20 × 3	20 × 20 × 12	2.0	14.1	Mouse
Eichhorn et al. 177	2013	[1- ¹³ C] pyr	[1- ¹³ C] lac	bSSFP	1 × 1 × 5	5.0	30 × 30 × 1	30 × 30 × 5	3.0	9.4	Mouse
Peeters et al. 386	2019	[1- ¹³ C] pyr	[1- ¹³ C] lac	Multigradient-echo	1.6 × 1.6 × 6	15.4	32 × 24 × 1	50 × 38 × 6	2.4	7.0	Mouse
Park et al. 393	2016	[2- ¹³ C] pyr	[2- ¹³ C] lac, [5- ¹³ C] glu	3D spiral CSI	2.7 × 2.7 × 5.4	39.4	16 × 16 × 12	43.5 × 43.5 × 64.8	6	3.0	Rat
Le Page et al. 394	2019	[1- ¹³ C] pyr, [¹³ C] urea	[1- ¹³ C] lac	2D FID-CSI	3 × 3 × 5	45.0	8 × 8 × 1	24 × 24 × 5	4.2	3.0	Mouse
Chen et al. 395	2015										
Guglielmetti et al. 396, 397, 398	2017, 2023	[1- ¹³ C] pyr	[1- ¹³ C] lac	2D FID-CSI	3 × 3 × 5	45.0	8 × 8 × 1	24 × 24 × 5	3.0-5.0	14.1	Mouse
Mikrogeorgiou et al. 399	2020										
Chaumeil et al. 400	2016	[1- ¹³ C] pyr	[1- ¹³ C] lac	2D FID-CSI	3.4 × 3.4 × 5	57.8	7 × 7 × 1	24 × 24 × 5	3.0	14.1	Mouse
Hurd et al. 401	2010	[1- ¹³ C] pyr	[1- ¹³ C] lac	Single-shot spiral CSI	2.7 × 2.7 × 10	72.9	16 × 16 × 1	43.5 × 43.5 × 10	3.0	3.0	Rat
Mayer et al. 251	2011	[1- ¹³ C] pyr	[1- ¹³ C] lac, [1- ¹³ C] ala, [¹³ C] bic	Single-shot spiral CSI	2.7 × 2.7 × 10	72.9	16 × 16 × 1	43.5 × 43.5 × 10	3.0	3.0	Rat
Josan et al. 402	2013	[1- ¹³ C] pyr/ [1- ¹³ C] KIC	[1- ¹³ C] lac, [¹³ C] bic/[1- ¹³ C] leu	Single-shot spiral CSI	2.7 × 2.7 × 10	72.9	16 × 16 × 1	43.5 × 43.5 × 10	3.0	3.0	Rat
Miller et al. 245	2018	ethyl-[1- ¹³ C] pyr	[1- ¹³ C] lac, [1- ¹³ C] pyr	IDEAL spiral CSI	2 × 2 × 30	120.0	40 × 40 × 1	80 × 80 × 30	1.8	7.0	Rat

Abbreviations: pyr: pyruvate, lac: lactate, bic: bicarbonate, ala: alanine, leu: leucine, glu: glutamate, KIC: ketoisocaproic acid

Table 6.2: Non-exhaustive list of single-time point ¹³C HP MRSI studies in mice or rat brain

Reference	Year	Substrate	Imaged downstream metabolites	MRSI sequence	Nominal voxel size (mm ³)	Nominal voxel volume (μL)	Matrix size	FOV (mm ³)	B ₀ (T)	Animal
Choi et al. 403, 404	2018, 2019	[1- ¹³ C] pyr	[1- ¹³ C] lac	2D FID-CSI	1 × 1 × 3.5	3.5	18 × 24 × 1	18 × 24 × 3.5	9.4	Mouse
Radoul et al. 405	2019	[1- ¹³ C] pyr	[1- ¹³ C] lac	2D FID-CSI	1.25 × 1.25 × 4	6.25	16 × 16 × 1	20 × 20 × 4	14.1	Mouse
Lee et al. 406	2015	[1- ¹³ C] pyr	[1- ¹³ C] lac	2D FID-CSI	2 × 2 × 2	8.0	8 × 8 × 1	16 × 16 × 2	9.4	Mouse
Mayer et al. 251	2011	[1- ¹³ C] pyr	[1- ¹³ C] lac, [1- ¹³ C] ala, [¹³ C] bic	Single-shot spiral CSI	1.5 × 1.5 × 5	11.3	32 × 32 × 1	48 × 48 × 5	3.0	Rat
Park et al. 407, 408	2013, 2021	[1- ¹³ C] pyr	[1- ¹³ C] lac	3D flyback echo-planar MRSI	2 × 2 × 5.4	21.6	20 × 16 × 16	40 × 32 × 86.4	3.0	Rat
Ruiz-Rodado et al. 409	2020	[1- ¹³ C] pyr	[1- ¹³ C] lac	2D FID-CSI	2 × 2 × 8	32.0	14 × 14 × 1	28 × 28 × 8	3.0	Mouse
Kawai et al. 410	2021									
Miller et al. 245	2018	[1- ¹³ C] pyr	[1- ¹³ C] lac	Flyback 3D SPSP EPI	2 × 2 × 4	16.0	32 × 32 × 8	64 × 64 × 36	7.0	Rat
Butt et al. 411	2012	[1- ¹³ C] pyr/ [1- ¹³ C] α-KIC	[1- ¹³ C] lac, [1- ¹³ C] ala, [¹³ C] bic/[1- ¹³ C] leu	2D FID-CSI	1.9 × 1.9 × 10	36.1	16 × 16 × 1	30 × 30 × 10	4.7	Rat
DeVience et al. 412, 413	2017, 2021	[1- ¹³ C] pyr	[1- ¹³ C] lac, [¹³ C] bic	2D FID-CSI	2.5 × 2.5 × 8	50.0	16 × 16 × 1	40 × 40 × 8	3.0	Rat
Harris et al. 414	2019	[1- ¹³ C] pyr	[1- ¹³ C] lac	2D FID-CSI	2.5 × 2.5 × 10	62.5	12 × 12 × 1	30 × 30 × 10	3.0	Mouse
Hurd et al. 415	2010	[1- ¹³ C] pyr	[1- ¹³ C] lac, [1- ¹³ C] ala	2D FID-CSI	2.5 × 2.5 × 10	62.5	16 × 16 × 1	40 × 40 × 10	9.4	Rat
Hackett et al. 416	2021	[1- ¹³ C] pyr	[1- ¹³ C] lac, [¹³ C] bic	2D FID-CSI	3 × 3 × 7.7	69.3	16 × 16 × 1	48 × 48 × 7.7	3.0	Rat
Park et al. 417	2013	[2- ¹³ C] pyr	[5- ¹³ C] glu, [1- ¹³ C] ACAR	2D FID-CSI	2.7 × 2.7 × 10	72.9	16 × 16 × 1	43.5 × 43.5 × 10	3.0	Rat
Miloushev et al. 221	2017	[1- ¹³ C] pyr	[1- ¹³ C] lac	2D EPSI	4 × 4 × 10	160.0			1.05	Mouse
Lim et al. 418	2020	[1- ¹³ C] pyr	[1- ¹³ C] lac	2D FID-CSI	5 × 5 × 10	250.0	12 × 12 × 1	60 × 60 × 10	3.0	Rat

Abbreviations: pyr: pyruvate, lac: lactate, bic: bicarbonate, ala: alanine, leu: leucine, glu: glutamate, ACAR: acetyl carnitine

6.6 Conclusion

In this chapter, several tools were developed to boost the sensitivity and efficiency of our HP dDNP/MRI setup to enable dynamic HP MRSI in the mouse brain. An RF cross-coil setup was developed, with a surface ^{13}C Rx-only coil to achieve highly sensitive signal detection in the mouse brain, and a volume $^1\text{H}/^{13}\text{C}$ Tx/Rx coil to provide uniform RF excitation. The latter facilitates the application of imaging sequences, and enables a more accurate characterization of the metabolic kinetics compared to the varying excitation profile of a transmit-receive surface coil. Efficient spatial and spectral encoding was achieved by implementing the IDEAL spiral CSI sequence on a 14.1T MRI scanner to allow efficient use of the HP signal, as well as multislice time-resolved measurements. To our knowledge, this is the first report of an implementation of the IDEAL spiral CSI sequence at such field strength or higher, although such a high field strength is less common for preclinical MRI and severely disadvantageous for hyperpolarized studies due to short relaxation times. The acquisition scheme and parameters were optimized in a multi-compartment phantom, which validated that a proper spatial registration was achieved.

Altogether, a substantially better technical platform is provided to observe new metabolic contrasts, allowing further characterization of molecular imaging biomarkers from hyperpolarized neuroprotective agents for stroke. Here, we successfully imaged the time-resolved metabolic response of an ischemic mouse brain to an HP pyruvate bolus with an effective $10.4\ \mu\text{L}$ voxel volume ($4\ \mu\text{L}$ nominal) and 2 s temporal resolution. The results illustrate a distinct dynamic metabolic profile in the ischemic region, with higher and faster lactate labeling compared to healthy tissues. Further measurements with control and stroke animals would be required to confirm these encouraging biological findings.

In this proof-of-concept experiment, we achieved a high spatiotemporal resolution similar to the best reports of HP MRSI performed in the small rodent brain, despite using a non-optimal dDNP/MRI setup from a physical point of view. Indeed, the sensitivity was intrinsically limited by the twofold lower polarization achievable in a 5T/1.15K DNP polarizer, and shorter liquid state T_1 in a 14.1T MRI compared to 7T/1K and 9.4T, respectively, as previously performed in Chapters 2 and 3. These technical upgrades were implemented on a state-of-the-art MRI platform from the major preclinical MRI vendor and could therefore be easily deployed on more suitable MRI setups from a physical perspective to enable an even higher sensitivity and imaging resolution.

7 General conclusions and outlook

This thesis focused on the development of novel theranostic approaches to acute ischemic stroke based on hyperpolarized neuroprotective agents in a preclinical mouse model. Specifically, it entailed the characterization of biomarkers provided by HP ^{13}C substrates in the ischemic brain, the design of cryogenic probes to improve the repeatability, performance and throughput of dDNP polarizers, as well as the development of MR sequences and hardware to map the metabolic processes in the stroke brain with high spatial and temporal resolution. In this concluding chapter, we summarize the major findings of this thesis, and discuss possible continuations of this journey.

Using global MRS at 9.4 T, we found that the cerebral metabolism of a bolus injection of either $[1-^{13}\text{C}]$ lactate or $[1-^{13}\text{C}]$ pyruvate, prepolarized at 7 T and 1 K, was substantially altered by ischemia, with slower and lower metabolic conversion. This confirms their potential as molecular biomarkers for stroke. We found that the kinetic modeling analysis improved the significance of contrasts from HP lactate metabolism between healthy and stroke brains compared a metabolite ratio analysis. Both agents investigate similar biochemistry and transport mechanisms and achieve comparable contrasts, but each has its own advantages. On the one hand, pyruvate benefits from a greater polarization and higher turnover into downstream molecules, which facilitates the measurement. On the other hand, the neuroprotective effect of lactate is better established, the therapeutic dose is better tolerated, and the visualization of subsequent steps allows discrimination between transport and metabolism. Nevertheless, due to the lack of spatial localization in these measurements, it was not possible to locate the origin of these metabolic alterations.

In the course of optimizing the $[1-^{13}\text{C}]$ lactate sample formulation, we investigated the effect of TEMPOL, a dDNP polarizing agent and known neuroprotectant, on the cerebral metabolism of HP $[1-^{13}\text{C}]$ lactate after stroke, with the aim of relating our results to previous studies. We concluded that the markedly increased $[1-^{13}\text{C}]$ pyruvate labeling in the presence

Chapter 7. General conclusions and outlook

of TEMPOL was consistent with its catalytic antioxidant properties. On a broader level, these results indicate that the formulation of dDNP samples needs to be chosen carefully to avoid causing experimental bias by certain biologically active reagents. This is particularly important to avoid aberrant results when this technique is transferred from preclinical to clinical research, for which the polarizing agent must be filtered.

A new cryogenic probe was developed to implement the custom fluid path on a 5T/1.15K wet dDNP polarizer. The upgraded system improves the DNP enhancement and buildup time constant by a factor of 1.5, achieved better repeatability, simplifies sample handling, consumes 20% less helium, and enables us to perform LOD-ESR measurements. Overall, we concluded that the new dDNP polarizer could serve applications with better reliability, performance, capabilities, and at lower running costs.

A multi-sample cryogenic probe was designed to substantially increase the throughput and versatility of the dDNP polarizer. We demonstrate that three samples, even with distinct nuclei/radicals, can be simultaneously polarized, monitored, and dispensed at short time intervals. This original feature opens the possibility of using multiple HP agents to study several aspects of a disease condition.

Spatially resolved measurements of the metabolism of hyperpolarized neuroprotective agents were implemented on a 14.1T MR scanner. A ^{13}C cross-coil setup was built, and the IDEAL spiral CSI encoding scheme was constructed to efficiently utilize the hyperpolarized signals. In a proof-of-concept experiment, the biodistribution and metabolism of HP [1- ^{13}C] pyruvate in the ischemic mouse brain was dynamically mapped. This revealed a faster and higher ratio of [1- ^{13}C] lactate labeling within the lesion core. Therefore, we conclude from this preliminary result that imaging the conversion of HP [1- ^{13}C] pyruvate may allow detection of infarcted tissues. Unfortunately, imaging of HP [1- ^{13}C] lactate metabolism was not successful. Given its lower turnover into downstream metabolites, higher initial polarization and better acquisition/sampling efficiency would be required to reach the detection limit.

Overall, this thesis showed the potential of the HP neuroprotective agents [1- ^{13}C] lactate and [1- ^{13}C] pyruvate as metabolic biomarkers in a mouse model of transient ischemic stroke. In parallel, several methodological and material developments contributed to advance the performance and efficiency of HP MR via dDNP. Although the primary goal was to achieve ^{13}C HP imaging in the stroke brain, the tools developed in this framework can also be used for other applications or adapted to other HP MR setups. In particular, the cryogenic dDNP probe designs can be implemented on other polarizers, by modifying their diameter and length accordingly. The mouse head coil can be retuned to any $^1\text{H}/\text{X}$ frequency to benefit other hyperpolarized and non-hyperpolarized measurements. In particular, deuterium metabolic

imaging (DMI) is of growing interest⁴¹⁹ in the X-nuclei MR community, and could provide another method to map the disrupted glucose uptake and downstream processing in stroke.

A natural continuation of this thesis consists in studying the regional cerebral metabolic pattern of HP [1-¹³C] lactate and [1-¹³C] pyruvate in stroke to improve our understanding of their neuroprotective mechanisms of action. Ultimately, this could provide valuable information for future clinical trials. The first step would be to enable greater sensitivity for imaging [1-¹³C] lactate metabolism, which has a better therapeutic potential. During this thesis, the 7T/1K dDNP polarizer was being heavily used by several other users, therefore the technical developments had to be performed on a 5T/1.15K dDNP polarizer coupled to a 14.1T MRI scanner. As a result, the overall sensitivity was limited by the lower achievable polarization as well as the faster liquid-state spin-lattice relaxation. Implementing the same hardware and methods on the 7T/1K dDNP / 9.4T MRI setup would provide more favorable physical conditions. Since the 9.4T scanner is scheduled to receive a console upgrade in the coming year, the MRSI sequences will be transferred seamlessly. The LOD-ESR guided gadolinium doping procedure could increase [1-¹³C] lactate polarization to about 60-70% at 7T/1K. Switching to rats, in which the MCAO stroke model is also established²³⁹, could also improve HP MR measurement sensitivity and facilitate⁴²⁰ the use of functional MRI to characterize the neurological deficit. In addition, the inclusion of DWI and PWI, the standard contrasts to delineate the ischemic core and penumbra volumes, and ¹H MRSI would provide a comprehensive characterization of the ischemic brain using endogenous biomarkers. Because stroke is a multifaceted disease, one could envision a multi-agent theranostic approach using the triple dDNP probe to target multiple pathological aspects.

In this work, the focus was on investigating the diagnostic components of HP lactate and pyruvate, whereas their therapeutic component was not studied but was assumed from previous studies in identical or similar preclinical stroke models⁵⁶⁻⁶⁶. Future works should aim at the combined evaluation of both therapeutic and diagnostic aspects. This would require evaluating the stroke outcome at later timepoints than in the present work, since the injury continues to develop in the days following stroke onset⁴²¹. The stroke severity, for example assessed with behavioral tests, conventional MRI or histology, could then be compared with the HP measurements. Observing correlations between the metabolic pattern measured at early time-points and the long-term lesion or neurological deficit would strongly reinforce the potential of these agents as predictive biomarkers of the stroke outcome and to better evaluate the therapy efficacy. This would also mitigate the impact of experimental variability related to the stroke surgery.

The tools developed in this framework could also deepen our understanding of the physics of hyperpolarization via DNP. While in this thesis, the LOD-ESR capability was only used to optimize the [1-¹³C] lactate sample formulation, the hardware developed has also served to

Chapter 7. General conclusions and outlook

investigate the ESR properties of other neuroprotective agents relevant to stroke, in particular ^{129}Xe ²⁹⁶. Further work to understand and optimize its DNP sample properties to bring the polarization to imaging standards may allow investigation of xenon theranostics in the same HP MR setup.

In recent years, low-field MRI scanners (5-100 mT), based on either permanent^{422,423} or resistive^{424,425} magnets, have attracted increasing interest. Their low cost, low power consumption, and high portability enable point-of-care neuroimaging. This new paradigm is particularly promising for acute stroke care, as the scanner can be brought to the patient's bedside⁴²⁶, or driven to a remote location⁴²⁷ to provide biomedical imaging at the earliest possible time point. Despite the inherently low imaging quality, valuable medical diagnostics for stroke can still be achieved⁴²⁸⁻⁴³⁰. In this context, hyperpolarized probes, that decouple sensitivity from field strength, may be used to complement the capabilities of low-field MRI and provide highly-sensitive biomarkers for an early stroke assessment.

A Ancillary dDNP polarizer equipment

This section describes the ancillary devices developed in the framework of this thesis for performing dDNP and LOD-ESR experiments.

Part of the hardware is presented in the following papers:

- **Lê Thanh Phong**, Hyacinthe Jean-Noël, Capozzi Andrea. *How to improve the efficiency of a traditional dissolution dynamic nuclear polarization (dDNP) apparatus: Design and performance of a fluid path compatible dDNP/LOD-ESR probe*. Journal of Magnetic Resonance, 338:107197, 2022. doi:10.1016/j.jmr.2022.107197
- **Lê Thanh Phong**, Hyacinthe Jean-Noël, Capozzi Andrea. *Multi-sample/multi-nucleus parallel polarization and monitoring enabled by a fluid path technology compatible cryogenic probe for dissolution dynamic nuclear polarization*. Scientific Reports, 13:7962, 2023. doi:10.1038/s41598-023-34958-3

I designed, assembled and characterized all the equipment presented in this appendix.

A.1 CFP pressure-test station

The CFP pressure-test station (Figure A.1) has the double function of performing a leak test with He gas on the CFP prior to insertion of the sample inside the polarizer, as well as drying the CFP with compressed air following a dissolution.

Both gases enter the station built inside an aluminum enclosure (RND Components P/N 455-00441) through the 6 mm push-in connectors to the left (A-B). The compressed air circuit is completed with a quarter-turn plug valve (C, Swagelok P/N SS-6P4T-MM-RD, Cleveland, OH, USA), a flow speed restrictor (inside the box, SMC P/N AS1002F-06, Chiyoda, Japan), and a quick connect stem for the CFP connection (D, Swagelok P/N SS-QM2-2PF). The He gas circuit includes a pressure regulator (F, SMC P/N AR10-M5H-A) as well as a pressure gauge (E, Swagelok P/N PGI-63B-PG100-LAQX-J) for setting a specific pressure inside the CFP connected to the stem (G) and checking for leaks after closing the valve (H).

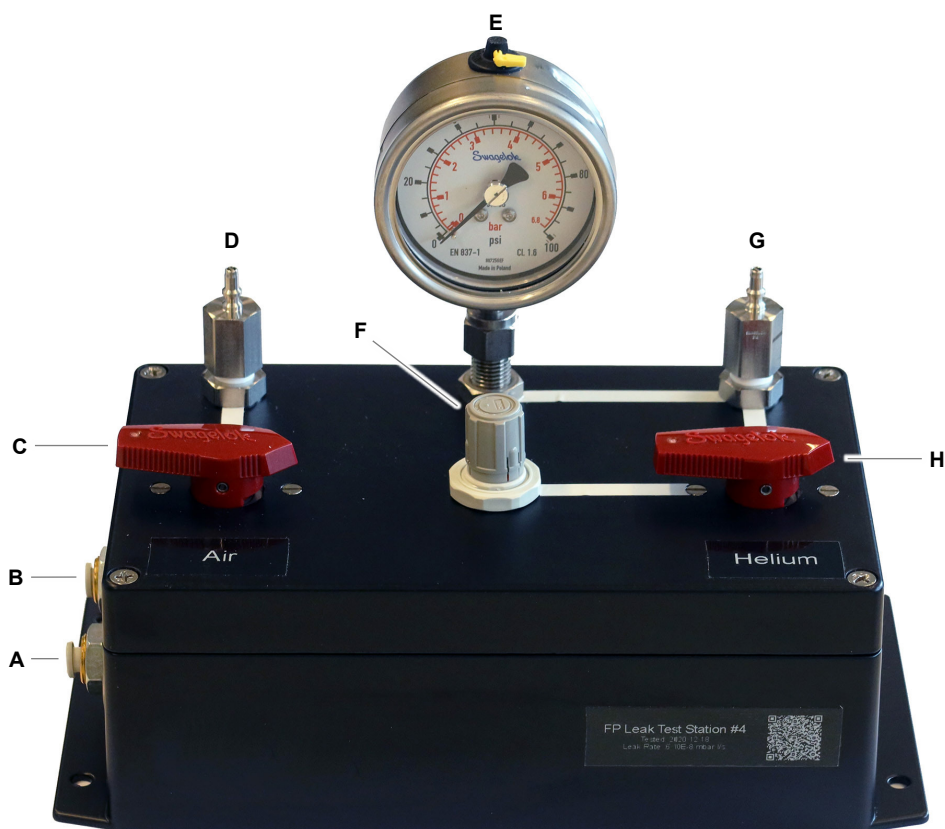


Figure A.1: CFP pressure-test station. The white lines painted on the enclosure describe the interconnections between the different elements. (A) Air inlet, (B) Helium inlet, (C) Air valve, (D) Air stem, (E) Pressure gauge, (F) Helium pressure regulator, (G) Helium stem, (H) Helium valve.

A.2 Dissolution head

The dissolution head (Figure A.2) heats up the dissolution buffer and releases it inside the CFP at high pressure. It is mounted above the polarizer on a double-swivel arm (Bosch Rexroth, Lohr am Main, Germany) to comfortably reach each slot of the triple DNP probe.

The dissolution happens as follows. Firstly, 5.5 mL of buffer are loaded inside the boiler (E) through the loading valve (D), which is then closed. The boiler is pressurized via a set of check valves (A) using He gas released by the low-pressure He valve (K) at 4 bar pressure set using the pressure regulator (C). The 220 W heater band (Industrial Molding Supplies P/N 150975, Chagrin Falls, OH, USA) heats the boiler until the pressure transducer (I, Swagelok P/N PTI-S-AG16-32AS, Cleveland, OH, USA) reads 12.0 bar (relative pressure) and stabilizes it within 0.5 bar of the target value, corresponding to a buffer temperature of about 180 °C. A 0.8 mm graphite thermal interface sheet (RS PRO P/N 794-3998, $\lambda_{XY} = 350 \text{ W m}^{-1} \text{ K}^{-1}$, $\lambda_Z = 13 \text{ W m}^{-1} \text{ K}^{-1}$) ensures contact between the boiler and the band heater.

In the meanwhile, the 100 W valve heater, a 10 Ω resistor (F, Ohmite P/N TGHDX10R0JE, Warrenville, IL, USA) stabilizes the temperature of both the quick-connect stem (H, Modified Swagelok P/N SS-QM2-2PM) and bottom dissolution pneumatic valve (G, Swagelok P/N 6LVV-DPVS6M-C) to 100 °C measured by a PT100 thermometer.

The user lifts the CFP by 10 cm to take the CFP vial away from liquid He, then docks the CFP to the quick-connect stem (H) and presses the dissolution button (B). An automated LabVIEW computer-controlled sequence opens the bottom dissolution valve to release the buffer into the CFP to melt the sample. Simultaneously, the top dissolution pneumatic valve (J) opens and He gas at 10 bar is blown through the CFP to eject and transfer the sample to the separator/infusion pump in the MRI scanner. After 5000 ms, both valves close, the MRI acquisition is automatically triggered, and the user can disconnect the CFP and remove it from the polarizer. Dissolutions to the benchtop spectrometer require 2500 ms pushing time at 8 bar.

Following the dissolution, the boiler and bottom valve are cooled-down and dried using compressed air flushed from (A) to (H). Fiberglass insulation (not shown) is wrapped around all hot components to prevent contact burns.

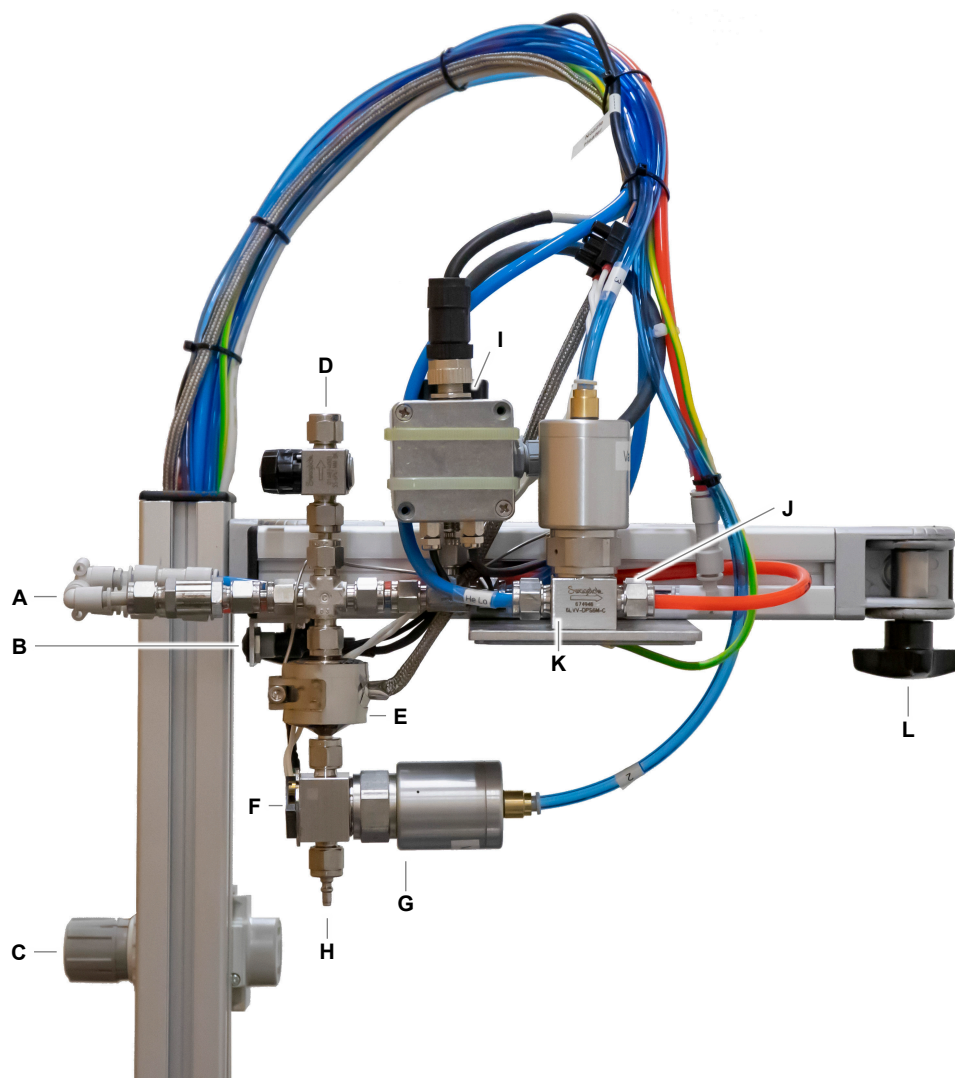


Figure A.2: Dissolution head. (A) Low-pressure helium and air inlet, (B) Dissolution button, (C) Pressure regulator for low helium gas, (D) Loading valve for dissolution solvent, (E) Water boiler and 220 W band heater, (F) 100 W valve heater, (G) Bottom dissolution pneumatic valve, (H) Quick-connect stem, (I) Pressure transducer (behind), (J) Top dissolution pneumatic valve, (K) Low-pressure helium pneumatic valve, (L) Swivel and ball screw.

A.3 LOD-ESR differential amplifier

LOD-ESR measurements are performed in a technically-challenging electromagnetic environment, surrounded by many pumps, LED lighting switching converters, and an MRI scanner. To minimize electromagnetic interference in low-frequency measurements, all signals were transferred in a differential mode. The wiring was done using Twin-BNC (Twinaxial BNC) connectors (Amphenol RF receptacles P/N 31-223 and plugs P/N 31-224, Danbury, CT, USA) and double-shielded twisted-pair cables (Belden P/N 9463, Chicago, IL, USA). Furthermore, the measurement resolution is doubled using differential signals that make better use of the fixed $\pm 10\text{V}$ digitization range.

The simplified schematics of the $200000\times$ voltage gain (106 dB) differential amplifier used for LOD-ESR measurements is shown in Figure A.3.

The circuit is powered by a single 9V PP3 battery (BT1) with an active rail splitter (U3D) providing a dual rail voltage supply (VCC and VEE).

The signal from the LOD-ESR coil is fed at connector J1. The first amplification stage is an instrumentation amplifier (U1, Analog Devices P/N AD8421BRZ, Norwood, MA, USA) set to a gain of 10000 via R2. The 400 mV voltage reference IC1, user-adjusted potentiometer RV1, and buffer amplifier U2B are used to set the reference voltage of U1 to cancel the voltage offset of the LOD-ESR probe due to thermocouple effects, as well as the input offset voltage of the amplifier. This reduces the baseline voltage at the output of U1 that could otherwise saturate the second and third amplifying stages. The gain of U2B can be inverted using additional components (not shown on the simplified schematics) to obtain a negative reference voltage if required.

The signal is then filtered by a first-order 10 Hz low-pass filter (R3 and C1). A 10-fold amplification stage is provided by an operational amplifier U2C (The second stage gain can be set to 5, 10, 25 or 50 using a microswitch not shown on the simplified schematics). The third amplification stage (U2A and U2D) doubles and converts the single-ended signal to a differential signal at connector J2. U3B and U3C provide a second differential output J3 with an additional 10 Hz first-order low-pass filter (R15 and C5) to provide additional noise reduction while measuring samples with a long relaxation time.

A double-layer printed circuit board was designed in KiCad 5.1, then externally manufactured on FR4 sheets. All components were hand-soldered. The board is mounted within an aluminum enclosure (RND 455-00768), holding the 9V PP3 battery, two input and one output Twinaxial connectors, an ON/OFF switch and a LED indicator (Figure A.4).

Appendix A. Ancillary dDNP polarizer equipment

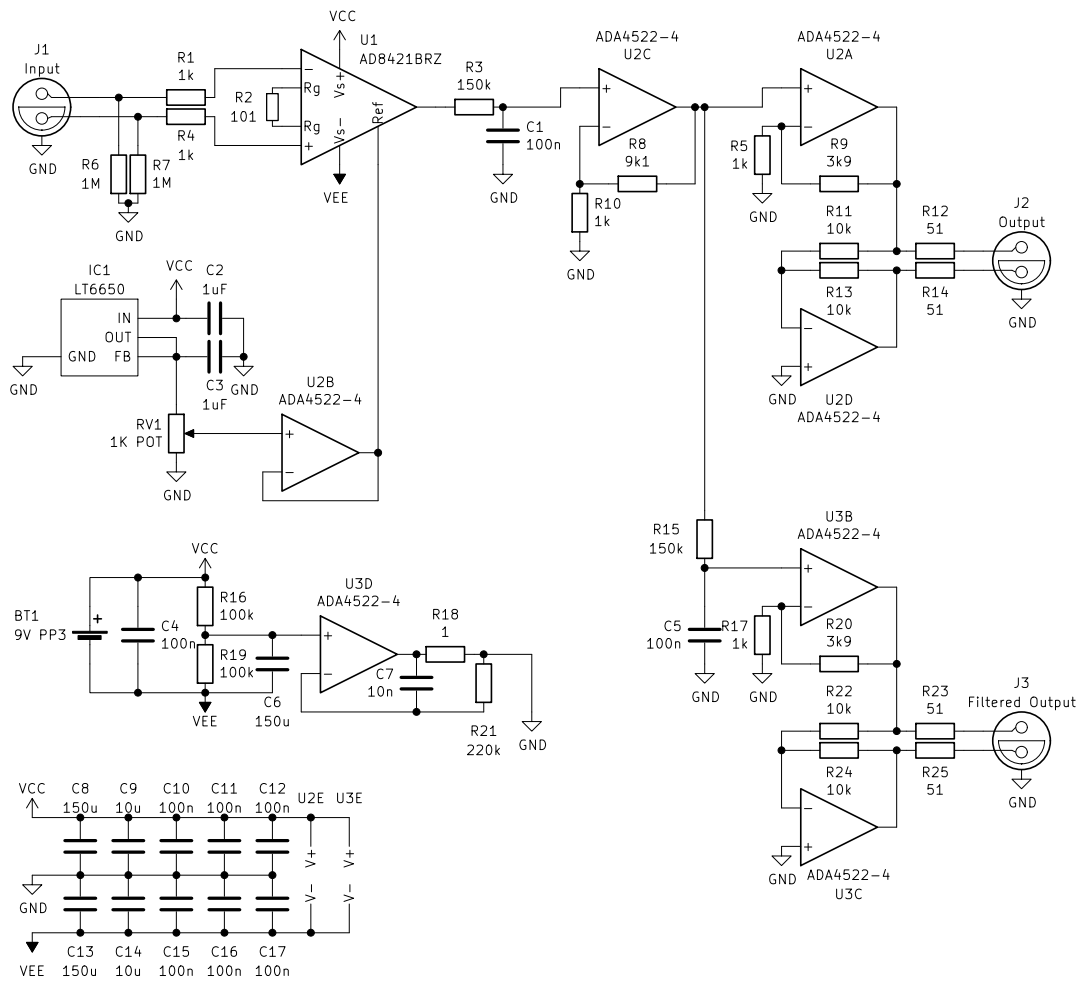


Figure A.3: Simplified schematics of the 20000x voltage gain LOD-ESR differential amplifier.



Figure A.4: Pictures of the LOD-ESR differential amplifier enclosure, and both sides of the assembled printed circuit board.

B NMR preamplifiers

This section describes the NMR signal preamplifiers designed for solid-state NMR measurements in the dDNP polarizer, as well as for the receive MR coil used in MRSI experiments.

Part of the hardware is presented in the following paper:

- **Lê Thanh Phong**, Hyacinthe Jean-Noël, Capozzi Andrea. *Multi-sample/multi-nucleus parallel polarization and monitoring enabled by a fluid path technology compatible cryogenic probe for dissolution dynamic nuclear polarization*. Scientific Reports, 13:7962, 2023. doi:10.1038/s41598-023-34958-3

I designed, assembled and characterized all the equipment presented in this appendix.

B.1 Design

Low noise preamplifiers were designed for both solid-state NMR measurements and MRSI measurements. They implement the E-pHEMTⁱ PGA-103+ (Mini-Circuits, Brooklyn, NY, USA) wideband amplifier, which provides a low noise figure in the relevant frequency range (50-250 MHz), sufficient gain (>22 dB), high power handling (+21 dBm), and is well documented in the amateur radio community.

In the NMR version (Figure B.1), varistors RV1 and RV2 protect the amplifier U1 against electrostatic discharges. Additionally, the Schottky cross-diodes D1 protect U1 against excessive input power. The low-dropout linear regulator U2 supplies the amplifier with a constant DC voltage and requires at least 6.5 V and preferably 7.0 V input voltage to achieve optimal performances, therefore the supply voltage at J3 is preferably 7.9 V after taking the forward voltage of D3 into account. The current required is typically 120 mA in normal operation.

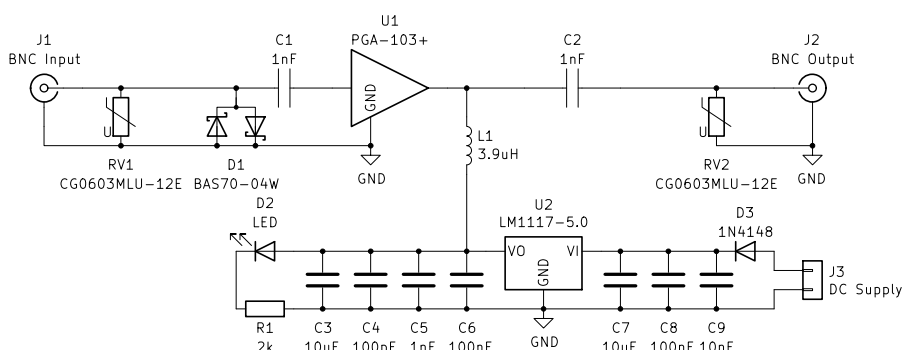


Figure B.1: Simplified schematics of the LNA designed for solid-state NMR measurements in the DNP polarizer.

The version for the MRI coil (Figure B.2) has a slightly different layout and includes an additional DC-block capacitor C1 due to the active-detuning DC voltage present at the input J1, and an additional inductor L2 to supply the linear regulator from a 10 V bias voltage on J2.

Printed circuit boards (PCB) for both versions were designed in KiCad 5.2, then manufactured by a third-party on double-layer FR4 boards. All components were hand-soldered on the boards (Figures B.3 and B.4). The NMR version is mounted onto an aluminum enclosure (Hammond/Eddystone P/N 11451PSLA, Guelph, ON, Canada) holding a 1000 pF feedthrough capacitor and a ground post connected to a benchtop power supply. The MRI version is directly stacked on the main board of the receive-coil.

ⁱEnhancement mode Pseudomorphic High Electron Mobility Transistor

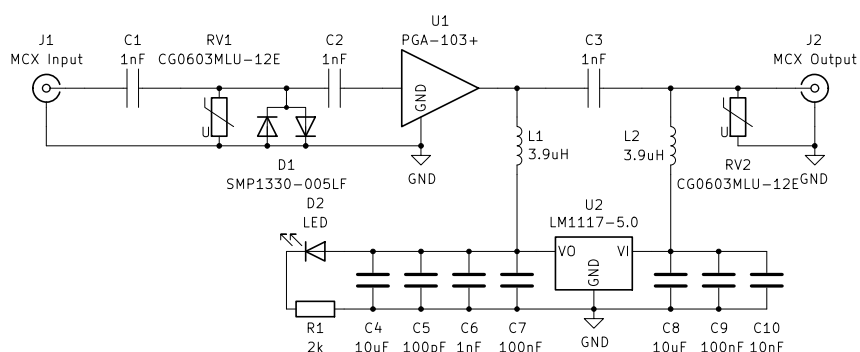


Figure B.2: Simplified schematics of the LNA designed for the Rx-only surface coil.

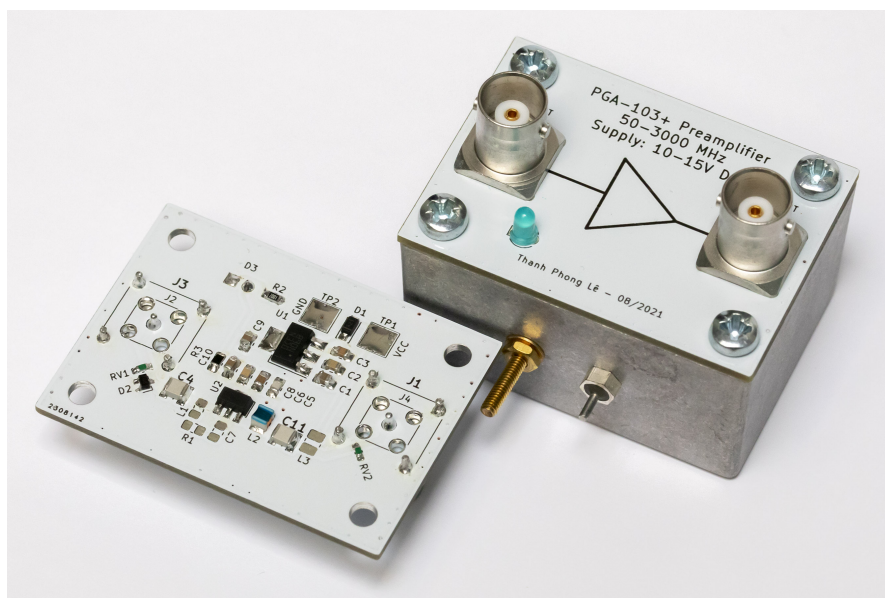


Figure B.3: Pictures of the LNA for NMR. The PCB is mounted as the lid of an aluminum enclosure. Note that the reference designators on the assembled boards do not match the simplified schematics.

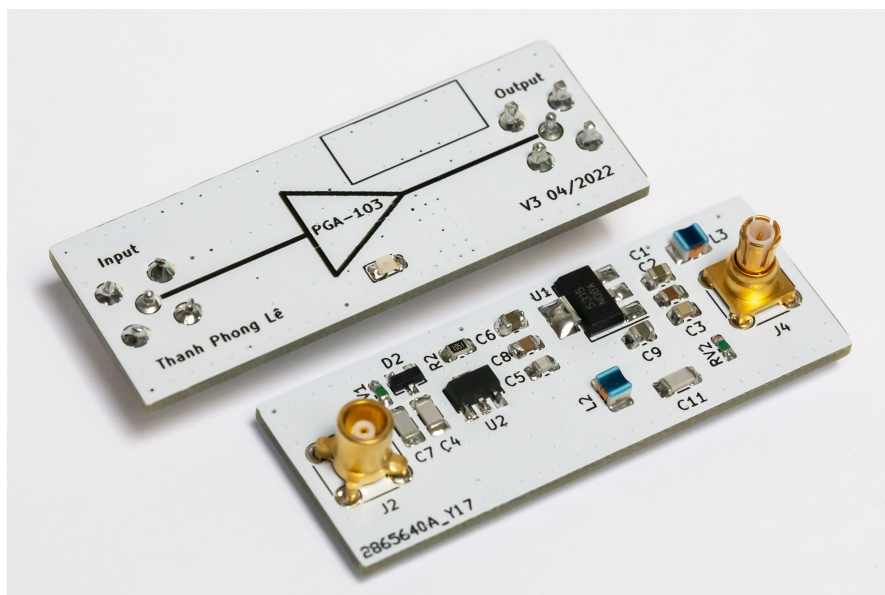


Figure B.4: Pictures of the LNA for the MRI coil. The preamplifier is directly stacked on the main board of the receive coil using the pair of MCX connectors as mechanical support. Note that the reference designators on the assembled boards do not match the simplified schematics.

B.2 Characterization

One assembled board of each version was characterized between 10 MHz and 300 MHz at zero magnetic field using a N8973A Noise Figure Analyzer (Agilent, Santa Clara, CA, USA) and a NS346A Calibrated Noise Source (Micronetics, Hudson, NH, USA). The gain and noise figure are reported in Figure B.5. Both versions provide similar performance. The NMR version provides 26.2 dB gain and 0.422 dB noise figure at 55 MHz (Approximately the ^{13}C or ^{129}Xe frequency at 5 T), and 23.6 dB gain and 0.646 dB noise figure at 210 MHz (Approximately the ^1H frequency at 5 T). In the MRI version, at 150 MHz (^{13}C at 14.1 T), the gain and noise figure are 24.9 dB and 0.532 dB, respectively.

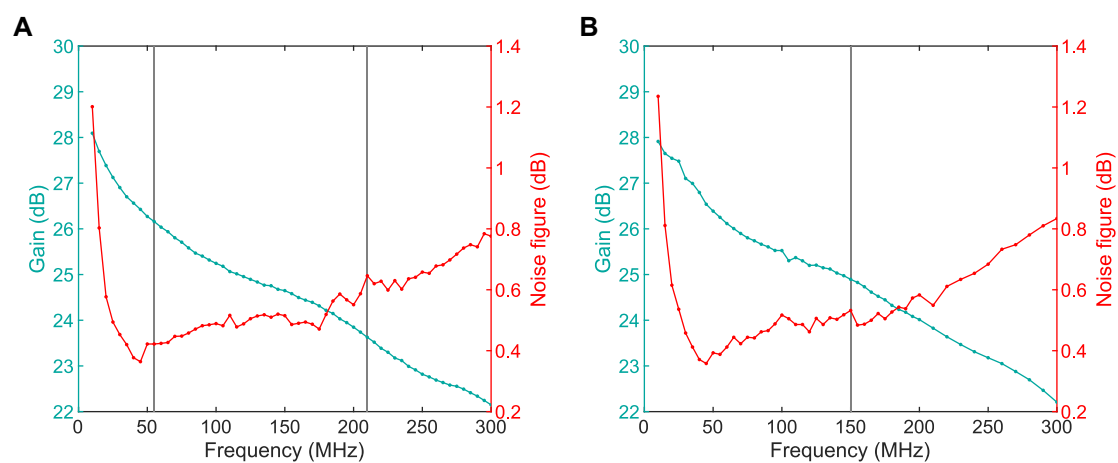


Figure B.5: Gain and noise figure of the in-house made low-noise preamplifiers for NMR (A) and MRI (B) applications.

C Metabolite-specific stack-of-spirals MRSI sequence

In this appendix, we present the implementation of an acquisition based on metabolite-specific RF excitation and 3D stack-of-spirals readout and related imaging tests in healthy mice.

The contributions are identical to Chapter 6.

C.1 Introduction

One of the difficulties encountered while acquiring the metabolism of HP [1-¹³C] lactate or [1-¹³C] pyruvate in the mouse brain is the small turnover into downstream metabolites. Indeed, the conversion ratio from pyruvate to bicarbonate, or from lactate to pyruvate is typically around 1% (Chapter 2). As a result, an acquisition scheme with a sufficiently wide dynamic range is required to detect both the intense MR signal of the injected substrate as well as the weak signal of downstream metabolites. In Chapter 6, we implemented an IDEAL spiral CSI³⁵³ acquisition scheme to perform HP MRSI in the mouse brain following an injection of HP [1-¹³C] pyruvate. While it enabled us to map the metabolism of pyruvate into lactate, the distribution of bicarbonate could not be imaged. Either the chemical shift reconstruction does not perform sufficiently well in the presence of substantial signal amplitudes difference between upstream and downstream metabolites, or the bicarbonate signal was not sufficient to enable detection.

Here, we aim to improve the dynamic range of our acquisition by implementing an MRSI sequence with a metabolite-specific RF excitation scheme and 3D stack-of-spirals readout. This acquisition scheme was tested *in vivo*, by imaging the metabolism of both HP [1-¹³C] lactate and [1-¹³C] pyruvate in the mouse brain.

C.2 MRSI sequence

A metabolite specific 3D stack-of-spirals sequence was implemented on the preclinical 14.1T MRI scanner previously described in Section 6.3.1. Each metabolite is acquired independently, enabling the individual adjustment of the RF excitation: a small tip angle is applied to the injected substrate to avoid wasting its nonrenewable hyperpolarization, while a larger tip angle is applied to downstream metabolites to obtain a higher MR signal.

The sequence, for the acquisition of N_M metabolites each with N_S axial (xy) phase-encoded slices, is schematically illustrated in Figure C.1 and described below:

1. A narrow-bandwidth RF pulse, here calculated via the Shinnar-Le Roux algorithm, provides the chemical shift encoding by exciting a single metabolite at once. No gradients are applied during the RF excitation. Note that here, the RF pulse is not spatially-selective. Instead, the volume coil was shifted away from the animal body such that the B_1^+ amplitude profile decreases beyond the mouse neck.
2. A phase-encoding is applied along the slice direction (z).

3. The MR signal is acquired while applying a spiral readout gradient. The trajectory starts at the origin of the k -space and evolves outwards in the slice plane (xy).
4. The remaining transverse magnetization is then destroyed by a gradient spoiler.
5. The procedure (1)-(4) is repeated for each of the N_S slice-phase encoding steps in centric order.
6. Finally, the steps (1)-(5) are repeated for each of the remaining N_M metabolites.

The images are reconstructed using a Fourier-transform along the slice direction, followed by the spiral reconstruction previously described in Section 6.2.2.3.

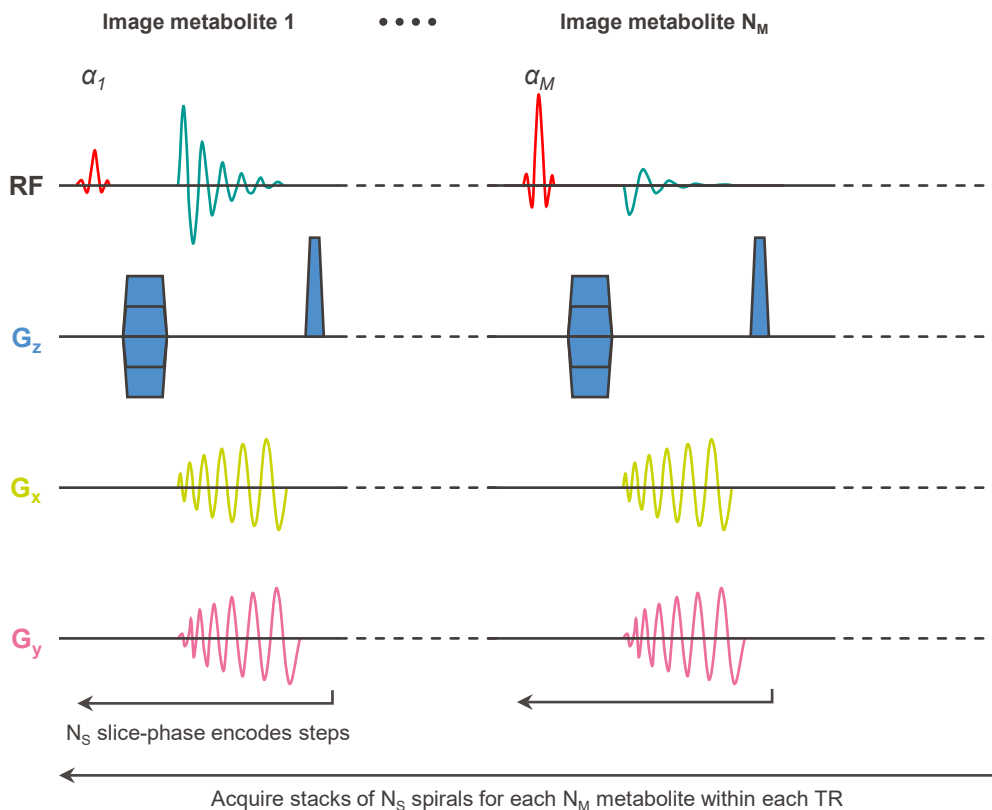


Figure C.1: Schematic representation of the metabolite specific 3D stack-of-spirals acquisition scheme. A frequency selective RF pulse is applied to only excite a single metabolite. The metabolite is then mapped in 3D using a phase encoding gradient, here along the z -direction to acquire axial slices, together with spiral gradients applied during the readout. A gradient spoiler destroys the remaining transverse magnetization. For each metabolite, N_S phase encoding steps are acquired. The scheme is repeated in rapid succession for all N_M metabolites within each repetition time.

C.3 Methods

A multi-substrate HP MRSI experiment was performed in a healthy mouse. The 5T dDNP polarizer was equipped with the multi-sample probe (Chapter 5) and loaded with two CFPs, one containing 65 μL of $[1-^{13}\text{C}]$ lactate preparation (Lac-sample) and the other 20 μL of $[1-^{13}\text{C}]$ pyruvate preparation (PA-sample), as previously described in Section 5.3.5. The samples were simultaneously polarized for 3 h at 139.86 GHz and 63 mW.

While the samples are being polarized, a healthy C57BL6/J male mouse (25.5 g) was anesthetized with 2% isoflurane in 60% oxygen, and a catheterized to allow for the administration of HP substrates. The catheter was connected to two separator-infusion pumps to allow for the multiple injections. The mouse was installed into the RF coil setup, composed of a $^1\text{H}/^{13}\text{C}$ volume coil and receive-only ^{13}C surface coil as previously described in Section 6.3.2 and Figure 6.7. Field map-based shimming was used to optimize static field homogeneity in the mouse brain prior to ^{13}C MRSI acquisitions.

The Lac-sample was dissolved first using 5.5 mL of D_2O , transferred to one separator-infusion pump, and a 325 μL bolus of 80 mM HP $[1-^{13}\text{C}]$ lactate was intravenously injected into the mouse. Immediately, HP MRSI was performed using the metabolite-specific stack-of-spirals sequence. For each metabolite, the 3D image was encoded with a stack of 5 spirals using the following parameters: Shinnar–Le Roux RF pulse (6.3 ms pulse length, 500 Hz bandwidth, 5° on $[1-^{13}\text{C}]$ lactate, 20° on $[1-^{13}\text{C}]$ pyruvate and 30° on $[^{13}\text{C}]$ bicarbonate), 4.24 ms echo time, 5 phase-encoding steps in centric order, 10.3 ms spiral readout, 18 mm \times 18 mm \times 22 mm FOV, 10 \times 10 \times 5 image matrix, 1.8 mm \times 1.8 mm \times 4.4 mm nominal voxel size. The measurement was repeated every 2 s for 120 s.

25 minutes after the first dissolution, the PA-sample was dissolved in a buffer solution (60 mM tris(hydroxymethyl)aminomethane (TRIS) and 0.3 mM EDTA in D_2O balanced to pD = 7.6), transferred to the second separator-infusion pump, then a 325 μL bolus of 80 mM HP $[1-^{13}\text{C}]$ pyruvate was administered. Immediately, the dynamic MRSI acquisition was automatically performed with the following parameters: Shinnar–Le Roux RF pulse (6.3 ms pulse length, 500 Hz bandwidth, 5° on $[1-^{13}\text{C}]$ pyruvate, 15° on $[1-^{13}\text{C}]$ pyruvate hydrate, 15° on $[1-^{13}\text{C}]$ lactate, and 30° on $[^{13}\text{C}]$ bicarbonate), 4.24 ms echo time, 5 centric phase-encoding steps, 16.5 ms spiral readout, 18 mm \times 18 mm \times 20 mm FOV, 16 \times 16 \times 5 image matrix, 1.125 mm \times 1.125 mm \times 4 mm nominal voxel size. The measurement was repeated every 2 s for 120 s.

C.4 Results

Following the injection of HP [1-¹³C] lactate, the dynamic distribution of the injected substrate was successfully imaged (Figure C.2). However, no signal from the expected downstream metabolites, [1-¹³C] pyruvate and [¹³C] bicarbonate, could be measured in either dynamic or static spectroscopic images (Figures C.2 and C.3).

Dynamic spectroscopic images acquired following the injection of HP [1-¹³C] pyruvate illustrates the arrival of the injected substrate into the brain and surrounding blood vessels, and its turnover into lactate (Figures C.4 and C.5). However, no bicarbonate signal could be measured, neither in dynamic nor averaged images (Figures C.4, C.5 and C.6).

C.5 Discussion

A metabolite specific stack-of-spirals acquisition scheme was implemented to achieve a better dynamic range, particularly by using a metabolite-specific flip angle scheme, which enables one to apply larger tip angles to downstream metabolites to increase the measured MR signal. The implemented scheme successfully imaged the turnover of [1-¹³C] pyruvate into [1-¹³C] lactate in the healthy mouse brain, similarly to the results achieved with the IDEAL spiral CSI sequence (Chapter 6). Despite these improvements, the sensitivity was not sufficient to detect the production of bicarbonate, nor the turnover of lactate into pyruvate.

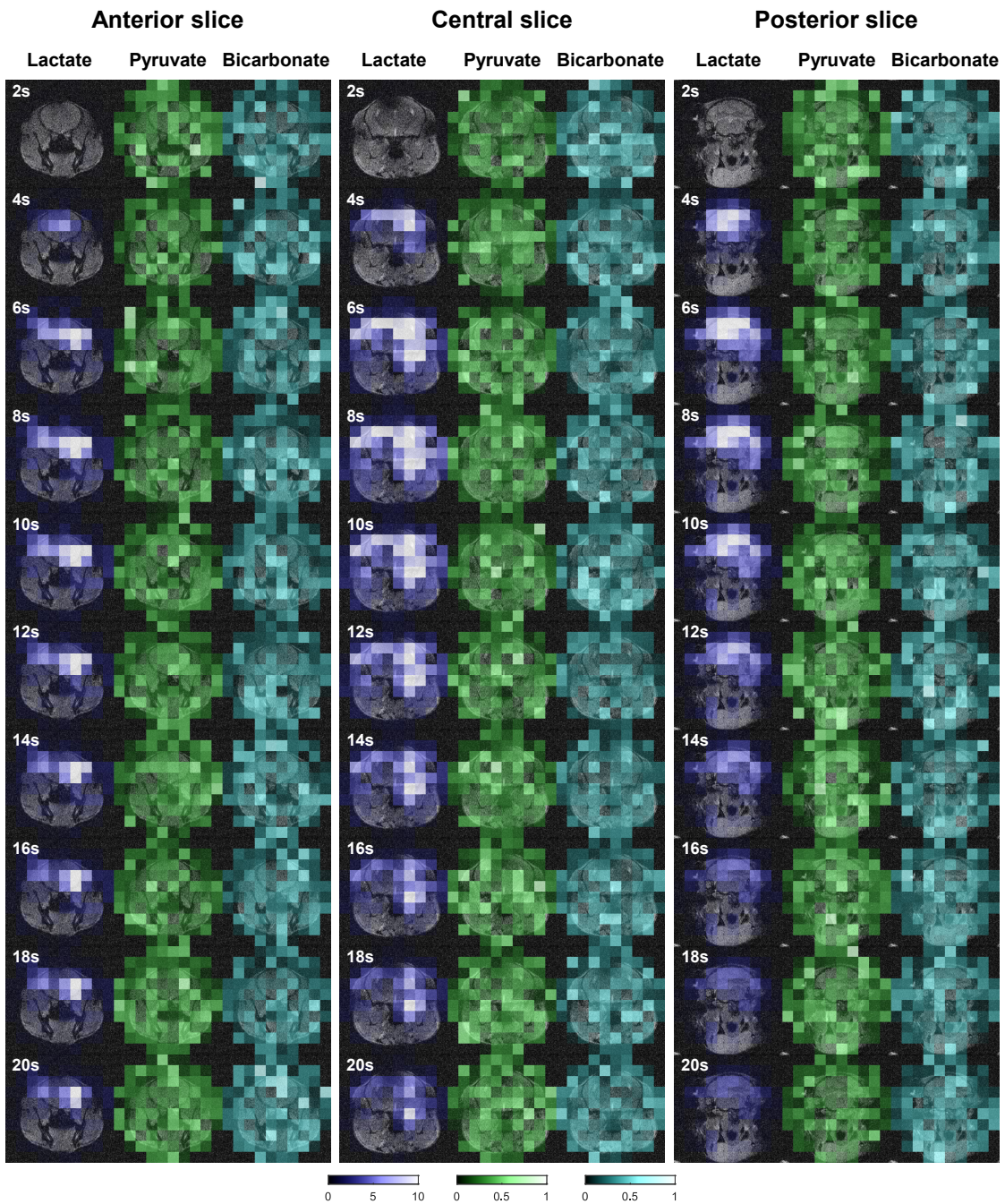


Figure C.2: Dynamic HP MRSI acquired in a healthy mouse following an injection of HP [1-¹³C] lactate using a metabolite specific stack-of-spirals acquisition scheme. The scales represent the MR signal amplitude.

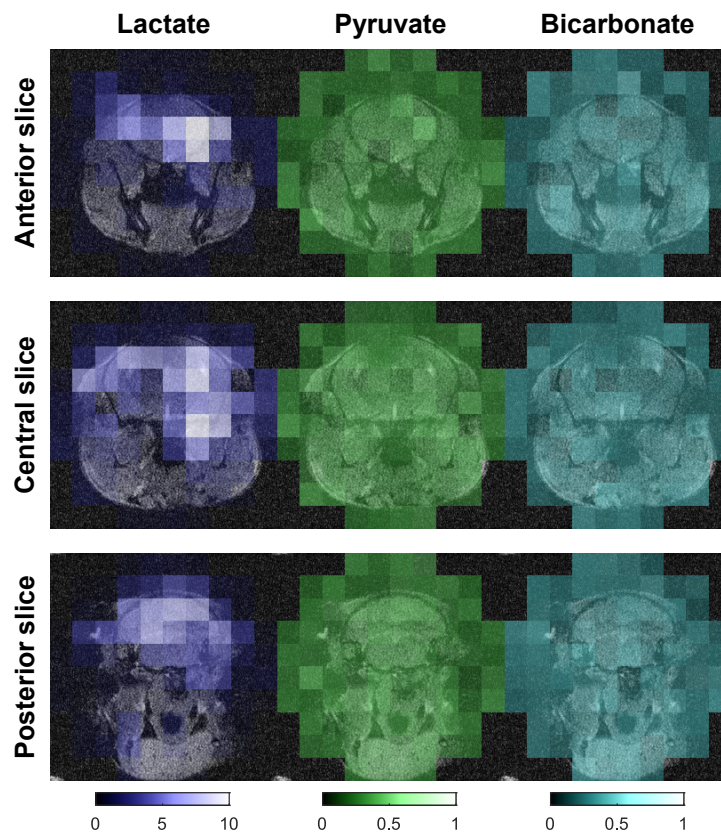


Figure C.3: Averaged maps of $[1-^{13}\text{C}]$ lactate, $[1-^{13}\text{C}]$ pyruvate and $[^{13}\text{C}]$ bicarbonate over the repetitions 3 to 11, 4 s to 20 s following an injection of HP $[1-^{13}\text{C}]$ lactate. The scales represent the MR signal amplitude.

Appendix C. Metabolite-specific stack-of-spirals MRSI sequence

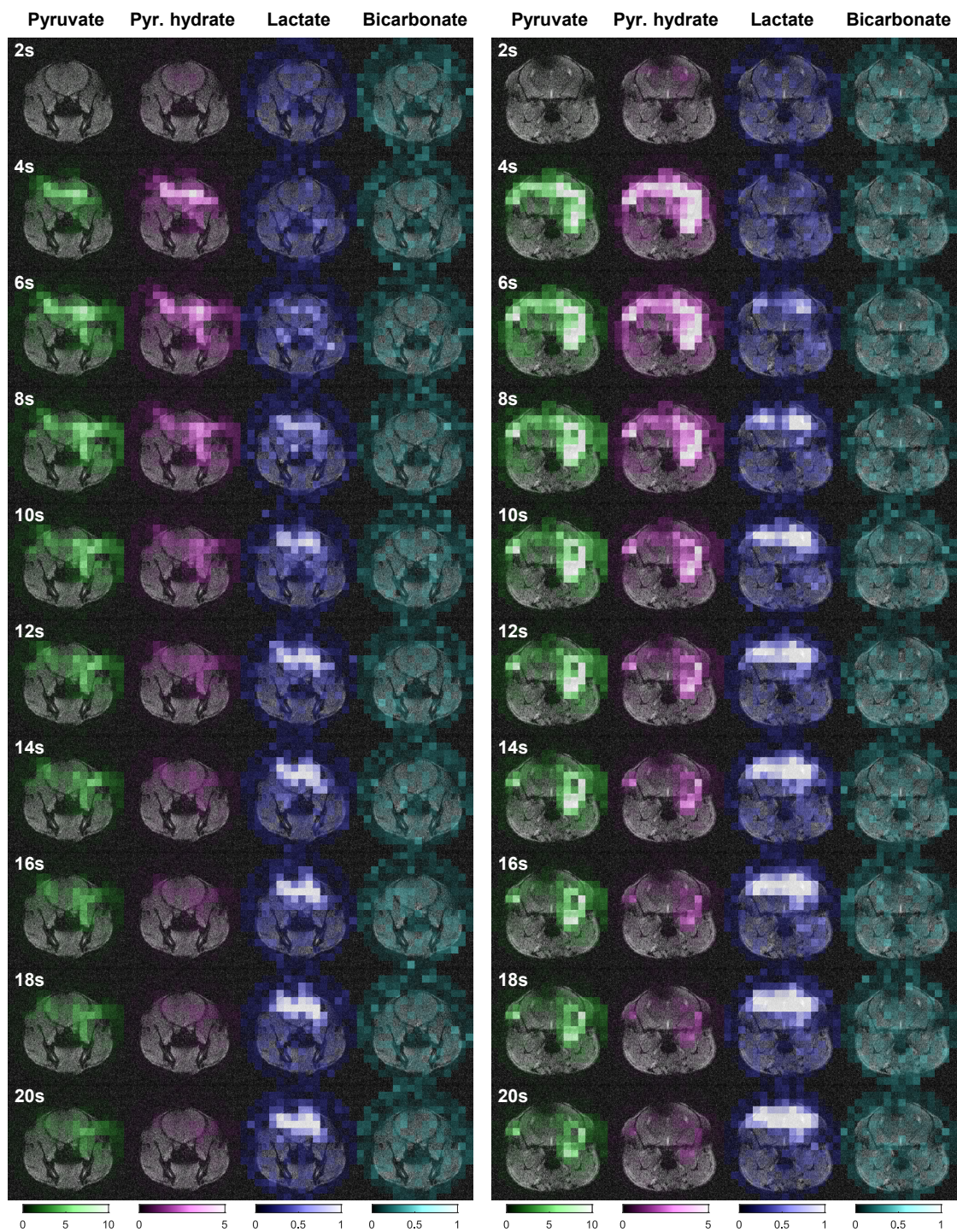


Figure C.4: Anterior (left panel) and central (right panel) slices of the dynamic HP MRSI acquired in a healthy mouse following an injection of HP [1-¹³C] pyruvate using a metabolite specific stack-of-spirals acquisition scheme. The scales represent the MR signal amplitude.

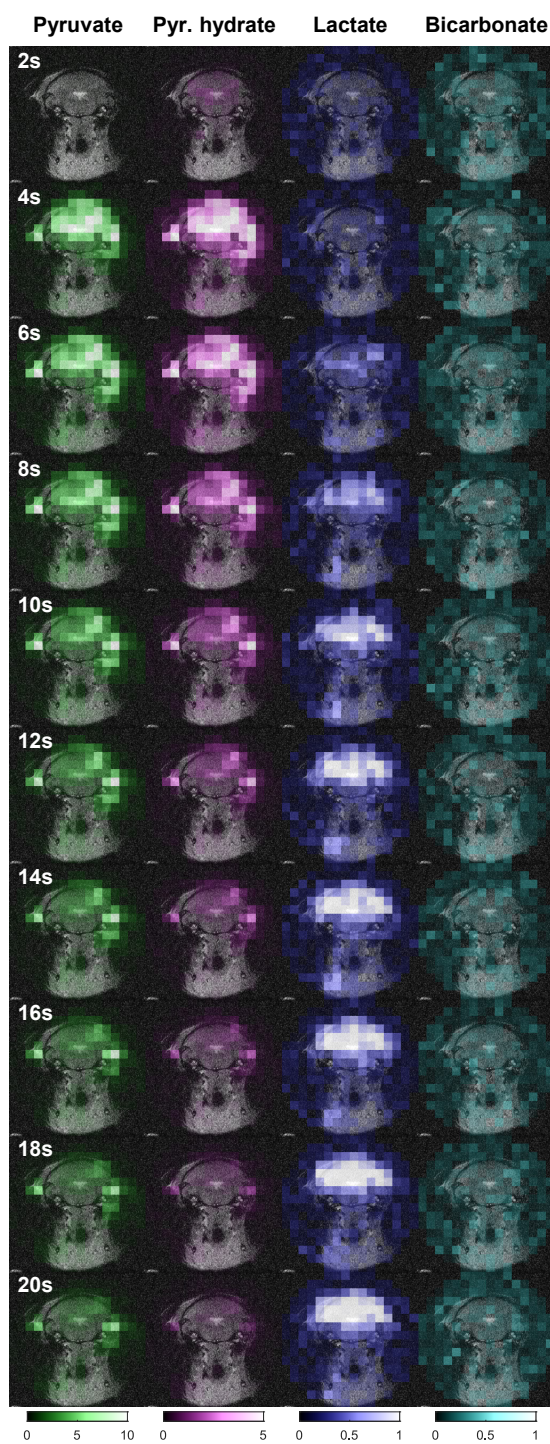


Figure C.5: Posterior slice of the dynamic HP MRSI acquired in a healthy mouse following an injection of HP [1-¹³C] pyruvate using a metabolite specific stack-of-spirals acquisition scheme. The scales represent the MR signal amplitude.

Appendix C. Metabolite-specific stack-of-spirals MRSI sequence

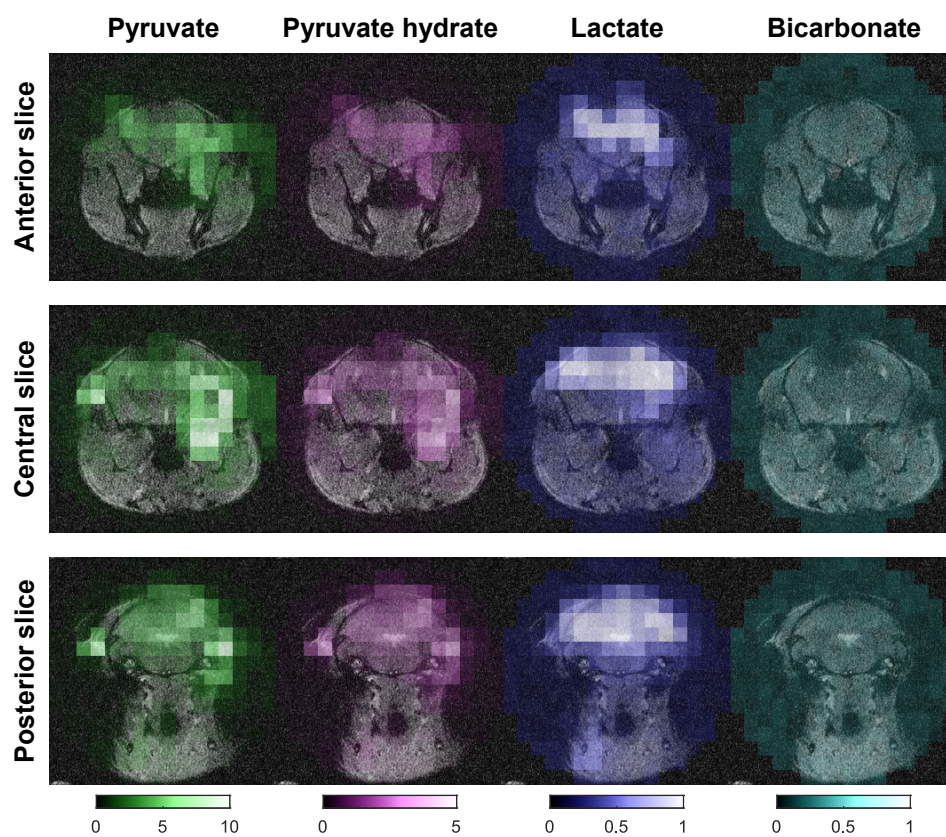


Figure C.6: Averaged maps of $[1-^{13}\text{C}]$ pyruvate, $[1-^{13}\text{C}]$ pyruvate hydrate, $[1-^{13}\text{C}]$ lactate and $[^{13}\text{C}]$ bicarbonate over the repetitions 3 to 11, 4 s to 20 s following an injection of HP $[1-^{13}\text{C}]$ pyruvate. The scales represent the MR signal amplitude.

Bibliography

- [1] Azevedo Frederico A.C., Carvalho Ludmila R.B., Grinberg Lea T., Farfel José Marcelo, Ferretti Renata E.L., Leite Renata E.P., Filho Wilson Jacob, Lent Roberto, and Herculano-Houzel Suzana. Equal numbers of neuronal and nonneuronal cells make the human brain an isometrically scaled-up primate brain. *Journal of Comparative Neurology*, 513(5):532–541, 2009. doi:10.1002/cne.21974.
- [2] Muoio V., Persson P. B., and Sendeski M. M. The neurovascular unit – concept review. *Acta Physiologica*, 210(4):790–798, 2014. doi:10.1111/apha.12250.
- [3] Tiedt Steffen, Buchan Alastair M., Dichgans Martin, Lizasoain Ignacio, Moro Maria A., and Lo Eng H. The neurovascular unit and systemic biology in stroke — implications for translation and treatment. *Nature Reviews Neurology*, 18(10):597–612, 2022. doi:10.1038/s41582-022-00703-z.
- [4] Sokoloff L., Reivich M., Kennedy C., Rosiers M. H. Des, Patlak C. S., Pettigrew K. D., Sakurada O., and Shinohara M. The [¹⁴C]deoxyglucose Method for the Measurement of Local Cerebral Glucose Utilization: Theory, Procedure, and Normal Values in the Conscious and Anesthetized Albino Rat I. *Journal of Neurochemistry*, 28(5):897–916, 1977. doi:10.1111/j.1471-4159.1977.tb10649.x.
- [5] Feigin Valery L., Stark Benjamin A., Johnson Catherine Owens, et al. Global, regional, and national burden of stroke and its risk factors, 1990–2019: A systematic analysis for the Global Burden of Disease Study 2019. *The Lancet Neurology*, 20(10):795–820, 2021. doi:10.1016/S1474-4422(21)00252-0.
- [6] Feigin Valery L., Brainin Michael, Norrving Bo, Martins Sheila, Sacco Ralph L., Hacke Werner, Fisher Marc, Pandian Jeyaraj, and Lindsay Patrice. World Stroke Organization (WSO): Global Stroke Fact Sheet 2022. *International Journal of Stroke*, 17(1):18–29, 2022. doi:10.1177/174749302111065917.
- [7] Observatoire suisse de la santé, Attaques cérébrales; OFS – Statistique médicale des hôpitaux (MS), Statistique des causes de décès (TU) et Statistique de la population et des ménages (STATPOP), 2022.
- [8] Adams H. P., Bendixen B. H., Kappelle L. J., Biller J., Love B. B., Gordon D. L., and Marsh E. E. Classification of subtype of acute ischemic stroke. Definitions for use in a multicenter clinical trial. TOAST. Trial of Org 10172 in Acute Stroke Treatment. *Stroke*, 24(1):35–41, 1993. doi:10.1161/01.STR.24.1.35.
- [9] Rennert Robert C., Wali Arvin R., Steinberg Jeffrey A., Santiago-Dieppa David R., Olson Scott E., Pannell J. Scott, and Khalessi Alexander A. Epidemiology, Natural History, and Clinical Presentation of Large Vessel Ischemic Stroke. *Neurosurgery*, 85(suppl_1):S4, 2019. doi:10.1093/neuros/nyz042.
- [10] Yoshimoto Takeshi, Inoue Manabu, Tanaka Kanta, Kanemaru Kodai, Koge Junpei, Shiozawa Masayuki, Kamogawa Naruhiko, Kimura Shunsuke, Chiba Tetsuya, Satow Tetsu, Takahashi Jun C., Toyoda Kazunori, Koga Masatoshi, and Ihara Masafumi. Identifying large ischemic core volume ranges in acute stroke that can benefit from mechanical thrombectomy. *Journal of NeuroInterventional Surgery*, 13(12):1081–1087, 2021. doi:10.1136/neurintsurg-2020-016934.
- [11] Malhotra Konark, Gornbein Jeffrey, and Saver Jeffrey L. Ischemic Strokes Due to Large-Vessel Occlusions Contribute Disproportionately to Stroke-Related Dependence and Death: A Review. *Frontiers in Neurology*, 8, 2017. doi:10.3389/fneur.2017.00651.
- [12] Minhas Jatinder S., Wang Xia, Lindley Richard I., Delcourt Candice, Song Lili, Woodward Mark, Lee Tsong-Hai, Broderick Joseph P., Pontes-Neto Octavio M., Kim Jong S., Ricci Stefano, Lavados Pablo M., Bath Philip M., Durham Alice C., Wang Ji-Guang, Sharma Vijay K., Demchuk Andrew M., Martins Sheila O., Chalmers John, Anderson Craig S., Robinson Thompson G., and Investigators on behalf of the ENCHANTED. Comparative effects of intensive-blood pressure versus standard-blood pressure-lowering treatment in patients with severe ischemic stroke in the ENCHANTED trial. *Journal of Hypertension*, 39(2):280, 2021. doi:10.1097/HJH.0000000000002640.

Bibliography

- [13] Lo Eng H., Dalkara Turgay, and Moskowitz Michael A. Mechanisms, challenges and opportunities in stroke. *Nature Reviews Neuroscience*, 4(5):399–414, 2003. doi:10.1038/nrn1106.
- [14] Stokum Jesse A., Gerzanich Volodymyr, and Simard J. Marc. Molecular pathophysiology of cerebral edema. *Journal of Cerebral Blood Flow & Metabolism*, 36(3):513–538, 2016. doi:10.1177/0271678X15617172.
- [15] Dirnagl Ulrich, Iadecola Costantino, Moskowitz Michael A., Dirnagl Ulrich, Iadecola Costantino, and Moskowitz Michael A. Pathobiology of ischaemic stroke: An integrated view. *Trends in Neurosciences*, 22(9): 391–397, 1999. doi:10.1016/S0166-2236(99)01401-0.
- [16] O’Collins Victoria, Howells David, and Markus Romesh. Neurotoxicity and Stroke. In Kostrzewa Richard M., editor, *Handbook of Neurotoxicity*, 1483–1509. Springer, New York, NY, 2014. doi:10.1007/978-1-4614-5836-4_132.
- [17] Lee Deok Hee, Kang Dong-Wha, Ahn Jae Sung, Choi Choong Gon, Kim Sang Joon, and Suh Dae Chul. Imaging of the Ischemic Penumbra in Acute Stroke. *Korean Journal of Radiology*, 6(2):64, 2005. doi:10.3348/kjr.2005.6.2.64.
- [18] Figure partly created with BioRender.
- [19] Saver Jeffrey L. Time Is Brain—Quantified. *Stroke*, 37(1):263–266, 2006. doi:10.1161/01.STR.0000196957.55928.ab.
- [20] Gács G., Fox A. J., Barnett H. J., and Vinuela F. CT visualization of intracranial arterial thromboembolism. *Stroke*, 14(5):756–762, 1983. doi:10.1161/01.STR.14.5.756.
- [21] Pressman B. D., Tourje E. J., and Thompson J. R. An early CT sign of ischemic infarction: Increased density in a cerebral artery. *American Journal of Roentgenology*, 149(3):583–586, 1987. doi:10.2214/ajr.149.3.583.
- [22] Chalela Julio A., Kidwell Chelsea S., Nentwich Lauren M., Luby Marie, Butman John A., Demchuk Andrew M., Hill Michael D., Patronas Nicholas, Latour Lawrence, and Warach Steven. Magnetic resonance imaging and computed tomography in emergency assessment of patients with suspected acute stroke: A prospective comparison. *The Lancet*, 369(9558):293–298, 2007. doi:10.1016/S0140-6736(07)60151-2.
- [23] van Everdingen K.J., van der Grond J., Kappelle L.J., Ramos L.M.P., and Mali W.P.T.M. Diffusion-Weighted Magnetic Resonance Imaging in Acute Stroke. *Stroke*, 29(9):1783–1790, 1998. doi:10.1161/01.STR.29.9.1783.
- [24] Bang Oh Young and Li Wenyu. Applications of diffusion-weighted imaging in diagnosis, evaluation, and treatment of acute ischemic stroke. *Precision and Future Medicine*, 3(2):69–76, 2019. doi:10.23838/pfm.2019.00037.
- [25] Hacke Werner, Kaste Markku, Bluhmki Erich, Brozman Miroslav, Dávalos Antoni, Guidetti Donata, Larrue Vincent, Lees Kennedy R., Medeghri Zakaria, Machnig Thomas, Schneider Dietmar, von Kummer Rüdiger, Wahlgren Nils, and Toni Danilo. Thrombolysis with Alteplase 3 to 4.5 Hours after Acute Ischemic Stroke. *New England Journal of Medicine*, 359(13):1317–1329, 2008. doi:10.1056/NEJMoa0804656.
- [26] Saver Jeffrey L., Goyal Mayank, van der Lugt Aad, et al. Time to Treatment With Endovascular Thrombectomy and Outcomes From Ischemic Stroke: A Meta-analysis. *JAMA*, 316(12):1279, 2016. doi:10.1001/jama.2016.13647.
- [27] Mulder Maxim J.H.L., Jansen Ivo G.H., Goldhoorn Robert-Jan B., Venema Esmee, Chalos Vicky, Compagne Kars C.J., Roozenbeek Bob, Lingsma Hester F., Schonewille Wouter J., van den Wijngaard Ido R., Boiten Jelis, Albert Vos Jan, Roos Yvo B.W.E.M., van Oostenbrugge Robert J., van Zwam Wim H., Majoie Charles B.L.M., van der Lugt Aad, Dippel Diederik W.J., and MR CLEAN Registry Investigators. Time to Endovascular Treatment and Outcome in Acute Ischemic Stroke. *Circulation*, 138(3):232–240, 2018. doi:10.1161/CIRCULATIONAHA.117.032600.
- [28] Kägi Georg, Schurter David, Niederhäuser Julien, De Marchis Gian Marco, Engelter Stefan, Arni Patrick, Nyenhuis Olivier, Imboden Paul, Bonvin Christophe, Luft Andreas, Renaud Susanne, Nedeltchev Krassen, Carrera Emmanuel, Cereda Carlo, Fischer Urs, Arnold Marcel, and Michel Patrik. Swiss guidelines for the prehospital phase in suspected acute stroke. *Clinical and Translational Neuroscience*, 5(1):2514183X2199923, 2021. doi:10.1177/2514183X21999230.
- [29] Thomalla Götz and Gerloff Christian. Acute imaging for evidence-based treatment of ischemic stroke. *Current Opinion in Neurology*, 32(4):521–529, 2019. doi:10.1097/WCO.0000000000000716.
- [30] Ma Henry, Campbell Bruce C.V., Parsons Mark W., et al. Thrombolysis Guided by Perfusion Imaging up to 9 Hours after Onset of Stroke. *New England Journal of Medicine*, 380(19):1795–1803, 2019. doi:10.1056/NEJMoa1813046.
- [31] Nogueira Raul G., Jadhav Ashutosh P., Haussen Diogo C., et al. Thrombectomy 6 to 24 Hours after Stroke with a Mismatch between Deficit and Infarct. *New England Journal of Medicine*, 378(1):11–21, 2018.

- doi:10.1056/NEJMoa1706442.
- [32] Löuvbld Karl-Olof, Baird Alison E., Schlaug Gottfried, Benfield Andrew, Siewert Bettina, Voetsch Barbara, Connor Ann, Burzynski Cara, Edelman Robert R., and Warach Steven. Ischemic lesion volumes in acute stroke by diffusion-weighted magnetic resonance imaging correlate with clinical outcome. *Annals of Neurology*, 42(2):164–170, 1997. doi:10.1002/ana.410420206.
- [33] Raper Vivienne. Stroke thrombectomies can improve outcome, but implementation issues remain. <https://ecrtoday.myesr.org/highlights/stroke-thrombectomies-can-improve-outcome-but-implementation-issues-remain/>, 2020.
- [34] Lin L., Wang X., and Yu Z. Ischemia-reperfusion Injury in the Brain: Mechanisms and Potential Therapeutic Strategies. *Biochemistry & pharmacology : open access*, 5(4):213, 2016. doi:10.4172/2167-0501.1000213.
- [35] Krueger Martin, Bechmann Ingo, Immig Kerstin, Reichenbach Andreas, Härtig Wolfgang, and Michalski Dominik. Blood–Brain Barrier Breakdown Involves Four Distinct Stages of Vascular Damage in Various Models of Experimental Focal Cerebral Ischemia. *Journal of Cerebral Blood Flow & Metabolism*, 35(2): 292–303, 2015. doi:10.1038/jcbfm.2014.199.
- [36] Bernardo-Castro Sara, Sousa João André, Brás Ana, Cecília Carla, Rodrigues Bruno, Almendra Luciano, Machado Cristina, Santo Gustavo, Silva Fernando, Ferreira Lino, Santana Isabel, and Sargento-Freitas João. Pathophysiology of Blood–Brain Barrier Permeability Throughout the Different Stages of Ischemic Stroke and Its Implication on Hemorrhagic Transformation and Recovery. *Frontiers in Neurology*, 11, 2020. doi:10.3389/fneur.2020.594672.
- [37] Bang Oh Young. Neuroprotective strategies for acute ischemic stroke: Recent progress and future perspectives. *Precision and Future Medicine*, 1(3):115–121, 2017. doi:10.23838/pfm.2017.00149.
- [38] Frank Dmitry, Zlotnik Alexander, Boyko Matthew, and Gruenbaum Benjamin Fredrick. The Development of Novel Drug Treatments for Stroke Patients: A Review. *International Journal of Molecular Sciences*, 23(10): 5796, 2022. doi:10.3390/ijms23105796.
- [39] Chamorro Ángel, Dirnagl Ulrich, Urra Xabier, and Planas Anna M. Neuroprotection in acute stroke: Targeting excitotoxicity, oxidative and nitrosative stress, and inflammation. *The Lancet Neurology*, 15(8):869–881, 2016. doi:10.1016/S1474-4422(16)00114-9.
- [40] Lai Ted Weita, Zhang Shu, and Wang Yu Tian. Excitotoxicity and stroke: Identifying novel targets for neuroprotection. *Progress in Neurobiology*, 115:157–188, 2014. doi:10.1016/j.pneurobio.2013.11.006.
- [41] Wu Qiu Jing and Tymianski Michael. Targeting NMDA receptors in stroke: New hope in neuroprotection. *Molecular Brain*, 11(1):15, 2018. doi:10.1186/s13041-018-0357-8.
- [42] Ma D., Wilhelm S., Maze M., and Franks N. P. Neuroprotective and neurotoxic properties of the ‘inert’ gas, xenon. *British Journal of Anaesthesia*, 89(5):739–746, 2002. doi:10.1093/bja/aef258.
- [43] Weigt Henry U., Fohr Karl J., Georgieff Michael, Georgieff Eva M., Senftleben Uwe, and Adolph Oliver. Xenon blocks AMPA and NMDA receptor channels by different mechanisms. *Acta Neurobiologiae Experimentalis*, 69(4):429–440, 2009.
- [44] Pan Yi, Zhang Haibo, VanDeripe Donald R., Cruz-Flores Salvador, and Panneton W. Michael. Heliox and oxygen reduce infarct volume in a rat model of focal ischemia. *Experimental Neurology*, 205(2):587–590, 2007. doi:10.1016/j.expneurol.2007.03.023.
- [45] David Hélène N., Haelewyn Benoît, Chazalviel Laurent, Lecocq Myriam, Degoulet Mickael, Risso Jean-Jacques, and Abraini Jacques H. Post-Ischemic Helium Provides Neuroprotection in Rats Subjected to Middle Cerebral Artery Occlusion-Induced Ischemia by Producing Hypothermia. *Journal of Cerebral Blood Flow & Metabolism*, 29(6):1159–1165, 2009. doi:10.1038/jcbfm.2009.40.
- [46] Lees Kennedy R., Zivin Justin A., Ashwood Tim, Davalos Antonio, Davis Stephen M., Diener Hans-Christoph, Grotta James, Lyden Patrick, Shuaib Ashfaq, Hårdemark Hans-Göran, and Wasiewski Warren W. NXY-059 for Acute Ischemic Stroke. *New England Journal of Medicine*, 354(6):588–600, 2006. doi:10.1056/NEJMoa052980.
- [47] Shuaib Ashfaq, Lees Kennedy R., Lyden Patrick, Grotta James, Davalos Antonio, Davis Stephen M., Diener Hans-Christoph, Ashwood Tim, Wasiewski Warren W., and Emeribe Ugochi. NXY-059 for the Treatment of Acute Ischemic Stroke. *New England Journal of Medicine*, 357(6):562–571, 2007. doi:10.1056/NEJMoa070240.
- [48] Lapchak Paul A. A critical assessment of edaravone acute ischemic stroke efficacy trials: Is edaravone an effective neuroprotective therapy? *Expert Opinion on Pharmacotherapy*, 11(10):1753–1763, 2010. doi:10.1517/14656566.2010.493558.
- [49] Xu Jie, Wang Anxin, Meng Xia, et al. Edaravone Dexborneol Versus Edaravone Alone for the Treatment of Acute Ischemic Stroke. *Stroke*, 52(3):772–780, 2021. doi:10.1161/STROKEAHA.120.031197.

Bibliography

- [50] Li William A., Moore-Langston Shannon, Chakraborty Tia, Rafols Jose A., Conti Alana C., and Ding Yuchuan. Hyperglycemia in stroke and possible treatments. *Neurological Research*, 35(5):479–491, 2013. doi:10.1179/1743132813Y.0000000209.
- [51] Bevers Matthew B., Vaishnav Neil H., Pham Ly, Battey Thomas W. K., and Kimberly W Taylor. Hyperglycemia is associated with more severe cytotoxic injury after stroke. *Journal of Cerebral Blood Flow & Metabolism*, 37(7):2577–2583, 2017. doi:10.1177/0271678X16671730.
- [52] Satoh Eiki and Takahashi Ayako. Experimental diabetes enhances Ca²⁺ mobilization and glutamate exocytosis in cerebral synaptosomes from mice. *Diabetes Research and Clinical Practice*, 81(2):e14–e17, 2008. doi:10.1016/j.diabres.2008.04.017.
- [53] Zhu Chang Z. and Auer Roland N. Optimal blood glucose levels while using insulin to minimize the size of infarction in focal cerebral ischemia. *Journal of Neurosurgery*, 101(4):664–668, 2004. doi:10.3171/jns.2004.101.4.0664.
- [54] Auer Roland N. Insulin, blood glucose levels, and ischemic brain damage. *Neurology*, 51(3 Suppl 3):S39–S43, 1998. doi:10.1212/WNL.51.3_Suppl_3.S39.
- [55] Bélanger Mireille, Allaman Igor, and Magistretti Pierre J. Brain Energy Metabolism: Focus on Astrocyte-Neuron Metabolic Cooperation. *Cell Metabolism*, 14(6):724–738, 2011. doi:10.1016/j.cmet.2011.08.016.
- [56] González-Falcón Armando, Candelario-Jalil Eduardo, Garcia-Cabrera Michel, and León Olga Sonia. Effects of pyruvate administration on infarct volume and neurological deficits following permanent focal cerebral ischemia in rats. *Brain Research*, 990(1-2):1–7, 2003. doi:10.1016/S0006-8993(03)03378-X.
- [57] Yi Jung-Sun, Kim Tae-Youn, Kyu Kim Dong, and Koh Jae-Young. Systemic pyruvate administration markedly reduces infarcts and motor deficits in rat models of transient and permanent focal cerebral ischemia. *Neurobiology of Disease*, 26(1):94–104, 2007. doi:10.1016/j.nbd.2006.12.007.
- [58] Ryou Myoung-Gwi, Liu Ran, Ren Ming, Sun Jie, Mallet Robert T., and Yang Shao-Hua. Pyruvate Protects the Brain Against Ischemia-Reperfusion Injury by Activating the Erythropoietin Signaling Pathway. *Stroke*, 43(4):1101–1107, 2012. doi:10.1161/STROKEAHA.111.620088.
- [59] Frank Dmitry, Kuts Ruslan, Tsenter Philip, Gruenbaum Benjamin F, Grinshpun Yulia, Zvenigorodsky Vladislav, Shelef Ilan, Natanel Dmitry, Brotfain Evgeny, Zlotnik Alexander, and Boyko Matthew. The effect of pyruvate on the development and progression of post-stroke depression: A new therapeutic approach. *Neuropharmacology*, 155:173–184, 2019. doi:10.1016/j.neuropharm.2019.05.035.
- [60] Zilberter Yuri, Gubkina Olena, and Ivanov Anton I. A unique array of neuroprotective effects of pyruvate in neuropathology. *Frontiers in Neuroscience*, 9, 2015. doi:10.3389/fnins.2015.00017.
- [61] Castillo Ximena, Rosafio Katia, Wyss Matthias T, Drandarov Konstantin, Buck Alfred, Pellerin Luc, Weber Bruno, and Hirt Lorenz. A Probable Dual Mode of Action for Both L- and D-Lactate Neuroprotection in Cerebral Ischemia. *Journal of Cerebral Blood Flow & Metabolism*, 35(10):1561–1569, 2015. doi:10.1038/jcbfm.2015.115.
- [62] Berthet Carole, Castillo Ximena, Magistretti Pierre J., and Hirt Lorenz. New Evidence of Neuroprotection by Lactate after Transient Focal Cerebral Ischaemia: Extended Benefit after Intracerebroventricular Injection and Efficacy of Intravenous Administration. *Cerebrovascular Diseases*, 34(5-6):329–335, 2012. doi:10.1159/000343657.
- [63] Berthet Carole, Lei Hongxia, Thevenet Jonathan, Gruetter Rolf, Magistretti Pierre J., and Hirt Lorenz. Neuroprotective Role of Lactate after Cerebral Ischemia. *Journal of Cerebral Blood Flow & Metabolism*, 29(11):1780–1789, 2009. doi:10.1038/jcbfm.2009.97.
- [64] Buscemi Lara, Blochet Camille, Price Melanie, Magistretti Pierre J., Lei Hongxia, and Hirt Lorenz. Extended preclinical investigation of lactate for neuroprotection after ischemic stroke. *Clinical and Translational Neuroscience*, 4(1):2514183X2090457, 2020. doi:10.1177/2514183X20904571.
- [65] Buscemi Lara, Price Melanie, Castillo-González Julia, Chatton Jean-Yves, and Hirt Lorenz. Lactate Neuroprotection against Transient Ischemic Brain Injury in Mice Appears Independent of HCAR1 Activation. *Metabolites*, 12(5):465, 2022. doi:10.3390/metabo12050465.
- [66] Bhatti Mehwish S. and Frostig Ron D. Astrocyte-neuron lactate shuttle plays a pivotal role in sensory-based neuroprotection in a rat model of permanent middle cerebral artery occlusion. *Scientific Reports*, 13(1):12799, 2023. doi:10.1038/s41598-023-39574-9.
- [67] Schurr Avital, West Catherine A., and Rigor Benjamin M. Lactate-Supported Synaptic Function in the Rat Hippocampal Slice Preparation. *Science*, 240(4857):1326–1328, 1988. doi:10.1126/science.3375817.

- [68] Schurr Avital. Lactate: The Ultimate Cerebral Oxidative Energy Substrate? *Journal of Cerebral Blood Flow & Metabolism*, 26(1):142–152, 2006. doi:10.1038/sj.jcbfm.9600174.
- [69] Magistretti Pierre J. and Allaman Igor. Lactate in the brain: From metabolic end-product to signalling molecule. *Nature Reviews Neuroscience*, 19(4):235–249, 2018. doi:10.1038/nrn.2018.19.
- [70] Buscemi Lara, Blochet Camille, Magistretti Pierre J., and Hirt Lorenz. Hydroxycarboxylic Acid Receptor 1 and Neuroprotection in a Mouse Model of Cerebral Ischemia-Reperfusion. *Frontiers in Physiology*, 12, 2021. doi:10.3389/fphys.2021.689239.
- [71] Oddo Mauro. Neuroprotective Role of Lactate Therapy in Humans With Traumatic Brain Injury. Clinical Trial Registration NCT01573507, clinicaltrials.gov, 2021.
- [72] Carteron Laurent, Solari Daria, Patet Camille, Quintard Hervé, Miroz John-Paul, Bloch Jocelyne, Daniel Roy T., Hirt Lorenz, Eckert Philippe, Magistretti Pierre J., and Oddo Mauro. Hypertonic Lactate to Improve Cerebral Perfusion and Glucose Availability After Acute Brain Injury*. *Critical Care Medicine*, 46(10):1649–1655, 2018. doi:10.1097/CCM.0000000000003274.
- [73] Patet Camille, Suys Tamarah, Carteron Laurent, and Oddo Mauro. Cerebral Lactate Metabolism After Traumatic Brain Injury. *Current Neurology and Neuroscience Reports*, 16(4):31, 2016. doi:10.1007/s11910-016-0638-5.
- [74] Hirt Lorenz. Exploring the Effect of Lactate Administration After Ischemic Stroke on Brain Metabolism. Clinical Trial Registration NCT04858139, clinicaltrials.gov, 2021.
- [75] Stankowski Jeannette N. and Gupta Rishi. Therapeutic Targets for Neuroprotection in Acute Ischemic Stroke: Lost in Translation? *Antioxidants & Redox Signaling*, 14(10):1841–1851, 2011. doi:10.1089/ars.2010.3292.
- [76] Paul Surojit and Candelario-Jalil Eduardo. Emerging neuroprotective strategies for the treatment of ischemic stroke: An overview of clinical and preclinical studies. *Experimental Neurology*, 335:113518, 2021. doi:10.1016/j.expneurol.2020.113518.
- [77] Demchuk Andrew M. and Buchan Alastair M. PREDICTORS OF STROKE OUTCOME. *Neurologic Clinics*, 18(2):455–473, 2000. doi:10.1016/S0733-8619(05)70202-4.
- [78] Gallacher Katie I., Batty G. David, McLean Gary, Mercer Stewart W., Guthrie Bruce, May Carl R., Langhorne Peter, and Mair Frances S. Stroke, multimorbidity and polypharmacy in a nationally representative sample of 1,424,378 patients in Scotland: Implications for treatment burden. *BMC Medicine*, 12(1):151, 2014. doi:10.1186/s12916-014-0151-0.
- [79] Schmidt-Pogoda Antje, Bonberg Nadine, Koecke Mailin Hannah Marie, Strecker Jan-Kolja, Wellmann Jürgen, Bruckmann Nils-Martin, Beuker Carolin, Schäbitz Wolf-Rüdiger, Meuth Sven G., Wiendl Heinz, Minnerup Heike, and Minnerup Jens. Why Most Acute Stroke Studies Are Positive in Animals but Not in Patients: A Systematic Comparison of Preclinical, Early Phase, and Phase 3 Clinical Trials of Neuroprotective Agents. *Annals of Neurology*, 87(1):40–51, 2020. doi:10.1002/ana.25643.
- [80] Jonas Saran, Aiyagari Venkatesh, Vieira Dorice, and Figueroa Miguel. The Failure of Neuronal Protective Agents Versus the Success of Thrombolysis in the Treatment of Ischemic Stroke. *Annals of the New York Academy of Sciences*, 939(1):257–267, 2001. doi:10.1111/j.1749-6632.2001.tb03633.x.
- [81] *Le secteur ambulatoire des hôpitaux en 2014*. Actualité OFS. Office fédéral de la statistique (OFS), 2016.
- [82] *Équipement médico-technique des hôpitaux et des cabinets médicaux en 2019*. Actualité OFS. Office fédéral de la statistique (OFS), 2021.
- [83] Albers G. W. Diffusion-weighted MRI for evaluation of acute stroke. *Neurology*, 51(3 Suppl 3):S47–49, 1998. doi:10.1212/wnl.51.3_suppl_3.s47.
- [84] Ward K. M, Aletras A. H, and Balaban R. S. A New Class of Contrast Agents for MRI Based on Proton Chemical Exchange Dependent Saturation Transfer (CEST). *Journal of Magnetic Resonance*, 143(1):79–87, 2000. doi:10.1006/jmre.1999.1956.
- [85] Sun Phillip Zhe, Zhou Jinyuan, Sun Weiyun, Huang Judy, and van Zijl Peter C. M. Suppression of lipid artifacts in amide proton transfer imaging. *Magnetic Resonance in Medicine*, 54(1):222–225, 2005. doi:10.1002/mrm.20530.
- [86] Sun Phillip Zhe, Zhou Jinyuan, Sun Weiyun, Huang Judy, and van Zijl Peter CM. Detection of the Ischemic Penumbra Using pH-Weighted MRI. *Journal of Cerebral Blood Flow & Metabolism*, 27(6):1129–1136, 2007. doi:10.1038/sj.jcbfm.9600424.
- [87] Berkelbach van der Sprenkel J. W., Luyten P. R., van Rijen P. C., Tulleken C. A., and den Hollander J. A. Cerebral lactate detected by regional proton magnetic resonance spectroscopy in a patient with cerebral infarction.

Bibliography

- Stroke*, 19(12):1556–1560, 1988. doi:10.1161/01.STR.19.12.1556.
- [88] Higuchi Toshihiro, Fernandez Erik J., Maudsley Andrew A., Shimizu Hiroaki, Weiner Michael W., and Weinstein Philip R. Mapping of Lactate and N-Acetyl-L-aspartate Predicts Infarction during Acute Focal Ischemia: In Vivo ^1H Magnetic Resonance Spectroscopy in Rats. *Neurosurgery*, 38(1):121, 1996. doi:10.1097/00006123-199601000-00030.
- [89] Barker Peter B. Magnetic resonance spectroscopy in cerebral ischemia and infarction. *Seminars in Cerebrovascular Diseases and Stroke*, 1(4):331–342, 2001. doi:10.1053/scds.2001.29101.
- [90] Stengel Astrid, Neumann-Haefelin Tobias, Singer Oliver C., Neumann-Haefelin Claudia, Zanella Friedhelm E., Lanfermann Heinrich, and Pilatus Ulrich. Multiple spin-echo spectroscopic imaging for rapid quantitative assessment of N-acetylaspartate and lactate in acute stroke. *Magnetic Resonance in Medicine*, 52(2):228–238, 2004. doi:10.1002/mrm.20171.
- [91] Li Yao, Wang Tianyao, Zhang Tianxiao, Lin Zengping, Li Yudu, Guo Rong, Zhao Yibo, Meng Ziyu, Liu Jun, Yu Xin, Liang Zhi-Pei, and Nachev Parashkev. Fast high-resolution metabolic imaging of acute stroke with 3D magnetic resonance spectroscopy. *Brain*, 143(11):3225–3233, 2020. doi:10.1093/brain/awaa264.
- [92] Lin Zengping, Meng Ziyu, Wang Tianyao, Guo Rong, Zhao Yibo, Li Yudu, Bo Bin, Guan Yue, Liu Jun, Zhou Hong, Yu Xin, Lin David J., Liang Zhi-Pei, Nachev Parashkev, and Li Yao. Predicting the Onset of Ischemic Stroke With Fast High-Resolution 3D MR Spectroscopic Imaging. *Journal of Magnetic Resonance Imaging*, 2023. doi:10.1002/jmri.28596.
- [93] Lei Hongxia, Berthet Carole, Hirt Lorenz, and Gruetter Rolf. Evolution of the Neurochemical Profile after Transient Focal Cerebral Ischemia in the Mouse Brain. *Journal of Cerebral Blood Flow & Metabolism*, 29(4):811–819, 2009. doi:10.1038/jcbfm.2009.8.
- [94] Yan Gen, Dai Zhuozhi, Xuan Yinghua, and Wu Renhua. Early metabolic changes following ischemia onset in rats: An in vivo diffusion-weighted imaging and ^1H -magnetic resonance spectroscopy study at 7.0 T. *Molecular Medicine Reports*, 11(6):4109–4114, 2015. doi:10.3892/mmr.2015.3283.
- [95] Boulant Nicolas, Quettier Lionel, Aubert G., Amadon A., Belorgey J., Berriard C., Bonnelye C., Bredy Ph., Chazel E., Dilasser G., Dubois O., Giacomini E., Gilgrass G., Gras V., Guihard Q., Jannot V., Juster F. P., Lannou H., Leprêtre E., Lerman C., Le Ster C., Luong M., Mauconduit F., Molinié F., Nunio F., Scola L., Sinanna A., Touzery R., Védrine P., Vignaud A., and the Iseult Consortium. Commissioning of the Iseult CEA 11.7 T whole-body MRI: Current status, gradient–magnet interaction tests and first imaging experience. *Magnetic Resonance Materials in Physics, Biology and Medicine*, 2023. doi:10.1007/s10334-023-01063-5.
- [96] Fu R., Brey W. W., Shetty K., Gor'kov P., Saha S., Long J. R., Grant S. C., Chekmenev E. Y., Hu J., Gan Z., Sharma M., Zhang F., Logan T. M., Brüschweiler R., Edison A., Blue A., Dixon I. R., Markiewicz W. D., and Cross T. A. Ultra-wide bore 900MHz high-resolution NMR at the National High Magnetic Field Laboratory. *Journal of Magnetic Resonance*, 177(1):1–8, 2005. doi:10.1016/j.jmr.2005.07.013.
- [97] Markiewicz W. Denis, Brey William W., Cross Timothy A., Dixon Iain R., Gor'kov Peter L., Grant Samuel C., Marks Emsley L., Painter Thomas A., Schepkin Victor D., and Swenson Charles A. A Decade of Experience With the UltraWide-Bore 900-MHz NMR Magnet. *IEEE Transactions on Applied Superconductivity*, 25(3):1–5, 2015. doi:10.1109/TASC.2014.2364540.
- [98] Wikus Patrick, Frantz Wolfgang, Kümmerle Rainer, and Vonlanthen Patrik. Commercial gigahertz-class NMR magnets. *Superconductor Science and Technology*, 35(3):033001, 2022. doi:10.1088/1361-6668/ac4951.
- [99] Houpt Thomas A., Cassell Jennifer A., Riccardi Christina, DenBleyker Megan D., Hood Alison, and Smith James C. Rats avoid high magnetic fields: Dependence on an intact vestibular system. *Physiology & Behavior*, 92(4):741–747, 2007. doi:10.1016/j.physbeh.2007.05.062.
- [100] Brewer W. and Kopp M. Brute-force nuclear orientation. *Hyperfine Interactions*, 2(1):299–305, 1976. doi:10.1007/BF01021151.
- [101] Hirsch Matthew L., Kalechofsky Neal, Belzer Avrum, Rosay Melanie, and Kempf James G. Brute-Force Hyperpolarization for NMR and MRI. *Journal of the American Chemical Society*, 137(26):8428–8434, 2015. doi:10.1021/jacs.5b01252.
- [102] Hirsch Matthew L., Smith Bryce A., Mattingly Mark, Goloshevsky Artem G., Rosay Melanie, and Kempf James G. Transport and imaging of brute-force ^{13}C hyperpolarization. *Journal of Magnetic Resonance*, 261:87–94, 2015. doi:10.1016/j.jmr.2015.09.017.
- [103] Owers-Bradley John R., Horsewill Anthony J., Peat David T., Goh Kelvin S. K., and Gadian David G. High polarization of nuclear spins mediated by nanoparticles at millikelvin temperatures. *Physical Chemistry Chemical Physics*, 15(25):10413–10417, 2013. doi:10.1039/C3CP51274F.

- [104] Bouchiat M. A., Carver T. R., and Varnum C. M. Nuclear Polarization in ^3He Gas Induced by Optical Pumping and Dipolar Exchange. *Physical Review Letters*, 5(8):373–375, 1960. doi:10.1103/PhysRevLett.5.373.
- [105] Walker Thad G. and Happer William. Spin-exchange optical pumping of noble-gas nuclei. *Reviews of Modern Physics*, 69(2):629–642, 1997. doi:10.1103/RevModPhys.69.629.
- [106] Nikolaou Panayiotis, Coffey Aaron M., Walkup Laura L., Gust Brogan M., LaPierre Cristen D., Koehnmann Edward, Barlow Michael J., Rosen Matthew S., Goodson Boyd M., and Chekmenev Eduard Y. A 3D-Printed High Power Nuclear Spin Polarizer. *Journal of the American Chemical Society*, 136(4):1636–1642, 2014. doi:10.1021/ja412093d.
- [107] Norquay Graham, Collier Guilhem J., Rodgers Oliver I., Gill Andrew B., Sreaton Nicholas J., and Wild Jim. Standalone portable xenon-129 hyperpolariser for multicentre clinical magnetic resonance imaging of the lungs. *The British Journal of Radiology*, 95(1132):20210872, 2022. doi:10.1259/bjr.20210872.
- [108] Khan Alixander S., Harvey Rebecca L., Birchall Jonathan R., Irwin Robert K., Nikolaou Panayiotis, Schrank Geoffry, Emami Kiarash, Dummer Andrew, Barlow Michael J., Goodson Boyd M., and Chekmenev Eduard Y. Enabling Clinical Technologies for Hyperpolarized ^{129}Xe Magnetic Resonance Imaging and Spectroscopy. *Angewandte Chemie International Edition*, 60(41):22126–22147, 2021. doi:10.1002/anie.202015200.
- [109] Fain Sean B., Korosec Frank R., Holmes James H., O'Halloran Rafael, Sorkness Ronald L., and Grist Thomas M. Functional lung imaging using hyperpolarized gas MRI. *Journal of Magnetic Resonance Imaging*, 25(5): 910–923, 2007. doi:10.1002/jmri.20876.
- [110] Center for Drug Evaluation and Research . Novel Drug Approvals for 2022. *FDA*, Tue, 01/10/2023 - 11:00.
- [111] Rao Madhwesha, Stewart Neil J., Norquay Graham, Griffiths Paul D., and Wild Jim M. High resolution spectroscopy and chemical shift imaging of hyperpolarized ^{129}Xe dissolved in the human brain in vivo at 1.5 Tesla. *Magnetic Resonance in Medicine*, 75(6):2227–2234, 2016. doi:10.1002/mrm.26241.
- [112] Marshall Helen, Stewart Neil J., Chan Ho-Fung, Rao Madhwesha, Norquay Graham, and Wild Jim M. In vivo methods and applications of xenon-129 magnetic resonance. *Progress in Nuclear Magnetic Resonance Spectroscopy*, 122:42–62, 2021. doi:10.1016/j.pnmrs.2020.11.002.
- [113] Natterer Johannes and Bargon Joachim. Parahydrogen induced polarization. *Progress in Nuclear Magnetic Resonance Spectroscopy*, 31(4):293–315, 1997. doi:10.1016/S0079-6565(97)00007-1.
- [114] Matsumoto Mitsuru and Espenson James H. Kinetics of the Interconversion of Parahydrogen and Orthohydrogen Catalyzed by Paramagnetic Complex Ions. *Journal of the American Chemical Society*, 127(32): 11447–11453, 2005. doi:10.1021/ja0524292.
- [115] Feng Bibo, Coffey Aaron M., Colon Raul D., Chekmenev Eduard Y., and Waddell Kevin W. A pulsed injection parahydrogen generator and techniques for quantifying enrichment. *Journal of Magnetic Resonance*, 214: 258–262, 2012. doi:10.1016/j.jmr.2011.11.015.
- [116] Hövener Jan-Bernd, Pravdivtsev Andrey N., Kidd Bryce, Bowers C. Russell, Glögler Stefan, Kovtunov Kirill V., Plaumann Markus, Katz-Brull Rachel, Buckenmaier Kai, Jerschow Alexej, Reineri Francesca, Theis Thomas, Shchepin Roman V., Wagner Shawn, Bhattacharya Pratip, Zacharias Niki M., and Chekmenev Eduard Y. Parahydrogen-Based Hyperpolarization for Biomedicine. *Angewandte Chemie International Edition*, 57(35): 11140–11162, 2018. doi:10.1002/anie.201711842.
- [117] Bowers C. Russell and Weitekamp D. P. Parahydrogen and synthesis allow dramatically enhanced nuclear alignment. *Journal of the American Chemical Society*, 109(18):5541–5542, 1987. doi:10.1021/ja00252a049.
- [118] Pravica Michael G. and Weitekamp Daniel P. Net NMR alignment by adiabatic transport of parahydrogen addition products to high magnetic field. *Chemical Physics Letters*, 145(4):255–258, 1988. doi:10.1016/0009-2614(88)80002-2.
- [119] Goldman Maurice, Jóhannesson Haukur, Axelsson Oskar, and Karlsson Magnus. Hyperpolarization of ^{13}C through order transfer from parahydrogen: A new contrast agent for MRI. *Magnetic Resonance Imaging*, 23(2):153–157, 2005. doi:10.1016/j.mri.2004.11.031.
- [120] Reineri Francesca, Viale Alessandra, Ellena Silvano, Alberti Diego, Boi Tommaso, Giovenzana Giovanni Battista, Gobetto Roberto, Premkumar Samuel S. D., and Aime Silvio. ^{15}N Magnetic Resonance Hyperpolarization via the Reaction of Parahydrogen with ^{15}N -Propargylcholine. *Journal of the American Chemical Society*, 134(27):11146–11152, 2012. doi:10.1021/ja209884h.
- [121] Adams Ralph W., Aguilar Juan A., Atkinson Kevin D., Cowley Michael J., Elliott Paul I. P., Duckett Simon B., Green Gary G. R., Khazal Iman G., López-Serrano Joaquín, and Williamson David C. Reversible Interactions with para-Hydrogen Enhance NMR Sensitivity by Polarization Transfer. *Science*, 323(5922):1708–1711, 2009. doi:10.1126/science.1168877.

Bibliography

- [122] Cowley Michael J., Adams Ralph W., Atkinson Kevin D., Cockett Martin C. R., Duckett Simon B., Green Gary G. R., Lohman Joost A. B., Kerssebaum Rainer, Kilgour David, and Mewis Ryan E. Iridium N-Heterocyclic Carbene Complexes as Efficient Catalysts for Magnetization Transfer from para-Hydrogen. *Journal of the American Chemical Society*, 133(16):6134–6137, 2011. doi:10.1021/ja200299u.
- [123] Reineri Francesca, Cavallari Eleonora, Carrera Carla, and Aime Silvio. Hydrogenative-PHIP polarized metabolites for biological studies. *Magnetic Resonance Materials in Physics, Biology and Medicine*, 34(1): 25–47, 2021. doi:10.1007/s10334-020-00904-x.
- [124] Knecht Stephan, Blanchard John W., Barskiy Danila, Cavallari Eleonora, Dagys Laurynas, Van Dyke Erik, Tsukanov Maksim, Bliemel Bea, Münnemann Kerstin, Aime Silvio, Reineri Francesca, Levitt Malcolm H., Buntkowsky Gerd, Pines Alexander, Blümmler Peter, Budker Dmitry, and Eills James. Rapid hyperpolarization and purification of the metabolite fumarate in aqueous solution. *Proceedings of the National Academy of Sciences*, 118(13):e2025383118, 2021. doi:10.1073/pnas.2025383118.
- [125] Schmidt Andreas B., Eills James, Dagys Laurynas, Gierse Martin, Keim Michael, Lucas Sebastian, Bock Michael, Schwartz Ilai, Zaitsev Maxim, Chekmenev Eduard Y., and Knecht Stephan. Over 20% Carbon-13 Polarization of Perdeuterated Pyruvate Using Reversible Exchange with Parahydrogen and Spin-Lock Induced Crossing at 50 μ T. *The Journal of Physical Chemistry Letters*, 14(23):5305–5309, 2023. doi:10.1021/acs.jpcclett.3c00707.
- [126] Gierse Martin, Nagel Luca, Keim Michael, Lucas Sebastian, Speidel Tobias, Lobmeyer Tobias, Winter Gordon, Josten Felix, Karaali Senay, Fellermann Maximilian, Scheuer Jochen, Müller Christoph, van Heijster Frits, Skinner Jason, Löffler Jessica, Parker Anna, Handwerker Jonas, Marshall Alastair, Salhov Alon, El-Kassem Bilal, Vassiliou Christophoros, Blanchard John W., Picazo-Frutos Román, Eills James, Barth Holger, Jelezko Fedor, Rasche Volker, Schilling Franz, Schwartz Ilai, and Knecht Stephan. Parahydrogen-Polarized Fumarate for Preclinical in Vivo Metabolic Magnetic Resonance Imaging. *Journal of the American Chemical Society*, 145(10):5960–5969, 2023. doi:10.1021/jacs.2c13830.
- [127] Nagel Luca, Gierse Martin, Gottwald Wolfgang, Ahmadova Zumrud, Grashei Martin, Wolff Pascal, Josten Felix, Karaali Senay, Müller Christoph A., Lucas Sebastian, Scheuer Jochen, Müller Christoph, Blanchard John, Topping Geoffrey J., Wendlinger Andre, Setzer Nadine, Sühnel Sandra, Handwerker Jonas, Vassiliou Christophoros, van Heijster Frits H.A., Knecht Stephan, Keim Michael, Schilling Franz, and Schwartz Ilai. Parahydrogen-Polarized [13 C]Pyruvate for Reliable and Fast Preclinical Metabolic Magnetic Resonance Imaging. *Advanced Science*, 2303441, 2023. doi:10.1002/advs.202303441.
- [128] Overhauser Albert W. Polarization of Nuclei in Metals. *Physical Review*, 92(2):411–415, 1953. doi:10.1103/PhysRev.92.411.
- [129] Carver T. R. and Slichter C. P. Polarization of Nuclear Spins in Metals. *Physical Review*, 92(1):212–213, 1953. doi:10.1103/PhysRev.92.212.2.
- [130] Jeffries C. D. Polarization of Nuclei by Resonance Saturation in Paramagnetic Crystals. *Physical Review*, 106(1):164–165, 1957. doi:10.1103/PhysRev.106.164.
- [131] Abragam Anatole and Proctor Warren George. Une nouvelle méthode de polarisation dynamique des noyaux atomiques dans les solides. In *Comptes Rendus Hebdomadaires Des Séances de l'Académie Des Sciences*, volume 246, 2253–2256. Commissariat à l'énergie atomique et aux énergies alternatives, 1958.
- [132] Wind R. A., Duijvestijn M. J., van der Lugt C., Manenschijn A., and Vriend J. Applications of dynamic nuclear polarization in 13 C NMR in solids. *Progress in Nuclear Magnetic Resonance Spectroscopy*, 17(Supplement C): 33–67, 1985. doi:10.1016/0079-6565(85)80005-4.
- [133] Ardenkjær-Larsen Jan H., Fridlund Björn, Gram Andreas, Hansson Georg, Hansson Lennart, Lerche Mathilde H., Servin Rolf, Thaning Mikkel, and Golman Klaes. Increase in signal-to-noise ratio of > 10,000 times in liquid-state NMR. *Proceedings of the National Academy of Sciences*, 100(18):10158–10163, 2003. doi:10.1073/pnas.1733835100.
- [134] Keshari Kayvan R. and Wilson David M. Chemistry and biochemistry of 13 C hyperpolarized magnetic resonance using dynamic nuclear polarization. *Chemical Society Reviews*, 43(5):1627–1659, 2014. doi:10.1039/C3CS60124B.
- [135] Comment A., Jannin S., Hyacinthe J.-N., Miéville P., Sarkar R., Ahuja P., Vasos P. R., Montet X., Lazeyras F., Vallée J.-P., Hautle P., Konter J. A., van den Brandt B., Ansermet J.-Ph., Gruetter R., and Bodenhausen G. Hyperpolarizing Gases via Dynamic Nuclear Polarization and Sublimation. *Physical Review Letters*, 105(1): 018104, 2010. doi:10.1103/PhysRevLett.105.018104.

- [136] Vuichoud Basile, Canet Estel, Milani Jonas, Bornet Aurélien, Baudouin David, Veyre Laurent, Gajan David, Emsley Lyndon, Lesage Anne, Copéret Christophe, Thieuleux Chloé, Bodenhausen Geoffrey, Koptyug Igor, and Jannin Sami. Hyperpolarization of Frozen Hydrocarbon Gases by Dynamic Nuclear Polarization at 1.2 K. *The Journal of Physical Chemistry Letters*, 7(16):3235–3239, 2016. doi:10.1021/acs.jpcllett.6b01345.
- [137] Tee Sui Seng, DiGialleonardo Valentina, Eskandari Roozbeh, Jeong Sangmoo, Granlund Kristin L., Miloushev Vesselin, Poot Alex J., Truong Steven, Alvarez Julio A., Aldeborgh Hannah N., and Keshari Kayvan R. Sampling Hyperpolarized Molecules Utilizing a 1 Tesla Permanent Magnetic Field. *Scientific Reports*, 6(1):32846, 2016. doi:10.1038/srep32846.
- [138] Yoshihara Hikari A. I., Can Emine, Karlsson Magnus, Lerche Mathilde H., Schwitter Juerg, and Comment Arnaud. High-field dissolution dynamic nuclear polarization of [1-¹³C]pyruvic acid. *Physical Chemistry Chemical Physics*, 18(18):12409–12413, 2016. doi:10.1039/C6CP00589F.
- [139] Ardenkjær-Larsen Jan Henrik, Bowen Sean, Petersen Jan Raagaard, Rybalko Oleksandr, Vinding Mads Sloth, Ullisch Marcus, and Nielsen Niels Chr. Cryogen-free dissolution dynamic nuclear polarization polarizer operating at 3.35 T, 6.70 T, and 10.1 T. *Magnetic Resonance in Medicine*, 81(3):2184–2194, 2019. doi:10.1002/mrm.27537.
- [140] Warburg Otto. On the Origin of Cancer Cells. *Science*, 123(3191):309–314, 1956. doi:10.1126/science.123.3191.309.
- [141] Nelson Sarah J., Kurhanewicz John, Vigneron Daniel B., Larson Peder E. Z., Harzstark Andrea L., Ferrone Marcus, van Criekinge Mark, Chang Jose W., Bok Robert, Park Ilwoo, Reed Galen, Carvajal Lucas, Small Eric J., Munster Pamela, Weinberg Vivian K., Ardenkjær-Larsen Jan Henrik, Chen Albert P., Hurd Ralph E., Odegardstuen Liv-Ingrid, Robb Fraser J., Tropp James, and Murray Jonathan A. Metabolic Imaging of Patients with Prostate Cancer Using Hyperpolarized [1-¹³C]Pyruvate. *Science Translational Medicine*, 5(198):198ra108–198ra108, 2013. doi:10.1126/scitranslmed.3006070.
- [142] Abragam A. and Goldman M. Principles of dynamic nuclear polarisation. *Reports on Progress in Physics*, 41(3):395, 1978. doi:10.1088/0034-4885/41/3/002.
- [143] Wenckebach W. T. The Solid Effect. *Applied Magnetic Resonance*, 34(3):227–235, 2008. doi:10.1007/s00723-008-0121-9.
- [144] Wolber J., Ellner F., Fridlund B., Gram A., Jóhannesson H., Hansson G., Hansson L. H., Lerche M. H., Månsson S., Servin R., Thaning M., Golman K., and Ardenkjær-Larsen J. H. Generating highly polarized nuclear spins in solution using dynamic nuclear polarization. *Nuclear Instruments and Methods in Physics Research Section A: Accelerators, Spectrometers, Detectors and Associated Equipment*, 526(1):173–181, 2004. doi:10.1016/j.nima.2004.03.171.
- [145] Wenckebach W. Th. Dynamic nuclear polarization via the cross effect and thermal mixing: B. Energy transport. *Journal of Magnetic Resonance*, 299:151–167, 2019. doi:10.1016/j.jmr.2018.12.020.
- [146] Wenckebach W. Th. Dynamic nuclear polarization via the cross effect and thermal mixing: A. The role of triple spin flips. *Journal of Magnetic Resonance*, 299:124–134, 2019. doi:10.1016/j.jmr.2018.12.018.
- [147] Wenckebach W. Th. Electron Spin–Spin Interactions in DNP: Thermal Mixing vs. the Cross Effect. *Applied Magnetic Resonance*, 52(7):731–748, 2021. doi:10.1007/s00723-021-01335-0.
- [148] Abragam A. and Proctor W. G. Spin Temperature. *Physical Review*, 109(5):1441–1458, 1958. doi:10.1103/PhysRev.109.1441.
- [149] Bornet Aurélien, Milani Jonas, Vuichoud Basile, Perez Linde Angel J., Bodenhausen Geoffrey, and Jannin Sami. Microwave frequency modulation to enhance Dissolution Dynamic Nuclear Polarization. *Chemical Physics Letters*, 602:63–67, 2014. doi:10.1016/j.cplett.2014.04.013.
- [150] Hartmann S. R. and Hahn E. L. Nuclear Double Resonance in the Rotating Frame. *Physical Review*, 128(5):2042–2053, 1962. doi:10.1103/PhysRev.128.2042.
- [151] Jannin Sami, Bornet Aurélien, Colombo Sonia, and Bodenhausen Geoffrey. Low-temperature cross polarization in view of enhancing dissolution Dynamic Nuclear Polarization in NMR. *Chemical Physics Letters*, 517(4):234–236, 2011. doi:10.1016/j.cplett.2011.10.042.
- [152] Bornet Aurélien, Melzi Roberto, Perez Linde Angel J., Hautle Patrick, van den Brandt Ben, Jannin Sami, and Bodenhausen Geoffrey. Boosting Dissolution Dynamic Nuclear Polarization by Cross Polarization. *The Journal of Physical Chemistry Letters*, 4(1):111–114, 2013. doi:10.1021/jz301781t.
- [153] Karlsson Magnus, Jensen Pernille R., Duus Jens Ø., Meier Sebastian, and Lerche Mathilde H. Development of Dissolution DNP-MR Substrates for Metabolic Research. *Applied Magnetic Resonance*, 43(1):223–236, 2012. doi:10.1007/s00723-012-0336-7.

Bibliography

- [154] Capozzi Andrea, Roussel Christophe, Comment Arnaud, and Hyacinthe Jean-Noël. Optimal Glass-Forming Solvent Brings Sublimation Dynamic Nuclear Polarization to ^{129}Xe Hyperpolarization Biomedical Imaging Standards. *The Journal of Physical Chemistry C*, 119(9):5020–5025, 2015. doi:10.1021/jp5124053.
- [155] Pourfathi Mehrdad, Clapp Justin, Kadlecik Stephen J., Keenan Caroline D., Ghosh Rajat K., Kuzma Nicholas N., and Rizi Rahim R. Low-temperature dynamic nuclear polarization of gases in Frozen mixtures. *Magnetic Resonance in Medicine*, 76(3):1007–1014, 2016. doi:10.1002/mrm.26002.
- [156] Lumata Lloyd, Kovacs Zoltan, Malloy Craig, Sherry A. Dean, and Merritt Matthew. The effect of ^{13}C enrichment in the glassing matrix on dynamic nuclear polarization of $[1-^{13}\text{C}]$ pyruvate. *Physics in Medicine & Biology*, 56(5):N85, 2011. doi:10.1088/0031-9155/56/5/N01.
- [157] Hurd Ralph E., Yen Yi-Fen, Chen Albert, and Ardenkjaer-Larsen Jan Henrik. Hyperpolarized ^{13}C metabolic imaging using dissolution dynamic nuclear polarization. *Journal of Magnetic Resonance Imaging*, 36(6):1314–1328, 2012. doi:10.1002/jmri.23753.
- [158] Jensen Pernille R., Karlsson Magnus, Meier Sebastian, Duus Jens Ø., and Lerche Mathilde H. Hyperpolarized Amino Acids for In Vivo Assays of Transaminase Activity. *Chemistry – A European Journal*, 15(39):10010–10012, 2009. doi:10.1002/chem.200901042.
- [159] Chen Albert P., Lau Justin Y.C., Alvares Rohan D.A., and Cunningham Charles H. Using $[1-^{13}\text{C}]$ lactic acid for hyperpolarized ^{13}C MR cardiac studies. *Magnetic Resonance in Medicine*, 73(6):2087–2093, 2015. doi:10.1002/mrm.25354.
- [160] Niedbalski Peter, Parish Christopher, Wang Qing, Hayati Zahra, Song Likai, Martins André F., Sherry A. Dean, and Lumata Lloyd. Transition Metal Doping Reveals Link between Electron T_1 Reduction and ^{13}C Dynamic Nuclear Polarization Efficiency. *The Journal of Physical Chemistry A*, 121(48):9221–9228, 2017. doi:10.1021/acs.jpca.7b09448.
- [161] Lumata Lloyd, Jindal Ashish K., Merritt Matthew E., Malloy Craig R., Sherry A. Dean, and Kovacs Zoltan. DNP by Thermal Mixing under Optimized Conditions Yields >60 000-fold Enhancement of 89Y NMR Signal. *Journal of the American Chemical Society*, 133(22):8673–8680, 2011. doi:10.1021/ja201880y.
- [162] Capozzi Andrea, Patel Saket, Wenckebach W. Thomas, Karlsson Magnus, Lerche Mathilde H., and Ardenkjær-Larsen Jan Henrik. Gadolinium Effect at High-Magnetic-Field DNP: 70% ^{13}C Polarization of $[\text{U-}^{13}\text{C}]$ Glucose Using Trityl. *The Journal of Physical Chemistry Letters*, 10(12):3420–3425, 2019. doi:10.1021/acs.jpcllett.9b01306.
- [163] Friesen-Waldner Lanette, Chen Albert, Mander Will, Scholl Timothy J., and McKenzie Charles A. Optimisation of dynamic nuclear polarisation of $[1-^{13}\text{C}]$ pyruvate by addition of gadolinium-based contrast agents. *Journal of Magnetic Resonance*, 223:85–89, 2012. doi:10.1016/j.jmr.2012.07.010.
- [164] Kiswandhi Andhika, Lama Bimala, Niedbalski Peter, Goderya Mudrekh, Long Joanna, and Lumata Lloyd. The effect of glassing solvent deuteration and Gd^{3+} doping on ^{13}C DNP at 5 T. *RSC Advances*, 6(45):38855–38860, 2016. doi:10.1039/C6RA02864K.
- [165] Sirusi Ali A., Suh Eul Hyun, Kovacs Zoltan, and Merritt Matthew E. The effect of Ho^{3+} doping on ^{13}C dynamic nuclear polarization at 5 T. *Physical Chemistry Chemical Physics*, 20(2):728–731, 2018. doi:10.1039/C7CP07198A.
- [166] Lumata Lloyd, Merritt Matthew E., and Kovacs Zoltan. Influence of deuteration in the glassing matrix on ^{13}C dynamic nuclear polarization. *Physical Chemistry Chemical Physics*, 15(19):7032–7035, 2013. doi:10.1039/C3CP50750E.
- [167] Parish Christopher, Niedbalski Peter, Wang Qing, Khashami Fatemeh, Hayati Zahra, Liu Mengtian, Song Likai, and Lumata Lloyd. Effects of glassing matrix deuteration on the relaxation properties of hyperpolarized ^{13}C spins and free radical electrons at cryogenic temperatures. *The Journal of Chemical Physics*, 150(23):234307, 2019. doi:10.1063/1.5096036.
- [168] Vuichoud Basile, Bornet Aurélien, de Nanteuil Florian, Milani Jonas, Canet Estel, Ji Xiao, Miéville Pascal, Weber Emmanuelle, Kurzbach Dennis, Flamm Andrea, Konrat Robert, Gossert Alvar D., Jannin Sami, and Bodenhausen Geoffrey. Filterable Agents for Hyperpolarization of Water, Metabolites, and Proteins. *Chemistry – A European Journal*, 22(41):14696–14700, 2016. doi:10.1002/chem.201602506.
- [169] Dollmann Björn C., Junk Matthias J. N., Drechsler Michelle, Spiess Hans W., Hinderberger Dariush, and Münnemann Kerstin. Thermoresponsive, spin-labeled hydrogels as separable DNP polarizing agents. *Physical Chemistry Chemical Physics*, 12(22):5879–5882, 2010. doi:10.1039/C003349A.
- [170] Cheng Tian, Mishkovsky Mor, Junk Matthias J. N., Münnemann Kerstin, and Comment Arnaud. Producing Radical-Free Hyperpolarized Perfusion Agents for In Vivo Magnetic Resonance Using Spin-

- Labeled Thermo-responsive Hydrogel. *Macromolecular Rapid Communications*, 37(13):1074–1078, 2016. doi:10.1002/marc.201600133.
- [171] Gajan David, Bornet Aurélien, Vuichoud Basile, Milani Jonas, Melzi Roberto, van Kalkeren Henri A., Veyre Laurent, Thieuleux Chloé, Conley Matthew P., Grüning Wolfram R., Schwarzwälder Martin, Lesage Anne, Copéret Christophe, Bodenhausen Geoffrey, Emsley Lyndon, and Jannin Sami. Hybrid polarizing solids for pure hyperpolarized liquids through dissolution dynamic nuclear polarization. *Proceedings of the National Academy of Sciences*, 111(41):14693–14697, 2014. doi:10.1073/pnas.1407730111.
- [172] Baudouin D., van Kalkeren H. A., Bornet A., Vuichoud B., Veyre L., Cavallès M., Schwarzwälder M., Liao W.-C., Gajan D., Bodenhausen G., Emsley L., Lesage A., Jannin S., Copéret C., and Thieuleux C. Cubic three-dimensional hybrid silica solids for nuclear hyperpolarization. *Chemical Science*, 7(11):6846–6850, 2016. doi:10.1039/C6SC02055K.
- [173] Grüning Wolfram R., Bieringer Harald, Schwarzwälder Martin, Gajan David, Bornet Aurélien, Vuichoud Basile, Milani Jonas, Baudouin David, Veyre Laurent, Lesage Anne, Jannin Sami, Bodenhausen Geoffrey, Thieuleux Chloé, and Copéret Christophe. Phenylazide Hybrid-Silica – Polarization Platform for Dynamic Nuclear Polarization at Cryogenic Temperatures. *Helvetica Chimica Acta*, 100(1):e1600122, 2017. doi:10.1002/hlca.201600122.
- [174] Cavallès Matthieu, Bornet Aurélien, Jaurand Xavier, Vuichoud Basile, Baudouin David, Baudin Mathieu, Veyre Laurent, Bodenhausen Geoffrey, Dumez Jean-Nicolas, Jannin Sami, Copéret Christophe, and Thieuleux Chloé. Tailored Microstructured Hyperpolarizing Matrices for Optimal Magnetic Resonance Imaging. *Angewandte Chemie*, 130(25):7575–7579, 2018. doi:10.1002/ange.201801009.
- [175] Blumberg W. E. Nuclear Spin-Lattice Relaxation Caused by Paramagnetic Impurities. *Physical Review*, 119(1):79–84, 1960. doi:10.1103/PhysRev.119.79.
- [176] Marco-Rius Irene, Cheng Tian, Gaunt Adam P., Patel Saket, Kreis Felix, Capozzi Andrea, Wright Alan J., Brindle Kevin M., Ouari Olivier, and Comment Arnaud. Photogenerated Radical in Phenylglyoxylic Acid for in Vivo Hyperpolarized ^{13}C MR with Photosensitive Metabolic Substrates. *Journal of the American Chemical Society*, 140(43):14455–14463, 2018. doi:10.1021/jacs.8b09326.
- [177] Eichhorn Tim R., Takado Yuhei, Salameh Najat, Capozzi Andrea, Cheng Tian, Hyacinthe Jean-Noël, Mishkovsky Mor, Roussel Christophe, and Comment Arnaud. Hyperpolarization without persistent radicals for in vivo real-time metabolic imaging. *Proceedings of the National Academy of Sciences*, 110(45):18064–18069, 2013. doi:10.1073/pnas.1314928110.
- [178] Capozzi Andrea, Patel Saket, Gunnarsson Christine Pepke, Marco-Rius Irene, Comment Arnaud, Karlsson Magnus, Lerche Mathilde H., Ouari Olivier, and Ardenkjær-Larsen Jan Henrik. Efficient Hyperpolarization of U- ^{13}C -Glucose Using Narrow-Line UV-Generated Labile Free Radicals. *Angewandte Chemie International Edition*, 58(5):1334–1339, 2019. doi:10.1002/anie.201810522.
- [179] Gaunt Adam P., Lewis Jennifer S., Hesse Friederike, Cheng Tian, Marco-Rius Irene, Brindle Kevin M., and Comment Arnaud. Labile Photo-Induced Free Radical in α -Ketoglutaric Acid: A Universal Endogenous Polarizing Agent for In Vivo Hyperpolarized ^{13}C Magnetic Resonance. *Angewandte Chemie International Edition*, 61(2):e202112982, 2022. doi:10.1002/anie.202112982.
- [180] Capozzi Andrea, Cheng Tian, Boero Giovanni, Roussel Christophe, and Comment Arnaud. Thermal annihilation of photo-induced radicals following dynamic nuclear polarization to produce transportable frozen hyperpolarized ^{13}C -substrates. *Nature Communications*, 8(1):15757, 2017. doi:10.1038/ncomms15757.
- [181] Peat David T., Hirsch Matthew L., Gadian David G., Horsewill Anthony J., Owers-Bradley John R., and Kempf James G. Low-field thermal mixing in [1- ^{13}C] pyruvic acid for brute-force hyperpolarization. *Physical Chemistry Chemical Physics*, 18(28):19173–19182, 2016. doi:10.1039/C6CP02853E.
- [182] Ji Xiao, Bornet Aurélien, Vuichoud Basile, Milani Jonas, Gajan David, Rossini Aaron J., Emsley Lyndon, Bodenhausen Geoffrey, and Jannin Sami. Transportable hyperpolarized metabolites. *Nature Communications*, 8(1):13975, 2017. doi:10.1038/ncomms13975.
- [183] Capozzi Andrea. Design and performance of a small bath cryostat with NMR capability for transport of hyperpolarized samples. *Scientific Reports*, 12(1):19260, 2022. doi:10.1038/s41598-022-23890-7.
- [184] El Daraï Théo, Cousin Samuel F., Stern Quentin, Ceillier Morgan, Kempf James, Eshchenko Dmitry, Melzi Roberto, Schnell Marc, Gremillard Laurent, Bornet Aurélien, Milani Jonas, Vuichoud Basile, Cala Olivier, Montarnal Damien, and Jannin Sami. Porous functionalized polymers enable generating and transporting hyperpolarized mixtures of metabolites. *Nature Communications*, 12(1):4695, 2021. doi:10.1038/s41467-021-24279-2.

Bibliography

- [185] Jannin S., Comment A., Kurdzesau F., Konter J. A., Hautle P., van den Brandt B., and van der Klink J. J. A 140GHz prepolarizer for dissolution dynamic nuclear polarization. *The Journal of Chemical Physics*, 128(24): 241102, 2008. doi:10.1063/1.2951994.
- [186] Jannin Sami, Bornet Aurélien, Melzi Roberto, and Bodenhausen Geoffrey. High field dynamic nuclear polarization at 6.7T: Carbon-13 polarization above 70% within 20min. *Chemical Physics Letters*, 549:99–102, 2012. doi:10.1016/j.cplett.2012.08.017.
- [187] Cheng Tian, Capozzi Andrea, Takado Yuhei, Balzan Riccardo, and Comment Arnaud. Over 35% liquid-state ^{13}C polarization obtained via dissolution dynamic nuclear polarization at 7 T and 1 K using ubiquitous nitroxyl radicals. *Physical Chemistry Chemical Physics*, 15(48):20819–20822, 2013. doi:10.1039/C3CP53022A.
- [188] Comment A., van den Brandt B., Uffmann K., Kurdzesau F., Jannin S., Konter J.A., Hautle P., Wenckebach W.Th., Gruetter R., and van der Klink J.J. Design and performance of a DNP prepolarizer coupled to a rodent MRI scanner. *Concepts in Magnetic Resonance Part B: Magnetic Resonance Engineering*, 31B(4):255–269, 2007. doi:10.1002/cmr.b.20099.
- [189] Batel Michael, Krajewski Marcin, Weiss Kilian, With Oliver, Däpp Alexander, Hunkeler Andreas, Gimersky Martin, Pruessmann Klaas P., Boesiger Peter, Meier Beat H., Kozerke Sebastian, and Ernst Matthias. A multi-sample 94GHz dissolution dynamic-nuclear-polarization system. *Journal of Magnetic Resonance*, 214: 166–174, 2012. doi:10.1016/j.jmr.2011.11.002.
- [190] Crémillieux Yannick, Goutailler Florent, Montcel Bruno, Grand Dominique, Vermeulen Gérard, and Wolf Pierre-Etienne. A Super-Wide Bore DNP System for Multiple Sample Polarization: Cryogenic Performance and Polarization at Low Temperature. *Applied Magnetic Resonance*, 43(1):167–180, 2012. doi:10.1007/s00723-012-0354-5.
- [191] Kiswandhi Andhika, Niedbalski Peter, Parish Christopher, Ferguson Sarah, Taylor David, McDonald George, and Lumata Lloyd. Construction and ^{13}C hyperpolarization efficiency of a 180 GHz dissolution dynamic nuclear polarization system. *Magnetic Resonance in Chemistry*, 55(9):828–836, 2017. doi:10.1002/mrc.4597.
- [192] Ardenkjaer-Larsen Jan H., Leach Andrew M., Clarke Neil, Urbahn John, Anderson Denise, and Skloss Timothy W. Dynamic nuclear polarization polarizer for sterile use intent. *NMR in Biomedicine*, 24(8): 927–932, 2011. doi:10.1002/nbm.1682.
- [193] Baudin Mathieu, Vuichoud Basile, Bornet Aurélien, Bodenhausen Geoffrey, and Jannin Sami. A cryogen-consumption-free system for dynamic nuclear polarization at 9.4 T. *Journal of Magnetic Resonance*, 294: 115–121, 2018. doi:10.1016/j.jmr.2018.07.001.
- [194] Cheng Tian, Gaunt Adam P., Marco-Rius Irene, Gehrung Marcel, Chen Albert P., van der Klink Jacques J., and Comment Arnaud. A multisample 7 T dynamic nuclear polarization polarizer for preclinical hyperpolarized MR. *NMR in Biomedicine*, 33(5):e4264, 2020. doi:10.1002/nbm.4264.
- [195] Albannay Mohammed M., Vinther Joachim M. O., Capozzi Andrea, Zhurbenko Vitaliy, and Ardenkjaer-Larsen Jan Henrik. Optimized microwave delivery in dDNP. *Journal of Magnetic Resonance*, 305:58–65, 2019. doi:10.1016/j.jmr.2019.06.004.
- [196] Himmler Aaron, Albannay Mohammed M., von Witte Gevin, Kozerke Sebastian, and Ernst Matthias. Electroplated waveguides to enhance DNP and EPR spectra of silicon and diamond particles. *Magnetic Resonance*, 3(2):203–209, 2022. doi:10.5194/mr-3-203-2022.
- [197] Cho Andrew, Eskandari Roozbeh, Miloushev Vesselin Z., and Keshari Kayvan R. A non-synthetic approach to extending the lifetime of hyperpolarized molecules using D_2O solvation. *Journal of Magnetic Resonance*, 295:57–62, 2018. doi:10.1016/j.jmr.2018.08.001.
- [198] Krajewski Marcin, Wespi Patrick, Busch Julia, Wissmann Lukas, Kwiatkowski Grzegorz, Steinhauser Jonas, Batel Michael, Ernst Matthias, and Kozerke Sebastian. A multisample dissolution dynamic nuclear polarization system for serial injections in small animals. *Magnetic Resonance in Medicine*, 77(2):904–910, 2017. doi:10.1002/mrm.26147.
- [199] Kress Thomas, Che Kateryna, Epasto Ludovica M., Kozak Fanny, Negroni Mattia, Olsen Gregory L., Selimovic Albina, and Kurzbach Dennis. A novel sample handling system for dissolution dynamic nuclear polarization experiments. *Magnetic Resonance*, 2(1):387–394, 2021. doi:10.5194/mr-2-387-2021.
- [200] Capozzi Andrea, Kilund Jan, Karlsson Magnus, Patel Saket, Pinon Arthur Cesar, Vibert François, Ouari Olivier, Lerche Mathilde H., and Ardenkjær-Larsen Jan Henrik. Metabolic contrast agents produced from transported solid ^{13}C -glucose hyperpolarized via dynamic nuclear polarization. *Communications Chemistry*, 4(1):1–11, 2021. doi:10.1038/s42004-021-00536-9.

- [201] Capozzi Andrea, Karlsson Magnus, Petersen Jan Raagaard, Lerche Mathilde Hauge, and Ardenkjaer-Larsen Jan Henrik. Liquid-State ^{13}C Polarization of 30% through Photoinduced Nonpersistent Radicals. *The Journal of Physical Chemistry C*, 122(13):7432–7443, 2018. doi:10.1021/acs.jpcc.8b01482.
- [202] Pinon Arthur C., Capozzi Andrea, and Ardenkjær-Larsen Jan Henrik. Hyperpolarized water through dissolution dynamic nuclear polarization with UV-generated radicals. *Communications Chemistry*, 3(1):1–9, 2020. doi:10.1038/s42004-020-0301-6.
- [203] Kouřil Karel, Kouřilová Hana, Bartram Samuel, Levitt Malcolm H., and Meier Benno. Scalable dissolution-dynamic nuclear polarization with rapid transfer of a polarized solid. *Nature Communications*, 10(1):1733, 2019. doi:10.1038/s41467-019-09726-5.
- [204] Kouřil Karel, Gramberg Michel, Jurkatat Michael, Kouřilová Hana, and Meier Benno. A cryogen-free, semi-automated apparatus for bullet-dynamic nuclear polarization with improved resolution. *Magnetic Resonance*, 2(2):815–825, 2021. doi:10.5194/mr-2-815-2021.
- [205] Bowen Sean and Hilty Christian. Rapid sample injection for hyperpolarized NMR spectroscopy. *Physical Chemistry Chemical Physics*, 12(22):5766–5770, 2010. doi:10.1039/C002316G.
- [206] Cheng Tian, Mishkovsky Mor, Bastiaansen Jessica A. M., Ouari Olivier, Hautle Patrick, Tordo Paul, van den Brandt Ben, and Comment Arnaud. Automated transfer and injection of hyperpolarized molecules with polarization measurement prior to in vivo NMR. *NMR in Biomedicine*, 26(11):1582–1588, 2013. doi:10.1002/nbm.2993.
- [207] Katsikis Sotirios, Marin-Montesinos Ildefonso, Pons Miquel, Ludwig Christian, and Günther Ulrich L. Improved Stability and Spectral Quality in Ex Situ Dissolution DNP Using an Improved Transfer Device. *Applied Magnetic Resonance*, 46(7):723–729, 2015. doi:10.1007/s00723-015-0680-5.
- [208] Ceillier Morgan, Cala Olivier, El Daraï Théo, Cousin Samuel F., Stern Quentin, Guibert Sylvie, Elliott Stuart J., Bornet Aurélien, Vuichoud Basile, Milani Jonas, Pages Christophe, Eshchenko Dmitry, Kempf James G., Jose Catherine, Lambert Simon A., and Jannin Sami. An automated system for fast transfer and injection of hyperpolarized solutions. *Journal of Magnetic Resonance Open*, 8–9:100017, 2021. doi:10.1016/j.jmro.2021.100017.
- [209] Miéville Pascal, Jannin Sami, and Bodenhausen Geoffrey. Relaxometry of insensitive nuclei: Optimizing dissolution dynamic nuclear polarization. *Journal of Magnetic Resonance*, 210(1):137–140, 2011. doi:10.1016/j.jmr.2011.02.006.
- [210] Milani Jonas, Vuichoud Basile, Bornet Aurélien, Miéville Pascal, Mottier Roger, Jannin Sami, and Bodenhausen Geoffrey. A magnetic tunnel to shelter hyperpolarized fluids. *Review of Scientific Instruments*, 86(2):024101, 2015. doi:10.1063/1.4908196.
- [211] Schilling Franz, Düwel Stephan, Köllisch Ulrich, Durst Markus, Schulte Rolf F., Glaser Steffen J., Haase Axel, Otto Angela M., and Menzel Marion I. Diffusion of hyperpolarized ^{13}C -metabolites in tumor cell spheroids using real-time NMR spectroscopy. *NMR in Biomedicine*, 26(5):557–568, 2013. doi:10.1002/nbm.2892.
- [212] Hundshammer Christian, Grashei Martin, Greiner Alexandra, Glaser Steffen J., and Schilling Franz. pH Dependence of T_1 for ^{13}C -Labelled Small Molecules Commonly Used for Hyperpolarized Magnetic Resonance Imaging. *ChemPhysChem*, 20(6):798–802, 2019. doi:10.1002/cphc.201801098.
- [213] Miéville Pascal, Ahuja Puneet, Sarkar Riddhiman, Jannin Sami, Vasos Paul R., Gerber-Lemaire Sandrine, Mishkovsky Mor, Comment Arnaud, Gruetter Rolf, Ouari Olivier, Tordo Paul, and Bodenhausen Geoffrey. Scavenging Free Radicals To Preserve Enhancement and Extend Relaxation Times in NMR using Dynamic Nuclear Polarization. *Angewandte Chemie International Edition*, 49(35):6182–6185, 2010. doi:10.1002/anie.201000934.
- [214] Mishkovsky Mor and Comment Arnaud. Hyperpolarized MRS: New tool to study real-time brain function and metabolism. *Analytical Biochemistry*, 529(Supplement C):270–277, 2017. doi:10.1016/j.ab.2016.09.020.
- [215] Durst Markus, Koellisch Ulrich, Frank Annette, Rancan Giaime, Gringeri Concetta V., Karas Vincent, Wiesinger Florian, Menzel Marion I., Schwaiger Markus, Haase Axel, and Schulte Rolf F. Comparison of acquisition schemes for hyperpolarised ^{13}C imaging. *NMR in Biomedicine*, 28(6):715–725, 2015. doi:10.1002/nbm.3301.
- [216] Topping Geoffrey J., Hundshammer Christian, Nagel Luca, Grashei Martin, Aigner Maximilian, Skinner Jason G., Schulte Rolf F., and Schilling Franz. Acquisition strategies for spatially resolved magnetic resonance detection of hyperpolarized nuclei. *Magnetic Resonance Materials in Physics, Biology and Medicine*, 33(2):221–256, 2020. doi:10.1007/s10334-019-00807-6.
- [217] Larson Peder Eric Zufall and Gordon Jeremy W. Hyperpolarized Metabolic MRI—Acquisition, Reconstruction, and Analysis Methods. *Metabolites*, 11(6):386, 2021. doi:10.3390/metabo11060386.

Bibliography

- [218] Marques José P, Simonis Frank F.J., and Webb Andrew G. Low-field MRI: An MR physics perspective. *Journal of Magnetic Resonance Imaging*, 49(6):1528–1542, 2019. doi:10.1002/jmri.26637.
- [219] Vaeggemose Michael, F Schulte Rolf, and Laustsen Christoffer. Comprehensive Literature Review of Hyperpolarized Carbon-13 MRI: The Road to Clinical Application. *Metabolites*, 11(4):219, 2021. doi:10.3390/metabo11040219.
- [220] Le Page Lydia M., Guglielmetti Caroline, Taglang Celine, and Chaumeil Myriam M. Imaging Brain Metabolism Using Hyperpolarized ^{13}C Magnetic Resonance Spectroscopy. *Trends in Neurosciences*, 43(5):343–354, 2020. doi:10.1016/j.tins.2020.03.006.
- [221] Miloushev Vesselin Z., Di Galleonardo Valentina, Salamanca-Cardona Lucia, Correa Fabian, Granlund Kristin L., and Keshari Kayvan R. Hyperpolarized ^{13}C pyruvate mouse brain metabolism with absorptive-mode EPSI at 1T. *Journal of Magnetic Resonance*, 275:120–126, 2017. doi:10.1016/j.jmr.2016.12.009.
- [222] Coffey Aaron M., Truong Milton L., and Chekmenev Eduard Y. Low-field MRI can be more sensitive than high-field MRI. *Journal of Magnetic Resonance*, 237:169–174, 2013. doi:10.1016/j.jmr.2013.10.013.
- [223] Coffey Aaron M., Feldman Matthew A., Shchepin Roman V., Barskiy Danila A., Truong Milton L., Pham Wellington, and Chekmenev Eduard Y. High-resolution hyperpolarized in vivo metabolic ^{13}C spectroscopy at low magnetic field (48.7mT) following murine tail-vein injection. *Journal of Magnetic Resonance*, 281:246–252, 2017. doi:10.1016/j.jmr.2017.06.009.
- [224] Traechtler Julia, Fuetterer Maximilian, Albannay Mohammed M., Hoh Tobias, and Kozerke Sebastian. Considerations for hyperpolarized ^{13}C MR at reduced field: Comparing 1.5T versus 3T. *Magnetic Resonance in Medicine*, 89(5):1945–1960, 2023. doi:10.1002/mrm.29579.
- [225] Kelkar Sneha S. and Reineke Theresa M. Theranostics: Combining Imaging and Therapy. *Bioconjugate Chemistry*, 22(10):1879–1903, 2011. doi:10.1021/bc200151q.
- [226] Xu Yafang, Ringgaard Steffen, Mariager Christian Østergaard, Bertelsen Lotte Bonde, Schroeder Marie, Qi Haiyun, Laustsen Christoffer, and Stødkilde-Jørgensen Hans. Hyperpolarized ^{13}C Magnetic Resonance Imaging Can Detect Metabolic Changes Characteristic of Penumbra in Ischemic Stroke. *Tomography*, 3(2):67–73, 2017. doi:10.18383/j.tom.2017.00106.
- [227] Bøgh Nikolaj, Olin Rie B., Hansen Esben S. S., Gordon Jeremy W., Bech Sabrina K, Bertelsen Lotte B, Sánchez-Heredia Juan D., Blicher Jakob U., Østergaard Leif, Ardenkjær-Larsen Jan H., Bok Robert A., Vigneron Daniel B., and Laustsen Christoffer. Metabolic MRI with hyperpolarized [1- ^{13}C]pyruvate separates benign oligemia from infarcting penumbra in porcine stroke. *Journal of Cerebral Blood Flow & Metabolism*, 41(11):2916–2927, 2021. doi:10.1177/0271678X211018317.
- [228] Hyacinthe Jean-Noël, Buscemi Lara, Lê Thanh Phong, Lepore Mario, Hirt Lorenz, and Mishkovsky Mor. Evaluating the potential of hyperpolarised [1- ^{13}C] L-lactate as a neuroprotectant metabolic biosensor for stroke. *Scientific Reports*, 10(1):5507, 2020. doi:10.1038/s41598-020-62319-x.
- [229] Zhou Xin, Sun Yanping, Mazzanti Mary, Henninger Nils, Mansour Joey, Fisher Marc, and Albert Mitchell. MRI of stroke using hyperpolarized ^{129}Xe . *NMR in Biomedicine*, 24(2):170–175, 2011. doi:10.1002/nbm.1568.
- [230] Li Yan, Vigneron Daniel B., and Xu Duan. Current human brain applications and challenges of dynamic hyperpolarized carbon-13 labeled pyruvate MR metabolic imaging. *European Journal of Nuclear Medicine and Molecular Imaging*, 48(13):4225–4235, 2021. doi:10.1007/s00259-021-05508-8.
- [231] Kurhanewicz John, Vigneron Daniel B., Ardenkjaer-Larsen Jan Henrik, Bankson James A., Brindle Kevin, Cunningham Charles H., Gallagher Ferdia A., Keshari Kayvan R., Kjaer Andreas, Laustsen Christoffer, Mankoff David A., Merritt Matthew E., Nelson Sarah J., Pauly John M., Lee Philips, Ronen Sabrina, Tyler Damian J., Rajan Sunder S., Spielman Daniel M., Wald Lawrence, Zhang Xiaoliang, Malloy Craig R., and Rizi Rahim. Hyperpolarized ^{13}C MRI: Path to Clinical Translation in Oncology. *Neoplasia*, 21(1):1–16, 2019. doi:10.1016/j.neo.2018.09.006.
- [232] Campbell Bruce C.V., Mitchell Peter J., Kleinig Timothy J., et al. Endovascular Therapy for Ischemic Stroke with Perfusion-Imaging Selection. *New England Journal of Medicine*, 372(11):1009–1018, 2015. doi:10.1056/NEJMoa1414792.
- [233] The IST-3 collaborative group. The benefits and harms of intravenous thrombolysis with recombinant tissue plasminogen activator within 6 h of acute ischaemic stroke (the third international stroke trial [IST-3]): A randomised controlled trial. *The Lancet*, 379(9834):2352–2363, 2012. doi:10.1016/S0140-6736(12)60768-5.
- [234] Chen Albert P, Kurhanewicz John, Bok Robert, Xu Duan, Joun David, Zhang Vickie, Nelson Sarah J., Hurd Ralph E., and Vigneron Daniel B. Feasibility of using hyperpolarized [1- ^{13}C]lactate as a substrate for in vivo metabolic ^{13}C MRSI studies. *Magnetic Resonance Imaging*, 26(6):721–726, 2008.

- doi:10.1016/j.mri.2008.01.002.
- [235] Bastiaansen Jessica A. M., Yoshihara Hikari A. I., Takado Yuhei, Gruetter Rolf, and Comment Arnaud. Hyperpolarized ^{13}C lactate as a substrate for in vivo metabolic studies in skeletal muscle. *Metabolomics*, 10(5):986–994, 2014. doi:10.1007/s11306-014-0630-5.
- [236] Takado Yuhei, Cheng Tian, Bastiaansen Jessica A. M., Yoshihara Hikari A. I., Lanz Bernard, Mishkovsky Mor, Lengacher Sylvain, and Comment Arnaud. Hyperpolarized ^{13}C Magnetic Resonance Spectroscopy Reveals the Rate-Limiting Role of the Blood–Brain Barrier in the Cerebral Uptake and Metabolism of L -Lactate *in Vivo*. *ACS Chemical Neuroscience*, 9(11):2554–2562, 2018. doi:10.1021/acscchemneuro.8b00066.
- [237] Mayer Dirk, Yen Yi-Fen, Josan Sonal, Park Jae Mo, Pfefferbaum Adolf, Hurd Ralph E., and Spielman Daniel M. Application of hyperpolarized $[1-^{13}\text{C}]$ lactate for the in vivo investigation of cardiac metabolism. *NMR in Biomedicine*, 25(10):1119–1124, 2012. doi:10.1002/nbm.2778.
- [238] Lau Angus Z., Chen Albert P., and Cunningham Charles H. Cardiac metabolic imaging using hyperpolarized $[1-^{13}\text{C}]$ lactate as a substrate. *NMR in Biomedicine*, 34(7):e4532, 2021. doi:10.1002/nbm.4532.
- [239] Longa E. Z., Weinstein P. R., Carlson S., and Cummins R. Reversible middle cerebral artery occlusion without craniectomy in rats. *Stroke*, 20(1):84–91, 1989. doi:10.1161/01.STR.20.1.84.
- [240] Gruetter Rolf. Automatic, localized in Vivo adjustment of all first-and second-order shim coils. *Magnetic Resonance in Medicine*, 29(6):804–811, 1993. doi:10.1002/mrm.1910290613.
- [241] Gruetter Rolf and Tkáč Ivan. Field mapping without reference scan using asymmetric echo-planar techniques. *Magnetic Resonance in Medicine*, 43(2):319–323, 2000. doi:10.1002/(SICI)1522-2594(200002)43:2<319::AID-MRM22>3.0.CO;2-1.
- [242] Mlynárik Vladimír, Gambarota Giulio, Frenkel Hanne, and Gruetter Rolf. Localized short-echo-time proton MR spectroscopy with full signal-intensity acquisition. *Magnetic Resonance in Medicine*, 56(5):965–970, 2006. doi:10.1002/mrm.21043.
- [243] Provencher Stephen W. Estimation of metabolite concentrations from localized in vivo proton NMR spectra. *Magnetic Resonance in Medicine*, 30(6):672–679, 1993. doi:10.1002/mrm.1910300604.
- [244] Staewen R. Scott, Johnson Anton J., Ross Brian D., Parrish Todd, Merkle Hellmut, and Garwood Michael. 3-D FLASH Imaging Using a Single Surface Coil and a New Adiabatic Pulse, BIR-4. *Investigative Radiology*, 25(5): 559, 1990. doi:10.1097/00004424-199005000-00015.
- [245] Miller Jack J., Grist James T., Serres Sébastien, Larkin James R., Lau Angus Z., Ray Kevin, Fisher Katherine R., Hansen Esben, Tougaard Rasmus Stilling, Nielsen Per Mose, Lindhardt Jakob, Laustsen Christoffer, Gallagher Ferdia A., Tyler Damian J., and Sibson Nicola. ^{13}C Pyruvate Transport Across the Blood-Brain Barrier in Preclinical Hyperpolarized MRI. *Scientific Reports*, 8(1):15082, 2018. doi:10.1038/s41598-018-33363-5.
- [246] Christensen Caspar Elo, Karlsson Magnus, Winther Jakob R., Jensen Pernille Rose, and Lerche Mathilde H. Non-invasive In-cell Determination of Free Cytosolic $[\text{NAD}^+]/[\text{NADH}]$ Ratios Using Hyperpolarized Glucose Show Large Variations in Metabolic Phenotypes. *Journal of Biological Chemistry*, 289(4):2344–2352, 2014. doi:10.1074/jbc.M113.498626.
- [247] Hill Deborah K., Orton Matthew R., Mariotti Erika, Boulton Jessica K. R., Panek Rafal, Jafar Maysam, Parkes Harold G., Jamin Yann, Miniotis Maria Falck, Al-Saffar Nada M. S., Belouche-Babari Mounia, Robinson Simon P., Leach Martin O., Chung Yuen-Li, and Eykyn Thomas R. Model Free Approach to Kinetic Analysis of Real-Time Hyperpolarized ^{13}C Magnetic Resonance Spectroscopy Data. *PLOS ONE*, 8(9):e71996, 2013. doi:10.1371/journal.pone.0071996.
- [248] Rosafo K., Castillo X., Hirt L., and Pellerin L. Cell-specific modulation of monocarboxylate transporter expression contributes to the metabolic reprogramming taking place following cerebral ischemia. *Neuroscience*, 317:108–120, 2016. doi:10.1016/j.neuroscience.2015.12.052.
- [249] Ardenkjær-Larsen J. H., Laursen I., Leunbach I., Ehnholm G., Wistrand L. G., Petersson J. S., and Golman K. EPR and DNP Properties of Certain Novel Single Electron Contrast Agents Intended for Oximetric Imaging. *Journal of Magnetic Resonance*, 133(1):1–12, 1998. doi:10.1006/jmre.1998.1438.
- [250] Harris Talia, Azar Assad, Sapir Gal, Gamliel Ayelet, Nardi-Schreiber Atara, Sosna Jacob, Gomori J. Moshe, and Katz-Brull Rachel. Real-time ex-vivo measurement of brain metabolism using hyperpolarized $[1-^{13}\text{C}]$ pyruvate. *Scientific Reports*, 8(1):9564, 2018. doi:10.1038/s41598-018-27747-w.
- [251] Mayer Dirk, Yen Yi-Fen, Takahashi Atsushi, Josan Sonal, Tropp James, Rutt B. K., Hurd Ralph E., Spielman Daniel M., and Pfefferbaum Adolf. Dynamic and high-resolution metabolic imaging of hyperpolarized $[1-^{13}\text{C}]$ -pyruvate in the rat brain using a high-performance gradient insert. *Magnetic Resonance in Medicine*, 65(5):1228–1233, 2011. doi:10.1002/mrm.22707.

Bibliography

- [252] Eraković V., Župan G., Varljen J., Laginja J., and Simonić A. Altered Activities of Rat Brain Metabolic Enzymes in Electroconvulsive Shock—Induced Seizures. *Epilepsia*, 42(2):181–189, 2001. doi:10.1046/j.1528-1157.2001.30499.x.
- [253] Soto Marion, Orliaguet Lucie, Reyzer Michelle L., Manier M. Lisa, Caprioli Richard M., and Kahn C. Ronald. Pyruvate induces torpor in obese mice. *Proceedings of the National Academy of Sciences*, 115(4):810–815, 2018. doi:10.1073/pnas.1717507115.
- [254] Rodrigues Tiago B., Sierra Alejandra, Ballesteros Paloma, and Cerdán Sebastián. Pyruvate Transport and Metabolism in the Central Nervous System. In Choi In-Young and Gruetter Rolf, editors, *Neural Metabolism In Vivo*, Advances in Neurobiology, 715–753. Springer US, Boston, MA, 2012. doi:10.1007/978-1-4614-1788-0_24.
- [255] Alf Malte F., Lei Hongxia, Berthet Carole, Hirt Lorenz, Gruetter Rolf, and Mlynarik Vladimir. High-resolution spatial mapping of changes in the neurochemical profile after focal ischemia in mice. *NMR in Biomedicine*, 25(2):247–254, 2012. doi:10.1002/nbm.1740.
- [256] Berthet Carole, Lei Hongxia, Gruetter Rolf, and Hirt Lorenz. Early Predictive Biomarkers for Lesion After Transient Cerebral Ischemia. *Stroke*, 42(3):799–805, 2011. doi:10.1161/STROKEAHA.110.603647.
- [257] El Daraï Théo and Jannin Sami. Sample formulations for dissolution dynamic nuclear polarization. *Chemical Physics Reviews*, 2(4):041308, 2021. doi:10.1063/5.0047899.
- [258] Grist James T., Miller Jack J., Zaccagna Fulvio, McLean Mary A., Riemer Frank, Matys Tomasz, Tyler Damian J., Laustsen Christoffer, Coles Alasdair J., and Gallagher Ferdia A. Hyperpolarized ^{13}C MRI: A novel approach for probing cerebral metabolism in health and neurological disease. *Journal of Cerebral Blood Flow & Metabolism*, 40(6):1137–1147, 2020. doi:10.1177/0271678X20909045.
- [259] Henriksen Ole, Gideon Peter, Sperling Bjørn, Olsen Tom Skyhøj, Jørgensen Henrik S., and Arlien-Søborg Peter. Cerebral lactate production and blood flow in acute stroke. *Journal of Magnetic Resonance Imaging*, 2(5):511–517, 1992. doi:10.1002/jmri.1880020508.
- [260] Wilcox Christopher S. Effects of tempol and redox-cycling nitroxides in models of oxidative stress. *Pharmacology & Therapeutics*, 126(2):119–145, 2010. doi:10.1016/j.pharmthera.2010.01.003.
- [261] Cuzzocrea S., McDonald M.C., Mazzon E., Siriwardena D., Costantino G., Fulia F., Cucinotta G., Gitto E., Cordaro S., Barberi I., De Sarro A., Caputi A.P., and Thiemeermann C. Effects of tempol, a membrane-permeable radical scavenger, in a gerbil model of brain injury. *Brain Research*, 875(1-2):96–106, 2000. doi:10.1016/S0006-8993(00)02582-8.
- [262] Rak Ramin, Chao Daniel L., Pluta Ryszard M., Mitchell James B., Oldfield Edward H., and Watson Joe C. Neuroprotection by the stable nitroxide Tempol during reperfusion in a rat model of transient focal ischemia. *Journal of Neurosurgery*, 92(4):646–651, 2000. doi:10.3171/jns.2000.92.4.0646.
- [263] Lochhead Jeffrey J., McCaffrey Gwen, Quigley Colleen E., Finch Jessica, DeMarco Kristin M., Nametz Nicole, and Davis Thomas P. Oxidative Stress Increases Blood–Brain Barrier Permeability and Induces Alterations in Occludin during Hypoxia–Reoxygenation. *Journal of Cerebral Blood Flow & Metabolism*, 30(9):1625–1636, 2010. doi:10.1038/jcbfm.2010.29.
- [264] Dohare Preeti, Hyzinski-García María C., Vipani Aarshi, Bowens Nicole H., Nalwalk Julia W., Feustel Paul J., Keller Jr. Richard W., Jourdeuil David, and Mongin Alexander A. The neuroprotective properties of the superoxide dismutase mimetic tempol correlate with its ability to reduce pathological glutamate release in a rodent model of stroke. *Free Radical Biology and Medicine*, 77:168–182, 2014. doi:10.1016/j.freeradbiomed.2014.08.029.
- [265] Kato Noriyuki, Yanaka Kiyoyuki, Hyodo Koji, Homma Kazuhiro, Nagase Sohji, and Nose Tadao. Stable nitroxide Tempol ameliorates brain injury by inhibiting lipid peroxidation in a rat model of transient focal cerebral ischemia. *Brain Research*, 979(1):188–193, 2003. doi:10.1016/S0006-8993(03)02918-4.
- [266] Lumata Lloyd, Merritt Matthew E., Malloy Craig R., Sherry A. Dean, and Kovacs Zoltan. Impact of Gd^{3+} on DNP of $[1-^{13}\text{C}]$ Pyruvate Doped with Trityl OX063, BDPA, or 4-Oxo-TEMPO. *The Journal of Physical Chemistry A*, 116(21):5129–5138, 2012. doi:10.1021/jp302399f.
- [267] Soule Benjamin P., Hyodo Fuminori, Matsumoto Ken-ichiro, Simone Nicole L., Cook John A., Krishna Murali C., and Mitchell James B. The chemistry and biology of nitroxide compounds. *Free Radical Biology and Medicine*, 42(11):1632–1650, 2007. doi:10.1016/j.freeradbiomed.2007.02.030.
- [268] Zhelev Zhivko, Bakalova Rumiana, Aoki Ichio, Matsumoto Ken-ichiro, Gadjeva Veselina, Anzai Kazunori, and Kanno Iwao. Nitroxyl Radicals for Labeling of Conventional Therapeutics and Noninvasive Magnetic Resonance Imaging of Their Permeability for Blood-Brain Barrier: Relationship between Structure,

- Blood Clearance, and MRI Signal Dynamic in the Brain. *Molecular Pharmaceutics*, 6(2):504–512, 2009. doi:10.1021/mp800175k.
- [269] Rizzi Cécile, Samouilov Alexandre, Kumar Kutala Vijay, Parinandi Narasimham L., Zweier Jay L., and Kuppusamy Periannan. Application of a trityl-based radical probe for measuring superoxide. *Free Radical Biology and Medicine*, 35(12):1608–1618, 2003. doi:10.1016/j.freeradbiomed.2003.09.014.
- [270] Allaman Igor and Magistretti Pierre J. Brain Energy Metabolism. In *Fundamental Neuroscience*, 261–284. Elsevier, 2013. doi:10.1016/B978-0-12-385870-2.00012-3.
- [271] Dey Arnab, Charrier Benoît, Lemaitre Karine, Ribay Victor, Eshchenko Dmitry, Schnell Marc, Melzi Roberto, Stern Quentin, Cousin Samuel F., Kempf James G., Jannin Sami, Dumez Jean-Nicolas, and Giraudeau Patrick. Fine optimization of a dissolution dynamic nuclear polarization experimental setting for ^{13}C NMR of metabolic samples. *Magnetic Resonance*, 3(2):183–202, 2022. doi:10.5194/mr-3-183-2022.
- [272] Comment Arnaud and Merritt Matthew E. Hyperpolarized Magnetic Resonance as a Sensitive Detector of Metabolic Function. *Biochemistry*, 53(47):7333–7357, 2014. doi:10.1021/bi501225t.
- [273] Chen Hsin-Yu, Aggarwal Rahul, Bok Robert A., Ohliger Michael A., Zhu Zi, Lee Philip, Gordon Jeremy W., van Criekinge Mark, Carvajal Lucas, Slater James B., Larson Peder E. Z., Small Eric J., Kurhanewicz John, and Vigneron Daniel B. Hyperpolarized ^{13}C -pyruvate MRI detects real-time metabolic flux in prostate cancer metastases to bone and liver: A clinical feasibility study. *Prostate Cancer and Prostatic Diseases*, 23(2):269–276, 2020. doi:10.1038/s41391-019-0180-z.
- [274] Cherubini Andrea and Bifone Angelo. Hyperpolarised xenon in biology. *Progress in Nuclear Magnetic Resonance Spectroscopy*, 42(1):1–30, 2003. doi:10.1016/S0079-6565(02)00052-3.
- [275] Gallagher Ferdia A., Woitek Ramona, McLean Mary A., et al. Imaging breast cancer using hyperpolarized carbon-13 MRI. *Proceedings of the National Academy of Sciences*, 117(4):2092–2098, 2020. doi:10.1073/pnas.1913841117.
- [276] Bouchard Louis-S., Burt Scott R., Anwar M. Sabieh, Kovtunov Kirill V., Koptyug Igor V., and Pines Alexander. NMR Imaging of Catalytic Hydrogenation in Microreactors with the Use of para-Hydrogen. *Science*, 319(5862):442–445, 2008. doi:10.1126/science.1151787.
- [277] Golman K., Axelsson O., Jóhannesson H., Månsson S., Olofsson C., and Petersson J.s. Parahydrogen-induced polarization in imaging: Subsecond ^{13}C angiography. *Magnetic Resonance in Medicine*, 46(1):1–5, 2001. doi:10.1002/mrm.1152.
- [278] Berthault Patrick, Huber Gaspard, and Desvaux Hervé. Biosensing using laser-polarized xenon NMR/MRI. *Progress in Nuclear Magnetic Resonance Spectroscopy*, 55(1):35–60, 2009. doi:10.1016/j.pnmrs.2008.11.003.
- [279] Duhamel Guillaume, Choquet Philippe, Grillon Emmanuelle, Lamalle Laurent, Leviel Jean-Louis, Ziegler Anne, and Constantinesco André. Xenon-129 MR imaging and spectroscopy of rat brain using arterial delivery of hyperpolarized xenon in a lipid emulsion. *Magnetic Resonance in Medicine*, 46(2):208–212, 2001. doi:10.1002/mrm.1180.
- [280] Ardenkjaer-Larsen Jan-Henrik, Boebinger Gregory S., Comment Arnaud, Duckett Simon, Edison Arthur S., Engelke Frank, Griesinger Christian, Griffin Robert G., Hilty Christian, Maeda Hidaeki, Parigi Giacomo, Prisner Thomas, Ravera Enrico, van Bantum Jan, Vega Shimon, Webb Andrew, Luchinat Claudio, Schwalbe Harald, and Frydman Lucio. Facing and Overcoming Sensitivity Challenges in Biomolecular NMR Spectroscopy. *Angewandte Chemie International Edition*, 54(32):9162–9185, 2015. doi:10.1002/anie.201410653.
- [281] Szekely Or, Olsen Gregory Lars, Felli Isabella C., and Frydman Lucio. High-Resolution 2D NMR of Disordered Proteins Enhanced by Hyperpolarized Water. *Analytical Chemistry*, 90(10):6169–6177, 2018. doi:10.1021/acs.analchem.8b00585.
- [282] Pinon Arthur C., Capozzi Andrea, and Ardenkjær-Larsen Jan Henrik. Hyperpolarization via dissolution dynamic nuclear polarization: New technological and methodological advances. *Magnetic Resonance Materials in Physics, Biology and Medicine*, 34(1):5–23, 2021. doi:10.1007/s10334-020-00894-w.
- [283] Mishkovsky Mor, Gusyatiner Olga, Lanz Bernard, Cudalbu Cristina, Vassallo Irene, Hamou Marie-France, Bloch Jocelyne, Comment Arnaud, Gruetter Rolf, and Hegi Monika E. Hyperpolarized ^{13}C -glucose magnetic resonance highlights reduced aerobic glycolysis in vivo in infiltrative glioblastoma. *Scientific Reports*, 11(1):5771, 2021. doi:10.1038/s41598-021-85339-7.
- [284] Singh Kawarpal, Jacquemmoz Corentin, Giraudeau Patrick, Frydman Lucio, and Dumez Jean-Nicolas. Ultrafast 2D ^1H - ^1H NMR spectroscopy of DNP-hyperpolarised substrates for the analysis of mixtures. *Chemical Communications*, 57(65):8035–8038, 2021. doi:10.1039/D1CC03079E.

Bibliography

- [285] Jensen Pernille Rose, Sannelli Francesca, Stauning Ludvig Tving, and Meier Sebastian. Enhanced ^{13}C NMR detects extended reaction networks in living cells. *Chemical Communications*, 57(81):10572–10575, 2021. doi:10.1039/D1CC03838A.
- [286] Granwehr Josef, Leggett James, and Köckenberger Walter. A low-cost implementation of EPR detection in a dissolution DNP setup. *Journal of Magnetic Resonance*, 187(2):266–276, 2007. doi:10.1016/j.jmr.2007.05.011.
- [287] Duthil P. Material Properties at Low Temperature. *Proceedings of the CAS-CERN Accelerator School: Superconductivity for Accelerators*, 2014. doi:10.5170/CERN-2014-005.77.
- [288] Lê Thanh Phong, Hyacinthe Jean-Noël, and Capozzi Andrea. How to improve the efficiency of a traditional dissolution dynamic nuclear polarization (dDNP) apparatus: Design and performance of a fluid path compatible dDNP/LOD-ESR probe. *Journal of Magnetic Resonance*, 338:107197, 2022. doi:10.1016/j.jmr.2022.107197.
- [289] National Institute of Standards and Technology . Cryogenics Material Properties. <https://trc.nist.gov/cryogenics/materials/materialproperties.htm>.
- [290] Weisend II J.G., editor. *Cryostat Design: Case Studies, Principles and Engineering*. International Cryogenics Monograph Series. Springer International Publishing, Cham, 2016. doi:10.1007/978-3-319-31150-0.
- [291] Radaelli Alice, Yoshihara Hikari A. I., Nonaka Hiroshi, Sando Shinsuke, Ardenkjaer-Larsen Jan Henrik, Gruetter Rolf, and Capozzi Andrea. ^{13}C Dynamic Nuclear Polarization using SA-BDPA at 6.7 T and 1.1 K: Coexistence of Pure Thermal Mixing and Well-Resolved Solid Effect. *The Journal of Physical Chemistry Letters*, 11(16):6873–6879, 2020. doi:10.1021/acs.jpcclett.0c01473.
- [292] Wenckebach W. Th., Capozzi A., Patel S., and Ardenkjær-Larsen J. H. Direct measurement of the triple spin flip rate in dynamic nuclear polarization. *Journal of Magnetic Resonance*, 327:106982, 2021. doi:10.1016/j.jmr.2021.106982.
- [293] Wenckebach W. Th. Spectral diffusion and dynamic nuclear polarization: Beyond the high temperature approximation. *Journal of Magnetic Resonance*, 284:104–114, 2017. doi:10.1016/j.jmr.2017.10.001.
- [294] Jannin Sami, Comment Arnaud, and van der Klink J. J. Dynamic Nuclear Polarization by Thermal Mixing Under Partial Saturation. *Applied Magnetic Resonance*, 43(1):59–68, 2012. doi:10.1007/s00723-012-0363-4.
- [295] Becker Edwin D. and Shoup R. R. ^{13}C NMR spectroscopy: relaxation times of ^{13}C and methods for sensitivity enhancement. *Pure and Applied Chemistry*, 32(1-4):51–66, 1972. doi:10.1351/pac197232010051.
- [296] Zanella Claudia Christina. Methods to Enhance Nuclear Magnetic Resonance Sensitivity at High Magnetic Field. PhD thesis. EPFL, Lausanne, 2021. doi:10.5075/epfl-thesis-8460.
- [297] Radaelli Alice. Mechanistic studies of DNP and applications of hyperpolarized probes to study renal physiology and metabolism. PhD thesis. EPFL, Lausanne, 2021. doi:10.5075/epfl-thesis-10666.
- [298] Comment Arnaud. Dissolution DNP for in vivo preclinical studies. *Journal of Magnetic Resonance*, 264:39–48, 2016. doi:10.1016/j.jmr.2015.12.027.
- [299] Salamanca-Cardona Lucia and Keshari Kayvan R. ^{13}C -labeled biochemical probes for the study of cancer metabolism with dynamic nuclear polarization-enhanced magnetic resonance imaging. *Cancer & Metabolism*, 3(1):9, 2015. doi:10.1186/s40170-015-0136-2.
- [300] van Heeswijk Ruud B., Uffmann Kai, Comment Arnaud, Kurdzesau Fiodar, Perazzolo Chiara, Cudalbu Cristina, Jannin Sami, Konter Jacobus A., Hautle Patrick, van den Brandt Ben, Navon Gil, van der Klink Jacques J., and Gruetter Rolf. Hyperpolarized lithium-6 as a sensor of nanomolar contrast agents. *Magnetic Resonance in Medicine*, 61(6):1489–1493, 2009. doi:10.1002/mrm.21952.
- [301] Lipsø Kasper Wigh, Bowen Sean, Rybalko Oleksandr, and Ardenkjær-Larsen Jan Henrik. Large dose hyperpolarized water with dissolution-DNP at high magnetic field. *Journal of Magnetic Resonance*, 274:65–72, 2017. doi:10.1016/j.jmr.2016.11.008.
- [302] Brindle Kevin M. Imaging Metabolism with Hyperpolarized ^{13}C -Labeled Cell Substrates. *Journal of the American Chemical Society*, 137(20):6418–6427, 2015. doi:10.1021/jacs.5b03300.
- [303] Kurhanewicz John, Vigneron Daniel B., Brindle Kevin, Chekmenev Eduard Y., Comment Arnaud, Cunningham Charles H., DeBerardinis Ralph J., Green Gary G., Leach Martin O., Rajan Sunder S., Rizi Rahim R., Ross Brian D., Warren Warren S., and Malloy Craig R. Analysis of Cancer Metabolism by Imaging Hyperpolarized Nuclei: Prospects for Translation to Clinical Research. *Neoplasia*, 13(2):81–97, 2011. doi:10.1593/neo.101102.
- [304] Hu Simon, Larson Peder E. Z., VanCriekinge Mark, Leach Andrew M., Park Ilwoo, Leon Christine, Zhou Jenny, Shin Peter J., Reed Galen, Keselman Paul, von Morze Cornelius, Yoshihara Hikari, Bok Robert A., Nelson Sarah J., Kurhanewicz John, and Vigneron Daniel B. Rapid sequential injections of hyperpolarized

- [1-¹³C]pyruvate in vivo using a sub-kelvin, multi-sample DNP polarizer. *Magnetic Resonance Imaging*, 31(4):490–496, 2013. doi:10.1016/j.mri.2012.09.002.
- [305] Ball Daniel R., Cruickshank Rachel, Carr Carolyn A., Stuckey Daniel J., Lee Philip, Clarke Kieran, and Tyler Damian J. Metabolic imaging of acute and chronic infarction in the perfused rat heart using hyperpolarised [1-¹³C]pyruvate. *NMR in Biomedicine*, 26(11):1441–1450, 2013. doi:10.1002/nbm.2972.
- [306] Qin Hecong, Tang Shuyu, Riselli Andrew M., Bok Robert A., Delos Santos Romelyn, van Crieking Mark, Gordon Jeremy W., Aggarwal Rahul, Chen Rui, Goddard Gregory, Zhang Chunxin Tracy, Chen Albert, Reed Galen, Ruscitto Daniel M., Slater James, Sriram Renuka, Larson Peder E. Z., Vigneron Daniel B., and Kurhanewicz John. Clinical translation of hyperpolarized ¹³C pyruvate and urea MRI for simultaneous metabolic and perfusion imaging. *Magnetic Resonance in Medicine*, 87(1):138–149, 2022. doi:10.1002/mrm.28965.
- [307] von Morze Cornelius, Larson Peder E. Z., Hu Simon, Yoshihara Hikari A. I., Bok Robert A., Goga Andrei, Ardenkjaer-Larsen Jan Henrik, and Vigneron Daniel B. Investigating tumor perfusion and metabolism using multiple hyperpolarized ¹³C compounds: HP001, pyruvate and urea. *Magnetic Resonance Imaging*, 30(3):305–311, 2012. doi:10.1016/j.mri.2011.09.026.
- [308] Wilson David M., Keshari Kayvan R., Larson Peder E. Z., Chen Albert P., Hu Simon, Crieeking Mark Van, Bok Robert, Nelson Sarah J., Macdonald Jeffrey M., Vigneron Daniel B., and Kurhanewicz John. Multi-compound polarization by DNP allows simultaneous assessment of multiple enzymatic activities in vivo. *Journal of Magnetic Resonance*, 205(1):141–147, 2010. doi:10.1016/j.jmr.2010.04.012.
- [309] Elliott Stuart J., Cousin Samuel F., Chappuis Quentin, Cala Olivier, Ceillier Morgan, Bornet Aurélien, and Jannin Sami. Dipolar order mediated ¹H → ¹³C cross-polarization for dissolution-dynamic nuclear polarization. *Magnetic Resonance*, 1(1):89–96, 2020. doi:10.5194/mr-1-89-2020.
- [310] Elliott Stuart J., Cala Olivier, Stern Quentin, Cousin Samuel F., Ceillier Morgan, Decker Venita, and Jannin Sami. Boosting dissolution-dynamic nuclear polarization by multiple-step dipolar order mediated ¹H → ¹³C cross-polarization. *Journal of Magnetic Resonance Open*, 8–9:100018, 2021. doi:10.1016/j.jmro.2021.100018.
- [311] Elliott Stuart J., Ceillier Morgan, Cala Olivier, Stern Quentin, Cousin Samuel F., and Jannin Sami. Simple and cost-effective cross-polarization experiments under dissolution-dynamic nuclear polarization conditions with a 3D-printed ¹H-¹³C background-free radiofrequency coil. *Journal of Magnetic Resonance Open*, 10–11:100033, 2022. doi:10.1016/j.jmro.2022.100033.
- [312] Kurdzesau F., van den Brandt B., Comment A., Hautle P., Jannin S., van der Klink J. J., and Konter J. A. Dynamic nuclear polarization of small labelled molecules in frozen water–alcohol solutions. *Journal of Physics D: Applied Physics*, 41(15):155506, 2008. doi:10.1088/0022-3727/41/15/155506.
- [313] de Boer W., Borghini M., Morimoto K., Niinikoski T. O., and Udo F. Dynamic polarization of protons, deuterons, and carbon-13 nuclei: Thermal contact between nuclear spins and an electron spin-spin interaction reservoir. *Journal of Low Temperature Physics*, 15:249–267, 1974. doi:10.1007/BF00661185.
- [314] Borghini M., de Boer W., and Morimoto K. Nuclear dynamic polarization by resolved solid-state effect and thermal mixing with an electron spin-spin interaction reservoir. *Physics Letters A*, 48(4):244–246, 1974. doi:10.1016/0375-9601(74)90487-3.
- [315] Ferrari Arianna, Peters Josh, Anikeeva Mariia, Pravdivtsev Andrey, Ellermann Frowin, Them Kolja, Will Olga, Peschke Eva, Yoshihara Hikari, Jansen Olav, and Hövener Jan-Bernd. Performance and reproducibility of ¹³C and ¹⁵N hyperpolarization using a cryogen-free DNP polarizer. *Scientific Reports*, 12(1):11694, 2022. doi:10.1038/s41598-022-15380-7.
- [316] Filibian M., Serra S. Colombo, Moscardini M., Rosso A., Tedoldi F., and Carretta P. The role of the glassy dynamics and thermal mixing in the dynamic nuclear polarization and relaxation mechanisms of pyruvic acid. *Physical Chemistry Chemical Physics*, 16(48):27025–27036, 2014. doi:10.1039/C4CP02636E.
- [317] Equbal Asif, Li Yuanxin, Tabassum Tarnuma, and Han Songi. Crossover from a Solid Effect to Thermal Mixing ¹H Dynamic Nuclear Polarization with Trityl-OX063. *The Journal of Physical Chemistry Letters*, 11(9):3718–3723, 2020. doi:10.1021/acs.jpcllett.0c00830.
- [318] Kennedy Brett W. C., Kettunen Mikko I., Hu De-En, and Brindle Kevin M. Probing Lactate Dehydrogenase Activity in Tumors by Measuring Hydrogen/Deuterium Exchange in Hyperpolarized L-[1-¹³C,U-²H]Lactate. *Journal of the American Chemical Society*, 134(10):4969–4977, 2012. doi:10.1021/ja300222e.
- [319] Casals Juliana B., Pieri Naira C.G., Feitosa Matheus L.T., Ercolin Anna C.M., Roballo Kelly C.S., Barreto Rodrigo S.N., Bressan Fabiana F., Martins Daniele S., Miglino Maria A., and Ambrósio Carlos E. The Use of Animal Models for Stroke Research: A Review. *Comparative Medicine*, 61(4):305–313, 2011.

Bibliography

- [320] Macrae I.M. Preclinical stroke research – advantages and disadvantages of the most common rodent models of focal ischaemia. *British Journal of Pharmacology*, 164(4):1062–1078, 2011. doi:10.1111/j.1476-5381.2011.01398.x.
- [321] Kovačević N., Henderson J.T., Chan E., Lifshitz N., Bishop J., Evans A.C., Henkelman R.M., and Chen X.J. A Three-dimensional MRI Atlas of the Mouse Brain with Estimates of the Average and Variability. *Cerebral Cortex*, 15(5):639–645, 2005. doi:10.1093/cercor/bhh165.
- [322] Welniak–Kaminska Marlena, Fiedorowicz Michal, Orzel Jaroslaw, Bogorodzki Piotr, Modlinska Klaudia, Stryjek Rafal, Chrzanoska Anna, Pisula Wojciech, and Grieb Pawel. Volumes of brain structures in captive wild-type and laboratory rats: 7T magnetic resonance in vivo automatic atlas-based study. *PLOS ONE*, 14(4): e0215348, 2019. doi:10.1371/journal.pone.0215348.
- [323] Doty F David, Entzminger George, Kulkarni Jatin, Pamarthy Kranti, and Staab John P. Radio frequency coil technology for small-animal MRI. *NMR in Biomedicine*, 20(3):304–325, 2007. doi:10.1002/nbm.1149.
- [324] Gordon Jeremy W., Chen Hsin-Yu, Dwork Nicholas, Tang Shuyu, and Larson Peder E. Z. Fast Imaging for Hyperpolarized MR Metabolic Imaging. *Journal of Magnetic Resonance Imaging*, 53(3):686–702, 2021. doi:10.1002/jmri.27070.
- [325] Brown T. R., Kincaid B. M., and Ugurbil K. NMR chemical shift imaging in three dimensions. *Proceedings of the National Academy of Sciences*, 79(11):3523–3526, 1982. doi:10.1073/pnas.79.11.3523.
- [326] Mulkern Robert V. and Panych Lawrence P. Echo planar spectroscopic imaging. *Concepts in Magnetic Resonance*, 13(4):213–237, 2001. doi:10.1002/cmr.1011.
- [327] Mansfield P. Spatial mapping of the chemical shift in NMR. *Magnetic Resonance in Medicine*, 1(3):370–386, 1984. doi:10.1002/mrm.1910010308.
- [328] Adalsteinsson Elfar, Irrarrazabal Pablo, Topp Simon, Meyer Craig, Macovski Albert, and Spielman Daniel M. Volumetric spectroscopic imaging with spiral-based k-space trajectories. *Magnetic Resonance in Medicine*, 39(6):889–898, 1998. doi:10.1002/mrm.1910390606.
- [329] Mayer Dirk, Levin Yakir S., Hurd Ralph E., Glover Gary H., and Spielman Daniel M. Fast metabolic imaging of systems with sparse spectra: Application for hyperpolarized ^{13}C imaging. *Magnetic Resonance in Medicine*, 56(4):932–937, 2006. doi:10.1002/mrm.21025.
- [330] Ramirez Marc S., Lee Jaehyuk, Walker Christopher M., Sandulache Vlad C., Hennel Franciszek, Lai Stephen Y., and Bankson James A. Radial spectroscopic MRI of hyperpolarized $[1-^{13}\text{C}]$ pyruvate at 7 tesla. *Magnetic Resonance in Medicine*, 72(4):986–995, 2014. doi:10.1002/mrm.25004.
- [331] Furuyama Jon K., Wilson Neil E., and Thomas M. Albert. Spectroscopic imaging using concentric circular echo-planar trajectories in vivo. *Magnetic Resonance in Medicine*, 67(6):1515–1522, 2012. doi:10.1002/mrm.23184.
- [332] Reeder Scott B., Pineda Angel R., Wen Zhifei, Shimakawa Ann, Yu Huanzhou, Brittain Jean H., Gold Garry E., Beaulieu Christopher H., and Pelc Norbert J. Iterative decomposition of water and fat with echo asymmetry and least-squares estimation (IDEAL): Application with fast spin-echo imaging. *Magnetic Resonance in Medicine*, 54(3):636–644, 2005. doi:10.1002/mrm.20624.
- [333] Meyer Craig H., Pauly John M., Macovskiand Albert, and Nishimura Dwight G. Simultaneous spatial and spectral selective excitation. *Magnetic Resonance in Medicine*, 15(2):287–304, 1990. doi:10.1002/mrm.1910150211.
- [334] Cunningham Charles H., Chen Albert P., Lustig Michael, Hargreaves Brian A., Lupo Janine, Xu Duan, Kurhanewicz John, Hurd Ralph E., Pauly John M., Nelson Sarah J., and Vigneron Daniel B. Pulse sequence for dynamic volumetric imaging of hyperpolarized metabolic products. *Journal of Magnetic Resonance*, 193(1):139–146, 2008. doi:10.1016/j.jmr.2008.03.012.
- [335] Lau Angus Z., Chen Albert P., Ghugre Nilesh R., Ramanan Venkat, Lam Wilfred W., Connelly Kim A., Wright Graham A., and Cunningham Charles H. Rapid multislice imaging of hyperpolarized ^{13}C pyruvate and bicarbonate in the heart. *Magnetic Resonance in Medicine*, 64(5):1323–1331, 2010. doi:10.1002/mrm.22525.
- [336] Michel Keith A., Ragavan Mukundan, Walker Christopher M., Merritt Matthew E., Lai Stephen Y., and Bankson James A. Comparison of selective excitation and multi-echo chemical shift encoding for imaging of hyperpolarized $[1-^{13}\text{C}]$ pyruvate. *Journal of Magnetic Resonance*, 325:106927, 2021. doi:10.1016/j.jmr.2021.106927.
- [337] Gordon Jeremy W., Vigneron Daniel B., and Larson Peder E.Z. Development of a symmetric echo planar imaging framework for clinical translation of rapid dynamic hyperpolarized ^{13}C imaging. *Magnetic Resonance in Medicine*, 77(2):826–832, 2017. doi:10.1002/mrm.26123.

- [338] Svensson Jonas, Månsson Sven, Johansson Edvin, Petersson J. Stefan, and Olsson Lars E. Hyperpolarized ^{13}C MR angiography using trueFISP. *Magnetic Resonance in Medicine*, 50(2):256–262, 2003. doi:10.1002/mrm.10530.
- [339] Milshteyn Eugene, von Morze Cornelius, Reed Galen D., Shang Hong, Shin Peter J., Zhu Zihan, Chen Hsin-Yu, Bok Robert, Goga Andrei, Kurhanewicz John, Larson Peder E. Z., and Vigneron Daniel B. Development of high resolution 3D hyperpolarized carbon-13 MR molecular imaging techniques. *Magnetic Resonance Imaging*, 38:152–162, 2017. doi:10.1016/j.mri.2017.01.003.
- [340] Grashei Martin, Hundshammer Christian, van Heijster Frits H. A., Topping Geoffrey J., and Schilling Franz. pH Dependence of T_2 for Hyperpolarizable ^{13}C -Labelled Small Molecules Enables Spatially Resolved pH Measurement by Magnetic Resonance Imaging. *Pharmaceuticals*, 14(4):327, 2021. doi:10.3390/ph14040327.
- [341] Scheffler Klaus, Heid Oliver, and Hennig Jürgen. Magnetization preparation during the steady state: Fat-saturated 3D TrueFISP. *Magnetic Resonance in Medicine*, 45(6):1075–1080, 2001. doi:10.1002/mrm.1142.
- [342] Bieri Oliver and Scheffler Klaus. Fundamentals of balanced steady state free precession MRI. *Journal of Magnetic Resonance Imaging*, 38(1):2–11, 2013. doi:10.1002/jmri.24163.
- [343] Leupold Jochen, Wieben Oliver, Månsson Sven, Speck Oliver, Scheffler Klaus, Petersson J. Stefan, and Hennig Jürgen. Fast chemical shift mapping with multiecho balanced SSFP. *Magnetic Resonance Materials in Physics, Biology and Medicine*, 19(5):267–273, 2006. doi:10.1007/s10334-006-0056-9.
- [344] Shang Hong, Sukumar Subramaniam, von Morze Cornelius, Bok Robert A., Marco-Rius Irene, Kerr Adam, Reed Galen D., Milshteyn Eugene, Ohliger Michael A., Kurhanewicz John, Larson Peder E.Z., Pauly John M., and Vigneron Daniel B. Spectrally selective three-dimensional dynamic balanced steady-state free precession for hyperpolarized C-13 metabolic imaging with spectrally selective radiofrequency pulses. *Magnetic Resonance in Medicine*, 78(3):963–975, 2017. doi:10.1002/mrm.26480.
- [345] Skinner Jason G., Topping Geoffrey J., Nagel Luca, Heid Irina, Hundshammer Christian, Grashei Martin, van Heijster Frits H. A., Braren Rickmer, and Schilling Franz. Spectrally selective bSSFP using off-resonant RF excitations permits high spatiotemporal resolution 3D metabolic imaging of hyperpolarized $[1-^{13}\text{C}]$ Pyruvate-to- $[1-^{13}\text{C}]$ lactate conversion. *Magnetic Resonance in Medicine*, 2023. doi:10.1002/mrm.29676.
- [346] Leupold Jochen, Månsson Sven, Stefan Petersson J., Hennig Jürgen, and Wieben Oliver. Fast multiecho balanced SSFP metabolite mapping of ^1H and hyperpolarized ^{13}C compounds. *Magnetic Resonance Materials in Physics, Biology and Medicine*, 22(4):251–256, 2009. doi:10.1007/s10334-009-0169-z.
- [347] Shrot Yoav and Frydman Lucio. Spatially encoded NMR and the acquisition of 2D magnetic resonance images within a single scan. *Journal of Magnetic Resonance*, 172(2):179–190, 2005. doi:10.1016/j.jmr.2004.09.024.
- [348] Tal Assaf and Frydman Lucio. Spectroscopic imaging from spatially-encoded single-scan multidimensional MRI data. *Journal of Magnetic Resonance*, 189(1):46–58, 2007. doi:10.1016/j.jmr.2007.08.003.
- [349] Schmidt Rita and Frydman Lucio. In vivo 3D spatial/1D spectral imaging by spatiotemporal encoding: A new single-shot experimental and processing approach. *Magnetic Resonance in Medicine*, 70(2):382–391, 2013. doi:10.1002/mrm.24470.
- [350] Schmidt Rita, Laustsen Christoffer, Dumez Jean-Nicolas, Kettunen Mikko I., Serrao Eva M., Marco-Rius Irene, Brindle Kevin M., Ardenkjaer-Larsen Jan Henrik, and Frydman Lucio. In vivo single-shot ^{13}C spectroscopic imaging of hyperpolarized metabolites by spatiotemporal encoding. *Journal of Magnetic Resonance*, 240: 8–15, 2014. doi:10.1016/j.jmr.2013.12.013.
- [351] Nagel Luca, Topping Geoffrey, and Schilling Franz. B₁-Compensating RF Excitation for Imaging hyperpolarized ^{13}C nuclei with bSSFP using a ^{13}C Cryo-Coil. In *Proc. ISMRM*, 2933, 2022.
- [352] Schmidt Rita, Mishkovsky Mor, Hyacinthe Jean-Noel, Kunz Nicolas, Gruetter Rolf, Comment Arnaud, and Frydman Lucio. Correcting surface coil excitation inhomogeneities in single-shot SPEN MRI. *Journal of Magnetic Resonance*, 259:199–206, 2015. doi:10.1016/j.jmr.2015.08.018.
- [353] Wiesinger Florian, Weidl Eliane, Menzel Marion I., Janich Martin A., Khegai Oleksandr, Glaser Steffen J., Haase Axel, Schwaiger Markus, and Schulte Rolf F. IDEAL spiral CSI for dynamic metabolic MR imaging of hyperpolarized $[1-^{13}\text{C}]$ pyruvate. *Magnetic Resonance in Medicine*, 68(1):8–16, 2012. doi:10.1002/mrm.23212.
- [354] Dixon W. T. Simple proton spectroscopic imaging. *Radiology*, 153(1):189–194, 1984. doi:10.1148/radiology.153.1.6089263.
- [355] Reeder Scott B., Brittain Jean H., Grist Thomas M., and Yen Yi-Fen. Least-squares chemical shift separation for ^{13}C metabolic imaging. *Journal of Magnetic Resonance Imaging*, 26(4):1145–1152, 2007. doi:10.1002/jmri.21089.

Bibliography

- [356] Brodsky Ethan K., Holmes James H., Yu Huanzhou, and Reeder Scott B. Generalized k-space decomposition with chemical shift correction for non-cartesian water-fat imaging. *Magnetic Resonance in Medicine*, 59(5): 1151–1164, 2008. doi:10.1002/mrm.21580.
- [357] Ahn C. B., Kim J. H., and Cho Z. H. High-Speed Spiral-Scan Echo Planar NMR Imaging-I. *IEEE Transactions on Medical Imaging*, 5(1):2–7, 1986. doi:10.1109/TMI.1986.4307732.
- [358] Delattre Bénédicte M. A., Heidemann Robin M., Crowe Lindsey A., Vallée Jean-Paul, and Hyacinthe Jean-Noël. Spiral demystified. *Magnetic Resonance Imaging*, 28(6):862–881, 2010. doi:10.1016/j.mri.2010.03.036.
- [359] Liao Jan-Ray, Pauly John M., Brosnan Thomas J., and Pelc Norbert J. Reduction of motion artifacts in cine MRI using variable-density spiral trajectories. *Magnetic Resonance in Medicine*, 37(4):569–575, 1997. doi:10.1002/mrm.1910370416.
- [360] Meyer Craig H., Hu Bob S., Nishimura Dwight G., and Macovski Albert. Fast Spiral Coronary Artery Imaging. *Magnetic Resonance in Medicine*, 28(2):202–213, 1992. doi:10.1002/mrm.1910280204.
- [361] Thedens Daniel R., Irarrazaval Pablo, Sachs Todd S., Meyer Craig H., and Nishimura Dwight G. Fast magnetic resonance coronary angiography with a three-dimensional stack of spirals trajectory. *Magnetic Resonance in Medicine*, 41(6):1170–1179, 1999. doi:10.1002/(SICI)1522-2594(199906)41:6<1170::AID-MRM13>3.0.CO;2-J.
- [362] Gurney Paul T., Hargreaves Brian A., and Nishimura Dwight G. Design and analysis of a practical 3D cones trajectory. *Magnetic Resonance in Medicine*, 55(3):575–582, 2006. doi:10.1002/mrm.20796.
- [363] Pipe James G., Zwart Nicholas R., Aboussouan Eric A., Robison Ryan K., Devaraj Ajit, and Johnson Kenneth O. A new design and rationale for 3D orthogonally oversampled k-space trajectories. *Magnetic Resonance in Medicine*, 66(5):1303–1311, 2011. doi:10.1002/mrm.22918.
- [364] Pauly J., Le Roux P., Nishimura D., and Macovski A. Parameter relations for the Shinnar-Le Roux selective excitation pulse design algorithm (NMR imaging). *IEEE Transactions on Medical Imaging*, 10(1):53–65, 1991. doi:10.1109/42.75611.
- [365] Levin Y.s., Mayer D., Yen Y.-E., Hurd R.e., and Spielman D.m. Optimization of fast spiral chemical shift imaging using least squares reconstruction: Application for hyperpolarized ¹³C metabolic imaging. *Magnetic Resonance in Medicine*, 58(2):245–252, 2007. doi:10.1002/mrm.21327.
- [366] Jackson J.I., Meyer C.H., Nishimura D.G., and Macovski A. Selection of a convolution function for Fourier inversion using gridding (computerised tomography application). *IEEE Transactions on Medical Imaging*, 10(3):473–478, 1991. doi:10.1109/42.97598.
- [367] O’Sullivan J. D. A Fast Sinc Function Gridding Algorithm for Fourier Inversion in Computer Tomography. *IEEE Transactions on Medical Imaging*, 4(4):200–207, 1985. doi:10.1109/TMI.1985.4307723.
- [368] Rasche V., Proksa R., Sinkus R., Bornert P., and Eggers H. Resampling of data between arbitrary grids using convolution interpolation. *IEEE Transactions on Medical Imaging*, 18(5):385–392, 1999. doi:10.1109/42.774166.
- [369] Kaiser J. F. Nonrecursive digital filter design using the I_0 -sinh window function. In *Proc IEEE International Symposium on Circuits & Systems*, 1974.
- [370] Kaiser J. and Schafer R. On the use of the I_0 -sinh window for spectrum analysis. *IEEE Transactions on Acoustics, Speech, and Signal Processing*, 28(1):105–107, 1980. doi:10.1109/TASSP.1980.1163349.
- [371] Hayes Cecil E., Edelstein William A., Schenck John F., Mueller Otward M., and Eash Matthew. An efficient, highly homogeneous radiofrequency coil for whole-body NMR imaging at 1.5 T. *Journal of Magnetic Resonance (1969)*, 63(3):622–628, 1985. doi:10.1016/0022-2364(85)90257-4.
- [372] Garbow Joel R., Mcintosh Charlie, and Conradi Mark S. Actively decoupled transmit–receive coil-pair for mouse brain MRI. *Concepts in Magnetic Resonance Part B: Magnetic Resonance Engineering*, 33B(4):252–259, 2008. doi:10.1002/cmr.b.20124.
- [373] Ahmad Sheikh Faisal, Kim Young Cheol, Choi Ick Chang, and Kim Hyun Deok. Recent Progress in Birdcage RF Coil Technology for MRI System. *Diagnostics*, 10(12):1017, 2020. doi:10.3390/diagnostics10121017.
- [374] Roemer P. B., Edelstein W. A., Hayes C. E., Souza S. P., and Mueller O. M. The NMR phased array. *Magnetic Resonance in Medicine*, 16(2):192–225, 1990. doi:10.1002/mrm.1910160203.
- [375] Reykowski Arne, Wright Steven M., and Porter Jay R. Design of Matching Networks for Low Noise Preamplifiers. *Magnetic Resonance in Medicine*, 33(6):848–852, 1995. doi:10.1002/mrm.1910330617.
- [376] Possanzini C. and Boutelje M. Influence of magnetic field on preamplifiers using GaAs FET technology. In *Proc. ISMRM*, 1123, 2008.

- [377] Doty F D, Connick T. J, Ni X. Z, and Clingan M. N. Noise in high-power, high-frequency double-tuned probes. *Journal of Magnetic Resonance (1969)*, 77(3):536–549, 1988. doi:10.1016/0022-2364(88)90011-X.
- [378] Insko E. K. and Bolinger L. Mapping of the Radiofrequency Field. *Journal of Magnetic Resonance, Series A*, 103(1):82–85, 1993. doi:10.1006/jmra.1993.1133.
- [379] Larsson Erik G., Erdogmus Deniz, Yan Rui, Principe Jose C., and Fitzsimmons Jeffrey R. SNR-optimality of sum-of-squares reconstruction for phased-array magnetic resonance imaging. *Journal of Magnetic Resonance*, 163(1):121–123, 2003. doi:10.1016/S1090-7807(03)00132-0.
- [380] Adriany Gregor and Gruetter Rolf. A Half-Volume Coil for Efficient Proton Decoupling in Humans at 4 Tesla. *Journal of Magnetic Resonance*, 125(1):178–184, 1997. doi:10.1006/jmre.1997.1113.
- [381] Junge Sven. Cryogenic and Superconducting Coils for MRI. In *eMagRes*. John Wiley & Sons, Ltd, 2012. doi:10.1002/9780470034590.emrstm1162.
- [382] Kumar Ananda, Edelstein William A., and Bottomley Paul A. Noise figure limits for circular loop MR coils. *Magnetic Resonance in Medicine*, 61(5):1201–1209, 2009. doi:10.1002/mrm.21948.
- [383] Sack M., Wetterling F, Sartorius A., Ende G., and Weber-Fahr W. Signal-to-noise ratio of a mouse brain ^{13}C CryoProbe™ system in comparison with room temperature coils: Spectroscopic phantom and in vivo results. *NMR in Biomedicine*, 27(6):709–715, 2014. doi:10.1002/nbm.3110.
- [384] Ratering David, Baltes Christof, Nordmeyer-Massner Jurek, Marek Daniel, and Rudin Markus. Performance of a 200-MHz cryogenic RF probe designed for MRI and MRS of the murine brain. *Magnetic Resonance in Medicine*, 59(6):1440–1447, 2008. doi:10.1002/mrm.21629.
- [385] Baltes Christof, Radzwill Nicole, Bosshard Simone, Marek Daniel, and Rudin Markus. Micro MRI of the mouse brain using a novel 400 MHz cryogenic quadrature RF probe. *NMR in Biomedicine*, 22(8):834–842, 2009. doi:10.1002/nbm.1396.
- [386] Peeters Tom H., Kobus Thiele, Breukels Vincent, Lenting Krissie, Veltien Andor, Heerschap Arend, and Scheenen Tom W. J. Imaging Hyperpolarized Pyruvate and Lactate after Blood–Brain Barrier Disruption with Focused Ultrasound. *ACS Chemical Neuroscience*, 10(5):2591–2601, 2019. doi:10.1021/acschemneuro.9b00085.
- [387] Sapir Gal, Shaul David, Lev-Cohain Naama, Sosna Jacob, Gomori Moshe J., and Katz-Brull Rachel. LDH and PDH Activities in the Ischemic Brain and the Effect of Reperfusion—An Ex Vivo MR Study in Rat Brain Slices Using Hyperpolarized $[1-^{13}\text{C}]$ Pyruvate. *Metabolites*, 11(4):210, 2021. doi:10.3390/metabo11040210.
- [388] Chattergoon N., Martínez-Santesteban F, Handler W. B., Ardenkjær-Larsen J. H., and Scholl T. J. Field dependence of T_1 for hyperpolarized $[1-^{13}\text{C}]$ pyruvate. *Contrast Media & Molecular Imaging*, 8(1):57–62, 2013. doi:10.1002/cmml.1494.
- [389] Blicharski J. Nuclear Magnetic Relaxation by Anisotropy of the Chemical Shift. *Zeitschrift für Naturforschung A*, 27(10):1456–1458, 1972. doi:10.1515/zna-1972-1012.
- [390] Juchem Christoph, Cudalbu Cristina, de Graaf Robin A., Gruetter Rolf, Henning Anke, Hetherington Hoby P., and Boer Vincent O. B_0 shimming for in vivo magnetic resonance spectroscopy: Experts' consensus recommendations. *NMR in Biomedicine*, 34(5):e4350, 2021. doi:10.1002/nbm.4350.
- [391] Haskell Melissa W., Nielsen Jon-Fredrik, and Noll Douglas C. Off-resonance artifact correction for MRI: A review. *NMR in Biomedicine*, n/a(n/a):e4867, 2022. doi:10.1002/nbm.4867.
- [392] Noll D.C., Meyer C.H., Pauly J.M., Nishimura D.G., and Macovski A. A homogeneity correction method for magnetic resonance imaging with time-varying gradients. *IEEE Transactions on Medical Imaging*, 10(4):629–637, 1991. doi:10.1109/42.108599.
- [393] Park Jae Mo, Josan Sonal, Jang Taichang, Merchant Milton, Watkins Ron, Hurd Ralph E., Recht Lawrence D., Mayer Dirk, and Spielman Daniel M. Volumetric spiral chemical shift imaging of hyperpolarized $[2-^{13}\text{C}]$ pyruvate in a rat C6 glioma model. *Magnetic Resonance in Medicine*, 75(3):973–984, 2016. doi:10.1002/mrm.25766.
- [394] Le Page Lydia M., Guglielmetti Caroline, Najac Chloé F, Tiret Brice, and Chaumeil Myriam M. Hyperpolarized ^{13}C magnetic resonance spectroscopy detects toxin-induced neuroinflammation in mice. *NMR in Biomedicine*, 32(11):e4164, 2019. doi:10.1002/nbm.4164.
- [395] Chen Yiran, Kim Hosung, Bok Robert, Sukumar Subramaniam, Mu Xin, Sheldon R. Ann, Barkovich A. James, Ferriero Donna M., and Xu Duan. Pyruvate to Lactate Metabolic Changes during Neurodevelopment Measured Dynamically Using Hyperpolarized ^{13}C Imaging in Juvenile Murine Brain. *Developmental Neuroscience*, 38(1):34–40, 2015. doi:10.1159/000439271.

Bibliography

- [396] Guglielmetti Caroline, Najac Chloé, Didonna Alessandro, Van der Linden Annemie, Ronen Sabrina M., and Chaumeil Myriam M. Hyperpolarized ^{13}C MR metabolic imaging can detect neuroinflammation in vivo in a multiple sclerosis murine model. *Proceedings of the National Academy of Sciences*, 114(33):E6982–E6991, 2017. doi:10.1073/pnas.1613345114.
- [397] Guglielmetti Caroline, Chou Austin, Krukowski Karen, Najac Chloe, Feng Xi, Riparip Lara-Kirstie, Rosi Susanna, and Chaumeil Myriam M. In vivo metabolic imaging of Traumatic Brain Injury. *Scientific Reports*, 7(1):17525, 2017. doi:10.1038/s41598-017-17758-4.
- [398] Guglielmetti Caroline, Cordano Christian, Najac Chloé, Green Ari J., and Chaumeil Myriam M. Imaging immunomodulatory treatment responses in a multiple sclerosis mouse model using hyperpolarized ^{13}C metabolic MRI. *Communications Medicine*, 3(1):1–11, 2023. doi:10.1038/s43856-023-00300-1.
- [399] Mikrogeorgiou Alkisti, Chen Yiran, Lee Byong Sop, Bok Robert, Sheldon R. Ann, Barkovich A. James, Xu Duan, and Ferriero Donna M. A Metabolomics Study of Hypoxia Ischemia during Mouse Brain Development Using Hyperpolarized ^{13}C . *Developmental Neuroscience*, 42(1):49–58, 2020. doi:10.1159/000506982.
- [400] Chaumeil Myriam M., Radoul Marina, Najac Chloé, Eriksson Pia, Viswanath Pavithra, Blough Michael D., Chesnelong Charles, Luchman H. Artee, Cairncross J. Gregory, and Ronen Sabrina M. Hyperpolarized ^{13}C MR imaging detects no lactate production in mutant IDH1 gliomas: Implications for diagnosis and response monitoring. *NeuroImage: Clinical*, 12:180–189, 2016. doi:10.1016/j.nicl.2016.06.018.
- [401] Hurd Ralph E., Yen Yi-Fen, Tropp James, Pfefferbaum Adolf, Spielman Daniel M., and Mayer Dirk. Cerebral Dynamics and Metabolism of Hyperpolarized $[1-^{13}\text{C}]$ pyruvate Using Time-Resolved MR Spectroscopic Imaging. *Journal of Cerebral Blood Flow & Metabolism*, 30(10):1734–1741, 2010. doi:10.1038/jcbfm.2010.93.
- [402] Josan Sonal, Hurd Ralph, Billingsley Kelvin, Senadheera Lasitha, Park Jae Mo, Yen Yi-Fen, Pfefferbaum Adolf, Spielman Daniel, and Mayer Dirk. Effects of isoflurane anesthesia on hyperpolarized ^{13}C metabolic measurements in rat brain. *Magnetic Resonance in Medicine*, 70(4):1117–1124, 2013. doi:10.1002/mrm.24532.
- [403] Choi Young-Suk, Kang Somang, Ko Sang-Yoon, Lee Saeram, Kim Jae Young, Lee Hansol, Song Jae Eun, Kim Dong-Hyun, Kim Eosu, Kim Chul Hoon, Saksida Lisa, Song Ho-Taek, and Lee Jong Eun. Hyperpolarized $[1-^{13}\text{C}]$ pyruvate MR spectroscopy detect altered glycolysis in the brain of a cognitively impaired mouse model fed high-fat diet. *Molecular Brain*, 11(1):74, 2018. doi:10.1186/s13041-018-0415-2.
- [404] Choi Young-Suk, Song Jae Eun, Lee Jong Eun, Kim Eosu, Kim Chul Hoon, Kim Dong-Hyun, and Song Ho-Taek. Hyperpolarized $[1-^{13}\text{C}]$ lactate flux increased in the hippocampal region in diabetic mice. *Molecular Brain*, 12(1):88, 2019. doi:10.1186/s13041-019-0505-9.
- [405] Radoul Marina, Najac Chloé, Viswanath Pavithra, Mukherjee Joydeep, Kelly Mark, Gillespie Anne Marie, Chaumeil Myriam M., Eriksson Pia, Delos Santos Romelyn, Pieper Russell O., and Ronen Sabrina M. HDAC inhibition in glioblastoma monitored by hyperpolarized ^{13}C MRSI. *NMR in Biomedicine*, 32(2):e4044, 2019. doi:10.1002/nbm.4044.
- [406] Lee Hansol, Lee Joonsung, Joe Eunhae, Yang Seungwook, Choi Young-suk, Wang Eunkyung, Song Ho-Taek, and Kim Dong-Hyun. Determination of Optimal Scan Time for the Measurement of Downstream Metabolites in Hyperpolarized ^{13}C MRSI. *Investigative Magnetic Resonance Imaging*, 19(4):212, 2015. doi:10.13104/imri.2015.19.4.212.
- [407] Park Ilwoo, Hu Simon, Bok Robert, Ozawa Tomoko, Ito Motokazu, Mukherjee Joydeep, Phillips Joanna J., James C. David, Pieper Russell O., Ronen Sabrina M., Vigneron Daniel B., and Nelson Sarah J. Evaluation of heterogeneous metabolic profile in an orthotopic human glioblastoma xenograft model using compressed sensing hyperpolarized 3D ^{13}C magnetic resonance spectroscopic imaging. *Magnetic Resonance in Medicine*, 70(1):33–39, 2013. doi:10.1002/mrm.24434.
- [408] Park Ilwoo, Kim Seulkee, Pucciarelli Daniela, Song Juhyun, Choi Jin Myung, Lee Kyung-Hwa, Kim Yun Hyeon, Jung Shin, Yoon Woong, and Nakamura Jean L. Differentiating Radiation Necrosis from Brain Tumor Using Hyperpolarized Carbon-13 MR Metabolic Imaging. *Molecular Imaging and Biology*, 23(3):417–426, 2021. doi:10.1007/s11307-020-01574-w.
- [409] Ruiz-Rodado Victor, Malta Tathiane M, Seki Tomohiro, Lita Adrian, Dowdy Tyrone, Celiku Orieta, Cavazos-Saldana Alejandra, Li Aiguo, Liu Yang, Han Sue, Zhang Wei, Song Hua, Davis Dionne, Lee Sunmin, Trepel Jane B, Sabedot Thais S, Munasinghe Jeeva, Yang Chunzhang, Herold-Mende Christel, Gilbert Mark R, Cherukuri Murali Krishna, Noushmehr Houtan, and Larion Mioara. Metabolic reprogramming associated with aggressiveness occurs in the G-CIMP-high molecular subtypes of IDH1mut lower grade gliomas. *Neuro-Oncology*, 22(4):480–492, 2020. doi:10.1093/neuonc/noz207.

- [410] Kawai Tatsuya, Brender Jeffrey R., Lee Jennifer A., Kramp Tamalee, Kishimoto Shun, Krishna Murali C., Tofilon Philip, and Camphausen Kevin A. Detection of metabolic change in glioblastoma cells after radiotherapy using hyperpolarized ^{13}C -MRI. *NMR in Biomedicine*, 34(7):e4514, 2021. doi:10.1002/nbm.4514.
- [411] Butt Sadia A, Sogaard Lise V, Magnusson Peter O, Lauritzen Mette H, Laustsen Christoffer, Åkeson Per, and Ardenkjær-Larsen Jan H. Imaging Cerebral 2-Ketoisocaproate Metabolism with Hyperpolarized ^{13}C Magnetic Resonance Spectroscopic Imaging. *Journal of Cerebral Blood Flow & Metabolism*, 32(8):1508–1514, 2012. doi:10.1038/jcbfm.2012.34.
- [412] DeVience Stephen J., Lu Xin, Proctor Julie, Rangghran Parisa, Melhem Elias R., Gullapalli Rao, Fiskum Gary M., and Mayer Dirk. Metabolic imaging of energy metabolism in traumatic brain injury using hyperpolarized [1- ^{13}C]pyruvate. *Scientific Reports*, 7(1):1907, 2017. doi:10.1038/s41598-017-01736-x.
- [413] DeVience Stephen J., Lu Xin, Proctor Julie L., Rangghran Parisa, Medina Juliana A., Melhem Elias R., Gullapalli Rao P., Fiskum Gary, and Mayer Dirk. Enhancing Metabolic Imaging of Energy Metabolism in Traumatic Brain Injury Using Hyperpolarized [1- ^{13}C]Pyruvate and Dichloroacetate. *Metabolites*, 11(6):335, 2021. doi:10.3390/metabo11060335.
- [414] Harris Richard A., Lone Asad, Lim Heeseung, Martinez Francisco, Frame Ariel K., Scholl Timothy J., and Cumming Robert C. Aerobic Glycolysis Is Required for Spatial Memory Acquisition But Not Memory Retrieval in Mice. *eNeuro*, 6(1), 2019. doi:10.1523/ENEURO.0389-18.2019.
- [415] Hurd Ralph E., Yen Yi-Fen, Mayer Dirk, Chen Albert, Wilson David, Kohler Susan, Bok Robert, Vigneron Daniel, Kurhanewicz John, Tropp James, Spielman Daniel, and Pfefferbaum Adolf. Metabolic imaging in the anesthetized rat brain using hyperpolarized [1- ^{13}C] pyruvate and [1- ^{13}C] ethyl pyruvate. *Magnetic Resonance in Medicine*, 63(5):1137–1143, 2010. doi:10.1002/mrm.22364.
- [416] Hackett Edward P., Shah Bhavya R., Cheng Bingbing, LaGue Evan, Vemireddy Vamsidihara, Mendoza Manuel, Bing Chenchen, Bachoo Robert M., Billingsley Kelvin L., Chopra Rajiv, and Park Jae Mo. Probing Cerebral Metabolism with Hyperpolarized ^{13}C Imaging after Opening the Blood–Brain Barrier with Focused Ultrasound. *ACS Chemical Neuroscience*, 12(15):2820–2828, 2021. doi:10.1021/acschemneuro.1c00197.
- [417] Park Jae Mo, Josan Sonal, Grafendorfer Thomas, Yen Yi-Fen, Hurd Ralph E., Spielman Daniel M., and Mayer Dirk. Measuring mitochondrial metabolism in rat brain in vivo using MR Spectroscopy of hyperpolarized [2- ^{13}C]pyruvate. *NMR in Biomedicine*, 26(10):1197–1203, 2013. doi:10.1002/nbm.2935.
- [418] Lim Heeseung, Martínez-Santesteban Francisco, Jensen Michael D., Chen Albert, Wong Eugene, and Scholl Timothy J. Monitoring Early Changes in Tumor Metabolism in Response to Therapy Using Hyperpolarized ^{13}C MRSI in a Preclinical Model of Glioma. *Tomography*, 6(3):290–300, 2020. doi:10.18383/j.tom.2020.00024.
- [419] De Feyter Henk M. and de Graaf Robin A. Deuterium metabolic imaging – Back to the future. *Journal of Magnetic Resonance*, 326:106932, 2021. doi:10.1016/j.jmr.2021.106932.
- [420] Jonckers Elisabeth, Shah Disha, Hamaide Julie, Verhoye Marleen, and Van der Linden Annemie. The power of using functional fMRI on small rodents to study brain pharmacology and disease. *Frontiers in Pharmacology*, 6, 2015. doi:10.3389/fphar.2015.00231.
- [421] Buscemi Lara, Price Melanie, Bezzi Paola, and Hirt Lorenz. Spatio-temporal overview of neuroinflammation in an experimental mouse stroke model. *Scientific Reports*, 9(1):507, 2019. doi:10.1038/s41598-018-36598-4.
- [422] Cooley Clarissa Z., McDaniel Patrick C., Stockmann Jason P., Srinivas Sai Abitha, Cauley Stephen E., Śliwiak Monika, Sappo Charlotte R., Vaughn Christopher F., Guerin Bastien, Rosen Matthew S., Lev Michael H., and Wald Lawrence L. A portable scanner for magnetic resonance imaging of the brain. *Nature Biomedical Engineering*, 5(3):229–239, 2021. doi:10.1038/s41551-020-00641-5.
- [423] O'Reilly Thomas, Teeuwisse Wouter M., de Gans Danny, Koolstra Kirsten, and Webb Andrew G. In vivo 3D brain and extremity MRI at 50 mT using a permanent magnet Halbach array. *Magnetic Resonance in Medicine*, 85(1):495–505, 2021. doi:10.1002/mrm.28396.
- [424] Tsai L. L., Mair R. W., Rosen M. S., Patz S., and Walsworth R. L. An open-access, very-low-field MRI system for posture-dependent ^3He human lung imaging. *Journal of Magnetic Resonance*, 193(2):274–285, 2008. doi:10.1016/j.jmr.2008.05.016.
- [425] Sarraçanie Mathieu, LaPierre Cristen D., Salameh Najat, Waddington David E. J., Witzel Thomas, and Rosen Matthew S. Low-Cost High-Performance MRI. *Scientific Reports*, 5(1):15177, 2015. doi:10.1038/srep15177.
- [426] Sheth Kevin N., Mazurek Mercy H., Yuen Matthew M., Cahn Bradley A., Shah Jill T., Ward Adrienne, Kim Jennifer A., Gilmore Emily J., Falcone Guido J., Petersen Nils, Gobeske Kevin T., Kaddouh Firas, Hwang David Y., Schindler Joseph, Sansing Lauren, Matouk Charles, Rothberg Jonathan, Sze Gordon, Siner Jonathan, Rosen Matthew S., Spudich Serena, and Kimberly W. Taylor. Assessment of Brain Injury Using Portable,

Bibliography

- Low-Field Magnetic Resonance Imaging at the Bedside of Critically Ill Patients. *JAMA Neurology*, 78(1): 41–47, 2021. doi:10.1001/jamaneurol.2020.3263.
- [427] Deoni Sean C. L., Medeiros Paul, Deoni Alexandra T., Burton Phoebe, Beauchemin Jennifer, D'Sa Viren, Boskamp Eddy, By Samantha, McNulty Chris, Mileski William, Welch Brian E., and Huentelman Matthew. Development of a mobile low-field MRI scanner. *Scientific Reports*, 12(1):5690, 2022. doi:10.1038/s41598-022-09760-2.
- [428] Shahrestani Shane, Wishart Danielle, Han Sung Min J., Strickland Ben A., Bakhsheshian Joshua, Mack William J., Toga Arthur W., Sanossian Nerses, Tai Yu-Chong, and Zada Gabriel. A systematic review of next-generation point-of-care stroke diagnostic technologies. *Neurosurgical Focus*, 51(1):E11, 2021. doi:10.3171/2021.4.FOCUS21122.
- [429] Hovis Gabrielle, Langdorf Mark, Dang Eric, Chow Daniel, Hovis Gabrielle, Langdorf Mark I., Dang Eric, and Chow Daniel. MRI at the Bedside: A Case Report Comparing Fixed and Portable Magnetic Resonance Imaging for Suspected Stroke. *Cureus*, 13(8), 2021. doi:10.7759/cureus.16904.
- [430] Yuen Matthew M., Prabhat Anjali M., Mazurek Mercy H., Chavva Isha R., Crawford Anna, Cahn Bradley A., Beekman Rachel, Kim Jennifer A., Gobeske Kevin T., Petersen Nils H., Falcone Guido J., Gilmore Emily J., Hwang David Y., Jasne Adam S., Amin Hardik, Sharma Richa, Matouk Charles, Ward Adrienne, Schindler Joseph, Sansing Lauren, de Havenon Adam, Aydin Ani, Wira Charles, Sze Gordon, Rosen Matthew S., Kimberly W. Taylor, and Sheth Kevin N. Portable, low-field magnetic resonance imaging enables highly accessible and dynamic bedside evaluation of ischemic stroke. *Science Advances*, 8(16):eabm3952, 2022. doi:10.1126/sciadv.abm3952.

Publications and conference proceedings

Publications in peer-reviewed scientific journals

- Hyacinthe Jean-Noël, Buscemi Lara, **Lê Thanh Phong**, Lepore Mario, Hirt Lorenz, Mishkovsky Mor. *Evaluating the potential of hyperpolarised [1-¹³C] L-lactate as a neuro-protectant metabolic biosensor for stroke*. Scientific Reports, 10:5507, 2020. doi:10.1038/s41598-020-62319-x
- **Lê Thanh Phong**, Hyacinthe Jean-Noël, Capozzi Andrea. *How to improve the efficiency of a traditional dissolution dynamic nuclear polarization (dDNP) apparatus: Design and performance of a fluid path compatible dDNP/LOD-ESR probe*. Journal of Magnetic Resonance, 338:107197, 2022. doi:10.1016/j.jmr.2022.107197
- **Lê Thanh Phong**, Hyacinthe Jean-Noël, Capozzi Andrea. *Multi-sample/multi-nucleus parallel polarization and monitoring enabled by a fluid path technology compatible cryogenic probe for dissolution dynamic nuclear polarization*. Scientific Reports, 13:7962, 2023. doi:10.1038/s41598-023-34958-3
- **Lê Thanh Phong**, Buscemi Lara, Lepore Mario, Mishkovsky Mor, Hyacinthe Jean-Noël, Hirt Lorenz. *Influence of DNP Polarizing Agents on Biochemical Processes: TEMPOL in Transient Ischemic Stroke*. ACS Chemical Neuroscience, 2023. doi:10.1021/acchemneuro.3c00137

In preparation

- **Lê Thanh Phong**, Buscemi Lara, Lepore Mario, Hirt Lorenz, Hyacinthe Jean-Noël, Mishkovsky Mor. *In vivo assessment of the metabolic impact of cerebral ischemia using MRS and hyperpolarized [1-¹³C] lactate and [1-¹³C] pyruvate*. In preparation

Other works

- **Lê Thanh Phong**, Gruetter Rolf, Jorge João, Ipek Özlem. *Segmenting electroencephalography wires reduces radiofrequency shielding artifacts in simultaneous electroencephalography and functional magnetic resonance imaging at 7 T*. *Magnetic Resonance in Medicine*, 88:1450-1464, 2022. doi:10.1002/mrm.29298
- Alves Brayan, Šimičić Dunja, Mosso Jessie, **Lê Thanh Phong**, Briand Guillaume, Bogner Wolfgang, Lanz Bernard, Strasser Bernhard, Klausner Antoine, Cudalbu Cristina. *Noise-reduction techniques for ¹H-FID-MRSI at 14.1T: Monte-Carlo validation & in vivo application*. Submitted to NMR in Biomedicine.
- Šimičić Dunja, Alves Brayan, Mosso Jessie, Briand Guillaume, **Lê Thanh Phong**, van Heeswijk Ruud, Starčuková Jana, Lanz Bernard, Klausner Antoine, Strasser Bernhard, Bogner Wolfgang, Cudalbu Cristina. *Fast high-resolution metabolite mapping in the rat brain using ¹H-FID-MRSI at 14.1T*. Submitted to NMR in Biomedicine.
- Lanz Bernard, Flatt Emmanuelle Ines, **Lê Thanh Phong**, Gruetter Rolf, Mishkovsky Mor. *Kinetic Modeling of Cerebral Lactate Production After Hyperpolarized [²H₇, U-¹³C₆]-D-Glucose Bolus*. In preparation

Datasets

- Capozzi Andrea, **Lê Thanh Phong**, Hyacinthe Jean-Noël. *How to improve the efficiency of a traditional dissolution dynamic nuclear polarization (dDNP) apparatus: Design and performance of a fluid path compatible dDNP/LOD-ESR probe*. Dataset. Mendeley Data, 2022. doi:10.17632/45jvgf589x.2
- **Lê Thanh Phong**, Hyacinthe Jean-Noël, Capozzi Andrea. *Multi-sample/multi-nucleus parallel polarization and monitoring enabled by a fluid Path technology compatible cryogenic probe for dissolution dynamic nuclear polarization*. Dataset. Zenodo, 2023. doi:10.5281/zenodo.7937983

Abstracts in peer-reviewed conference proceedings

- HYP18, International Conference on Nuclear Hyperpolarization, Southampton (UK), September 2-5 2018
 - **Lê Thanh Phong**, Buscemi Lara, Lepore Mario, Gruetter Rolf, Hirt Lorenz, Hyacinthe Jean-Noël, Mishkovsky Mor. *Probing Real-Time Metabolism and Neuroprotection of Hyperpolarized L-[1-¹³C] Lactate in a Mouse Model of Stroke*. (Poster)

- Zanella Claudia, Capozzi Andrea, **Lê Thanh Phong**, Gruetter Rolf and Hyacinthe Jean-Noël. *Boosting ^{129}Xe DNP Efficiency Using Ultrasonic Sample Mixing and Microwave Frequency Modulation*. (Oral)
- Arn Lionel, Zanella Claudia, **Lê Thanh Phong**, Capozzi Andrea and Bastiaansen Jessica. *Boosting the Dynamical Nuclear Polarization of $[1-^{13}\text{C}]$ Butyrate with Microwave Frequency Modulation*. (Poster)
- 14th European Molecular Imaging Meeting, Glasgow (UK), March 19-22 2019
 - **Lê Thanh Phong**, Buscemi Lara, Vinckenbosch Elise, Lepore Mario, Gruetter Rolf, Hirt Lorenz, Hyacinthe Jean-Noël, Mishkovsky Mor. *Kinetic Modeling of Hyperpolarized $L-[1-^{13}\text{C}]$ Lactate Cerebral Metabolism in a Mouse Model of Ischemic Stroke*. (Oral)
- 60th Experimental Nuclear Magnetic Resonance Conference, Pacific Grove (USA), April 7-12 2019
 - **Lê Thanh Phong**, Buscemi Lara, Vinckenbosch Elise, Lepore Mario, Gruetter Rolf, Hirt Lorenz, Hyacinthe Jean-Noël, Mishkovsky Mor. *Comparison of Kinetic Models for Hyperpolarized $L-[1-^{13}\text{C}]$ Lactate Cerebral Metabolic Kinetics in a Mouse Model of Ischemic Stroke*. (Poster)
 - Zanella Claudia, Capozzi Andrea, **Lê Thanh Phong**, Radaelli Alice, Gruetter Rolf, Hyacinthe Jean-Noël. *Solvent-dependent DNP of Embedded Xenon upon Microwave Frequency Modulation*. (Poster)
- 27th International Society for Magnetic Resonance in Medicine (ISMRM) Annual Meeting, Montréal (CA), May 11-16 2019
 - **Lê Thanh Phong**, Buscemi Lara, Vinckenbosch Elise, Lepore Mario, Gruetter Rolf, Hirt Lorenz, Hyacinthe Jean-Noël, Mishkovsky Mor. *Kinetic Modeling of Hyperpolarized $L-[1-^{13}\text{C}]$ Lactate Metabolism in a Mouse Model of Ischemic Stroke*. (Oral pitch)
- International Society for Magnetic Resonance in Medicine (ISMRM) Virtual Conference & Exhibition, Online, August 8-14 2020
 - **Lê Thanh Phong**, Buscemi Lara, Vinckenbosch Elise, Lepore Mario, Hirt Lorenz, Hyacinthe Jean-Noël, Mishkovsky Mor. *Metabolism of the hyperpolarized neuroprotective agents $[1-^{13}\text{C}]$ lactate and $[1-^{13}\text{C}]$ pyruvate in a mouse model of stroke*. (Oral)
- 15th European Molecular Imaging Meeting, Online, August 24-28 2020
 - **Lê Thanh Phong**, Buscemi Lara, Vinckenbosch Elise, Lepore Mario, Hirt Lorenz, Hyacinthe Jean-Noël, Mishkovsky Mor. *Cerebral metabolism of the hyperpolarized*

Publications and conference proceedings

neuroprotective agents [1-¹³C] lactate and [1-¹³C] pyruvate in a mouse model of transient ischemic stroke. (Oral)

- International Society for Magnetic Resonance in Medicine (ISMRM) Annual Meeting & Exhibition, Online, May 15-20 2021
 - **Lê Thanh Phong**, Buscemi Lara, Lepore Mario, Hirt Lorenz, Hyacinthe Jean-Noël, Mishkovsky Mor. *DNP Polarizing Agents in Preclinical HP MRS: Influence in the Context of Transient Ischemic Stroke.* (Poster)
 - **Lê Thanh Phong**, Capozzi Andrea, Hyacinthe Jean-Noël. *Hyperpolarized in-vivo Metabolic Imaging at 14.1T: dDNP Cryogenic Insert Redesign and Implementation.* (Poster)
 - Šimičić Dunja, Mosso Jessie Julie, **Lê Thanh Phong**, van Heeswijk Ruud B., Jelescu Ileana Ozana, and Cudalbu Cristina. *The impact of Marchenko-Pasteur principal component analysis denoising on high-resolution MR spectroscopic imaging in the rat brain at 9.4T.* (Poster)
- International Hyperpolarization Conference, Lyon (FR), September 5-9 2021
 - Capozzi Andrea, **Lê Thanh Phong**, Hyacinthe Jean-Noël. *Hyperpolarize ¹²⁹Xe gas via dissolution DNP: Tips and tricks.* (Poster)
 - **Lê Thanh Phong**, Hyacinthe Jean-Noël, Capozzi Andrea. *Retrofit of a wet DNP polarizer with a custom fluid path: better polarization and cryogenic performances.* (Poster)
- Joint Annual Meeting ISMRM-ESMRMB & ISMRT 31st Annual Meeting, London (UK), May 7-12 2022
 - **Lê Thanh Phong**, Wiström Emma, Hyacinthe Jean-Noël, Capozzi Andrea. *Triple Multinuclear Probe: Expanding the Throughput and Versatility of a dDNP Polarizer.* (Poster)
 - Wiström Emma Linnea, Capozzi Andrea, **Lê Thanh Phong**, Gruetter Rolf, Hyacinthe Jean-Noël. *Hyperpolarization of ¹²⁹Xe gas via dissolution DNP: beneficial tips and tricks.* (Poster)
 - Šimičić Dunja, Alves Brayan, Mosso Jessie Julie, **Lê Thanh Phong**, van Heeswijk Ruud B., Starčuková Jana, Klauser Antoine, Strasser Bernhard, Bogner Wolfgang, Cudalbu Cristina. *Fast high-resolution metabolite mapping on a preclinical 14.1T scanner using ¹H-FID-MRSI.* (Oral)
- MRS Workshop 2022: Overcoming the Barriers to Clinical Use, Lausanne (CH), August 22-24 2022
 - Wiström Emma, Capozzi Andrea, **Lê Thanh Phong**, Gruetter Rolf, Hyacinthe Jean-Noël. *Hyperpolarization of ¹²⁹Xe gas via dissolution DNP: beneficial tips and tricks.* (Poster)

- Šimičić Dunja, Alves Brayan, Mosso Jessie, **Lê Thanh Phong**, Starčuková Jana, Klauser Antoine, Strasser Bernhard, Bogner Wolfgang, Cudalbu Cristina. *Validation, quality control and reproducibility of ^1H FID-MRSI on a preclinical 14.1T.* (Poster)
- ISMRM & ISMRT Annual Meeting & Exhibition, Toronto (CA), June 3-8 2023
 - **Lê Thanh Phong**, Buscemi Lara, Lepore Mario, Capozzi Andrea, Hirt Lorenz, Mishkovsky Mor, Hyacinthe Jean-Noël. *Development and application of dynamic MRSI of an HP neuroprotective agent in an MCAO mouse model of ischemic stroke at 14.1T.* (Poster)
 - Wiström Emma Linnea, Hyacinthe Jean-Noël, **Lê Thanh Phong**, Gruetter Rolf, Capozzi Andrea. *^{129}Xe sublimation DNP towards hyperpolarized imaging standards.* (Poster)
 - Buscemi Lara, Lepore Mario, **Lê Thanh Phong**, Hirt Lorenz, and Mishkovsky Mor. *Does sex matter? A ^1H MRS metabolic study in a mouse model of transient ischemic stroke.* (Poster)

Thanh Phong Kevin LÊ

Swiss citizenship

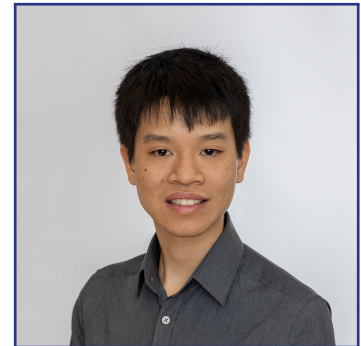
Place of origin: Ecublens VD

Date of birth: 14th May 1994

✉ thanh.le@alumni.epfl.ch

in thanh-phong-le

id 0000-0002-9615-5642



Education

- 2017-2023 **Doctor of Sciences**, *Laboratory of Functional and Metabolic Imaging, Doctoral Program in Physics*, École polytechnique fédérale de Lausanne (EPFL), Switzerland.
- 2015-2017 **Master of Science in Physics**, Minor in Computational Science and Engineering, *École polytechnique fédérale de Lausanne*, 5.69/6.00.
Master project: *Characterization and Mitigation of the Impact of Electroencephalography on Magnetic Resonance Imaging Data Quality at 7 Tesla*, supervised by Dr. Özlem Ipek and Dr. João Jorge.
Minor project: *Comparison of the Quasi-harmonic Debye Model to Experimental Thermophysical Data*, supervised by Prof. Nicola Marzari, Dr. Nicolas Hörmann and Dr. Nicolas Mounet.
- 2012-2015 **Bachelor of Science in Physics**, *École polytechnique fédérale de Lausanne*, 5.28/6.00.
 Exchange during the 3rd year at the University of Waterloo, ON, Canada.
Bachelor project: *Hall Effect Measurement on Thermoelectric Materials*, supervised by Prof. Jan Kycia.
- 2009-2012 **Cantonal Baccalaureate and Gymnasial Matura**, *Major in Physics and Applications of Mathematics and Minor in Chemistry*, Gymnase cantonal du Bugnon, Lausanne, Switzerland, 5.50/6.00.
Matura work: *Synthesis and Characterization of Ferrofluids*, supervised by Claude Montandon.

Work and Teaching Experience

- Sept. 2022 - **École polytechnique fédérale de Lausanne**
 Sept. 2023 Doctoral assistant. Teaching assistant for General Physics courses.
- Oct. 2017 - **Geneva School of Health Sciences, University of Applied Sciences and Arts Western Switzerland**
 Aug. 2022 Research and teaching assistant. Teaching the physics of MRI to 1st and 2nd year Bachelor students in Medical radiology technology. Conception, procurement and implementation of education and research infrastructure.
- Sept. 2016 - **École polytechnique fédérale de Lausanne**
 June 2017 Teaching assistant for the Massive Open Online Course of *Fundamentals of Biomedical Imaging*.
- May-Sept. **L&V Design, Mex, Switzerland**
 2015 Software/hardware development and testing for embedded measurement systems.

Extracurricular activities

- 2012-present **Swiss Physics Olympiad**
Teaching general physics to high school students, redaction of exam questions, mentoring of students at international contests, organization of events and training camps.
- 2012-present **Swiss Chemistry Olympiad**
Teaching theoretical and experimental chemistry to high school students, mentoring of students at international events.

Further achievements

- 2022 **Best Trainee Presentation**, *ISMARM Hyperpolarization Methods & Equipment Study Group*.
- 2020 **Magna Cum Laude** (15% percentile), *2020 ISMARM & SMRT Virtual Conference*.
- 2012 **Bronze Medal**, *44th International Chemistry Olympiad*, Washington DC, USA.
- 2012 **Bronze Medal**, *43rd International Physics Olympiad*, Estonia.
- 2012 **Materials Prize for the Matura work**, *Section of Materials Science and Engineering, École polytechnique fédérale de Lausanne*.
- 2012 **Young Talent Award**, *Swiss Physical Society (SPS)*.

Competences

- Laboratory Dynamic nuclear polarization; Nuclear magnetic resonance (Bruker, RS2D and Magritek systems); Preclinical magnetic resonance imaging and X-nuclei spectroscopy (Bruker and Varian); Electron spin resonance (ESR); Mechatronic, electronic and RF instrumentation; Cryogenic and vacuum systems; Basic machining (lathe and mill).
- Computer C, C++, Java, MATLAB, Python, LabVIEW, Sim4Life, AutoCAD.
- Animal experimentation RESAL Module 1 qualification (equivalent FELASA EU functions ACD).

Languages

- French Native language
- English CEFR C1
- German CEFR B2
- Vietnamese Basic knowledge